EFFECT OF SURFACE PROTRUSIONS AND CAVITIES ON AIRFOIL AERODYNAMIC EFFICIENCY AT LOW REYNOLDS NUMBER

A thesis submitted to the
University of Petroleum & Energy Studies

For the award of
DOCTOR OF PHILOSOPHY
in
Aerospace Engineering

BY

Bodavula Aslesha

October 2020

SUPERVISOR (S)

Dr. Rajesh Yadav
Dr. Ugur Guven

UPES
UNIVERSITY WITH A PURPOSE

Department of Aerospace Engineering
School of Engineering
University of Petroleum and Energy Studies
DEHRADUN-248007: Uttarakhand

EFFECT OF SURFACE PROTRUSIONS AND CAVITIES ON AIRFOIL AERODYNAMIC EFFICIENCY AT LOW REYNOLDS NUMBER

A thesis submitted to the
University of Petroleum & Energy Studies

For the award of
DOCTOR OF PHILOSOPHY
in
Aerospace Engineering

BY

Bodavula Aslesha
(SAP ID- 500049141)

October 2020

Supervisor

Dr. Rajesh Yadav
Assistant Professor – Selection Grade
Department of Aerospace Engineering
University of Petroleum and Energy Studies

External Supervisor

Dr. Ugur Guven
Professor

UNIVERSITY WITH A PURPOSE

Department of Aerospace Engineering
School of Engineering
University of Petroleum and Energy Studies
DEHRADUN-248007: Uttarakhand

DECLARATION

I declare that the thesis entitled **"Effect of Surface Protrusions and Cavities on Airfoil Aerodynamic Efficiency at Low Reynolds Number"** has been prepared by me under the guidance of **Dr. Rajesh Yadav**, Assistant professor in Department of Aerospace Engineering, University of Petroleum & Energy Studies and **Dr. Ugur Guven.** No part of this thesis has formed the basis for the award of any degree or fellowship previously.

Bodavula Aslesha

School of Engineering
University of Petroleum & Energy Studies
Dehradun-248007: Uttarakhand

DATE: 03/03/2021

UPES
UNIVERSITY WITH A PURPOSE

Great Place To Work. Certified
MAR 2020-FEB 2021
INDIA

CERTIFICATE

I certify that **Bodavula Aslesha** has prepared her thesis entitled "**Effect of Surface Protrusions and Cavities on Airfoil Aerodynamic Efficiency at Low Reynolds Number**", for the award of PhD degree of the University of Petroleum & Energy Studies, under my guidance. She has carried out the work at the Department of Aerospace Engineering, University of Petroleum & Energy Studies.

Supervisor

Dr. Rajesh Yadav
Assistant Professor – Selection Grade
Department of Aerospace Engineering
University of Petroleum and Energy Studies

Date: 03/03/2021

CERTIFICATE

I certify that **Bodavula Aslesha** has prepared her thesis entitled "**Effect of Surface Protrusions and Cavities on Airfoil Aerodynamic Efficiency at Low Reynolds Number**", for the award of PhD degree of the University of Petroleum & Energy Studies, under my guidance. She has carried out the work at the Department of Aerospace Engineering, University of Petroleum & Energy Studies.

External Supervisor

Dr. Ugur Guven
Professor
Date: 03/03/2021

ABSTRACT

With increasing the demand of the Unmanned Aerial Vehicles (UAVs) and Micro Aerial Vehicles (MAVs) form the past few years, researchers are started to develop their interest in this area. These vehicles fly at very low Reynolds Number. Under this low Reynolds number one more area is of the wind turbines. Researchers studied the effect of the flow at the low Reynolds number but still there is need to study more. At this Reynolds flow generally tends to separate from the surface of the airfoil at low angle of attack. Based on the profile of the airfoil the separation point on the airfoil varies. To control the flow mechanism, there are two basic types, one is passive control flow mechanism and other one is active flow control mechanism. In this research passive flow control mechanism is used to study the effect over a surface of the symmetrical airfoil NACA0012.

In this study, the numerical analysis carried out over a NACA0012 airfoil to inspect the effect of protrusion and cavity for both static stall and dynamic stall. For the Static stall, numerical analysis of the protrusion and cavity is conducted at the Reynolds number of 100000 and 50000 at the different angle of starting from the 0° to 20° with gap of the 2°. For Dynamic stall numerical analysis carried out at the Reynolds number of 135000, with airfoil pitching about its quarter chord. Along with the grid independence study, solver validation studies were conducted against the experimental observations by Ohtake et al., Rinoie and Takemura and at in-house experimental facility for the static case. For the dynamic airfoil case, the experimental validation was done against the findings of Lee et al.

From the results, circular protrusions at the leading do not destroy the lift much but increases drag irrespective of height. Circular protrusion at all other locations on the suction surface diminishes lift with enhancement in drag. It was observed the circular shaped protrusion showed the better results at 0.05c, 0.10c location with protrusion height 0.005c for the Reynolds number 100000. An

exception is observed for a smaller protrusion at 10% chord wherein the lift marginally with increased aerodynamic efficiency at moderate AOAs, mitigating the phenomena of stall. In pre-stall regime, as the height of the protrusion height increase at all location the values of the lift coefficient and L/D are reduced drastically. All the protrusions exhibit an improvement in time averaged lift coefficients comes with enhanced flow unsteadiness due to vigorous vortex shedding in the post-stall regime. With reduction in Reynolds number, the lift further deteriorates, especially at low AOAs. Even a triangle shaped protrusions at the leading edge and at 5% chord on the pressure surface offer no improvement in lift or aerodynamic efficiency. The small triangular protrusion at 5% chord on the suction surface however, mitigates the stall without degrading aerodynamic efficiency. The larger protrusion of both shapes however, eliminates vortex shedding and flow unsteadiness at low AOAs.

Even a circular cavities on the suction surface, offers no improvement in the lift in the pre-stall regime, with significant reductions in aerodynamic efficiency, other than the shallower cavity at 0.1c location at a Reynolds number of 10^5. This configuration offers some improvement in aerodynamic efficiency at moderate AOAs, due to reduction drag. The circular cavities at 10% chord and 25% chord however diminishes the vortex shedding frequency at low AOAs, in fact the deeper cavities eliminates them in most cases. At a Reynolds number of 50000 however, these cavities offer significant improvements in aerodynamic efficiency due to reduction drag primarily, at moderated AOAs, when located at 10% chord. Cavities at other locations offer no improvements in either lift or aerodynamic efficiency, except at few AOAs. The deeper cavity that offers reductions in drag also eliminate vortex shedding in the pre-stall regime. The circular shallower cavity at all locations however, enhances the frequency of vortex shedding. Triangular cavity at a Reynolds number of 10^5 mitigates the stall with lift increasing monotonically with AOAs, but comes with penalty of drag rise. The drag rise and reductions in aerodynamic efficiency diminishes as the cavity moves downstream. However, the triangular

cavity at downstream location induces vortex shedding at lower AOAs in the post stall regime. The triangular cavity offers mitigation of stall even for a Reynolds number of 50000, however, with little or no reduction in aerodynamic efficiency at almost all AOA. In fact, significant improvements in L/D values can be observed at some AOAs and at all AOAs for the mid-chord location. The triangular cavities however, fail to eliminate vortex shedding though.

From the results of the effect of dynamic stall on protrusion and cavity. All protrusions, at small positive AOAs, create a strong suction aft of the protrusion while destroying the suction ahead of it. The only noticeable favourable finding for the protrusion on airfoil is the occurrence of positive lift for a protrusion height of 0.01c, at very low AOAs. The protrusions on the suction surface deteriorates the performance of the airfoil in pitch motion with enhanced drag and reduced dynamic stalling angle. The only favourable finding for the protrusion on airfoil is the occurrence of positive lift for a protrusion height of 0.01c, at very low AOAs. The cavities showed significant improvements in the dynamic aerodynamic characteristics. Most cavities eliminate the small-scale oscillations in lift and drag during upstroke motion at low and moderate AOAs. For all cavities, time averaged lift is increased during downstroke motion, reducing the hysteresis loss. Even a positive lift is obtained for the deeper cavity at quarter-chord, at low AOAs during downstroke motion. Lift is increased marginally, with reductions in drag as well, during the upstroke motion for the deeper cavity at the quarter chord. The airfoil with deeper cavity at mid-chord shows no stall during the upstroke motion i.e. up to $\alpha = 25°$, with favourable reductions in the drag as well. The C_l value of 2.5 was observed at this AOA.

ACKNOWLEDGMENT

I would first like to thank my Ph.D. advisors Dr. Rajesh Yadav and Dr. Ugur Guven, for the constant support and encouragement during this research work. Their passion and determination towards research have constantly inspired me during my Ph.D. study. I am very grateful to my guides to support me at every step of research articles and to train me in presenting skills that help me to build my confidence and become a qualified researcher. Without their constant support, I would never be able to accomplish my Ph.D. work. The knowledge and excellence that my guides passed on me, have made me today and will continue helping my future life.

I would like to express gratitude to Dr. S. J. Chopra (Chancellor), Dr. Sunil Rai (Vice-Chancellor), and Dr. Kamal Bansal (Dean), at the University of Petroleum & Energy Studies for their esteemed support for my research work. A special thanks to Dr. Jitendra K. Pandey and his R&D team at UPES for financial support through SEED, and further, acknowledge the continuous encouragement received from Dr. Kamal Bansal for supporting this work in all its stages.

I am grateful to the Head of the Department of Aerospace Engineering and faculty members of the Department of Aerospace Engineering for their continuous encouragement and support throughout my Ph.D. I am also grateful to Shikhar Purohit (Doctoral Research Fellow in Department of Aerospace Engineering), lab technicians of Aerospace Engineering and Mechanical Engineering for their support in wind tunnel experimental setup at our Institute (UPES). I would like to thank Mr. Deepak Rawat, Microsoft Associate of IT for his support in the CFD lab. I want to thank the University management for supporting us to complete this research work.

I would like to express my special thanks to Dr. Meera C S for her continuous support and encouragement throughout my Ph.D. I would like to continue this special thanks to my friends Dr. P. Swami Sairam, Dr. S R V S Prasanna, Dr. Caneon Kurien, and Dr. Debajyoti Bose for all the discussions and inputs provided. I also thank Ms. Ila Singhal, Mr. Balaji K, Ms. Varnita Varma, Mr. Krishna Moorty R, and Glen Bennet Hermon for their support.

Finally, I express my deepest gratitude to my parents Bodavula Laxmi Narasimha Swamy, Bodavula Kateswaramma, my sisters Nammi Anantha Lakshmi, Alladi Naga Anusha, Bodavula Amitha, and my brother Bodavula Naga Sai Srinivas for their constant support and love at every stage of my life. I would like to extend my thanks to Nammi Kiran Kumar, Alladi Pawan Kumar, Alladi Krithi, Nammi Lakshmi Chaitrika, Alladi Meghana, and family members. I am very grateful for their sacrifices and efforts made by them during my Ph.D. Completing this degree would never be possible without their love and encouragement.

Dedicated

To my family

TABLE OF CONTENTS

DECLARATION.....i

CERTIFICATE.....Error! Bookmark not defined.

CERTIFICATE..... iii

ABSTRACT.....iv

ACKNOWLEDGMENT vii

LIST OF FIGURES xvi

LIST OF TABLES xxix

LIST OF SYMBOLS xxx

ABBREVATION..... xxxii

CHAPTER 1. INTRODUCTION.....33

1.1 OVERVIEW 33

1.2 MOTIVATION AND OBJECTIVES OF RESEARCH.....40

1.3 STRUCTURE OF THE THESIS.....41

CHAPTER 2. LITERATURE REVIEW 43

2.1 AIRFOIL AT LOW REYNOLDS NUMBER.....43

2.2 PROTUBERANCES.....51

2.3 LITERATURE REVIEW ON CAVITIES 55

2.4 LITERATURE REVIEW ON DYNAMIC STALL.....58

2.5 SUMMARY OF LITERATURE REVIEW.....62

CHAPTER 3. METHODOLOGY 64

3.1 GOVERNING EQUATIONS 64

3.1.1 CONTINUITY EQUATION 64

3.1.2 MOMENTUM EQUATION.....65

3.2 TURBULENCE MODELING.....66

3.3 GEOMETRIC MODELING AND GRID GENERATION.....71

3.4 SOLVER SETUP.....76

3.4.1 SPATIAL AND TEMPORAL DISCRETIZATION 78

3.4.2 BOUNDARY CONDITIONS 80

3.4.3 GRID INDEPENDENCE AND SOLVER VALIDATION 81

3.5 EXPERIMENTAL SET-UP 85

3.5.1 WIND TUNNEL SPECIFICATIONS.....85

3.5.2 WIND TUNNEL MODEL AND ACCESSORIES 87

3.5.3 WIND TUNNEL PROCEDURE.....91

CHAPTER 4. EFFECT OF PROTRUSION 94

4.1 EFFECT OF CIRCULAR PROTRUSION AT REYNOLDS NUMBER 10^5 94

4.1.1 CIRCULAR PROTRUSION AT THE LEADING EDGE.....94

4.1.2 CIRCULAR PROTRUSION AT 0.05C ON THE UPPER SURFACE.....98

4.1.3 CIRCULAR PROTRUSION AT 0.1C ON SUCTION SURFACE 103

4.1.4 CIRCULAR PROTRUSION AT 0.25C ON SUCTION SURFACE 108

4.1.5 CIRCULAR PROTRUSION AT 0.50C ON SUCTION SURFACE 112

4.1.6 CIRCULAR PROTRUSION AT 0.05C ON PRESSURE SURFACE 115

4.1.7 EFFECT OF CIRCULAR PROTRUSIONS ON STROUHAL NUMBER 118

4.2 EFFECT OF CIRCULAR PROTRUSION AT Re = 50,000.....120

4.2.1 EFFECT OF PROTRUSION AT LEADING EDGE 120

4.2.2 EFFECT OF PROTRUSION ON SUCTION SURFACE AT 0.05C 125

4.2.3 EFFECT OF PROTRUSION ON PRESSURE SURFACE AT 0.05C 129

4.2.4 EFFECT OF PROTRUSION ON STROUHAL NUMBER.....132

4.3 EFFECT OF TRIANGLE SHAPED PROTRUSION AT REYNOLDS NUMBER 10^5 135

4.3.1 TRIANGLE SHAPED PROTRUSION AT THE LEADING EDGE 136

4.3.2 TRIANGLE SHAPED PROTRUSION AT 0.05C ON THE SUCTION SURFACE 140

4.3.3 TRIANGULAR PROTRUSION AT 0.05C ON THE PRESSURE SURFACE.....147

4.3.4 EFFECT OF TRIANGULAR PROTRUSIONS ON STROUHAL NUMBER 152

4.4 SUMMARY 155

CHAPTER 5. EFFECT OF CAVITY 160

5.1 EFFECT OF CIRCULAR CAVITY AT Re =10^5 160

5.1.1 CAVITY AT 0.10C LOCATION ON SUCTION SURFACE.....160

5.1.2 CAVITY AT 0.25C LOCATION ON the SUCTION surface 164

5.1.3 CAVITY AT 0.50C LOCATION ON SUCTION PRESSURE ...168

5.1.4 EFFECT OF CAVITY ON STROUHAL NUMBER.....170

5.2 EFFECT OF CIRCULAR CAVITY AT REYNOLDS NUMBER 50000 172

5.2.1 EFFECT OF CIRCULAR CAVITY AT 0.10C LOCATION 172

5.2.2 EFFECT OF CIRCULAR CAVITY AT 0.25C LOCATION 176

5.2.3 EFFECT OF CIRCULAR CAVITY AT 0.50C LOCATION 181

5.2.4 EFFECT OF CIRCULAR CAVITY ON STROUHAL NUMBER 183

5.3 EFFECT OF TRIANGLE SHAPED CAVITY AT REYNOLDS NUMBER 10^5 185

5.3.1 EFFECT OF TRIANGLE SHAPED CAVITY AT 0.10C LOCATION 185

5.3.2 EFFECT OF TRIANGLE SHAPED CAVITY AT 0.25C LOCATION 188

5.3.3 EFFECT OF TRIANGLE SHAPED CAVITY AT 0.50C LOCATION 192

5.3.4 EFFECT OF TRIANGULAR CAVITY ON STROUHAL NUMBER 196

5.4 EFFECT OF TRIANGLE SHAPED CAVITY AT REYNOLDS NUMBER 50000 198

5.4.1 EFFECT OF TRIANGLE SHAPED CAVITY AT 0.10C LOCATION 198

5.4.2 EFFECT OF TRIANGLE SHAPED CAVITY AT 0.25C LOCATION 204

5.4.3 EFFECT OF TRIANGLE SHAPED CAVITY AT 0.50C LOCATION 206

5.4.4. EFFECT OF TRIANGULAR CAVITY ON STROUHAL NUMBER 209

5.5 SUMMARY 211

CHAPTER 6. EFFECT OF PROTRUSION AND CAVITY ON DYNAMIC STALL.....220

6.1 EFFECT OF TRIANGLE SHAPED CAVITY ON DYNAMIC STALL 220

6.1.1 EFFECT OF TRIANGLE SHAPED CAVITY AT 0.10C LOCATION 220

6.1.2 EFFECT OF TRIANGLE SHAPED CAVITY AT 0.25C LOCATION 230

6.1.3 EFFECT OF TRIANGLE SHAPED cavity AT 0.50C LOCATION 238

6.2 CIRCULAR PROTRUSION ON DYNAMIC STALL 246

6.2.1 EFFECT OF CIRCULAR PROTRUSION AT 0.05C LOCATION 246

6.2.2 EFFECT OF CIRCULAR PROTRUSION AT 0.10C LOCATION 253

6.3 SUMMARY 260

CHAPTER 7. CONCLUSION AND FUTURE WORK 263

On Static Aerodynamic Characteristics of an Airfoil 263

On Dynamic Aerodynamic Characteristics of an Airfoil 279

Future Work 282

REFERENCES.....284

APPENDICES 303

LIST OF FIGURES

Figure 1.1:Predator [3].....33

Figure 1.2: Flight Speed Versus Reynolds number for flying vehicles [2] 34

Figure 1.3: Laminar Separation Bubble [21] 36

Figure 1.4: Pressure distribution at the suction surface [22].....36

Figure 1.5: Vortex generator [31] 39

Figure 1.6: Hypothesized GF mechanism [29] 39

Figure 3.1: Geometries of the airfoil with (a) Clean Configuration (b) Circular Shaped Protrusion (c) Triangle Shaped Protrusion (d) Circular Shaped Cavity (e) Triangle shaped cavity 72

Figure 3.2 Multi-block grid around NACA 0012 airfoil with protrusions and cavities 75

Figure 3.3. Quad dominant grid generation 76

Figure 3.4: Pressure Based segregated Algorithm [144] 78

Figure 3.5: Graphic representation of Pitching Motion 80

Figure 3.6: Grid Independence Study for Reynolds Number 100000 81

Figure 3.7: Grid Independence Study for Reynolds Number 50000 82

Figure 3.8: Solver Validation Study 83

Figure 3.9: Evolution of lift coefficient at $\alpha = 8^{o}$.....83

Figure 3.10: Grid Independence Study of an oscillating airfoil.....84

Figure 3.11: C_l-α curve for oscillating NACA 0012.....84

Figure 3.12: Low-Speed Wind tunnel at UPES 86

Figure 3.13: Schematic Diagram of Wind tunnel 87

Figure 3.14: Wind Tunnel Airfoil Model.....87

Figure 3.15: 32-Port Electronic Pressure Scanner 88

Figure 3.16: Smoke Generator for Wind Tunnel 88

Figure 3.17: 6-Component Balance system used in the wind tunnel [148] 89

Figure 3.18: Hot-Wire Anemometer Setup [149] 90

Figure 3.19: Mounted Model inside the Wind Tunnel.....93

Figure 3.20: Pressure distribution around clean NACA 0012 at α = 8°.....93

Figure 4.1: Aerodynamic coefficients for NACA 0012 with a circular protrusion at the leading edge 95

Figure 4.2: Vortex structure for an airfoil with leading-edge protrusion of h= 0.005c and α=16º 96

Figure 4.3: Intermittency Contours for Airfoil with Protrusion of height 0.005c at LE 97

Figure 4.4: Intermittency Contours for Airfoil with Circular Protrusions of heights 0.01c and 0.02c at the LE.....98

Figure 4.5: Lift Coefficient and Aerodynamics Efficiency of an Airfoil with Protrusion at 0.05c on the upper surface 99

Figure 4.6: Instantaneous streamlines at α= 8º for (a) clean airfoil, and (b) protrusion at 0.05c.....100

Figure 4.7: Surface pressure distribution for an airfoil with protrusion of h=0.01c at 0.05c on the upper surface 101

Figure 4.8: Skin friction coefficient for an airfoil with protrusion of h=0.01c at 0.05c on the upper surface.....101

Figure 4.9: Intermittency Contour for Airfoil with Protrusion located at 0.05c with h= 0.01c and α = 8º 101

Figure 4.10: Velocity profile's over airfoil with protrusion h=0.02c, located at 0.05c, at 8º 102

Figure 4.11: Aerodynamic coefficients of an airfoil with a protrusion at 0.10c on the upper surface 103

Figure 4.12: Vorticity magnitude for circular protrusion at 0.10c with h = 0.005c at α=20^0 105

Figure 4.13: Velocity profile's over airfoil with protrusion h=0.02c, located at 0.10c, at 8º 106

Figure 4.14: Instantaneous surface pressure distribution over an airfoil with protrusion of height 0.01c, located at 0.1c 107

Figure 4.15: Instantaneous skin friction coefficient over an airfoil with protrusion of height 0.01c, located at 0.1c 107

Figure 4.16: Variation of aerodynamic coefficients for an airfoil with a protrusion at 0.25c 108

Figure 4.17: Instantaneous surface pressure for an airfoil with a protrusion at 0.25c and α =16º 109

Figure 4.18: Instantaneous skin friction for an airfoil with a protrusion at 0.25c and α =16º 110

Figure 4.19: Instantaneous vortex structure at α =16º for airfoil with protrusion at 0.25c location and h = 0.005 110

Figure 4.20: Lift history for an airfoil with a protrusion at 0.25c and α = 16º 111

Figure 4.21: Instantaneous streamlines for an airfoil with protrusion of h = 0.02c located at 0.25c 112

Figure 4.22: Lift Coefficient and Aerodynamic Efficiency for an airfoil with a protrusion at 0.50c 113

Figure 4.23: Lift history for an airfoil with a protrusion at 0.5c and α=16º..... 113

Figure 4.24: Instantaneous surface pressure distribution for an airfoil with protrusion of h = 0.02c at 0.5c 114

Figure 4.25: Vortex system for an airfoil with a protrusion at 0.5c on the suction surface with h=0.02c 115

Figure 4.26: Aerodynamics characteristic of an airfoil with protrusion located at 0.05c on the Pressure surface 116

Figure 4.27: Intermittency of Protrusion with height 0.01c at pressure surface 0.05c location at a different angle of attack..... 116

Figure 4.28: Intermittency for the protrusion location at pressure surface 0.05c location at 8º 117

Figure 4.29: Strouhal Number for airfoil with a circular protrusion..... 119

Figure 4.30: Aerodynamics characteristic of an airfoil with a protrusion at LE..... 120

Figure 4.31: Vorticity Contours for airfoil at α = 4º, with protrusion of height 0.005c and located at LE 121

Figure 4.32: Pressure distribution and Skin friction over an airfoil with protrusion height 0.005c located at the leading edge, at 4º 121

Figure 4.33: Intermittency for an airfoil with a protrusion at the leading edge, α = 4º 122

Figure 4.34: Vorticity magnitude over an airfoil protrusion height 0.01c located at the leading edge, at 4º 123

Figure 4.35: Vorticity magnitude over an airfoil protrusion height 0.02c located at the leading edge, at 4º 124

Figure 4.36: Roll up vortices for the protrusion height 0.02c located at the leading edge, at α = 4º 125

Figure 4.37: Aerodynamics characteristic of an airfoil with protrusion located at 0.05c on the Suction surface 126

Figure 4.38: Streamlines over an airfoil with protrusion height 0.005c located at 0.05c and clean configuration at 0º 127

Figure 4.39: Intermittency contour for airfoil at α =6º, with a protrusion at 0.05c on the suction surface 128

Figure 4.40: Instantaneous streamlines over an airfoil at α=14º with protrusion of height 0.02c at 0.05c on the suction surface 128

Figure 4.41: Pressure distribution over an airfoil at α=14º with protrusion of height 0.02c at 0.05c on the suction surface 129

Figure 4.42: Aerodynamics characteristic of an airfoil with protrusion located at 0.05c on the pressure surface 129

Figure 4.43: Vorticity magnitude for the protrusion height 0.005c located at pressure surface 0.05c, at 2º 130

Figure 4.44: Vorticity magnitude for the protrusion height 0.01c located at pressure surface 0.05c, at 2º 131

Figure 4.45: Roll up vortices for the protrusion height 0.02c located on the pressure surface, at 4º 131

Figure 4.46: Intermittency contours for airfoil at α = 8º, with a protrusion at 0.05c on the pressure surface 132

Figure 4.47: Transient oscillations in the lift of airfoil with circular protrusion for Re = 50000, α =4° 133

Figure 4.48: Strouhal Number for various protrusion configurations 135

Figure 4.49: Aerodynamic characteristics of with Triangular Protrusion at Leading Edge 136

Figure 4.50: Vorticity contour over an airfoil with protrusion of height 0.02c located at the leading edge at α = 0º 137

Figure 4.51: Vorticity magnitude over an airfoil with protrusion height 0.02c located at the leading edge at α = 4º 138

Figure 4.52: Intermittency for the protrusion at the leading edge, at 4º 138

Figure 4.53: Lift coefficient history for an airfoil with a protrusion at the leading edge and α=16° 139

Figure 4.54: Aerodynamic characteristics of NACA0012 with a triangular protrusion on the suction surface at 0.05c 140

Figure 4.55: Streamlines over an airfoil at α = 0°, with protrusion of height 0.01c located at 0.05c on the suction surface 141

Figure 4.56: Instantaneous vortex structure for airfoil with protrusion at 5%c, h = 0.005c and α =18^0 142

Figure 4.57: Laminar separation for bubble at α = 8° for NACA 0012 143

Figure 4.58: Velocity Profile over an airfoil with protrusion height 0.01c located at 0.05c, at 8° 143

Figure 4.59: Streamlines for flow over an airfoil with protrusion of height h= 2%c located at 5%c 145

Figure 4.60: Intermittency contour over an airfoil at α=4º, with protrusion of height=0.02c, located at 0.05c 145

Figure 4.61: Velocity Profile over an airfoil with protrusion height 0.02c located at 0.05c, at 8° 145

Figure 4.62: Lift coefficient history of triangular protrusion at 0.05c and α = 16° .. 146

Figure 4.63: Lift and drag variations of NACA0012 with a protrusion at 5%c on the pressure surface.....147

Figure 4.64: Pressure distribution for minimum and maximum lifts for protrusion with h=0.01c at α = 12°.....148

Figure 4.65: Skin Friction coefficient for minimum and maximum lifts for protrusion with h=0.01c at α = 12°.....149

Figure 4.66: Streamlines over an airfoil with protrusion height 0.01clocated at suction surface 0.05c, at 0º.....150

Figure 4.67: Intermittency contours for airfoil at α = 4°, with a protrusion at 0.05c on the pressure surface.....151

Figure 4.68: Lift coefficient history at $\alpha=16^0$ on the pressure surface.....151

Figure 4.69: Strouhal Number for different circular protrusion arrangements.....154

Figure 5.1: Aerodynamic characteristics of NACA0012 airfoil with a cavity at 0.10c on the suction surface 161

Figure 5.2: Aerodynamic Characteristics of NACA0012 airfoil with cavity depth 0.025c at 0.10c location 162

Figure 5.3: Intermittency contours for an airfoil with a circular cavity at 0.1c, on the suction surface. 163

Figure 5.4: Lift coefficient versus time for the cavity depth 0.05c at 0.10c on the suction surface.....164

Figure 5.5: Aerodynamic Characteristics of NACA0012 airfoil with a cavity at 0.25c location.....165

Figure 5.6: Vorticity magnitude of the cavity with depth 0.025c at 0.25c location at 2º 166

Figure 5.7: Intermittency in the flow for the cavity at 0.25c location 166

Figure 5.8: Pressure distribution over an airfoil at α= 2º, with the cavity of depth 0.025c, located at 0.25c on the suction surface 167

Figure 5.9: Skin friction over an airfoil at α= 2º, with the cavity of depth 0.025c, located at 0.25c on the suction surface 167

Figure 5.10: Aerodynamic Characteristics of NACA0012 airfoil with a cavity at 0.50c location..... 169

Figure 5.11: Intermittency in the flow for the cavity depth 0.05c at 0.50c location . 169

Figure 5.12: Vorticity contour over an airfoil at α = 14°, with a cavity at 0.5c location on the suction surface 170

Figure 5.13: Strouhal Number for an airfoil with various cavities 172

Figure 5.14: Aerodynamic characteristics of an airfoil with a circular cavity at 0.10c location..... 173

Figure 5.15: Vorticity contours over an airfoil at α = 0°, with a cavity of depth 0.05c, located at 0.10c 174

Figure 5.16: Intermittency contour for an airfoil with cavity located at 0.10c 175

Figure 5.17: Vorticity contour for an airfoil with cavity located at 0.10c 175

Figure 5.18: Aerodynamic Characteristics of Circular Cavity at 0.25c location 176

Figure 5.19: Vorticity contour for an airfoil with the cavity of depth 0.025c located at 0.25c, at α= 0° 177

Figure 5.20: Vorticity contours for an airfoil with cavity depth 0.05c located at 0.25c, at α = 0°..... 178

Figure 5.21: Intermittency for the cavity with depth 0.025c located at 0.25c. 178

Figure 5.22: Vorticity magnitude over an airfoil with cavity depth 0.025c located at 0.25c, at 6° 179

Figure 5.23: Contours of intermittency and vorticity magnitude over an airfoil with cavity depth 0.05c, located at 0.25c, at α =6° 180

Figure 5.24: Vorticity contours over an airfoil with a cavity at 0.25c, at α = 16° 180

Figure 5.25: Aerodynamic characteristics of an airfoil with a circular cavity at 0.5c location on the suction surface 181

Figure 5.26: Vorticity contour over an airfoil with cavity depth 0.05c located at 0.50c, at α =2° 182

Figure 5.27: Flow intermittency for the cavity depth 0.05c located at 0.50c 182

Figure 5.28: Vorticity contour for an airfoil with cavity located at 0.50c, at α = 4° 183

Figure 5.29: Strouhal number for an airfoil with a circular cavity at Re = 50000 184

Figure 5.30: Aerodynamic Characteristics of an airfoil with a triangular cavity at 0.10c location 185

Figure 5.31: Small separation bubbles on the surface of the airfoil with cavity depth 0.025c at 0.10c location, at α = 4º 187

Figure 5.32: Intermittency for the cavity at 0.10c location at 4º 187

Figure 5.33: Vorticity contours for an airfoil with a cavity at 0.1c location 188

Figure 5.34: Aerodynamic Characteristics of NACA0012 airfoil with a cavity at 0.25c location 189

Figure 5.35: Vorticity contours over an airfoil with the cavity of depth 0.025c located at 0.25c, at α = 4° 191

Figure 5.36: Intermittency over an airfoil with a triangular cavity at 0.25c location, at α = 4° 191

Figure 5.37: Instantaneous vortex structure for airfoil with cavity depth 0.05c at the location 0.25c at α = 18º 191

Figure 5.38: Aerodynamic Characteristics of NACA0012 airfoil with cavity at 0.50c location.....192

Figure 5.39: Intermittency for the cavity at 0.50c location, at 6º.....193

Figure 5.40: Instantaneous vortical structures over an airfoil with cavity located at 0.50c, at α = 12°.....194

Figure 5.41: Pressure distribution over an airfoil with cavity located at 0.50c, at α = 12°.....195

Figure 5.42: Skin friction over an airfoil with cavity located at 0.50c, at α = 12°....195

Figure 5.43: Pressure distribution for minimum and maximum lifts by airfoil cavity with depth = 0.025c, at α = 16º.....195

Figure 5.44: Strouhal Number for various cavity configurations.....197

Figure 5.45: Aerodynamic Characteristics of Circular Cavity at 0.10c location.....199

Figure 5.46: Vorticity contour over an airfoil with cavity depth 0.05c located at 0.10c, at α =0°.....200

Figure 5.47: Intermittency contour over an airfoil with triangular cavity located at 0.10c, at α =8°.....201

Figure 5.48: Vorticity contour over an airfoil with triangular cavity located at 0.10c, at α = 8° 201

Figure 5.49: Pressure distribution over an airfoil with triangular cavity located at 0.10c 203

Figure 5.50: Skin friction over an airfoil with triangular cavity located at 0.10c.....203

Figure 5.51: Vortex structure for the cavity with depth 0.025c at 0.10c location, at 16º 203

Figure 5.52: Aerodynamic Characteristics of Triangle shaped Cavity at 0.25c location 204

Figure 5.53: Flow-field around an airfoil at α = 2°, with a triangular cavity of depth 0.05c at 0.25c 205

Figure 5.54: Flow-field around an airfoil at α = 6°, with a triangular cavity of depth 0.05c at 0.25c 205

Figure 5.55: Aerodynamic Characteristics of Circular Cavity at 0.50c location 206

Figure 5.56: Vorticity contours over an airfoil with cavity located at 0.50c, at α = 12° 207

Figure 5.57: Intermittency over an airfoil with cavity located at 0.50c, at α = 12° .. 208

Figure 5.58: Pressure variation over an airfoil with cavity located at 0.50c, at α = 14° 208

Figure 5.59: Skin friction over an airfoil with cavity located at 0.50c, at α = 14°.... 209

Figure 5.60: Strouhal number for an airfoil with a triangular cavity 210

Figure 6.1: Aerodynamic characteristics of the Cavity at 0.10c Location 221

Figure 6.2: Vorticity Magnitude for the airfoil with cavity located at 0.10c during upstroke motion 223

Figure 6.3: Surface pressure and skin friction distribution during upstroke motion. 226

Figure 6.4: Vorticity Magnitude for the airfoil with cavity located at 0.10c during down-stroke motion 228

Figure 6.5: Surface pressure distribution during upstroke motion 229

Figure 6.6: Flow Intermittency for various airfoil configurations α = 3.98º, during down-stroke 230

Figure 6.7: Aerodynamic characteristics of the cavity at 0.25c Location 231

Figure 6.8: Vorticity magnitude at the Triangle shaped cavity with depth at 0.25 location 232

Figure 6.9: Surface pressure distribution during upstroke motion.....233

Figure 6.10: Skin Friction variation during upstroke motion 234

Figure 6.11: Vorticity magnitude at the Triangle shaped cavity with depth at 0.25 location.....236

Figure 6.12: Intermittency Contours for airfoil with cavity at 0.25 location, α = 3.98° 237

Figure 6.13: Surface pressure distribution during down-stroke motion 237

Figure 6.14: Skin Friction distribution during down-stroke motion.....238

Figure 6.15: Aerodynamic characteristics of the circular protrusion at 0.50c location 239

Figure 6.16: Vorticity contours for airfoils with cavity at 0.50c location, during upstroke motion 240

Figure 6.17: Intermittency Contours for airfoil with cavity at 0.5c location, α = 14.76°, during upstroke 241

Figure 6.18: Intermittency Contours for airfoil with cavity at 0.5c location, α = 22.66°, during upstroke 241

Figure 6.19: Surface pressure distribution over airfoil with cavity located at 0.50c, during upstroke motion.....242

Figure 6.20: Vorticity contours for airfoils with cavity at 0.50c location, during down-stroke motion 243

Figure 6.21: Surface pressure distribution over airfoil with cavity located at 0.50c, during down-stroke motion.....245

Figure 6.22: Skin Friction distribution over airfoil with cavity located at 0.50c, during up and down-stroke motion 246

Figure 6.23: Aerodynamic characteristics of the circular protrusion at 0.05c location 247

Figure 6.24: Vorticity contours for airfoils with protrusion at 0.05c location, during upstroke motion 248

Figure 6.25: Surface pressure distribution over airfoil with protrusion located at 0.05c, during upstroke motion 250

Figure 6.26: Vorticity contours for airfoils with protrusion at 0.05c location, during down-stroke motion 251

Figure 6.27: Surface pressure distribution over airfoil with protrusion located at 0.05c, during down-stroke motion.....252

Figure 6.28: Aerodynamic characteristics of the circular protrusion at 0.10c Location 254

Figure 6.29: Vorticity contours for airfoils with protrusion at 0.1c location, during upstroke motion 255

Figure 6.30: Surface pressure distribution over airfoil with protrusion located at 0.1c, during upstroke motion 257

Figure 6.31: Vorticity contours for airfoils with protrusion at 0.1c location, during down-stroke motion 259

Figure 6.32: Surface pressure distribution over airfoil with protrusion located at 0.1c, during down-stroke motion.....259

LIST OF TABLES

Table 3.1: Shape, Location, and Height of Protrusions Investigated.....73

Table 3.2: Shape, Location, and Depth of Cavity Investigated 74

LIST OF SYMBOLS

c	Chord length, m
c_d	Drag coefficient
Cl	Lift coefficient
$Cl_{, max}$	Maximum value of lift coefficient
c_p	Pressure coefficient
h	Height of protrusion normal to surface, m
k	Turbulent kinetic energy, m^2/s^2
k	Reduced Frequency
L/D	Lift to drag ratio
p	Pressure, Pa
p	Position of the Protrusion or Cavity
$Re_{\theta t}$	Momentum-thickness Reynolds number
$\widetilde{Re_{\theta t}}$	Transition thickness Reynolds number
t	Time, second
Tu	Turbulent Intensity

u	Cartesian components of velocity vector
$\overrightarrow{V}$	Velocity vector
x	Spatial coordinate
$y+$	Non-dimensional cell wall distance
α	Angle of attack (AOA), degrees (º)
γ	Intermittency
ρ	Density, kg/m^3
μ	Molecular viscosity, $kg/m\text{-}s$
μ_t	Turbulent viscosity
$\boldsymbol{\tau}_{ij}$	Viscous stress tensor
ω	Specific dissipation rate, s^{-1}

Subscripts

i, j = Spatial coordinate directions

ABBREVATION

AOA	Angle of Attack
CFD	Computational Fluid Dynamics
DMD	Dynamic Mode Decomposition
GF	Gurney Flap
LES	Large Eddy Simulation
LSB	Laminar Separation Bubble
MAV	Micro Aerial Vehicles
RANS	Reynolds Averaged Navier-Stokes
Re	Reynolds Number
SST	Shear Stress Transport
TVC	Trapped Vortex Cell
UAV	Unmanned Aerial Vehicles
UDF	User Defined Function
URANS	Unsteady Reynolds Averaged Navier-Stokes
VIV	Vortex Induced Vibrations

CHAPTER 1. INTRODUCTION

1.1 OVERVIEW

From the past few eras, there is prompt progress towards remotely guided aerial vehicles known as Unmanned Aerial Vehicles (UAVs) as shown in Fig 1.1. Smaller versions of these vehicles are known as Micro Aerial vehicles (MAVs). There are a few UAVs and MAVs that are bio-inspired. The application of these vehicles can be seen in both military and civilian sectors. These vehicles operate in a speed range of 15-85 km/h and the range of the Reynolds number between 40,000 and 1000,000 [1][2] with a maximum dimension of 15cm.

Figure 1.1:Predator [3]

These vehicles play a key role in different missions headed by military and civilian purposes. Usage of UAVs can be found for surveillance, cargo/payload drop, rescue missions, and geological surveying applications. Even other sectors find the application of these vehicles like chemical industries for inspecting the pipelines, wildlife photography, rescuing wild animals, and agricultural areas. These vehicles fly at very small Reynolds numbers and have to travel in restrained places with a basic minimum speed. At this speed, these

vehicles should possess a very high aerodynamic lift and efficiency. Enhancement in technology has caught the attention of many researchers onto investigating the aerodynamics and control of these vehicles.

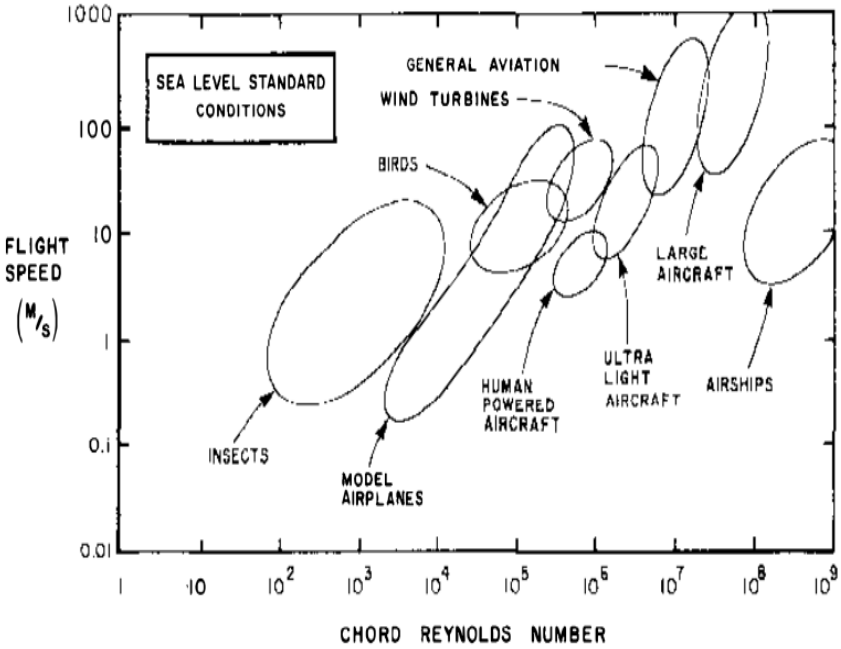

Figure 1.2: Flight Speed Versus Reynolds number for flying vehicles [2]

Apart from these vehicles, low Reynolds number aerodynamics finds its application in the study of wind turbines, used to extract wind energy. It is trending in renewable energy sources. Wind energy is a single station of energy being used broadly as a substitute to escape global warming due to chemical productions, power plants, and fossil fuel-based industries. Wind turbines are used to extract electricity, and there are different types of turbines available depending on the location and purpose. Wind turbines are located near offshore mainly used to generate electricity for providing navy and port; the typical height is 50-80 meters. Onshore wind turbines used for large scales applications have a maximum height of up to 150 meters. Small wind turbines are captive power generators, used mostly in schools, business places, and homes. These are clean and economical to maintain. The range of Reynolds number for wind turbines is $2x10^5$ to $2x10^7$ as given in Fig.1.2. Operating wind turbines at this Reynolds number is very stimulating because of changes in the flow direction,

turbulence effects, and some other factors. So while designing the wind turbine, the factors mentioned above have to be measured to assess the performance of the wind turbine. For small wind turbines, which are captive power generators, the range of Reynolds number is between 10^5 and 10^7. Apart from conventional wind turbines, renewable energy from wind kinetic energy can be extracted through wing-mills [4][5][6][7][8], kites [9], [10], [11], mechanisms based on Vortex-Induced Vibrations (VIV) [12], [13], [14], [15], [16], [17], [18], [19]. . Kites are used to extract energy from the high altitude winds. All these energy extraction mechanisms use some form of movement of wings, flat plates, or cylindrical objects through the application of aerodynamic forces at low Reynolds number[20]. Besides, micro and unmanned aerial vehicles, a high-altitude flight of space-crafts, and robots during earth's re-entry and planetary entries are interesting applications of flight at low Reynolds number.

Flight of these vehicles at low Reynolds number is associated with few problems. A major problem is a reduction in the lift coefficient due to flow separation, which is also associated with increased drag. Flow separation takes place over an airfoil due to the adverse pressure gradient. Usually, the flow gets separated and reattaches to the surface to produce the laminar separation bubble (LSB) while the flow is transitioning from laminar to turbulent. LSB can alter the actual profile of the airfoil and can influence aerodynamics characteristics. An LSB formed on the surface of the airfoil runs into an adverse pressure gradient to excite the flow to detach. In an adverse pressure gradient, the point of inflection takes place at the boundary layer, and the point of inflection rises with the strong suit of the adverse pressure gradient. For a moderate pressure gradient, a separation point occurs where the shear stress value goes to zero. At this condition, the boundary layer thickens, and the main flow lifts off the surface. Downstream of the point of separation, denoted by S in Fig. 1.3 [21], the flow can be approximately separated into two key regions, as clearly shown in Fig. 1.4.

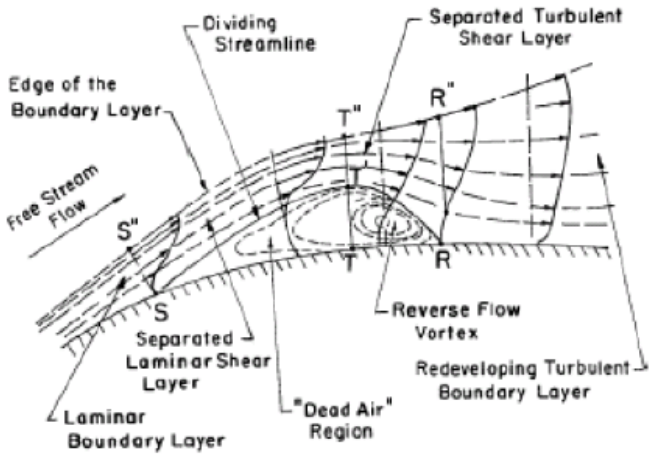

Figure 1.3: Laminar Separation Bubble [21]

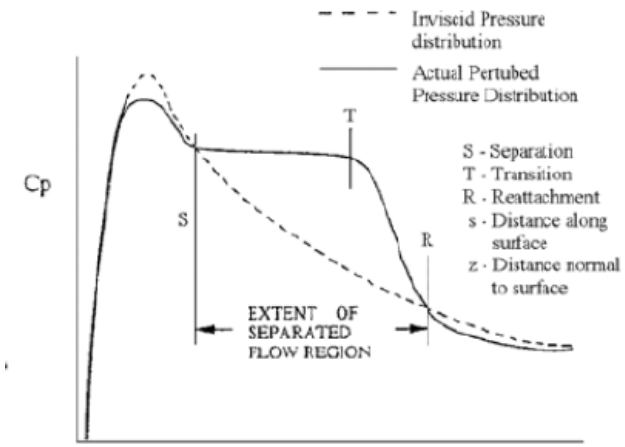

Figure 1.4: Pressure distribution at the suction surface [22]

The first region is bounded by the mean dividing streamline ST'R and the airfoil surface. The mean dividing streamlines generally regarded as the collection of points across each velocity profile at which the integrated mass flow is zero. This first region represents the relatively slow re-circulatory flow forming the bubble. The second region of flow consists of the free shear layer contained between the outer edge of the boundary layer S" T" R" and the dividing streamline. This separated shear layer undergoes transition at a location denoted by T due to disturbance amplification occurring in the unstable laminar layer. Momentum transfer due to turbulent mixing eventually eliminates the reverse flow near the wall and the flow attaches at point R. This process of separation,

transition and reattachment result in a laminar separation bubble that has a predominant effect on the entire airfoil flow-field. Pressure distribution over an airfoil with a separation bubble is shown in Fig 1.4.

The configuration of the LSBs dictates the performance and stalling behavior of the airfoils [23][24]. The stalling of airfoils is classified into 4 types: Trailing edge stall, Leading edge stall, Thin-airfoil stall, and a combination of both trailing and leading-edge stalls.

In the Trailing edge stall, the flow separation travels frontward from the trailing edge as the angle of attack surges while in the Leading edge stall there is a sudden separation of flow near the leading edge which fails to reattach onto the rear surface [25]. The thin airfoil stall is led by the flow separation at the leading edge and reattachment at a point that moves progressively backward as the angle of attack increases. Sometimes an airfoil stall could be a combination of both the leading edge and trailing edge stall [23][26].

The LSBs that control the behavior of airfoils at low Reynolds number are of two types, based on their length viz. long bubble, and the short bubble [22]. If the separation bubble is a small percent of the chord when the Reynolds number is lesser than 10^5, the LSB is a short bubble and the bubble is stable for a very short period [2]. The long bubble, on the other hand, covers 20-40% of the chord [23]. Carmichael [27] has reported that below a Reynolds number of 5×10^4, an LSB causes an extreme drop in the lift. As the Reynolds number is increased above 10^5, a long separation bubble is formed which spreads to about 20–30% along the chord and disturbs the flow significantly. For airfoils operating in the Re range of 10^6, the flow separation is suppressed by the turbulence. An increase in Reynolds number makes the boundary layer turbulent, inducing high energy to the sluggish boundary layer to act against separation. The nature of the bubble depends upon the characteristics of the airfoil, angle of attack, and Reynolds Number. As the laminar separation bubble and hence the flow separation deteriorates the performance of low Reynolds number airfoils, the

control of flow at these Reynolds numbers is necessary. There are two major categories of flow control mechanisms that alter the flow by either using external energy or by altering the geometry through obstacles or surface modifications. The first one is called an active flow control mechanism whereas the latter is known as a passive control mechanism. In the passive flow control mechanism, flow is controlled or deviated by using external devices like vortex generators, flaps, slots, and so on, whereas, in the active flow control mechanism, external power/energy is required to control the flow [28]. These control mechanisms help in delaying the flow separation, which results in delay in the stall, increment in lift-to-drag ratio, and trapping of vortices. Some popular passive flow control devices are leading edge high lift devices, trailing edge high lift devices, Vortex generators, Gurney flap, and Bio-inspired flow control mechanisms to name a few. Leading and trailing edge high lift devices like flaps, slats, or slots and multi-element airfoils are developed and applied in the 1900-1960 period. These devices are used to allow the air to flow from the pressure surface to the suction surface to control the boundary layer [29]. The main utilization of these devices is in Unmanned Aerial Vehicles is to augment the lift, delay the stall, and consent to activate at lower airspeeds, which leads to shorter runway necessities [30]. And there are few innovative passive flow control mechanisms like vortex generators, gurney flap, and protuberances/ tubercles, and some other flow control mechanisms.

Vortex generators, shown in Fig.1.5, are used to generate vortices that stimulate augmented mixing among high-speed air in the mainstream and outside boundary layer with the moderately low-speed air nearer to the surface so that the boundary layer is reactivated, and thus delaying the stall. Even the leading-edge protrusions have a similar effect land produces counter-rotating chord-wise vortices but along the y-axis [32]. These chord-wise vortices also reenergize the boundary layer.

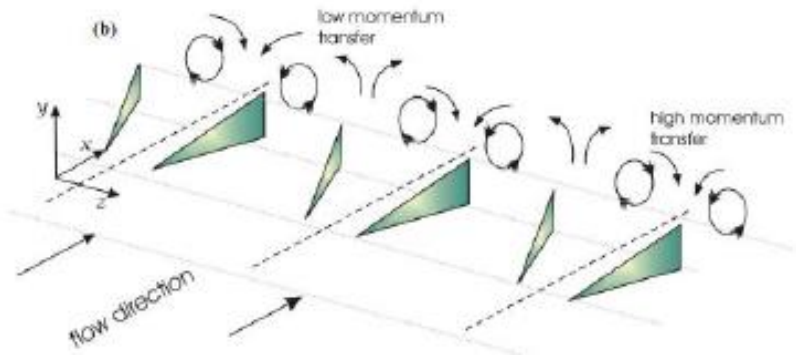

Figure 1.5: Vortex generator [31]

Liebeck [29] was the first to introduce the concept of Gurney Flap(GF) on wings of race cars, which were placed inverted and used to deliver downforce as opposed to lift. This downforce acts to increase the connection of the tires during acceleration, braking, and cornering. Gurney flaps (GFs) are small tabs located in the trailing edge of the airfoil on the lower side, which is perpendicular to the free stream velocity or the chord line, as shown in Fig.1.6. The height of the GF is about 1% to less than 5% of the chord and these GFs increase the overall aerodynamic performance of the wing. The other major benefit of GFs is low maintenance and manufacturing cost.

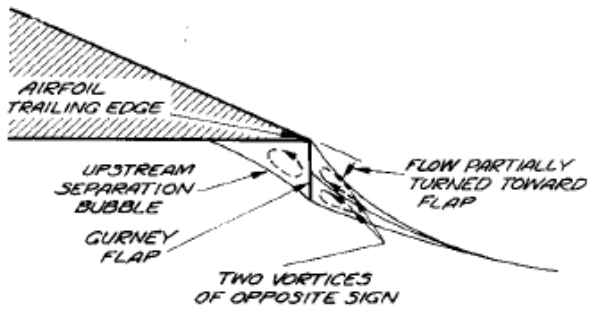

Figure 1.6: Hypothesized GF mechanism [29]

Bio-inspired flow control mechanisms are inspired by aerial or aquatic animals. These devices include leading-edge protuberances/ tubercles, corrugated airfoils, and serrated trailing edge [29], [32],[33]. This research too focuses on the effect of passive control devices on the performance of a generic airfoil at low Reynolds numbers.

1.2 MOTIVATION AND OBJECTIVES OF RESEARCH

The need for micro aerial vehicles and Unmanned Air Vehicles is multiplying due to military and commercial applications. These vehicles fly at very small Reynolds numbers and have to move in confined spaces with a bare minimum speed. It requires these vehicles to possess very high aerodynamic lift and efficiency. There are large numbers of high lift devices such as flaps and slats that are currently in use, but lift enhancement due to these devices is limited. There are some other mechanisms such as blowing and suction, which are effective but require the expenditure of a considerable amount of energy along with housing space. Thus there is a need to search for innovative passive flow control devices that can considerably progress the aerodynamic performance of wings and aerial vehicles. Some ques can be obtained from biological wings whose shapes and designs are significantly different from those of human-made aerial vehicles.

Because of this, the current research focused on enhancing the performance of existing standard wings and airfoils with geometrical modifications through biologically inspired flow control devices like surface protuberances and cavities. With this motivation, the objectives of the current doctoral dissertation are to:

1. "Investigate the effect of variations in the shape and size of protrusions on the aerodynamic performance of selected airfoils at various Reynolds numbers".
2. "Investigate the effect of variations in the shape and size of cavities on the aerodynamic performance of selected airfoils at various Reynolds numbers".
3. "Investigate the effect of Protrusion and Cavity on dynamic stall".

1.3 STRUCTURE OF THE THESIS

The thesis begins with the introduction of the low Reynolds number vehicles and other application areas of the low Reynolds number followed by discussing problems associated with the low Reynolds number flows. A detailed explanation about laminar separation bubbles and their effect on the performance of the airfoil is then provided. Flow control mechanisms like flaps, slots/slats, vortex generators, protuberances, and gurney flaps are discussed and illustrated with pictures. Finally, the chapter ends with the motivation for carrying out this research and the objectives of the research work.

In **chapter 2,** a detailed survey of the state of the art of existing literature in the domain of low Reynolds number flows including the effects of icing, gurney flaps, protuberances, cavities is discussed. Works of literature on the dynamic stall phenomena are also discussed later in the chapter. Finally, the shortcoming in the existing literature is presented to formulate the objectives of this research.

Chapter 3 presents the methodology used to carry out this research in detail. Two methodologies have been used in this research, viz. the numerical simulations and wind tunnel experiments. In the first part of this chapter, the numerical methodology is described in detail. This includes the equations solved, the geometric modeling, grid generation, solver setup, evolution schemes, and turbulence models used. Secondly, the experimental setup is described which includes the subsonic wind tunnel, its sensors, and data acquisition systems, and flow visualization systems. The experimental methodology is, however, restricted to validating the numerical findings.

Chapter 4 embodies the results attained from the numerical analysis of the NACA0012 airfoil with protrusions. A detailed discussion about the aerodynamic characteristics and aerodynamic efficiency of the airfoil with protrusions at a different location on the surface of the airfoil is discussed in this chapter.

Chapter 5 illustrates the results achieved from the numerical analysis of the NACA0012 airfoil with cavities. A detailed argument about the aerodynamic characteristics and aerodynamic efficiency of the airfoil with cavities at a different location on the surface of the airfoil in this section.

Chapter 6 characterizes the effect of protrusions and cavities on the dynamic stall of NACA 0012. An exhaustive discussion about the aerodynamic characteristics of the moving airfoil with protrusions and cavities at a different location on the surface of the airfoil.

Subsequently, after a comprehensive discussion of the results in chapters 4, 5, and 6, a conclusion has been drawn out highlighting the effects of protrusions, and cavities, on static and dynamic NACA airfoil. The conclusion section emphasizes the important finding of this research and further discussion are made towards future research by potential researchers.

CHAPTER 2. LITERATURE REVIEW

2.1 AIRFOIL AT LOW REYNOLDS NUMBER

At low Reynolds number (*Re*), the flow phenomenon is very complex and interesting. The main focus area in such flows are flow separated region near the leading edge or trailing edge, adverse pressure gradient, and transition to turbulence region [34]. These are very delicate phenomena when the flow happens at low Reynolds numbers [35]. The effects and the behavior of the laminar separation bubbles on airfoils in incompressible flows were studied in detail by Julian [36]. Meara and Mueller conducted experiments to study the effect of the laminar separation bubble over a NACA 66_3-018 airfoil at the *Re* between 50000 and 20000 at an angle of attack (AOA, α) in the range 8°-12°. From their investigation, it was observed that as the Reynolds number increases, the length and thickness of the LSB diminishes and as the AOA rises, the LSB length and thickness are increases [21]. Hsiao et.al.,[37] conducted wind tunnel experiments over NACA 6-series airfoil at Reynolds number between 3.0×10^5 and 7.74×10^5. Based on the observations, it was concluded that the length of the separation bubble increased as the angle of attack increases up to 6°, a further increase in the AOA resulted in the disappearance of the separation bubble. They also recommended a criterion to detect the bubble height as the position where the boundary layer touches 75% of its edge velocity.

Lin and Pauley [38] conducted an experimental and computational analysis of airfoils at three different Reynolds numbers 60000, $10^{5,}$ and 2.0×10^5 at a single angle of attack of 4°. From their results, it can be said that with increments in an angle of attack and Reynolds number, the separation point moves ahead and the time-averaged length of the separation bubble diminishes. With an increase in the Reynolds number, it was observed that there is a decrement in the unsteady separation portion, shifting of the point of separation rearward on the surface, and with a reduced separation angle [38].

Rinoie and Takemura [39], conducted experiments over a NACA0012 airfoil at the Reynolds number 1.35 x 10^5 to study the oscillatory behavior of the laminar separation bubble near the stall. From the observations of the mean velocity measurements at α=11.5º, a long separation bubble of 35% chord length was detected. It was also observed that a tiny separation-reattachment bubble has a moderately alike flow configuration to that of a short bubble at a smaller α=10° [39]. In a comparative experimental and numerical study by Serhiy et al., over a NACA 0025 airfoil, it was suggested that the inviscid linear stability theory can be used to illustrate the early stage of the separated shear layer transition over an airfoil at a low Reynolds number. It was also found that as the Reynolds number is lowered from 1.5 x 10^5 to 1.0 x 10^5, the separated shear layer fails to reattach onto the surface of the airfoil [40][41].

Yuan et al. performed numerical and experimental investigations over an SD7003 airfoil at the Reynolds number of 60000. They used two numerical approaches viz. Large-Eddy simulations (LES) and Unsteady Reynolds Averaged Navier-Stokes (URANS) simulations. Reynolds Averaged Navier-Stokes (RANS) analysis was carried out by considering the production terms as zero ahead of the transition point, in the nominated turbulence model. Based on their observations, both approaches can forecast the laminar separation bubble along with the transition, and the findings are in good arrangement with experimental outcomes [42][43].

Counsil and Boulama executed numerical investigation over a NACA0012 airfoil at three Reynolds numbers of 5x10^4, 1x10^5, and 2.5x10^5 at 0º, 4º, 8º angles of attack. From the established results, it was found that the shear stress transport γ-Re_θ model can capture the laminar separation bubble, and consequently the aerodynamic performance at low Reynolds numbers with promising accuracy [44]. Juanmian et al. carried out a numerical analysis on symmetrical SD8020 airfoil at the Reynolds number 40000. Outcomes of the work revealed that at lower angles of attack, laminar separation takes place on

both sides of the airfoil, and as the angle of attack increases the laminar separation bubble appears on the suction surface of the airfoil [45].

Kojima et al. performed large-eddy simulations on an airfoil at the Reynolds number of 23000. The analysis exposed that the separation point on the suction surface translates forward towards the leading edge as the angle of attack increases, and the mode of separation varies, from trailing edge separation to leading-edge separation, as the separation bubble forms near the leading edge[46]. Boutilier and Serhiy carried out the wind tunnel experiments to study the development of a shear layer over a NACA0018 airfoil at the Reynolds number 10^5. The outcomes of their findings suggest that as the angle of attack increases, the separation bubble jumps ahead, with a reduction in bubble length, demonstrating advanced disturbance growth rates [47][48].

Wang et al. investigated the aerodynamics in the wake of a NACA0012 airfoil for Reynolds number between 5300 and 20000 [50]. They have suggested the four distinct flow regimes based on the chord Reynolds number, i.e.

- Ultra-low Reynolds number ($<1.0 \times 10^4$) wherein the separated shear layer fails to reattach on the surface,
- Low Reynolds number (1.0×10^4–3.0×10^5): In this regime, the formation of a separation bubble takes place, when α is small. The transformation of the flow from transition to turbulence occurs when the separated flow reattaches to the surface, for higher α, and it takes place before reattachment,
- Moderate Reynolds number (3.0×10^5–5.0×10^6): This regime is also accompanied by a separation bubble, the transition, however, occurs before the reattachment, closer to the separation point.
- High Reynolds number ($>5.0 \times 10^6$): In this regime, the transition occurs in the boundary layer, before flow separation.

The above-mentioned four Reynolds number regimes are exhibit eight discrete flow patterns on the suction side of the airfoil. The flow patterns are given as,

A (fully attached laminar boundary layer), B (partially attached laminar boundary layer), C (fully separated laminar shear layer), D (laminar bubble), E (partially laminar bubble), F (fully attached turbulent boundary layer), G (trailing-edge-separated turbulent boundary layer), and H (fully separated turbulent shear layer). With increasing α, the flow structure changes differently in different Reynolds number regimes, and the sequences are,

- In the ultra-low Re_c regime, A→B→C
- In the low Re_c regime, B→D →E→ stall →C,
- In the moderate Re_c regime, E→ stall →C,
- And in the high Re_c regime, F→G→ stall →H.

At lower angles of attack less than 5º, the lift coefficient C_l is lower in the ultra-low and low Reynolds number regimes, as compared to the lift coefficients for moderate and high Reynolds number regimes. As the angle of attack is increased above 5º, the lift coefficient increases more or less linearly to $C_{l,\,max}$ in the ultra-low Reynolds number regime. This is connected with the rollup of the laminar shear layer over the airfoil surface without reattachment. In the low Reynolds number regime, $dC_l/d\alpha$ may improve and deteriorate based on whether the detached shear layer transits to turbulent after and before reattachment [49].

Wang et al. experimentally analyzed the effect of varying turbulent intensity (T_u) on the aerodynamic performance of an airfoil at ultra-low Reynolds number regime. An increase in either the Reynolds number or the turbulent intensity has a similar effect on the flow in the wake of the airfoil wherein the airfoil performance is enhanced. The difference, however, in the two is that enhancing the T_u delays flow separation due to enriched mixing; whereas the augmented Reynolds number grounds a more noticeable adverse pressure gradient, which modifies little with T_u, in the boundary layer and thus endorses flow separation [49].

Lee et al., carried out large-eddy simulations (LES) over about a 5% thick blunt flat plate at chord Reynolds number $Re_c = 5.0 \times 10^3$, 6.1×10^3, 1.1×10^4, and 2.0×10^4 to study the characteristics of the laminar separation bubble and the mechanisms of surface pressure distributions within the LSB at various Reynolds numbers. Lee et al. proposed a Reynolds averaged stream-wise pressure gradient (Momentum budget) equation to expose the comprehensive flow mechanisms of LSB and subsequent pressure distributions and were able to predict the pressure distribution on the airfoil surface [50]. Choudhry et al. performed a numerical investigation to study the effect of a long separation bubble on thick NACA0021 airfoil at low Reynolds number and turbulent intensities. Two transition models were chosen to check the prediction of the bubble length. Both γ–Re_θ model and the K–K_L–ω model were able to predict the laminar boundary layer separation and the point of transition. From the results, it was suggested that the γ–Re_θ model forces an earlier flow reattachment than the K–K_L–ω model and the experiments, due to extra turbulence. It was detected that there is a reduction in the bubble size due to an increase in the angle of attack, Reynolds number, and turbulent intensities [51].

Ducoin et al. conducted a direct numerical simulation, with the Nek5000 code, to study the transition of the flow from laminar to turbulent over a wing cross-section (SD7003) at a Re of 20000 with $\alpha = 4^o$. The mechanisms yielding transition to turbulence have been studied by the joint use of space-time analysis of the flow physics and Dynamic Mode Decomposition (DMD) to extract key physical modes of the flow at transition and its relation to the wake of the flow. The outcomes that were put forward suggested that the transition process appears to be physically independent of the wake flow, while the LSB shedding process is locked-in with the von Kármán instability [52]. Almutairi et al. conducted a numerical investigation to gain knowledge of the low-frequency oscillation of flow around NACA-0012 airfoil at 11.5^o for a $Re_c = 1.3\times10^5$. Dynamic mode decomposition was used on a trial of instantaneous pressure field at the center of the spanwise plane. Based on the Dynamic mode

decomposition analysis, two main modes were observed in the flow. The primary one was low-frequency oscillation mode similar to experiments, and the second mode was trailing edge vortex shedding mode, similar to findings by Yarusevych et al for universal scaling [53].

A detailed numerical study to understand the aerodynamics of various airfoils at low Reynolds numbers done by Winslow et al. [54]. Besides re-establishing a nonlinear lift curve behavior at a low Reynolds number for NACA 0012, they suggested a reduction of about 46% in the maximum coefficient of lift for Reynolds number between 10^4 and 10^5, due to the inability of the prematurely separated flow to reattach. Winslow et al. also suggested that an airfoil with a sharper leading edge provides better reattachment of the flow and hence a better low Reynolds number performance. An increase in the camber was also found to increase the lift to drag ratio at a lower Reynolds number [54]. Koca et al. performed experiments on the NACA4412 wind turbine airfoil at various Reynolds numbers to study the characteristics of LSB and shedding frequency. Observations made suggested a similar behavior of the LSB as reported by Kojima et al. and Boutilier and Sehriy [55]. At the higher angles of attack, the shedding frequency was found to be, St=0.17 irrespective of the Reynolds number and the aspect ratio. A similar suggestion was provided by Rojratsirikul et al [56] for the Strouhal number for an airfoil. At angles of attack lower than 10°, the vortex shedding frequency is small due to the formation of LSB [55].

Arunvinthan and Nadaraja conducted experiments over NACA2415 airfoil at different Reynolds numbers by altering the turbulent intensity at different angles of attack [57]. The investigation revealed that an increase in the turbulent intensity can enhance the lift coefficient and delay the stall by keeping the flow attached to the surface for longer [57]. Jan et al. investigated the flow over an NREL S825 airfoil by changing the range of the Reynolds number from $0.5x10^5$ to $6x10^5$ [58]. In their investigation, low Reynolds number effects like the presence of LSB was observed for Reynolds number less than $0.75x10^5$. It was also suggested that the transitional γ- Re_θ model, predicts the presence of the

LSBs in the flow accurately [58]. Marchman and Werme conducted experiments on Clark-Y airfoil at the Reynolds number between 50000 and 200000. They found that, despite being considered a good low Reynolds airfoil, the aerodynamic efficiency of Clark-Y airfoil deteriorates dramatically as the Reynolds number is reduced to 75000 [59]. A recent study on very low Reynolds number aerodynamics of NACA 0012 airfoil also reported a highly nonlinear lift curve, with abrupt changes in the C_l-α curve for the Reynolds number in a range of 2500 to 5000 [60]. Zhang et al. proposed a new methodology to design the airfoil profile for low Reynolds number flows with airfoil thickness, camber, the position of maximum thickness, and position of maximum camber [61].

One of the peculiar behavior of airfoil at low Reynolds number is vortex shedding. The characteristics of the vortex shedding on rigid circular cylinders were studied by Lienhard and he detected four characteristic modes of vortex shedding viz. laminar, subcritical, transitional, and supercritical [62][63]. Zaman et al. observed that the phenomenon of low-frequency oscillation of flow over an airfoil is dissimilar to the popular von Karman vortex shedding. The source of the low-frequency vortex shedding phenomenon was suggested to be the periodic swapping between the stalled and un-stalled flow-field near the leading edge of the suction surface. The strength of the fluctuations is moreover, higher near the leading surface of the airfoil and the strength diminishes downstream. The unsteady flow-filed around the bluff-body vortex shedding is unaffected to airfoil shape and Reynolds number [64]. Pauley et al. studied the structure of the 2-D laminar boundary layer using numerical solutions of N-S equations. Based on the outcomes, it was suggested that the periodic vortex shedding is due to the strong adverse pressure gradient from separation. The Strouhal number based on the shedding frequency, local freestream velocity, and boundary-layer momentum thickness at separation was found to be independent of the Reynolds number and the pressure gradient. The shedding frequency was found to accurately predict the linear inviscid instability of the

separated shear layer [65]. Vortex shedding, which is affected by the leading inviscid instability wave is brought by the inflection velocity profile downstream of the separation point [38].

Ripley and Pauley suggested that the large-scale two-dimensional structures regulate the bubble reattachment and small-scale turbulence backs the secondary role [66]. Huang and Lee performed wind tunnel tests on NACA0012 airfoil at various Reynolds numbers and turbulent intensity to suggest the existence of instability waves low angles of attack and Reynolds numbers [67]. The vortex shedding from airfoil is also affected by the angle of attack, with a higher angle of attack accounting for longer the vortex shedding cycles [45]. Huang and Lin examined the flow structures over the NACA0012 cantilever wing and reported a vortex shedding pattern in the wake that was similar in characteristics to the von Karman vortex street behind circular cylinders [69]. The vortex shedding frequency was found, to increase with an increase in the Reynolds number and, to decrease with an increase in the angle of attack. At low angles of attack, the progress of vortex shedding is correlated with the shear layer instabilities. The patterns of the shear layer instabilities resemble the vortex shedding characteristics. At the low angle of attack, the shear layer instability waves control in the laminar shedding mode wherein the frequency of the shear layer instabilities decreases with increasing α [68]. Huang et al., in an investigation of flow over NACA0012 wing, concluded that at large Reynolds number the inertial forces are supreme, and found the Strouhal number to be 0.159, which slightly higher than the Strouhal number for flat vertical plate and smaller than the Strouhal number for a circular cylinder [70]. They also concluded that a maximum Strouhal number is obtained for the profiles with sharper ends.

Airfoil aerodynamic behavior and coherent structures are mainly dependent on the flow Reynolds number and angle of attack. If the separation bubble is created on the suction surface of the airfoil, it decreases the coherence and wakes vortices length scale [69]. Serhiy Yarusevych et al. proposed alternative

scaling for fundamental frequency and the wake vortex shedding frequency. In the separated shear layer, the fundamental frequency scaled with the wavelength of the fundamental disturbance leads to a fall in the Strouhal number between 0.45 and 0.5. In the near wake region, the vertical distance between two vortices was considered as a scaling factor, resulting in the reduction of the Strouhal number to 0.17 [69]. Serhiy and Boutilier tested the experiments over NACA0018 airfoil and proposed yet another alternative scaling and found the Strouhal number to be constant at 0.18 [70]. Vortex shedding frequency of flat plate is nearly the same for angles of attack higher than 50°, and it varies in proportion with the angle of attack for lower angles. As the Reynolds number increases, there is a reduction in the Strouhal number [71]. The vortex shedding phenomena at the Reynolds number of 10^6, was investigated for wind turbine blade section (NREL S809 airfoil) at angles of attack from -40º to -150º and from +40º to +150º, by Pellegrino and Meskell [72]. They found the Strouhal number to vary between 0.12 and 0.16 for negative angles of attack, and between 0.11and 0.15 for positive angles of attack [72].

2.2 PROTUBERANCES

The low Reynolds number characterization of airfoils reported in the above-mentioned literature is mostly for the clean airfoil configurations. But during actual operations, these low Reynolds number configurations are susceptible to surface roughness of various forms, sizes, and origin. The deformation in the geometry of the airfoil may be concave or convex. The protrusions on the wing surface may be due to dirt deposition, insect deposits, ice formation, or bird littering. At low Reynolds number, the flow is highly susceptible to surface characteristics and hence these protrusions can alter the aerodynamics of these wings considerably. For NACA 66_3-018 airfoil, a distributed grit roughness on the leading edge lead to a rapid increase in lift coefficient with angle of attack; however, with decreased $C_{l,\ max}$ at 40,000 Reynolds number. At a higher Reynolds number of 130,000, the negative lift at small angles of attack was

eliminated by the use of grit roughness at the leading edge [73]. As the Reynolds number increases the formation of the LSB occurs at 8º, the similar formation was seen for grit roughness which promotes the transition and the flow is attached to the surface [73][74].

Larger protrusions like a rough ice accretion are found to reduce the $C_{l,\,max,}$ and the stall angle drastically with a premature stall of NACA 0012 in the Reynolds number range of 0.36 x 10^6 to 3.36 x 10^6. It was found to accompany a large rise in drag and pitching moment coefficients. Korkan et al. observed that aerodynamic characteristics of the airfoil with leading-edge ice accretion are to some extent reliant on the Reynolds number [75]. Bragg developed a computer code to predict the droplet trajectories and impingement parameters [76][77]. Bragg et al. deliberated about empirical and numerical methods for forecasting the performance of the airfoil characteristics because of ice accretions on the surface of an airfoil [78]. Potapczuk performed a numerical analysis over NACA0012 airfoil with leading-edge ice and found the results in the pre-stall regime to be in good agreement with experimental results [79]. For this larger protrusion, however, the Reynolds number variations, in the moderate range, were found to have an insignificant effect on the aerodynamic coefficients. As the height of these ice accretions increased, a severe degradation in the aerodynamics of airfoils is observed, except when the protuberance is located at the leading edge [80]. As far as the shape of these icy protrusions is concerned, the circular or hemispherical accretion gives the highest lift coefficient as compared to conical and triangular protrusions. Mirzaei et al. [81] reported the characteristics of the separation bubble behind protrusion caused by icing and its effect on flow unsteadiness. They found that increasing the angle of attack for NLF - 0414 airfoil results in longer separation bubbles at moderate Reynolds numbers. They also reported a reduction in vortex shedding frequency as the angle of incidence is increased.

Zhang et al., in their study of the performance degradation of low Reynolds number airfoil due to insect debris, reported that although protuberances

reduced the lift coefficient significantly, small roughness could delay the stalling significantly [82]. The protuberances are not necessarily always associated with the performance degradation of airfoils. Some bio-inspired wings, with leading-edge sinusoidal protuberance named tubercles, may increase the aerodynamic efficiency of wings. Low-pressure pockets are formed in the troughs between the protuberances, which results in an augmented lift coefficient at all angles of attack for an extensive choice of Reynolds numbers in the range between 1.8×10^5 and 3.0×10^6. These sinusoidal tubercles with a height of 0.12c and wavelength of 0.5c could delay the stalling to up to 39º for the NACA 63_4-021 airfoils along with a decreased minimum drag coefficient and a softer stall [83]. The sinusoidal protrusions at the leading edge are helpful in the post-stall regime as well, for conventional NACA 4-digit airfoils [84].

The smaller the protrusion height or the gap between protrusions, the higher are the lift coefficients and stalling angles, with better post-stall characteristics. A larger gap between the tubercles leads to a dip in the aerodynamic efficiency of the airfoils [85]. The enhancements in post-stall aerodynamic characteristics and increase in the stall angle strengthen further with growing Reynolds number in the range 75000-300000 [86]. Besides these, the protrusions perform better on thicker airfoils as compared to thinner ones [87].

Leading edges are not the only place where the protrusions can be placed. Two- and three-dimensional bumps located at the various chord-wise location also show significant changes in the aerodynamic performance of airfoils. At a Reynolds number of 64,200, a discrete roughness of height 1.25 times the local boundary layer thickness near the leading edge induces a prior interruption of the separated laminar boundary layer, resulting in increased lift coefficients [88]. Vortex shedding does not appear for roughness elements with a height less than 50% of boundary layer thickness for NACA 64_3-618 at $\alpha = 8º$, and hence the lift coefficient is unaffected. In an investigation over a wing, with two discrete roughness elements at low Reynolds number, it was found that the larger and taller bumps trigger vortex breakdown and delay separation and may

increase the *L/D* ratio of airfoils [89]. The macroscopic alteration in the surface of airfoils due to insect deposits can reduce the output power of wind turbines by 25% [90]. Huang et.al. examined the protuberance effect of wind turbine blade performance. Upgrade in the l/d ratios observed at a negative angle of attack. Higher amplitude and small wavelength degraded the performance of the blade. The pressure coefficient is enhanced at the stall region [91]. Sudhakar et. al conducted experiments on the aerodynamic performance of UAV by inserting the tubercles on leading-edge at the Reynolds number 0.18 million and 0.27 million. At a low Reynolds number, there is an upgrade in the lift coefficient values, delay in the stall, and also a reduction in the drag. The overall aerodynamic performance increased by 25%. Similarly, at a high Reynolds number, enhanced lift coefficient values are detected. These tubercles are helpful when the UAVs are undergoing unexpected gusts while they operated [92]. Bolzon et. al mounted the single tubercle at the tip of the swept wing and study its effect. Based on the results, it was found at pre-stall regime there is no considerable improvement in the aerodynamic performance. Change in the vortex strength in the order of 2.2% [93].

Study on NERL S809 wind turbine airfoil with the help of passive flow control mechanism. Aerodynamic characteristics have been improved, upgrade in the lift coefficient values, flow separation moved towards the trailing edge and there is a flow stall phenomenon. Based on this it was suggested to use this flow control mechanism that is vortex generators on wind turbines [94].

A new concept of passive flow control mechanism proposed by Luo et. al, introducing the micro cylinder near the leading edge of a NACA0012 stalled airfoil. Upgrade in the aerodynamic values of lift coefficient, lift to drag ratio detected and there is a reduction in the drag coefficient values as well. From the results it was suggested with help of this micro cylinder stall can be efficiently delayed, the size of the separation on the suction of the airfoil also can be diminished [95].

A numerical study was conducted over an E216 airfoil with boundary layer trips at the Reynolds number 100000. Based on the study, it was found these trips able to disappear the LSB moderately and upgrade the aerodynamic performance. Drag is increased by 15 % and the l/d ratio is upgraded by 21.6% at an angle of attack of 6° [96].

Over an SD 7032 airfoil profile, flow characteristics for straight leading and tubercles leading edge have been studied at the Reynolds number 14000. LE tubercles mitigate the flow separation downstream of crests and troughs. Counter-rotating vortex pairs are generated on the LE tubercles, these counter-rotating vortex pairs showed the influence on the flow separation over an airfoil [97]. At a higher angle of attack, a wing with a large LE tubercle was witnessed to bring considerably attached flows on the suction surface, particularly downstream of tubercle peaks [98].

Chen et. al performed numerical analysis over a NACA0012 airfoil with wavy leading edges. Based on their observation, it was pointed out that the aerodynamic characteristics are very sensitive towards the amplitude and wavelength of the wavy leading edge airfoils. Larger amplitude and smaller wavelength degrade the aerodynamic performance. At a higher angle of attack, a reduction in the drag values is observed. A decent stall process was detected without abrupt loss in the lift values [99].

2.3 LITERATURE REVIEW ON CAVITIES

In recent times, many researchers and scientists have shown ample interest in the Kasper vortex wing. The concept of this Kasper vortex wing is to trap the vortices and attain a high *L/D* ratio compared with other plain configuration wings [100]. Kasper successfully did the flight testing but failed to capture these fascinating results in wind tunnel testing. Despite this, the concept of the trapping of vortices is very beneficial, to attain a high *L/D* ratio and to avoid

vortex shedding. Plenty of research has been done with rectangular cavities on the flat surface very few articles are available airfoil with cavities, Trapped Vortex Cell (TVC), and dimples specifically at low Reynolds number. The key motive of these cavities/dimples is to attach the separated flow by a strong vortex fastened in a cavity. Wang et al. conducted a numerical analysis in a channel with a single dimple at a very low Reynolds number. With the reduction in Reynolds number, the stretching of the 3D vortex and the separation region diminishes gradually [101]. Faure et al. visualized flow inside an open cavity at the Reynolds number1, $150 \leq Re \leq 10{,}670$. Formation of the 3D structures was observed and which were not instigated by shear layer secondary instabilities [102].

Only a few researchers have studied the trapped vortex cell concept. Vortexcell2050 is a European project designed to study the actively flow-controlled vortex cell [103]. The trapped Vortex Cell technique used on a thick airfoil, augments lift and decrease drag, and leads to high aerodynamic efficiency. The cavity with distributed suction was found to be the ultimate in terms of aerodynamic performances and power desired to understand the control of the suction [104]. Passive trapped vortex flow control is incapable of regulating the flow separation, which leads to declining the aerodynamic characteristics of the original airfoil. Whereas active trapped vortex flow control can switch the flow separation, for partial values of the blowing coefficient, and full reattachment is attained [105],[104], [106].

Taherian [107] in 2016, examined the unsteady flow-field after the Riso airfoil and that with an increase in the Reynolds number, there is an alteration in the length of the wake and with this airfoil configuration, there is a reduction in the drag. An experimental and computational analysis carried over a two-dimensional NACA0018 airfoil with and without cavity at a Reynolds number of 20000, suggested that the *L/D* ratio of the airfoil with the cavity improves with cavity [108]. The cavity degrades the performance at lower angles of attack, but as the angle of attack is increased to 12^0, enhancement in

performance of airfoil is observed. The best location of the cavity is at the separation point of the flow field [109]. Recently, chord-wise elliptical slots joining the leading and trailing edges of the wing at various locations of the span were studied and it was found that the wingtip vortices, circulation, and turbulent intensity significantly dropped with a slight reduction in aerodynamic efficiency [110].

Sun et. al examined the flow over a tidal turbine blade airfoil with the help of the cavitation and roughness over an airfoil. Numerical analysis was carried out to study the effect of the cavity and rough over an airfoil, based on the results it was concluded the better aerodynamic performance compared with the clean airfoil configuration. The L/D ratio is also upgraded by an average of 20% for both optimized airfoils [111].

Numerical investigation carried out over an airfoil by placing the cavities along the chordwise starting from the leading edge to the trailing edge at the Reynolds number 150000, 600000. From the observation, it was detected that placing the cavities at the leading edge is not helpful in terms of aerodynamic efficiency. The trailing edge cavities showed better aerodynamic efficiency. Whereas the elliptical showed good output until $\alpha=10°$ [112]. Based on the Sobhani et al. study it was detected placing the circular dimple diameter that is 8% of the chord length, located at the pressure side near the leading edge of the airfoil, upgraded the efficiency [113].

CFD analyses are carried over a NACA4415 airfoil to study the aerodynamic behavior of the airfoil with surface grooves. The shape of the grooves is in arc and rectangular. With the help of the numerical simulations, it was concluded that the rectangular groove showed better performance compared with the arc. The rectangular groove able to constraint the flow motion inside whereas the arc groove is failed [114].

Surface concaved deep, distributed shallow defects are inserted on the S809 airfoil and performed the numerical study. For deep defects elongated LSB is

shown on the suction surface, as the angle of attack increases flow separation is detected both from the leading edge and trailing edge. In the case of shallow defects, the shape has an impact on the aerodynamic characteristics. The lift coefficient values are degraded up to 61% with a significant rise in the drag coefficient values up to 217% [115].

Numerical analysis carried over a slotted NACA0018 airfoil mostly used in the Darrieus turbines. Results suggested that at a higher angle of attack, slotted airfoil delays the flow separation [116]. Sooraj et al. examined the flow characteristics on the local strouhal number in the corrugations of the airfoil. Change in the pressure in individual corrugation leads to vortex integration and separation. More Strouhal numbers witnessed close to active corrugations. A positive angle of attack contributes a greater value of the Strouhal number as related to the negative angle of attacks [117].

2.4 LITERATURE REVIEW ON DYNAMIC STALL

Dynamic stall is a very complex phenomenon and many researchers have been working worked on this topic for decades, as it is a common phenomenon in vertical wind turbines and helicopter blades. The lift induced by the dynamic stall of the blade was first documented by Kramen who conducted an experimental study on a symmetrical and a cambered profile. The experiments wherein the blade was allowed to pitch from an angle of 0° to 30°, confirmed that with a sudden increase in AOA, the maximum lift value increases [118]. Later in the year 1972, Peter. Crimi developed a method of analyzing the dynamic stall on the helicopter rotor blade [119].

McCroskey is well known for his contribution to research in the field of dynamic stall. McCroskey and McAlister conducted an experimental analysis on NACA 0012 airfoil pitching from angle of 5° to 25° having reduced frequency, κ value of 0.25 and 0.15, and pitching magnitude varied from 6° to 14° at Re = 2.5×10^6. Two types of leading-edge stall formed due to the bursting of the leading-edge bubble. It was found that the shedding of the vortex is due

to the separation of the turbulent boundary layer and not because of the laminar bubble. They also suggested that irrespective of how the boundary layer separates, the distinguishable character between the static and dynamic stall is vortex shedding. For a wide range of Reynolds numbers, the vortex shedding is common for all airfoil which is oscillating but there is a significant modification in the forces acting on the airfoil [120]. Further experimental research was conducted by the duo on different airfoil profiles, for phenomena like light stall and deep dynamic stall. For deep dynamic stall, the airfoil was allowed to pitch from 5° to 25° for deep stall and from 5° to 15° for the light stall with $\kappa = 0.1$. It was found that with a low reduced frequency ($\kappa = 0.025$), a light dynamic stall is observed wherein the lift values are very similar to static stall, but as the reduced frequency is increased the vortex shedding begin to show up increase further, leading to a deep dynamic stall ($\kappa = 0.2$). He concluded later that an airfoil with good static stall behavior performs better when subjected to dynamic stall, i.e. more increment in lift coefficient [121].

McAlister conducted experiments in a water tunnel for the visualization of dynamic stall over a NACA0012 airfoil at Re=21000, $\kappa = 0.25$, and pitch angle from 0° to 20°. The dynamic stall starts as the flow reversal happens towards the leading edge, the instability in the shear layer converts it into a shear layer vortex [122]. T. Lee and P.Gerontakos conducted experiments to study the flow transition from laminar to turbulent on a NACA 0012 airfoil at a low Reynolds number of 1.35×10^5 and reduced frequency of 0.1. From the static analysis, it was observed that the bubble formation and separation of the boundary layer starts from the leading edge of the airfoil, and the bubble bursts at the angle of attack of 13° resulting in the reduction in lift. From the observations made on airfoil oscillating between $\alpha = -7.5°$ and 7.5° with $\kappa = 0.05$, between $\alpha = -5°$ to 25°, the dynamic stall vortex is not made by the bursting of the laminar bubble, which was previously believed [123].

Warnet conducted an experimental and numerical analysis for the dynamic stall of a pitching airfoil at a low Reynolds number, wherein the airfoil was allowed

to pitch from 5° to 25° with the frequency of 6.67Hz. The current numerical are inaccurate as they fail to accurately capture the laminar bubble formed during the pitching of the airfoil [124].

The experimental work employed by other researchers such as Wang, who investigated the dynamic stall numerically, found that few turbulence models are capable of solving flow problems involving laminar bubble formation, flow separation, reattachment, and vortex shedding. The results were close to the one obtained by the experimental case, but the models fail to accurately predict the changes at higher angles of attack (above 23°) [125]. Kobra Gharali conducted a numerical analysis on pitching airfoil for validation with experimental results [123]. For this numerical analysis, a dynamic mesh with pitching User Defined Function (UDF) was used along with Wilcox's Shear Stress Transport (SST) k-ω used for the turbulence modeling, and the airfoil was allowed to pitch from -5° to 25°. Another numerical investigation wherein the free-stream oscillated from 0° to 90° and this resulted in an enhancement in lift coefficient by 2.5 times as compared to a static free-stream [126].

An experimental investigation was carried out to study the unsteady characteristics of the vortex shedding at the wake near the airfoil, with different reduced frequencies [127]. From the results, the shedding frequency in the wake of the airfoil of an oscillating airfoil is unlike. The vortex-shedding frequency was originated to differ with the phase angle of oscillation, not with α, for a given reduced frequency. As the reduced frequency of oscillation is enhancing, the range of variation of the shedding frequency was shrunk [127].

Choudhry et. al studied the different methods to control the dynamic stall for wind turbine applications. These methods able to delay the flow separation, strength of the dynamic stall vortex [128]. Xu et. al. investigated the dynamic stall control of an S809 airfoil with the help of numerical analysis by applying a co-flow jet (CFJ). Based on the study, it was found that the dynamic stall can

be significantly crushed, improvement in the aerodynamic performance of the airfoil [129].

Numerical study on the effect of variable droop leading-edge on oscillating NACA 0012 airfoil conducted. Based on the analysis it was detected that the variable droop leading edge considerably enhanced the aerodynamic characteristics and degraded the dynamic stall [130]. Numerical analysis carried out for VAWT NACA0018 airfoil. After a thorough examination, it was confirmed as the Reynolds number increases there is a benefit in the airfoil's aerodynamic characteristics as a higher maximum tangential coefficient is achieved, in arrears to the delay in flow separation too much higher AOA [131].

Experimental analysis carried over an airfoil of dynamic stall control using plasma actuators. From the study, it was concluded the plasma actuation can efficiently regulate the airfoil dynamic stall, diminish the power of the dynamic separation vortex, increase the aerodynamic performance, efficiency and diminish the hysteresis loop region when the aerodynamic force differs with the AOA, particularly below both positive stroke and negative stroke. The average lift coefficient is increased by 7.1%, the stall angle of attack is delayed by 1.3°, and the hysteresis loop region is decreased by 4.5%; at the angle of attack of 4°–9°, the plasma actuator reduces the average drag coefficient of the airfoil by 44.5% [132].

The numerical investigation carried out using the Scale-Adaptive Simulation (SAS) approach has developed as an upgraded unsteady Reynolds-Averaged Navier-Stokes (URANS) formulation to examine the highly separated unsteady flows like a dynamic stall at the Reynolds number 50000. Based on the investigation, SAS able to predict close to the Hybrid RANS/LES. It was able to forecast the bursting of LSB, the formation of dynamic stall vortex, leading-edge vortex collapse, trailing edge vortex formation, its size, and strength and its shedding, drag prediction during the down-stroke. SAS unable to verify the formation of LSB, chordwise extent of LSB [133].

The effect of a dynamic stall for wind turbines is studied with various parameters like oscillation angle and reduced frequency. The increment in the lift coefficient was observed around 46%. During up and downstroke, the trailing edge vortex looks alongside the flow separation, and the trailing edge vortex changes to the front edge to enlarge the range of the vortex [134]. Numerical analysis carried out over a Clark-y airfoil at the Reynolds number 150000, for a dynamic stall, the effect of the dynamic stall on the aerodynamic characteristics has been studied. From their study, it was found that more than 5% of turbulence level in a turbulent flow is enhanced the aerodynamic performance [135].

2.5 SUMMARY OF LITERATURE REVIEW

Based on the literature study of the low Reynolds number flow over an airfoil, protuberances, cavities, and the effect of dynamic stall. At a low Reynolds number, based on the shape of the airfoil and thickness of the airfoil the flow phenomenon alters. From the literature survey, it was observed the maximum strouhal number of the airfoil is approximately 0.15-0.20, whereas for bluff bodies it is 0.21. The vortex shedding frequency was found, to increase with an increase in the Reynolds number and, to decrease with an increase in the angle of attack. At lower angles of attack, due to surface roughness, there is no negative lift coefficient observed. In the post-stall regime, the sinusoidal protrusions at the leading-edge showed a better output. The macroscopic alteration in the surface of airfoils like insect deposits can reduce the output power of wind turbines by 25%. It was found that at lower angles of attack there is a degradation in the performance of the airfoil. Effect of the protrusion with circular shape and triangle shape on strouhal number and flow transition phenomenon at low Reynolds numbers not investigated. Vortex trapped cell keeps the flow attach towards the surface of the airfoil. Effect of the cavity with circular shape and triangle shape on strouhal number at low Reynolds numbers not investigated. From the literature survey of the effect of airfoil on the

dynamic stall. The vortices forming in the dynamic stall are due to the separation of the turbulent boundary layer not due to the laminar bubble. The effect of airfoil on a dynamic stall at various reduced frequencies is studied and at a higher Reynolds number. But, the study on the effect of cavity and protrusion on a dynamic stall at a low Reynolds number was not investigated. In this study, numerical simulations were performed to study this effect.

Some surveys showed that, at a low Reynolds number, the smallest of deformations in the geometry of airfoils could produce significant alterations in its aerodynamic characteristics. The aerodynamic performance maybe enhance or degrade based on the size, shape, and location of the protrusions on the wing surface. The effects of these protrusions are also dependent on the thickness, location of maximum thickness, and the angle attack of the airfoil configuration.

CHAPTER 3. METHODOLOGY

In this research, two different methodologies, viz. numerical and experimental have been used to achieve the objectives of the dissertation. This research primarily uses Computational Fluid Dynamics (CFD) based numerical simulations to provide a solution to the complex physical flow phenomena. In recent years, the reliability of CFD has increased with modern algorithms and computing architecture. But CFD will never replace the pure theory or experiments, but CFD in conjunction with experiments can be a reliable tool for future research [136]. The experimental methodology is used primarily to validate the numerical findings for selected cases and hence the numerical methodology is presented here in detail. The key phases for numerically solving a fluid dynamics problem are an awareness of the mathematical model, selection of discretization method, choice and generation of the grid, selection of the solution methods, and temporal discretization. Discussion about the experimental methodology using a wind tunnel and laser sheet visualization is discussed as well.

3.1 GOVERNING EQUATIONS

At low Reynolds numbers, the viscous forces dominate the flow and thus can be represented by the two-dimensional unsteady Navier-Stokes equations. The Navier-Stokes equations are the mathematical statements of the conservation of the continuity and momentum equations are discussed below.

3.1.1 CONTINUITY EQUATION

A conversation of mass states that the mass is neither created nor destroyed in a system [137]. Eqn. 3.1 is the conservation of mass to an infinitesimally small volume fixed in space.

$$\frac{\partial \rho}{\partial t} + \nabla.(\rho\,\vec{\mathbf{V}}) = 0 \qquad (3.1)$$

In equation 3.1 ρ is the density of the fluid, the above equation, can be rearranged as an equation. 3.2 in the Cartesian coordinate system with u, v, w signifying the x, y, z components, of the velocity vector $\vec{V}$ is given as

$$\frac{\partial \rho}{\partial t} + \frac{\partial(\rho u)}{\partial x} + \frac{\partial(\rho v)}{\partial y} + \frac{\partial(\rho w)}{\partial z} = 0 \qquad (3.2)$$

3.1.2 MOMENTUM EQUATION

The momentum equation is based on Newton's Second law of motion applied to fluid motion. The momentum equation which is a statement of the conservation of momentum of the fluid volume fixed in space can be given as

$$\frac{\partial\,(\rho\,\vec{V})}{\partial t} + \nabla.\left(\rho\vec{\boldsymbol{V}}\right)\vec{\boldsymbol{V}} = -\nabla p + \nabla.(\bar{\bar{\tau}}) + \rho\vec{\boldsymbol{g}} + \vec{\boldsymbol{F}} \qquad (3.3)$$

Where p is the static pressure, $\bar{\bar{\tau}}$ is the stress tensor and $\rho\vec{\boldsymbol{g}}$ and $\vec{\boldsymbol{F}}$ are the gravitational body force and external body forces, respectively.

$\bar{\bar{\tau}}$ is the stress tensor as articulated in equation 3.4

$$\bar{\bar{\tau}} = \mu\left[\left(\nabla\vec{\boldsymbol{V}} + \nabla\vec{\boldsymbol{V}}^{\boldsymbol{T}}\right) - \frac{2}{3}\,\nabla.\vec{\boldsymbol{V}}I\right] \qquad (3.4)$$

μ is the molecular viscosity coefficient and I is the unit tensor, and the second term on the right-hand side is the effect of volume dilation.

In the Cartesian coordinate system, the above equation can be expressed with *u, v, and w* respectively as the *x, y, and z* component of the velocity as

X- momentum:

$$\frac{\partial(\rho u)}{\partial t} + \nabla.(\rho u V) = -\frac{\partial p}{\partial x} + \frac{\partial \tau_{xx}}{\partial x} + \frac{\partial \tau_{yx}}{\partial y} + \frac{\partial \tau_{zx}}{\partial z} + \rho.f_x \qquad (3.5a)$$

Y- momentum:

$$\frac{\partial(\rho v)}{\partial t} + \nabla.(\rho v V) = -\frac{\partial p}{\partial y} + \frac{\partial \tau_{xy}}{\partial x} + \frac{\partial \tau_{yy}}{\partial y} + \frac{\partial \tau_{zy}}{\partial z} + \rho.f_y \quad (3.5b)$$

Z- momentum:

$$\frac{\partial(\rho w)}{\partial t} + \nabla.(\rho w V) = -\frac{\partial p}{\partial z} + \frac{\partial \tau_{xz}}{\partial x} + \frac{\partial \tau_{yz}}{\partial y} + \frac{\partial \tau_{zz}}{\partial z} + \rho.f_z \quad (3.5c)$$

The components of the viscous stress tensor mentioned in the above equations are given as

$$\tau_{xx} = \lambda(\nabla.V) + 2\mu\frac{\partial u}{\partial x} \quad (3.6a)$$

$$\tau_{yy} = \lambda(\nabla.V) + 2\mu\frac{\partial v}{\partial y} \quad (3.6b)$$

$$\tau_{zz} = \lambda(\nabla.V) + 2\mu\frac{\partial w}{\partial z} \quad (3.6c)$$

$$\tau_{xy} = \tau_{yx} = \mu\left[\frac{\partial v}{\partial x} + \frac{\partial u}{\partial y}\right] \quad (3.6d)$$

$$\tau_{xz} = \tau_{zx} = \mu\left[\frac{\partial w}{\partial z} + \frac{\partial u}{\partial x}\right] \quad (3.6e)$$

$$\tau_{yz} = \tau_{zy} = \mu\left[\frac{\partial w}{\partial y} + \frac{\partial v}{\partial z}\right] \quad (3.6f)$$

3.2 TURBULENCE MODELING

Low Reynolds number flows are susceptible to laminar separation and a turbulent reattachment. The conventional turbulence models fail to capture the transition and give erroneous results in this regime [64]. In this research, the

turbulence model selected is Transition SST (4-Equation) model [138], [44]. This model is based on the correlation-based coupling of the two-equation SST k-ω model [139] with two extra equations. The intermittency transport equation is used to initiate transition locally. This is planted to crack on the production term of the turbulent kinetic energy in the boundary layer downstream of the transition spot. This contrasts with the classic usage of intermittency [140]. Another transport equation is of transition-onset momentum-thickness Reynolds number ($Re_{\theta t}$). It helps to trap the non-local influence of the turbulent intensity which alters because of the deterioration of the turbulent kinetic energy in freestream, and due to changes in the velocity outside of the boundary layer [141]. Since the model solves the above mentioned equations, it is called the γ-Re_{θ} transition turbulence model.

The transport equation of Intermittency is given as

$$\frac{\partial(\rho\gamma)}{\partial t} + \frac{\partial(\rho U_j \gamma)}{\partial x_j} = P_{\gamma 1} - E_{\gamma 1} + P_{\gamma 2} - E_{\gamma 2} + \frac{\partial}{\partial x_j}\left[\left(\mu + \frac{\mu_t}{\sigma_\gamma}\right)\frac{\partial \gamma}{\partial x_j}\right] \tag{3.7}$$

The transition sources are defines as follows:

$$P_{\gamma 1} = C_{a1} F_{length}\, \rho S [\gamma F_{onset}]^{c_{\gamma 3}} \tag{3.8}$$

$$E_{\gamma 1} = C_{e1} P_{\gamma 1} \gamma \tag{3.9}$$

Where S is strain rate magnitude, F_{length} is empirical correlation C_{a1}, $C_{e1}$are the values of the constants for the equations.

The destruction/relaminarization sources are expressed as:

$$P_{\gamma 2} = C_{a2} \rho \Omega \gamma F_{turb} \tag{3.10}$$

$$E_{\gamma 2} = C_{e2} P_{\gamma 2} \gamma \tag{3.11}$$

where Ω is vorticity mangnitude.

The transition onset is well-ordered by subsequent expressions:

$$Re_V = \frac{\rho y^2 S}{\mu} \tag{3.12}$$

$$Re_T = \frac{\rho k}{\mu \omega} \tag{3.13}$$

$$F_{onset1} = \frac{Re_V}{2.193 Re_{\theta c}} \tag{3.14}$$

$$F_{onset2} = \min\left(max\left(F_{onset1,} F_{onset1}^4\right), 2, 0\right) \tag{3.15}$$

$$F_{onset3} = \max\left[1 - \left[\frac{R_T}{2.5}\right]^3, 0\right] \tag{3.16}$$

$$F_{onset} = \max(F_{onset2} - F_{onset3}, 0) \tag{3.17}$$

$$F_{Turb} = e^{-[\frac{R_T}{4}]^4} \tag{3.18}$$

where y is the wall distance and $Re_{\theta c}$ is the critical Reynolds number where the intermittency initially jerks to rise in the boundary layer. The constants for the intermittency equation are:

C_{a1}=2, C_{e1}=1, C_{a2}=0.06, C_{e2}=50, $C_{\gamma 3}$=0.5, σ_γ=1

The transport equation for the transition momentum thickness Reynolds number is given as:

$$\frac{\partial(\rho R\tilde{e}_{\theta t})}{\partial t} + \frac{\partial(\rho U_j R\tilde{e}_{\theta t})}{\partial x_j} = P_{\theta t} + \frac{\partial}{\partial x_j}\left[\sigma_{\theta t}(\mu + \mu_t)\frac{\partial R\tilde{e}_{\theta t}}{\partial x_j}\right] \tag{3.19}$$

The source terms in Equation (3.19) is given as:

$$P_{\theta t} = c_{\theta t}\frac{\rho}{t}\,(Re_{\theta t} - R\tilde{e}_{\theta t})(1.0 - F_{\theta t}) \tag{3.20}$$

where,

$$t = \frac{500\mu}{\rho U^2} \tag{3.21}$$

$$F_{\theta t} = \min(\max\left(F_{wake}e^{\left(\frac{-y}{\delta}\right)^4}, 1.0 - \left(\frac{\gamma - 1/50}{1.0 - 1/50}\right)^2\right), 1.0) \tag{3.22}$$

$$\theta_{BL} = \frac{R\tilde{e}_{\theta t}\mu}{\rho U} \tag{3.23}$$

$$\delta_{BL} = \frac{15}{2}\theta_{BL} \tag{3.24}$$

$$\delta = \frac{50\Omega y}{U}\delta_{BL} \tag{3.25}$$

$$Re_{\omega} = \frac{\rho\omega y^2}{\mu} \tag{3.26}$$

and,

$$F_{wake} = e^{-(\frac{Re_{\omega}}{1E+5})^2} \tag{3.27}$$

The model constants for the $R\tilde{e}_{\theta t}$ equation is:

$c_{\theta t} = 0.03$; $\sigma_{\theta t} = 2.0$

The wall boundary condition for $R\tilde{e}_{\theta t}$is zero flux. At the inlet boundary condition for $R\tilde{e}_{\theta t}$ should be calculated from the empirical correlation based on the inlet turbulence intensity.

This model consists of three empirical correlations. $Re_{\theta t}$ is the transition onset modified by Menter et al.[138] to enhance the forecasts for a natural transition,

and F_{length} is the length of the transition zone. $Re_{\theta c}$ is the location where the model is stimulated to counterpart both F_{length} and $Re_{\theta t}$. These empirical correlations are delivered by Langtry and Menter [142].

$$Re_{\theta t} = f(Tu, \lambda) \tag{3.28}$$

$$F_{lenght} = f(R\tilde{e}_{\theta t}) \tag{3.29}$$

$$Re_{\theta c} = f(R\tilde{e}_{\theta t}) \tag{3.30}$$

The first empirical correlation is a function of the local turbulence intensity,

$$Tu = \frac{100}{U}\sqrt{\frac{2}{3}k} \tag{3.31}$$

where k is the turbulent energy.

The transition model interacts with the SST model as given by Equations (3.33) and (3.34) [139]:

$$\frac{\partial(\rho k)}{\partial t} + \frac{\partial(\rho U_j k)}{\partial x_j} = \widetilde{P_k} - \widetilde{D_k} + \frac{\partial}{\partial x_j}\left[(\mu + \sigma_k \mu_t)\frac{\partial k}{\partial x_j}\right] \tag{3.33}$$

$$\frac{\partial(\rho \omega)}{\partial t} + \frac{\partial(\rho U_j \omega)}{\partial x_j} = \alpha\frac{P_k}{v_t} - D_\omega + Cd_\omega + \frac{\partial}{\partial x_j}\left[(\mu + \sigma_\omega \mu_t)\frac{\partial \omega}{\partial x_j}\right] \tag{3.34}$$

$$\widetilde{P_k} = \gamma_{eff} P_k$$

$$\widetilde{D_k} = \min\left(\max\left(\gamma_{eff}, 0.1\right), 1.0\right) D_k$$

Where D_k and P_k destruction and production from the turbulent kinetic energy equations in the original SST model and γ_{eff} is the effective intermittency. ω

production term is not included. The resultant set of transport equations solved in this turbulence model is thus, given by Eqns. (3.7), (3.19), (3.33), (3.34).

Since the flow is a low Reynolds number, to see the fluctuations in the flow field parameters necessary to formulate the turbulence modeling which can capture the laminar to turbulence flow phenomenon feasibly. Here in this research, the turbulence model chosen is 4-equation model that is Transition $\gamma - Re_{\theta}$model.

3.3 GEOMETRIC MODELING AND GRID GENERATION

The geometries of the NACA0012 airfoil, clean configuration, and protrusion and cavities were generated using the ANSYS ICEMCFD®. The chord length of the airfoil in each case is 0.1m as shown in Fig 3.1. Since the airfoil leading edge is round, a C-topology computational domain was used for all simulations. The domain extends to 20 times the chord length in all the directions from the surface of the airfoil for all geometries with protrusions and cavities.

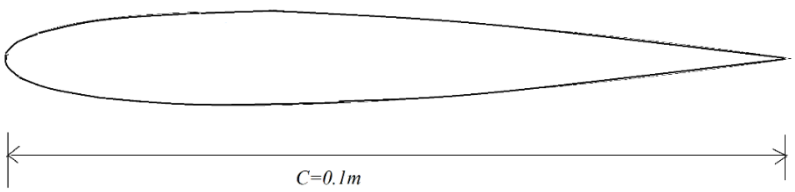

(a) Clean Airfoil Configuration

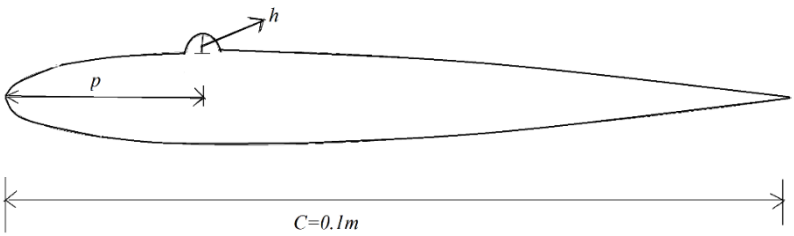

(b) Circular Shaped Protrusion

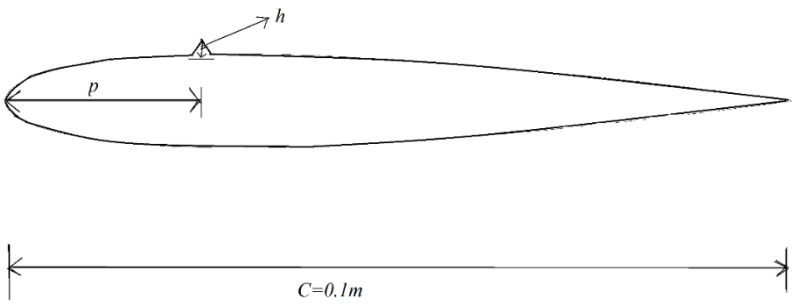

(c) Triangle Shaped Protrusion

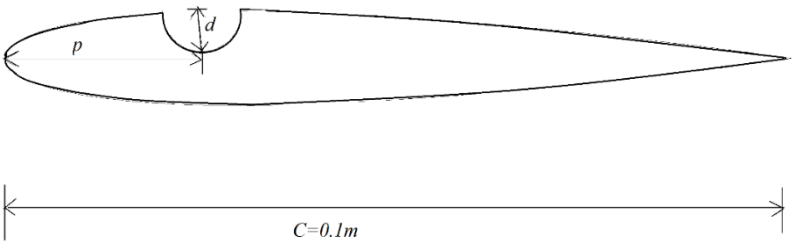

(d) Circular Shaped Cavity

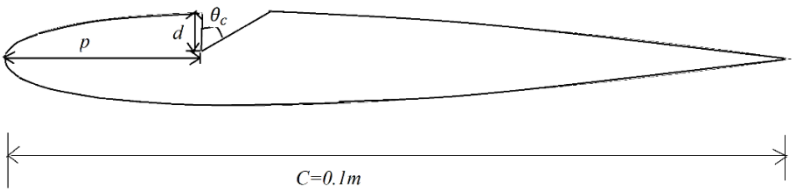

(e) Triangle Shaped Cavity

Figure 3.1: Geometries of the airfoil with (a) Clean Configuration (b) Circular Shaped Protrusion (c) Triangle Shaped Protrusion (d) Circular Shaped Cavity (e) Triangle shaped cavity

As shown in Fig. 3.1, three different shapes of protrusions viz. semi-circular, right triangle, and isosceles triangle and two different shapes of cavity viz. circular and right triangle, is chosen for the analysis. Further, for each protrusion located at different locations on the surface of the airfoil, three different heights are chosen. The details of the shapes, sizes, and locations of various protrusions are shown in Table 3.1. Similarly, the circular cavity, located at various

locations on the airfoil surface, has two different depths whereas the cavity with a triangle shape has a vertex angle $\theta_c = 60^o$ while the depths vary. The details of the various cavity configurations and their locations on the airfoil surface are provided in Table 3.2.

Table 3.1: Shape, Location, and Height of Protrusions Investigated

S.No	**Shape of Protrusion**	**Location (p)**	**Height(*h*)**
1	Circular	Leading edge **Suction Surface:** 0.05c 0.10c 0.25c 0.50c 0.75c **Pressure Surface:** 0.05c 0.10c 0.25c 0.50c 0.75c	0.005c 0.01c 0.02c
2	Triangular	Leading edge **Suction Surface:** 0.05c 0.10c 0.25c 0.50c 0.75c **Pressure Surface:** 0.05c 0.10c 0.25c 0.50c 0.75c	0.005c 0.01c 0.02c

Table 3.2: Shape, Location, and Depth of Cavity Investigated

S.No	Shape of Cavity	Position (p)	Height(h)	$\theta_c$cavity angle
1	Circular	**Suction Surface:** 0.10c 0.25c 0.50c	0.025c 0.05c	60º
2	Triangular	**Suction Surface:** 0.10c 0.25c 0.50c	0.025c 0.05c	60º

ANSYS ICEM CFD has been used to generate mapped quadrilateral meshes around all airfoil configurations using a multi-blocking strategy as shown in Fig. 3.2. A dense grid of O-topology stretching in all directions away from airfoil created around the airfoil. The first cell distance from the surface of the airfoil in each case is set to be 0.000019 m so that non-dimensional cell wall distance y+ ≈ 1. Based on a detailed grid independence study, the multi-block grid generated with 169750 quadrilateral elements is finalized to pursue the further simulation of an airfoil with protrusion and cavities. The orthogonal quality of the mesh was maintained for all the meshes above 0.45.

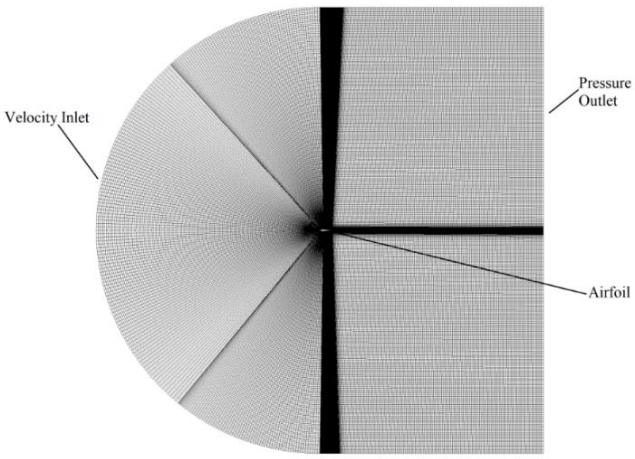

(a)

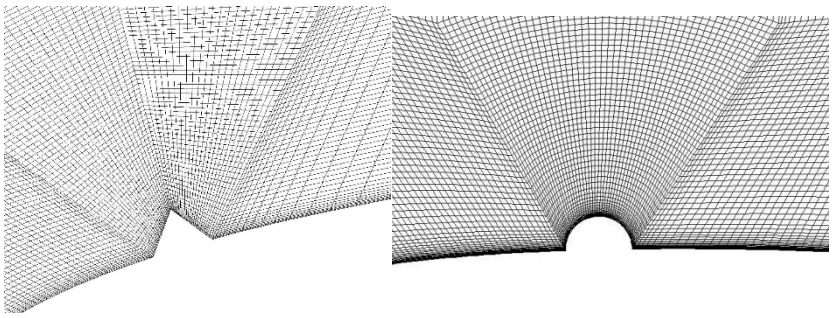

(b) *(c)*

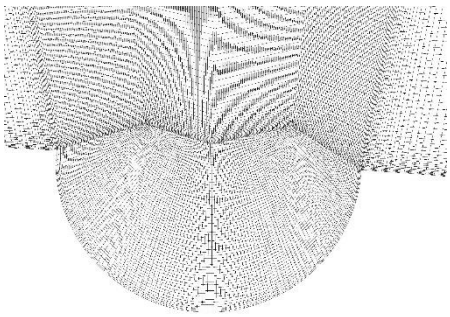

(d)

Figure 3.2 Multi-block grid around NACA 0012 airfoil with protrusions and cavities

For the oscillating airfoil, geometry was created in ANSYS Workbench, with the airfoil positioned at $\alpha=10^0$, at its mean position. Two different zones are generated, the zone associated with the airfoil has moving motion and while the outer zone is stationary. The size of the element is 0.75m, with curvature minimum sizing is 0.042m. For the oscillating airfoil cases, the quad-dominant grid was created around the airfoil with a body of influence sizing on the wake region, as shown in Fig.3.3. The Body of Influence will influence the mesh density of the body that it is scoped to, but it will not be a part of the model geometry nor will it be meshed. The specified body of influence sizing imposes a local maximum size on all elements that are inside the boundary of the body. The first cell length calculated using the Reynolds number, chord length, and by fixing the $y+=1$. Based on the thorough grid independence study, the mesh elements in the computational domain are finalized as 312000 elements.

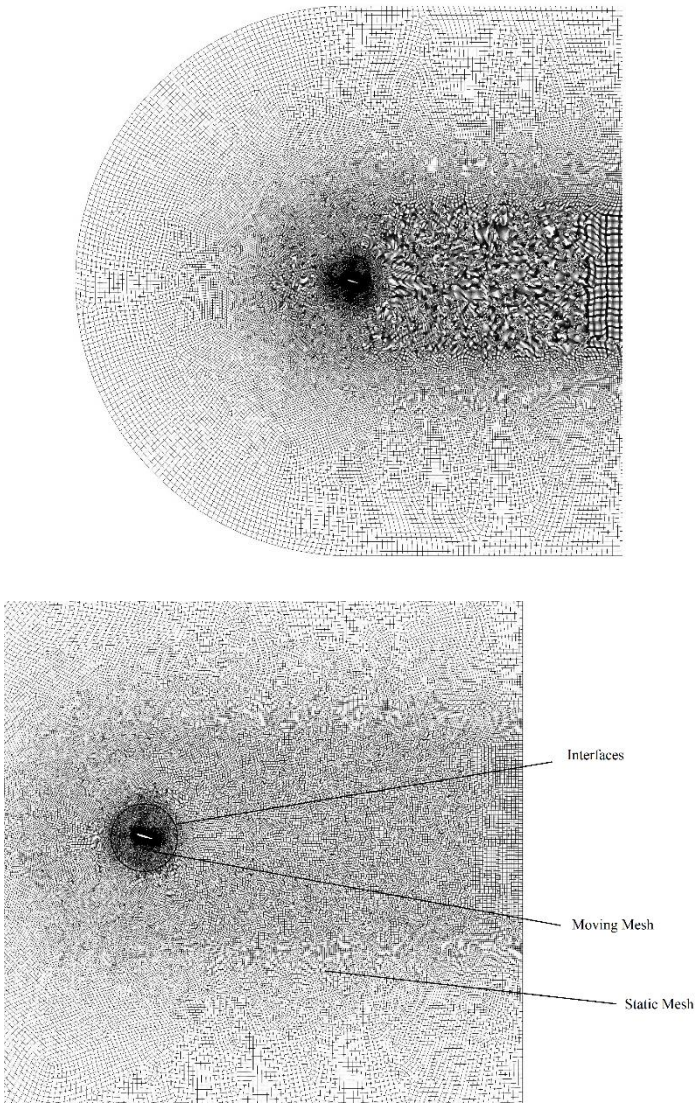

Figure 3.3. Quad dominant grid generation

3.4 SOLVER SETUP

To investigate the effect of protrusions and cavities, a pressure-based finite volume solver is chosen viz. ANSYS Fluent. ANSYS Fluent solver is a high-end solver having the capability of solving complex flow problems in the wide area of applications like incompressible flow, compressible flow, laminar flow, turbulent flow, transitional flow, and some other industrial applications. ANSYS Fluent solves the governing integral equations for the conservation of

mass and momentum, and (when applicable) for energy and other scalars such as turbulence and chemical species. In both cases a control-volume-based technique is used that consists of:

ANSYS Fluent uses a control-volume-based technique to convert a general scalar transport equation to an algebraic equation that can be solved numerically. This control volume technique involves integrating the transport equation at each control volume, yielding a discrete equation that states the conservation law on a control-volume basis. The discretization of the governing equations can be demonstrated most easily because of the unsteady conservation equation for the transport of a scalar quantity. This is demonstrated by the following equation written in integral form for an arbitrary control volume

$$\int \frac{\partial \rho \emptyset}{\partial t} \mathrm{dV} + \oint \rho \emptyset \vec{\boldsymbol{V}} . \mathrm{d}\vec{\boldsymbol{A}} = \oint \Gamma_{\emptyset} \nabla_{\emptyset} . \mathrm{d}\vec{\boldsymbol{A}} + \int \mathrm{S}_{\emptyset} \, \mathrm{dV} \qquad (3.35)$$

where ρ, V, dV, $\vec{\boldsymbol{V}}$ and $\vec{\boldsymbol{A}}$ respectively are density, control volume, differential control volume, velocity vector, and area vector while $\Gamma_{\emptyset}$ and $S_{\emptyset}$ are diffusion coefficient for $\emptyset$ and source of $\emptyset$ per unit volume. Equation 3.35 is applied to each control volume, or cell, in the computational domain.

Since this research work deals with low-speed flows, a pressure-based solver is chosen to calculate the flow field. The pressure-based solver works with an algorithm called the projection method, in which the limitation of mass conservation (continuity) of the velocity field is attained by solving a pressure (or pressure correction) equation [143]. The pressure correction equation is obtained from the continuity and the momentum equations in a way that the velocity field, corrected by the pressure, fulfills the continuity. Since the governing equations are nonlinear and coupled to one another, the solution process contains iterations where the complete set of governing equations is elucidated repetitively till the solution converges. The pressure-based segregated algorithm steps can be seen as shown in Fig. 3.4.

In the pressure-based solver, the governing equations are sequentially solved one after another. Since the governing equations are non-linear and coupled, the solution has to carry the loop until the solution attains the converged solution as shown in Fig.3.4.

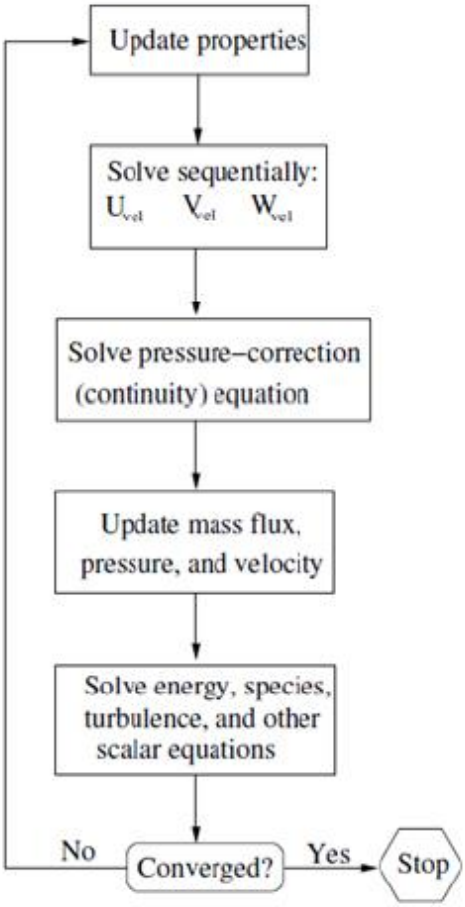

Figure 3.4: Pressure Based segregated Algorithm [144]

3.4.1 SPATIAL AND TEMPORAL DISCRETIZATION

All the conservation equations are discretized using a second-order upwind scheme with a higher-order under-relaxation factor of 0.75 applied to all flow variables. The viscous terms in the momentum equations, however, are discretized using a second-order upwind scheme. The second-order has been selected to get an accurate solution. In the second-order upwind scheme, quantities at cells are computed using a multi-dimensional linear construction

approach. At cell faces, higher-order accuracy is attained through a Taylor series expansion of the cell-centered solution about the cell centroid. The face value$\emptyset_f$, can compute using the equation.

$$\phi_{f,SOU} = \emptyset + \nabla\phi.\vec{\boldsymbol{r}} \tag{3.36}$$

Where ϕ and $\nabla\phi$ are the cell-centered value and gradient in the upstream cell, $\vec{r}$ is the displacement vector from the upstream cell centroid to the face centroid.

The gradient at cell centers is evaluated using the least square cell-based formula wherein the variables are assumed to vary linearly inside the cells. The change in the cell values between c0 and ci along the vector $\delta r_i$from the centroid of cell c0 to cell ci is given as

$$(\nabla\phi)_{c0}.\Delta r_i = (\phi_{ci} - \phi_{c0}) \tag{3.37}$$

As the low Reynolds number flows are inherently unsteady, the unsteadiness is resolved using a second-order accurate implicit transient formulation. The implicit time discretization of unsteady navies-stokes equations for the transient solution is completed by the introduction of a pseudo time variable τ and the accompanied preconditioned time derivative term, thus giving a dual time-stepping scheme. Thus the coupled navies-stokes equations with preconditioned pseudo time derivative term are expressed as

$$\frac{\partial}{\partial t}\int_V U\,dV\,\Gamma\frac{\partial}{\partial\tau}\int_V Q\,dV + \oint[F_i - F_v]\,.\,dA = \int_V S\,dV \tag{3.38}$$

Where t resembles physical time, τ represents a pseudo time variable. The transient terms in the equation are discretized using the second-order Euler backward difference scheme. The semi-discretized Navies-Stokes equations using dual time stepping formulation is prearranged by

$$\left[\frac{\Gamma}{\Delta\tau} + \frac{\varepsilon_0\partial U}{\Delta t\,\partial Q}\right]\Delta Q^{k+1} + \frac{1}{V}\oint[F_i - F_v].\,dA = S - \frac{1}{\Delta t}(\varepsilon_0 U^k - \varepsilon_1 U^n + \varepsilon_2 U^{n-1})$$

(3.39)

Where $\varepsilon_0 = 3/2$, $\varepsilon_1 = 2$, $\varepsilon_2 = 1/2$ are the coefficients for the second-order accuracy *k* is the inner iteration counter and n is the physical time step counter.

Starting with the steady-state or pseudo-steady-state solutions as an initial guess, the equations are solved iteratively at each time step before advancing to the next time level, with a fixed time step of 1e-05 seconds.

3.4.2 BOUNDARY CONDITIONS

For clean airfoil, airfoil with protrusions, and airfoil with cavities, the airfoil surface is a no-slip boundary with u = 0 and v = 0 imposed on it. The other boundaries, as shown in Fig. 3.2 (a), are velocity inlet and pressure outlet. At the velocity inlet, a uniform velocity of 15 m/s was specified with the intermittency of 1.0 and turbulent intensity of 0.1 and at the pressure outlet boundary, the static pressure of 1.0 *atm* was specified. The values at the inlet were used to initialize the solution. Steady-state solutions are used as initial values for the transient simulations. For the pitching airfoil, the Reynolds number used for performing the numerical analysis of dynamic stall is 135000. The intermittency of 1.0 and turbulent intensity of 0.08 from the Lee and Gerontakos [123], and at the pressure outlet boundary, the static pressure of 1.0 atm specified. The values at the inlet were used to set the solution. Initial solutions at steady-state are used as starting points for the transient ones. The motion of the airfoil is given using the user-defined function in the solver as shown in Fig. 3.5.

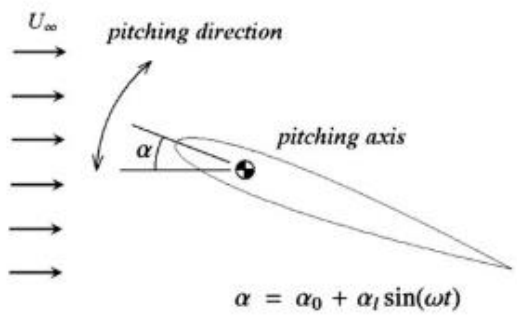

Figure 3.5: Graphic representation of Pitching Motion

$$\alpha = 10^{o} + 15^{o} \sin(\omega t),$$

In the above-mentioned expression for pitching motion, α_0 is the mean angle of attack, α_l is pitching magnitude.

3.4.3 GRID INDEPENDENCE AND SOLVER VALIDATION

A detailed grid independence study is done for clean NACA0012 airfoil to assess the number of cells essential for a grid-independent solution at the Reynolds Number of 100000 and 500000. As can be appreciated in Fig. 3.6 (a), the pressure distribution over the airfoil surface for grids with different element counts appears to be the same over the entire surface. A careful examination of the peak suction pressure in Fig. 3.6 (b) reveals that the solution becomes grid-independent only for meshes with an element count of 169750 and more. In the backdrop of this mesh independence study, all simulations started with a minimum element count of 170000, and the element count for all cases was increased to 300000 during the solution using dynamic mesh adaptation based on pressure gradients. Similarly in the case of the Reynolds number 50000 as can be seen in Fig. 3.7. The solution exhibited the same from 170000 elements onwards to 248000, which means the solution is independent on the grid. All the analyses were carried out with a minimum element count of 170000 elements.

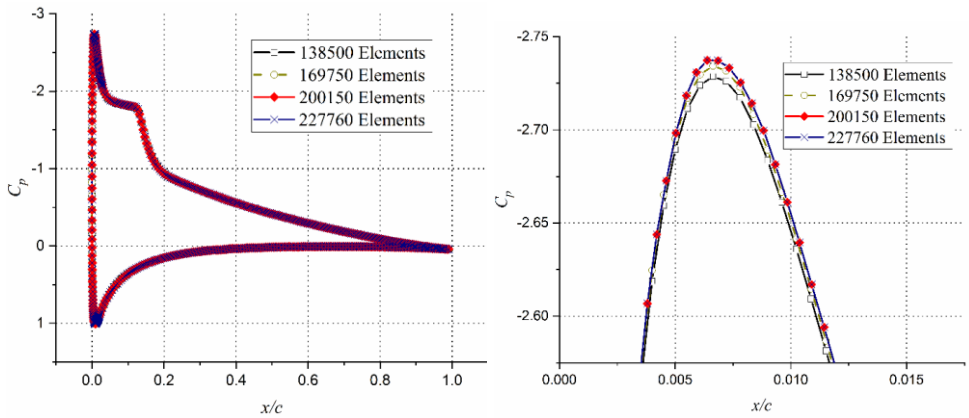

(a) Cp vs. x/c for NACA 0012 *(b) Cp vs. x/c near the point of maximum suction*

Figure 3.6: Grid Independence Study for Reynolds Number 100000

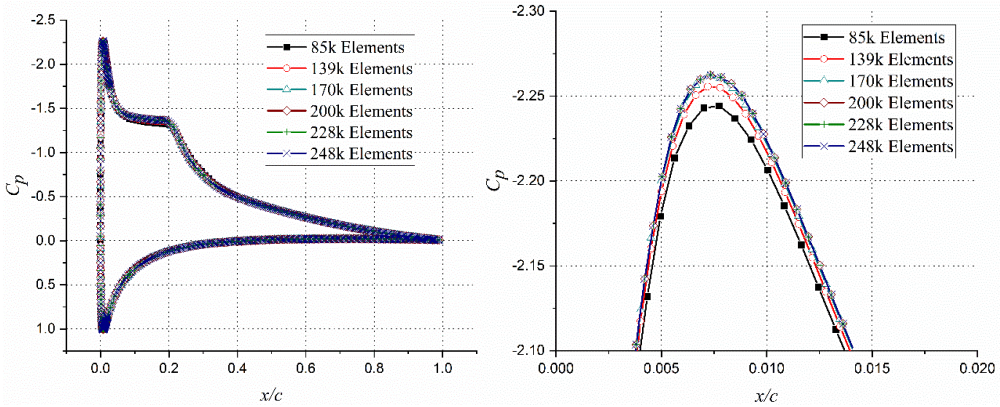

(a) Cp vs. x/c for NACA 0012 *(b) Cp vs. x/c near the point of maximum suction*

Figure 3.7: Grid Independence Study for Reynolds Number 50000

Besides the grid independence study, solver validation is conducted against the experimental observations by Ohtake et al. [145] and Rinoie and Takemura [39]. As can be seen in Fig. 3.8 (a), a very good arrangement is witnessed among the time-averaged lift coefficient values obtained in the current study and those obtained by Ohtake et al. Also, the time-averaged pressure distribution over NACA 0012 at a Reynolds number of 130000, obtained in the present validation study in close agreement with those obtained by Rinoie and Takemura, as can be observed in Fig. 3.8 (b). A slight disagreement in the surface pressures for $\alpha = 10^{o}$, seen in Fig. 3.8 (b) is primarily due to the dependence of laminar separation bubble size on the freestream turbulent intensity. Thus, it may safely be presumed that the numerical methodology adopted in the current study gives reasonably accurate solutions for scientific consumption.

A solver verification is also conducted against the numerical results obtained by Counsil and Boulama for the evolution of the lift coefficient of NACA 0012 at a Reynolds number of 10^5 [146]. As shown in Fig. 3.9, the lift coefficient for NACA 0012 settles to a steady value at $\alpha = 8^{o}$ and follows the findings of Counsil and Boulama. This verification is done as the current research uses a similar numerical methodology especially the turbulence model.

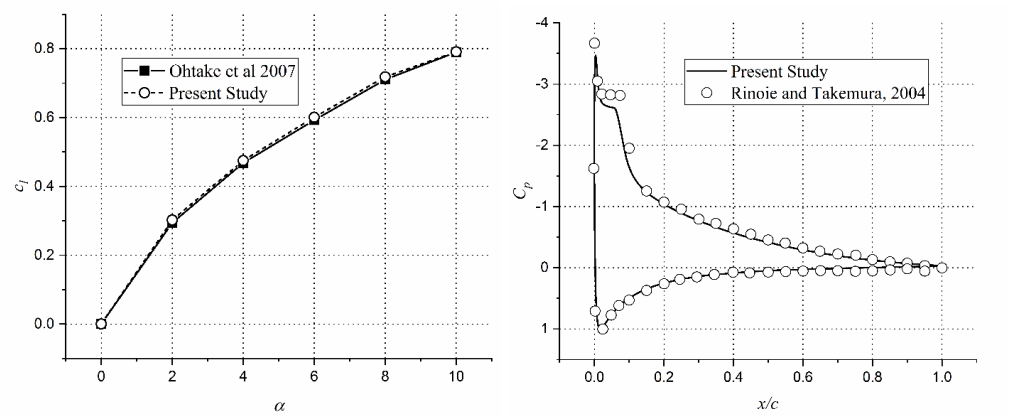

(a) Time-averaged Cl at Re=10^5

(b) Time-averaged surface pressure distribution at α=10º

Figure 3.8: Solver Validation Study

As observed by Counsil and Boulama, at a Reynolds number of 10^5, the converged lift coefficient of NACA 0012 shows non-oscillatory behavior at α = 8º. The primary reason suggested for this lift convergence is the amount of freestream turbulent intensity, the turbulence model, and comparatively high Reynolds number that might inhibit the vortex shedding [146].

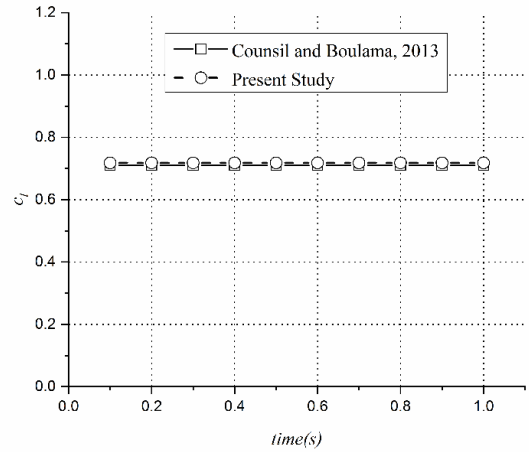

Figure 3.9: Evolution of lift coefficient at α = 8º

To analyze the cases with pitching airfoil, a detailed grid independence study is done for clean NACA0012 airfoil to assess the number of cells mandatory for a grid-independent solution. As can be observed in Fig.3.10, lift coefficient versus angle of attack for the airfoil with various element counts reveals that the

solution becomes grid-independent only for meshes with an element count of 312000 and more. In the backdrop of this mesh independence study, all simulations involving pitching airfoil were started with a minimum element count of 312000. As can be seen in Fig.3.11, the present the result from the present numerical analysis is in decent agreement with the experimental results of Lee [123], for the oscillating airfoil. This validates our numerical scheme for the pitching airfoil as well.

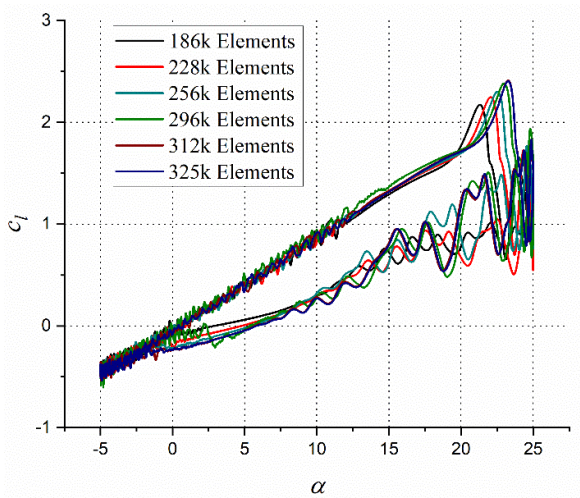

Figure 3.10: Grid Independence Study of an oscillating airfoil

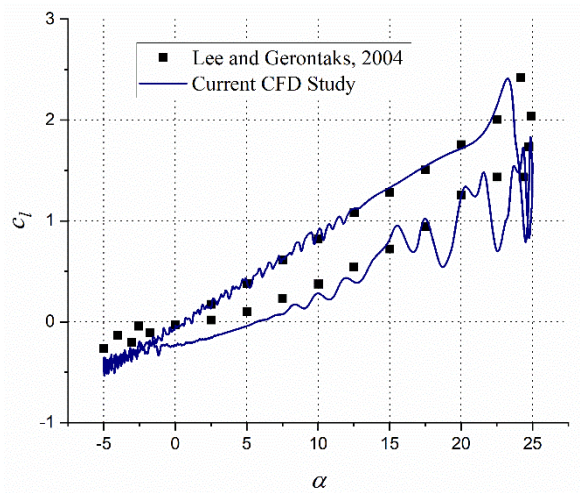

Figure 3.11: C_l-α curve for oscillating NACA 0012

3.5 EXPERIMENTAL SET-UP

Experimental set-ups are instrumental in establishing scientific conclusions and understanding complex aerodynamic and hydrodynamic problems. Some popular experimental instruments associated with aerodynamic research are flight tests, water tunnels, subsonic, near sonic, transonic, supersonic, and hypersonic wind tunnels, shock tubes, rocket flights, ballistic ranges, etc. Wind tunnels are frequently the utmost speedy, cost-effective, and precise means for directing aerodynamic research and tracking down aerodynamic data to backup design choices.

To conduct experiments in the wind tunnel, a scaled model is used to predict flow behavior over a full-sized prototype. The dynamic similarity is obtained by matching the dimensionless coefficients viz. the Reynolds number, the Mach number, and the Froude number [147]. For wind tunnel experiments, the Froude number is an important similarity parameter for dynamic tests in which model motion, as well as the aerodynamic forces, are entangled. If the model is stationary while performing wind tunnel testing, only the Reynolds number and Mach number can be considered as similarity parameters. If the prototype model in experiments is having alike Reynolds number and Mach number of the full-scale model, then the prototype model and full-scale models are similar. Despite similar Reynolds numbers, due to scale effects, the flow involving transition, may not be similar. In such situations, CFD comes to the rescue wherein full-scale models may be tested. In this research similarity parameter is the Reynolds number, ignoring the compressibility effects and they are fixed at 100000 and 50000.

3.5.1 WIND TUNNEL SPECIFICATIONS

All the wind tunnel experiments were in the Low-Speed Wind Tunnel shown in Fig. 3.12, at the Department of Aerospace Engineering, University of Petroleum and Energy Studies, Dehradun.

Figure 3.12: Low-Speed Wind tunnel at UPES

The test section of the wind tunnel has two compartments with an overall size of 600 mm×600 mm x 2000 mm as shown in Fig. 3.13. The maximum speed of the wind tunnel can go up to 60m/sec with an rpm of 1000. The turbulent intensity of the wind tunnel was fixed at 0.1%. The schematic diagram as given in the Fig. 3.13 of the wind tunnel parts are given below:

1. Bell mouthed section.

2. Honey Comb.

3. Settling Chamber, and screen sections.

4. Contraction cone.

5. Test Section.

6. Transition (square to circular)

7. Diffuser.

8. Fan Duct.

9. Motor and Stand.

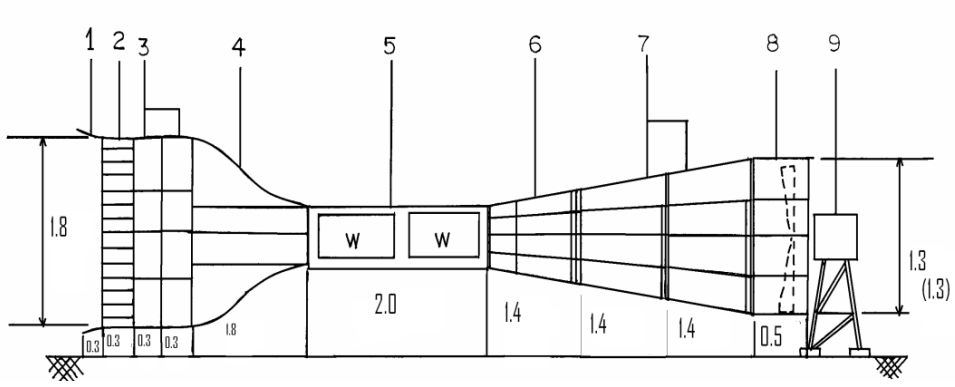

Figure 3.13: Schematic Diagram of Wind tunnel

3.5.2 WIND TUNNEL MODEL AND ACCESSORIES

NACA0012 airfoil models with and without protrusions and cavities are 3D printed to a size equal to use in numerical simulations. At the mid-section of selected mode16 pressure tapings are installed in a chordwise direction to study the pressure distribution over the surface of the airfoil as shown in Fig. 3.14. Locations of the various pressure tapings are provided in Appendix 1.

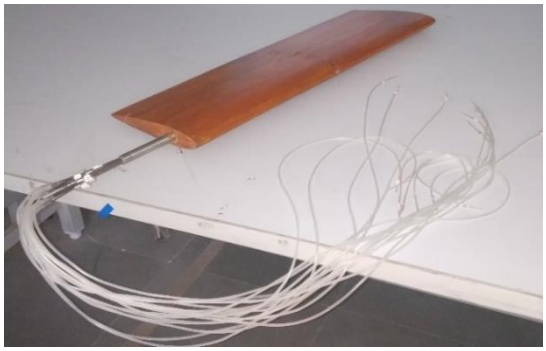

Figure 3.14: Wind Tunnel Airfoil Model

Electronic Pressure Scanner (32 PORT) contains 32 number temperature-compensated pressure sensors. All these instruments are microprocessor-based compact self-reliant units with secondary storage of 2GB. It can also be connected to the computer through an RS232 port and read on to a computer and data can be downloaded in Excel format or Text format for further analysis. The user-friendly operations using 4 keys and 4 lines 16 characters/line displays

allow the user to set the instrument easily and also display the pressure data on the system for monitoring the pressure as shown in Fig. 3.15.

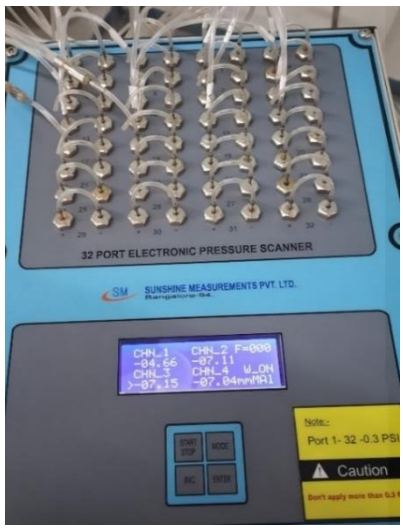

Figure 3.15: 32-Port Electronic Pressure Scanner

Figure 3.16: Smoke Generator for Wind Tunnel

Flow Visualization play as one of the key player to study the flow phenomenon. Significant characteristics of flows viz. separated shear layer, transition location, the extent of separated region and vortices, can be extracted using visualization techniques without any numerical computation [147]. In this

research, the basic flow visualization setup used is the smoke visualization in conjunction with a laser sheet. Liquid paraffin is used to generate smoke and it is introduced through in the contraction cone to the flow at an immovable location through a rake at several points to witness the flow pattern over the surface of the airfoil. The setup of the smoke generator is shown in Fig. 3.16.

6-Component Balance is used to analyze the forces acting on bodies that are moving in a fluid to analyze and design the bodies and vehicles for their aero/hydrodynamic characteristics. These forces are largely estimated by measurement on scaled models of the bodies kept in a wind tunnel operating at a suitable wind speed. The forces are then extrapolated to the full scale. The measurements of these forces are conveniently made by appropriate balances which are designed to suit certain specifications.

Figure 3.17: 6-Component Balance system used in the wind tunnel [148]

These specifications normally depend on the loads to be measured, size of the models and size of the wind tunnel, etc. The maximum load taken by the 6-component balance for the mentioned wind tunnel above is 10kg. The model is mounted on the stem that protrudes into the test section and has a simple mechanism for pitching and yawing the model. The stem is fixed on a metric plate which transfers the loads into 6 Strain elements. The outputs from the

Strain gauge mounted on the strain elements are amplified by appropriately designed amplifiers. These signal conditioners amplifiers are designed by Sunshine measurements using low noise and highly stable instrumentation amplifiers. The outputs from these amplifiers are measured using a microcontroller-based measurement system. The measurement system has a keyboard and a display which are useful in setting up the system and displaying the data from the instrumentation amplifiers. Fig.3.17 shows the entire setup of the 6-component balance system used in the wind tunnel.

Hot-Wire Anemometer used to measure the fluctuation and mean of velocities involving very high spatial and temporal resolutions. The hot-wire anemometer technique which uses a very small sensing element having a low response time, high sensitivity, and minimal flow interference is one of the most suitable methods adopted for measuring turbulence in fluids. Two modes of operation are possible for hot-wire anemometers. These modes depend on whether the current through the wire is kept constant or the resistance of the wire is kept constant. In the constant temperature, hot-wire anemometer the resistance of the wire is kept constant by an electric feedback arrangement. In the wind tunnel, a constant temperature hot-wire anemometer, designed using modern integrated chips is versatile, accurate, and suitable for research work as shown in Fig. 3.18.

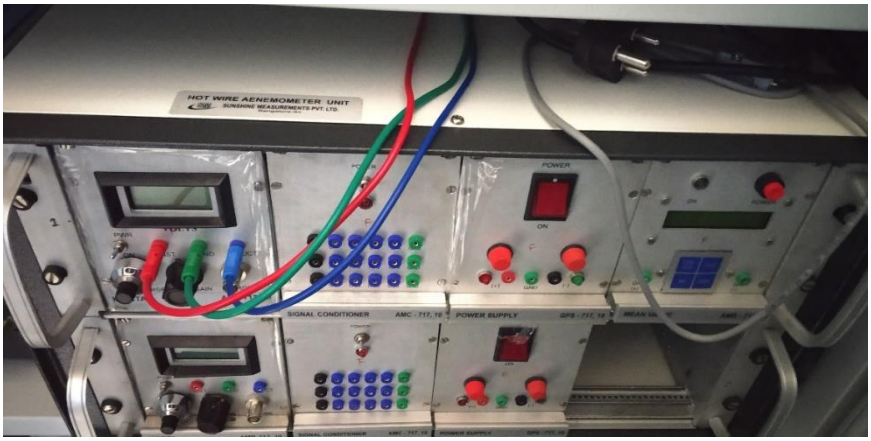

Figure 3.18: Hot-Wire Anemometer Setup [149]

3.5.3 WIND TUNNEL PROCEDURE

The wind tunnel airfoil model is inserted in the test section and connected the pressure probes to the electronic manometer to get the results digitally for more accuracy. Initially verified the angle of attack position by using the manometer and operated the wind tunnel for the Reynolds number 100000. Wind tunnel is operated at 157Rpm is set based on the calculation. 16 pressure tapings are connected on the surface of the airfoil at the mid of the span to the electronic manometer to collect the readings of the pressure values at every angle of attack starting from 0° to 20°, with 2° interval. The digital manometer scans and reports the average pressure at every 1s, which provides the average of pressure for 100 readings at each probe for every 1s. The pressure readings are collected once the flow is stabilized in the test section, the stabilization is concluded based on the fluctuation in the readings. After the readings are stabilized, readings are saved for up to one minute. Readings are taken for every 0.1sec and it will give the average value of 100 readings in that particular second. Data is saved a maximum of one minute, again the overall average value of pressure at each location is calculated. Based on the final average value using the pressure coefficient formula at each location on the surface of the airfoil. Once the readings are taken at each pressure probe, the pressure coefficient is calculated at every angle of attack.

$$C_p = \frac{p_1 - p_f}{q}$$

Cp= Pressure Coefficient

P_1 = static pressure at the location of taping on the surface of the airfoil

P_f = free stream pressure

q = dynamic pressure

$$C_l = C_n cos\alpha - C_a sin\alpha$$

$$C_d = C_n sin\alpha + C_a cos\alpha$$

$$C_n = \int \{C_{p,lower} d(x/c) - C_{p,upper} d(y/c)\}$$

$$C_a = \int \{C_{p,lower} d(y/c) - C_{p,upper} d(y/c)\}$$

Where C_n is normal force coefficient, C_a is axial force coefficient, C_l is coefficient of lift, C_d is drag coefficient

The wind tunnel airfoil model is inserted in the test section as shown in Fig.3.19 and connected the pressure probes to the electronic manometer to get the results digitally for more accuracy. Initially verified the angle of attack position by using the manometer and operated the wind tunnel for the Reynolds number 100000. Wind tunnel is operated at 157Rpm is set based on the calculation. Using the electronic manometer the readings of the pressure values are collected at every angle of attack starting from 0º to 20º, with 2º interval. The pressure readings are collected once the flow is stabilized in the test section, the stabilization is concluded based on the fluctuation in the readings. After the readings are stabilized, readings are saved for up to one minute. Readings are taken for every 0.1sec and it will give the average value of 100 readings in that particular second. Data is saved a maximum of one minute, again the overall average value of pressure at each location is calculated. Based on the final average value using the pressure coefficient formula at each location on the surface of the airfoil, the coefficient of the pressure data taken out. A similar procedure is repeated at every angle until 20º. Fig. 3.20 shows a typical pressure distribution over a surface of an airfoil at an 8º angle of attack based on the experimental results and the present CFD study. As can see in Fig. 3.20, it is clear that the numerical and experimental results are in good agreement with each other.

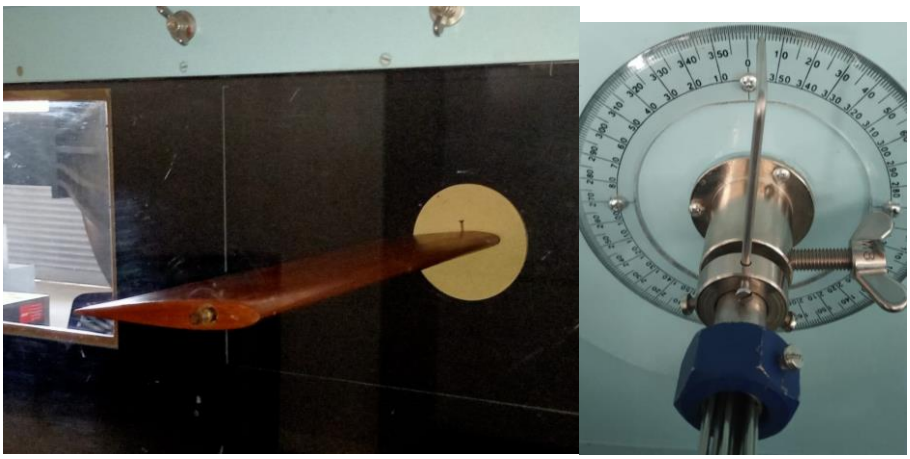

Figure 3.19: Mounted Model inside the Wind Tunnel

To check the mean velocity on the desired location over an airfoil surface, hot-wire anemometer is used. Hot-wire anemometer is placed near the airfoil trailing edge and connected the anemometer probe to the setup by setting voltage as 2.3 according to manual instructions. The voltages fluctuations can be seen in the computer created for the hot-wire anemometer set-up. From the voltages, it is converted into the mean velocity.

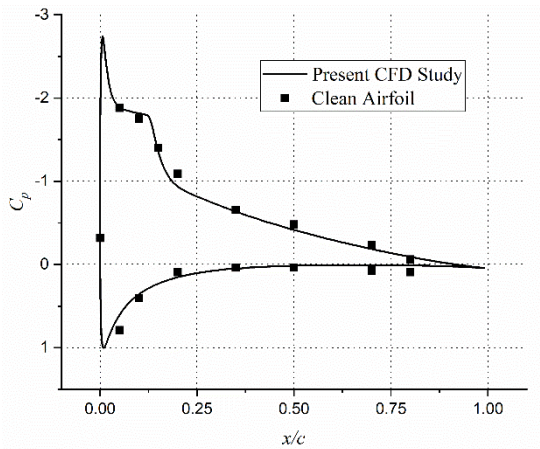

Figure 3.20: Pressure distribution around clean NACA 0012 at α = 8°

CHAPTER 4. EFFECT OF PROTRUSION

4.1 EFFECT OF CIRCULAR PROTRUSION AT REYNOLDS NUMBER 10^5

Numerical simulations are carried to examine the effect of circular protrusion placed at the leading edge, 0.05c, 0.25c, and 0.5c on the suction surface and 0.05c on the pressure surface. The current section presents the effect of these protrusions of varying heights on the aerodynamic lift and efficiency of NACA 0012 at a Reynolds number of 10^5. The angles of attack (AOA) are varied between 0º and 20º with 2º intervals and the protrusions have heights of 0.005c, 0.01c, and 0.02c.

4.1.1 CIRCULAR PROTRUSION AT THE LEADING EDGE

The airfoils with circular protrusions of smaller heights show marginal improvements in the lift coefficient and *L/D* values. In the range of AOA between α = 4º and 10º, the lift curve for an airfoil with circular protrusions overlaps that for a clean configuration as can be seen in Fig 4.1 (a). For a protrusion of height *h* = 0.005c, the peak lift coefficient is the same for that for the clean configuration, the recovery from a stall, however, for an airfoil with protrusion is immediate. As can be seen in fig 4.1 (b), the *L/D* ratio for airfoils with circular protrusions is slightly improved as compared to clean airfoil.

For angles of attack up to α=12°, the *L/D* values for configurations with protrusion heights of 0.005c and 0.01c almost similar to the clean airfoil. At angles of attack higher than α=12°, there is an enhancement in the L/D value by up to 68% for *h* = 0.01c. As the height of the protrusion is increased, there is a reduction in lift coefficient and increment in drag coefficient, which leads to the reduction in the *L/D* values by up to 34% for AOAs below α = 10º. Subsequently, as the angle of attack is increased for a given height of circular

protrusion, slight improvements in the *L/D* values are observed as can be seen in Fig. 4.1(b).

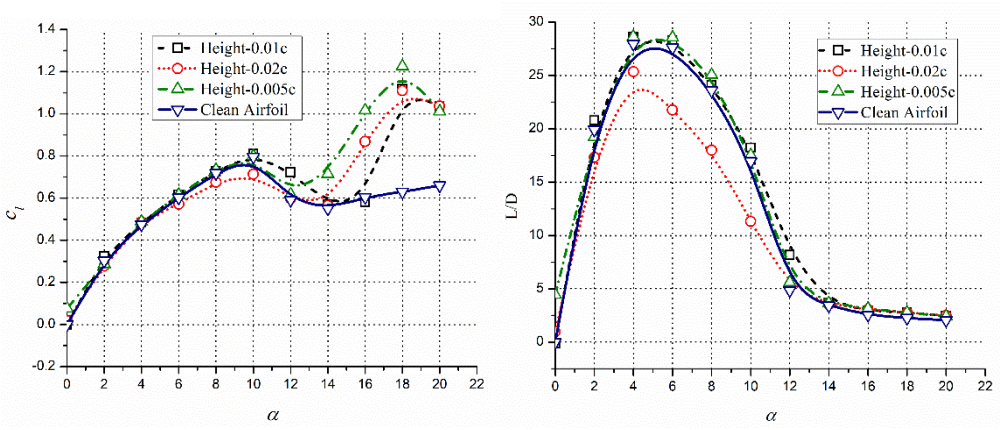

(a) Lift coefficient versus AOA *(b) L/D ratio versus AOA*

Figure 4.1: Aerodynamic coefficients for NACA 0012 with a circular protrusion at the leading edge

For leading-edge protrusions of height *h*=0.01c, the stall is slightly smoother with a full stall occurring at AOA between α=14º and 16º. At α = 12º and 18º, the protrusion with *h*=0.01c offers a significant improvement in time-averaged lift coefficients, due to cyclic vortex shedding which results in a downward flow of momentum immediately behind the trailing edge as a counter-clockwise vortex is shed away. The instantaneous vortical structures that result in the unsteadiness of the lift coefficient are shown in Fig. 4.2. As can be seen in Fig. 4.2 (a), with two counter-rotating vortices on the suction side, the lift is small as the flow separated from the leading edge, fails to curl downwards. As the trailing counter-clockwise vortex is shed away, clockwise circulation is imparted to the airfoil and the primary clockwise vortex becomes stronger and pushes the flow closer to the surface as can be appreciated in Fig. 4.2 (b). This results in an increased instantaneous lift coefficient. The smaller protrusions lead to more severe vortex shedding causing high amplitude oscillations in the lift and drag values. The time-averaged lift coefficients are thus, significantly improved for AOAs higher than α =12º. The drag, however, is essentially

unaffected by the existence of protrusions at the leading edge, for AOAs below α = 14º, as shown in Fig. 4.1 (b).

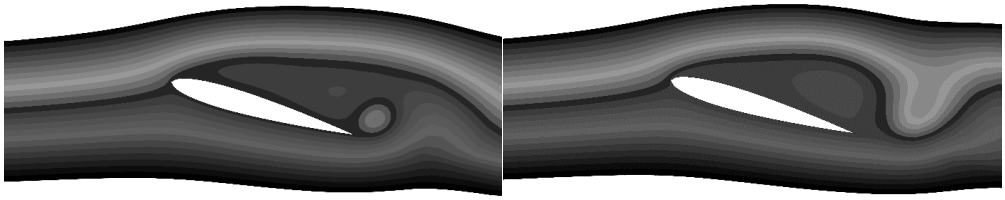

(a) Crest lift coefficient, C_l =0.865 *(b) Trough lift coefficient, C_l =1.17*

Figure 4.2: Vortex structure for an airfoil with leading-edge protrusion of h= 0.005c and α=16º

The placement of circular protrusions at the leading edge adds to the flow unsteadiness as the airfoil undergoes high-frequency vortex shedding of 100 Hz, at α=16º. The frequency of fluctuations in the lift coefficient is similar for all protrusion heights at α=18º. However, at α = 20º, the protrusion with height *h* = 0.01c lowers the fundamental frequency of oscillation to 40 Hz. This is primarily because of the fact the oscillation at α = 20º is purely a bluff body oscillation and the protrusions have no effect on the vortex shedding of the airfoil. The protrusions, however, cause the vortex shedding to start at this Reynolds number which otherwise is not present for the clean configuration.

The vortex-shedding pattern and the amplitude of oscillations in the lift coefficient are highly associated with the nature of the shear layer and the boundary layer. For a protrusion height of 0.005c at α = 0º, the flow on both the suction and pressure surface remain fully laminar throughout and separate near trailing edge shedding vortices periodically from the top and bottom surfaces as can be seen in Fig. 4.3 (a). This causes the lift coefficient at α = 0° to oscillate with a positive time-averaged lift coefficient. For the AOAs of α = 2°, the shear layer on the suction side separates with a turbulent reattachment close to the trailing and further turbulent separation as can be seen in Fig. 4.3 (b). As the AOA is further increased, the point of turbulent reattachment on the suction surface moves upstream towards the leading edge as is visible in Figs. 4.3 (c)-

(f). For AOAs of α = 10° and higher, the turbulent reattachment happens about to the leading edge, followed by a turbulent reattachment and a turbulent vortex shedding resulting in chaotic oscillations in lift coefficient especially at higher AOAs. The flow on the pressure side and subsequent separated shear layer, however, remain laminar at all AOAs other than α= 0°, as can be seen in the intermittency contours of Fig. 4.3.

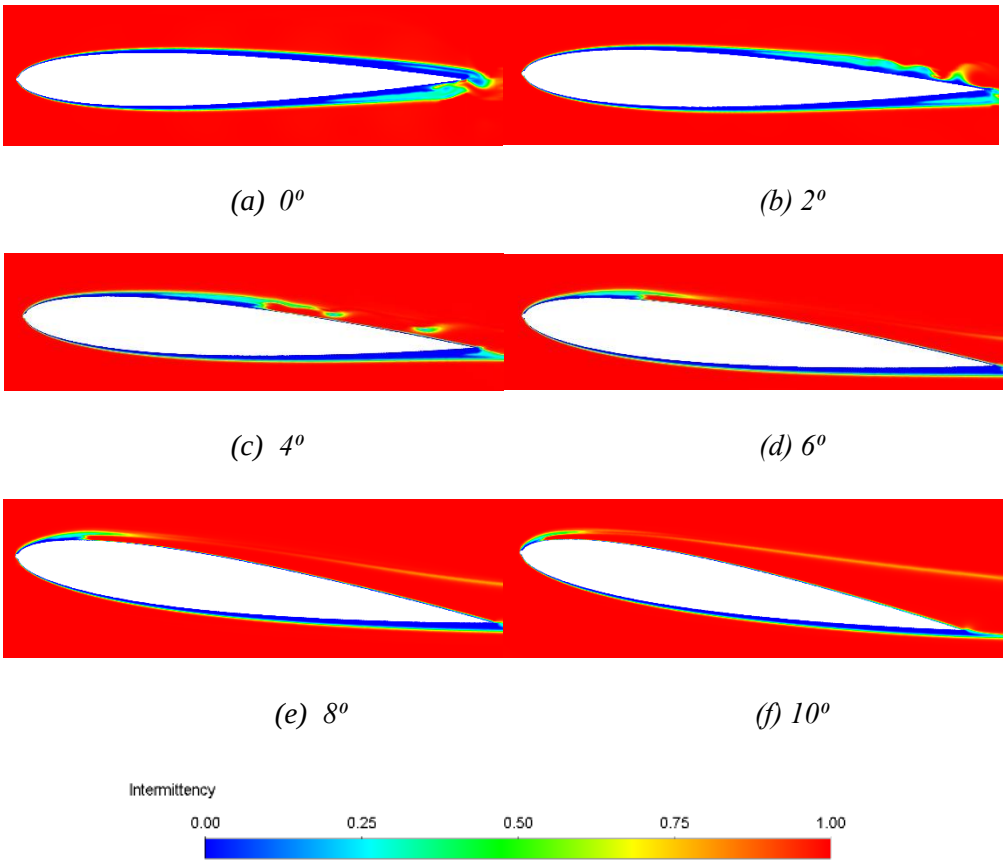

Figure 4.3: Intermittency Contours for Airfoil with Protrusion of height 0.005c at LE

As the height of the circular protrusion is increased, the flow separation starts early on the suction surface of the airfoil. At α = 0°, 2° and 4°, the intermittency contours for an airfoil with larger protrusion heights are similar to the intermittency contour seen for h = 0.005c. However, at AOAs of α = 6° and higher, the flow separation and reattachment characteristic for an airfoil with larger circular protrusions is slightly different from those of h = 0.005c, as can be seen in Fig. 4.4. For protrusion of height 0.01c, the shear layer separated at

the protrusion reattached at a further downstream point with a longer separation bubble as can be seen in Fig. 4.4 (c) and (e). This results in an increased lift coefficient and aerodynamic efficiency for these configurations. For the protrusion height of 0.02c however, the flow separated at the protrusion fails to reattach for α= 6° or higher as can be seen in Figs. 4.4 (d) and (f), resulting in overall loss of lift and degradation in aerodynamic efficiency.

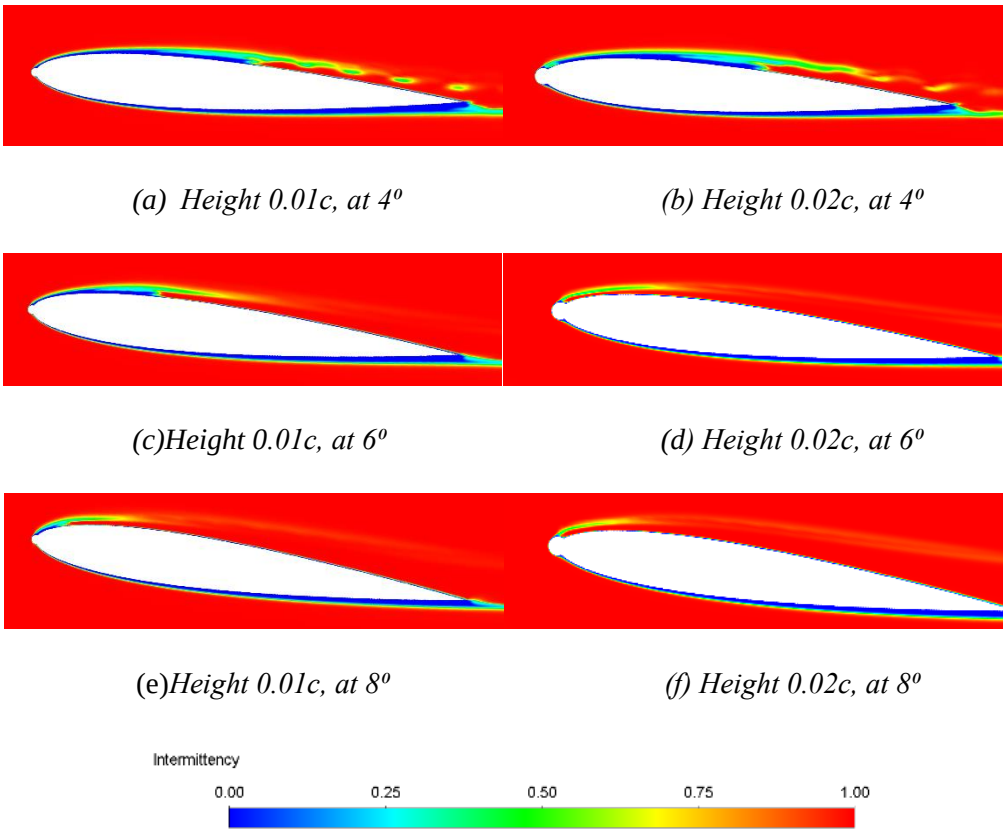

Figure 4.4: Intermittency Contours for Airfoil with Circular Protrusions of heights 0.01c and 0.02c at the LE

4.1.2 CIRCULAR PROTRUSION AT 0.05C ON THE UPPER SURFACE

The aerodynamic characteristics of an airfoil with protrusion located at 0.05c on the suction surface are considerably different from those of the clean configuration and those with protrusions at other locations. The lift curve for configuration with a protrusion height of 0.005c follows the one for clean configuration up to α=12º, as can be witnessed in Fig. 4.5 (a). In fact, for AOAs up to 4º, the protrusion with h = 0.005c provides a marginal increment in the lift

coefficients. At AOAs higher than 12º, the configurations with the smallest protrusion display a notable rise in the lift as compared to the clean configuration. The lift increases linearly from α =12º to 20º, giving increments of 20%, 30%, 63%, and 62.3% at α=14º, 16º, 18º, and 20º respectively.

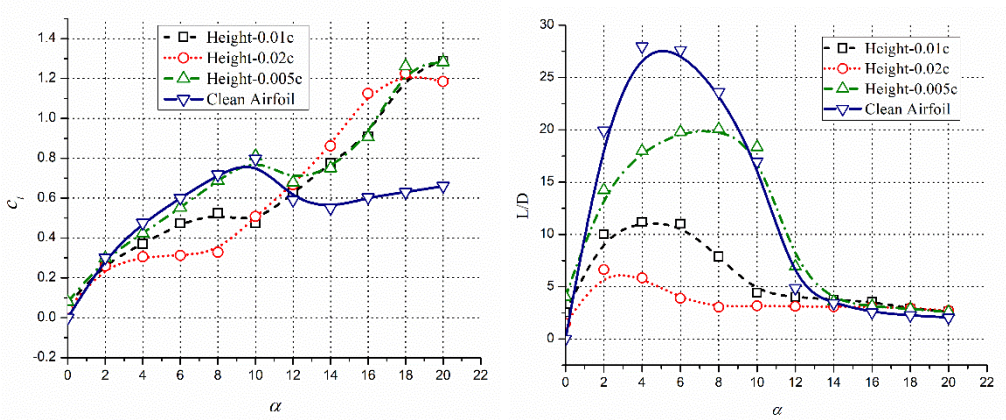

(a) Coefficient of Lift versus α *(b) Time-averaged L/D versus α*

Figure 4.5: Lift Coefficient and Aerodynamics Efficiency of an Airfoil with Protrusion at 0.05c on the upper surface

For the clean configuration, the flow is stalled at α =12º, however, for configurations with a protrusion at 0.05c location, the reversed flow on the suction surface is tripped at the protrusion bring about in the development of a small separation bubble ahead of the protrusion. The periodic washing away of this tiny vortex leads to flow unsteadiness, causing the primary vortex to be centered over the airfoil mid chord for a longer duration before being shed away. This enhances the suction causing the lift coefficient values to go up along with an increased drag, which leads to the decrement in the *L/D* ratio as shown in Fig. 4.5 (b). The increment in the drag observed is primarily due to viscous tugging at the protrusion. Due to the increased drag, the *L/D* ratio degrades by up to 36%, in the pre-stall regime, for the protrusion of height 0.005c. As the height of the protrusion, located at 0.05c is increased to *h*=0.01c, the flow pattern and unsteadiness remain unchanged, especially at a high angle of attack. The lift curve from α=12º onwards is similar to that for h = 0,005c protrusion. This makes the lift curve monotonically increasing in the entire range of AOA

from α=10º to 20º, with virtually no stalling with protrusion of *h*=0.01c located at 0.05c. The drag penalty, however, is higher, at all AOAs, resulting in lower *L/D* values as shown in Fig. 4.5 (b).

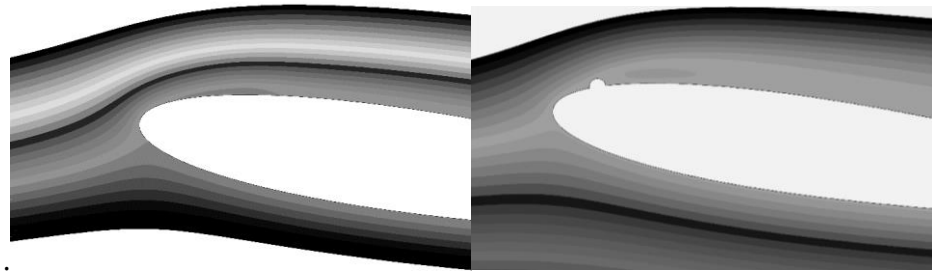

(a) Clean airfoil *(b) protrusion height, h = 0.01c*

Figure 4.6: Instantaneous streamlines at α= 8º for (a) clean airfoil, and (b) protrusion at 0.05c

At low AOAs between α = 4º and α = 10º, the aerodynamic performance is highly degraded with the lift coefficient falling significantly. At α = 4º, pressure on the lower surface is alike to that for a clean airfoil, the pressure on the suction surface is, however, slightly modified. As can be appreciated in Fig. 4.6, the formation of a small separation bubble forward of the protrusion results in a strong local suction which falls immediately due to the formation of a larger separation bubble aft of the protrusion. At α = 8º, the suction provided by the small vortex ahead of the protrusion is unable to match the peak suction by the clean configuration as can be comprehended in Fig. 4.7. From Fig.4.8 (b), it was seen that clean airfoil turbulent reattachment is around 10.75%, whereas the protrusion with h=0.01c turbulent reattachment takes aft compared with clean airfoil configuration this leads to the reduction in the lift. The intermittency contour of the airfoil with protrusion of height 0.01c, shown in Fig. 4.9, clearly demonstrates a turbulent reattachment and a turbulent separation causing a significant loss of lift. The flow pattern at α = 10º is similar with much-reduced suction and separation of flow aft of the protrusion leading to a higher loss in the lift. The *L/D* ratio, for the heights 0.01c, degrades by up to 75% in the pre-stall regime.

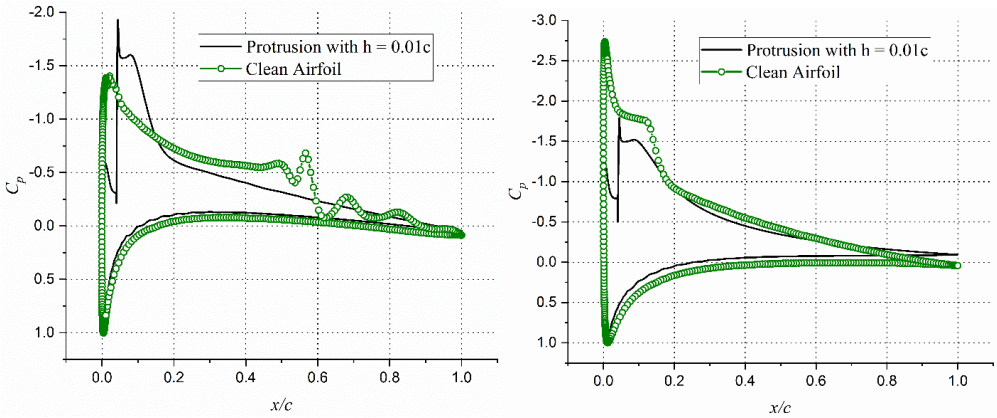

(a) α = 4º *(b) α = 8º*

Figure 4.7: Surface pressure distribution for an airfoil with protrusion of h=0.01c at 0.05c on the upper surface

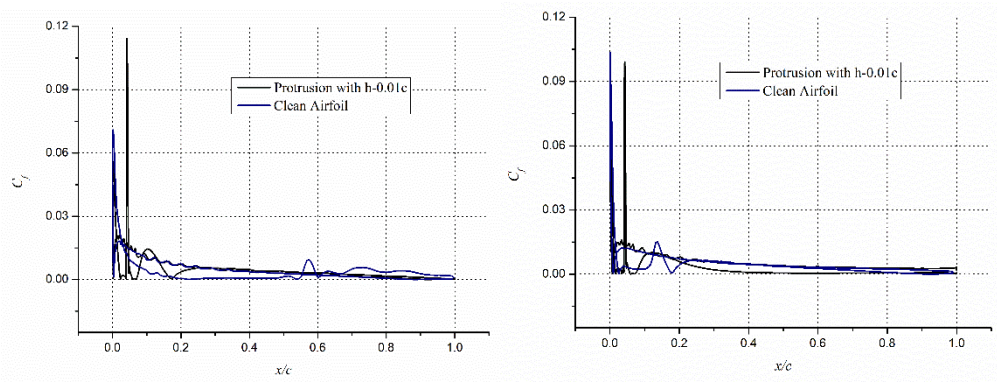

(a) α = 4º *(b) α = 8º*

Figure 4.8: Skin friction coefficient for an airfoil with protrusion of h=0.01c at 0.05c on the upper surface

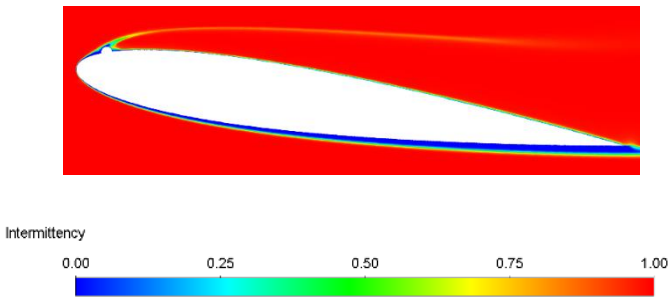

Figure 4.9: Intermittency Contour for Airfoil with Protrusion located at 0.05c with h= 0.01c and α = 8º

As the height of protrusion at 0.05c is increased to 0.02c, the aerodynamic performance is further degraded at small AOAs, with the highest reduction of 39.7% in C_l at α = 8º. The lift coefficient values remain almost unaltered between α = 2º and α= 8º, even as the drag coefficients continue to rise with AOA. This degradation in the lift is because of the inability of the flow separated from the protrusion surface to reattach as the separation bubble extends up to the trailing edge at AOAs up to α= 8º as can see in Fig. 4.10. This degrades the aerodynamics efficiency by 88%.

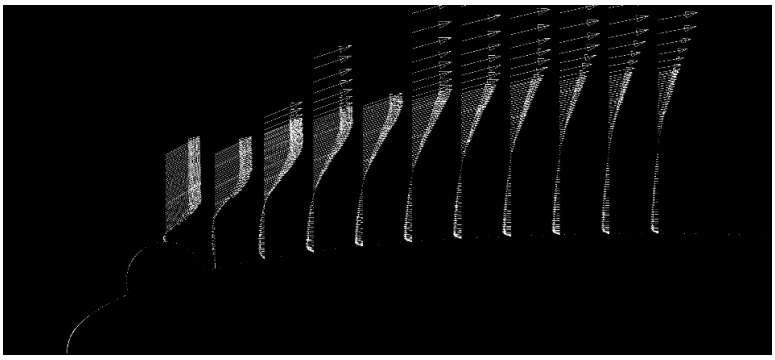

Figure 4.10: Velocity profile's over airfoil with protrusion h=0.02c, located at 0.05c, at 8º

The reduction in lift continues up to α = 14º. From α = 16º onwards, there is a slight improvement in the *L/D* values as can be observed in Fig. 4.5 (b). The steady increments in lift coefficient, observed for AOAs of α = 10° onwards, is because of the build-up of an anticlockwise vortex near the trailing edge which makes the primary vortex over the suction surface more coherent. Increments of 31.9%, 55.2%, and 64.6% in time-averaged lift coefficient values are observed at α = 14º, 16º, and 18º respectively.

The increment in vortical lift comes, however, at the cost of flow unsteadiness because of periodic vortex shedding from the trailing edge. Nevertheless, the time-averaged lift curve slope for an airfoil with 0.02c protrusion at 0.05c increases monotonically from α= 10º onwards. As the lift provided by these configurations is entirely vortical, a typical airfoil stall is not observed. The protrusions located at 0.05c on the suction surface thus induces high-frequency

vortex shedding at AOA as low as α=12º. For a protrusion of height *h* =0.005c and 0.01c, the frequency of lift oscillation is 120 Hz at α=14º, which reduces 100 Hz at α=16º. For the largest protrusion of *h=0.02c* at 0.05c location, an oscillation frequency of 120 Hz is achieved at α=12º, which diminishes to 100 Hz at AOAs of α=14º and 16º, and 40 Hz at α =20º.

4.1.3 CIRCULAR PROTRUSION AT 0.1C ON SUCTION SURFACE

As with the protrusion at 0.05c, the protrusions at 0.1c improves the lift characteristic of NACA 0012 significantly as can be appreciated in Fig. 4.11 (a). However, reductions of 23% and 52% in the *L/D* values are observed at low AOAs with protrusion heights of 0.005c and 0.01c respectively as shown in Fig. 4.11 (b). For smaller protrusions, increments of 11% to 61% in the lift coefficient values can be observed in the post-stall regime between α =12º and α = 20º. These increments come with no or little decline in the pre-stall regime and with no increase in drag coefficient values as well. The result is improved aerodynamic efficiency with increments in the *L/D* values by up to 94%, and 56% for h = 0.005c, *h* = 0.01c respectively.

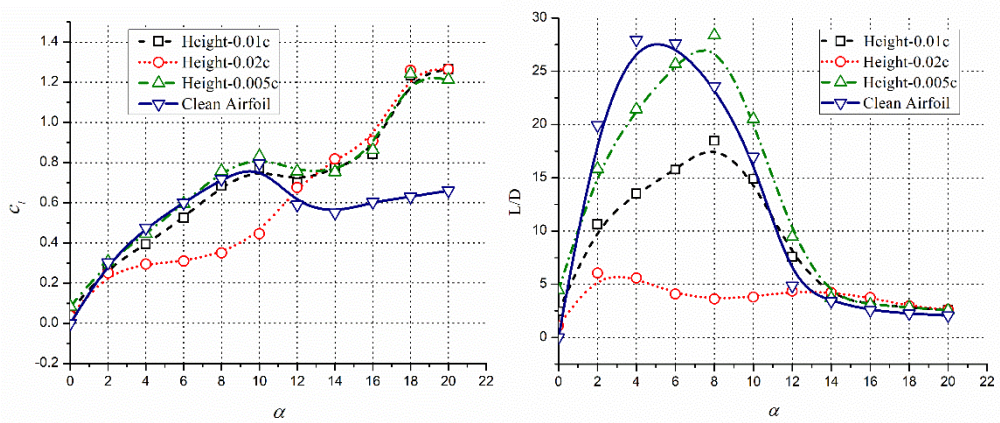

(a) Lift Coefficient versus α *(b) Time-averaged L/D versus α*

Figure 4.11: Aerodynamic coefficients of an airfoil with a protrusion at 0.10c on the upper surface

To enlighten the effect of vortex shedding on force fluctuations, the instantaneous time-averaged lift coefficient values are linked with the coherent

structures at the aft of the airfoil as shown in Fig. 4.12. Coherent structures at the aft of the airfoil are identified using the Q-identification method [150]. Figure 4.12 shows a series of circular anticlockwise and elliptical clockwise vortices in the wake of the airfoil. In Fig. 4.12 (a), two counter-rotating vortices on the suction surface with a longitudinally elongated clockwise vortex just shed from the airfoil. This results in a reduced lift coefficient as the anticlockwise circulation is added to the airfoil. As the shed clockwise vortex moves downstream, it becomes more coherent becoming elliptical as can be seen in Figs. 4.12 (b)-(f). During this movement, a counter-clockwise vortex builds up at the trailing edge. As the anti-clockwise vortex, after attaining maximum strength leaves the trailing edge, the primary clockwise vortex on gains maximum strength and covers the entire surface as can be seen in Fig. 4.12(g). This results in an enhanced suction pressure, which leads to a high lift coefficient. As the shed anti-clockwise vortex moves downstream, the primary vortex on the suction surface starts losing strength due to the formation of a small anti-clockwise vortex at the trailing edge. As the anti-clockwise vortex gains strength as seen in Figs. 4.12 (h)-(m), the lift coefficient diminishes.

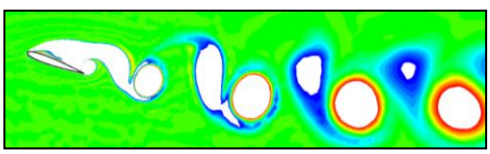

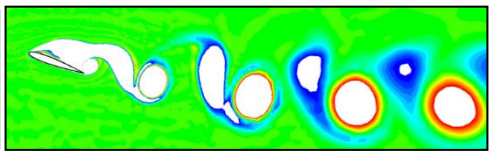

(a) c_l – 0.975 *(b) c_l – 0.984*

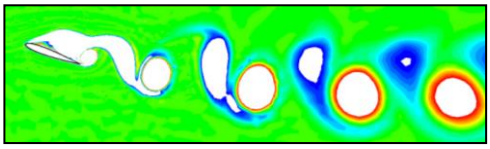

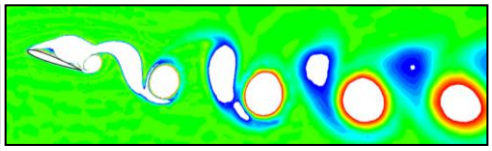

(c) c_l – 0.993 *(d) c_l – 1.075*

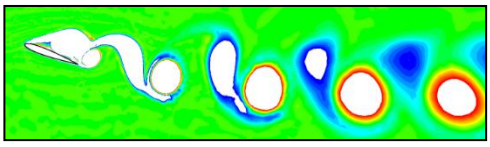

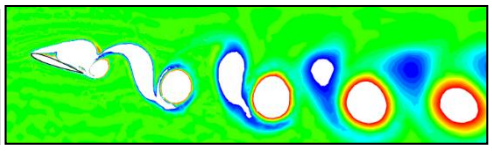

(e) c_l – 1.217 *(f) c_l – 1.358*

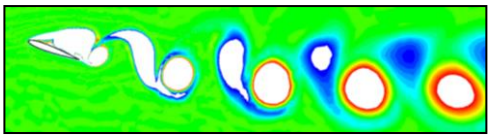

(g) c_l – 1.432

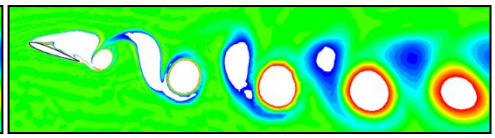

(h) c_l – 1.352

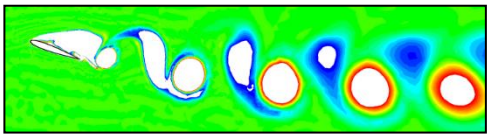

(i) c_l – 1.244

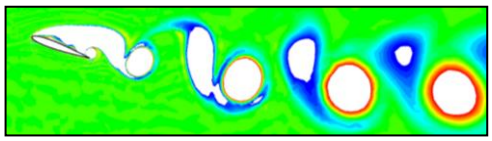

(j) c_l –1.037

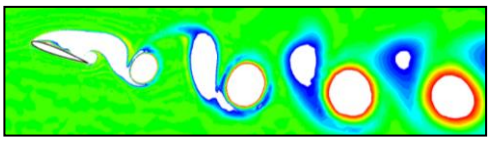

(k) c_l –0.994

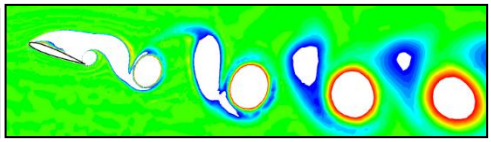

(l) c_l – 0.985

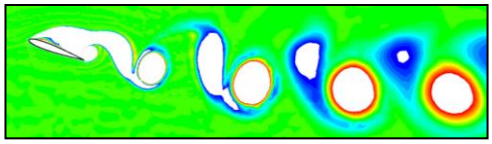

(m) c_l – 0.9758

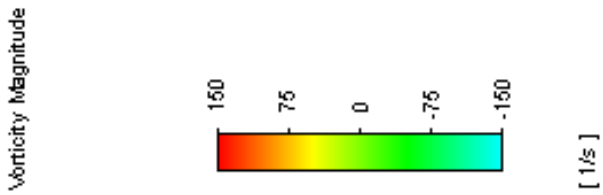

Figure 4.12: Vorticity magnitude for circular protrusion at 0.10c with h = 0.005c at $\alpha=20^0$

For protrusion height of 0.02c however, massive degradation in lift and increment in drag characteristics in the pre-stall regime is observed with a 37% reduction in lift coefficient values at $\alpha=8^o$. The overall *L/D* ratio is degraded by up to 85% at the pre-stall regime. The decrement in lift and increment in drag is due to the turbulent separation aft of the protrusion as can see in Fig. 4.13.

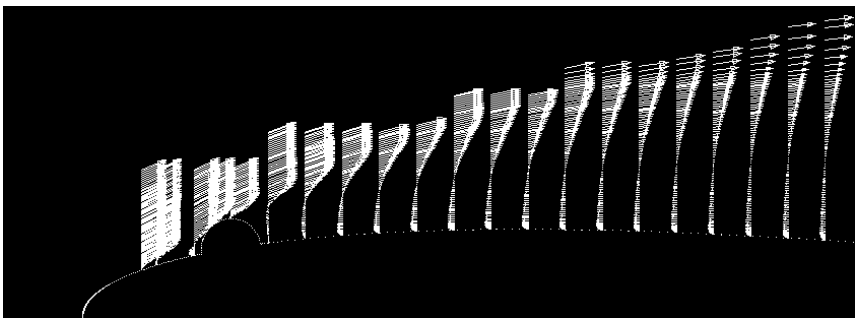

Figure 4.13: Velocity profile's over airfoil with protrusion h=0.02c, located at 0.10c, at 8º

However, in the post-stall regime, enhancement in the time-averaged lift coefficients is observed without much increase in the drag coefficients, which results in improvements in the *L/D* values, as can be seen in 4.11 (b). The increment in the lift, observed at α =12º and 14º, is due to the suction created by the separation bubble formed in front of the protrusion as can be appreciated in Fig. 4.14 (a). The flow detached from the surface of protrusion does not reattach on the airfoil, forming a vortical flow region aft of the protrusion, which is stable. The lift and drag coefficient values thus, do not fluctuate for AOAs up to α = 12º. At higher AOAs, the flow becomes unsteady and as the vortices are shed left from the surface, the separation bubble in front of the protrusion vanishes, and the flow fails to reattach on the protrusion. This results in diminished suction both ahead and aft of the protrusion as can be seen in Fig. 4.14 (b). The vortical lift on the rear of the surface, however, compensates for the suction destruction ahead of the protrusion. From the skin friction coefficient Fig. 4.15, at 0.10c location is visible the turbulent reattachment on the surface of the protrusion and at the aft, there is the presence of the turbulent separation over a surface of the airfoil.

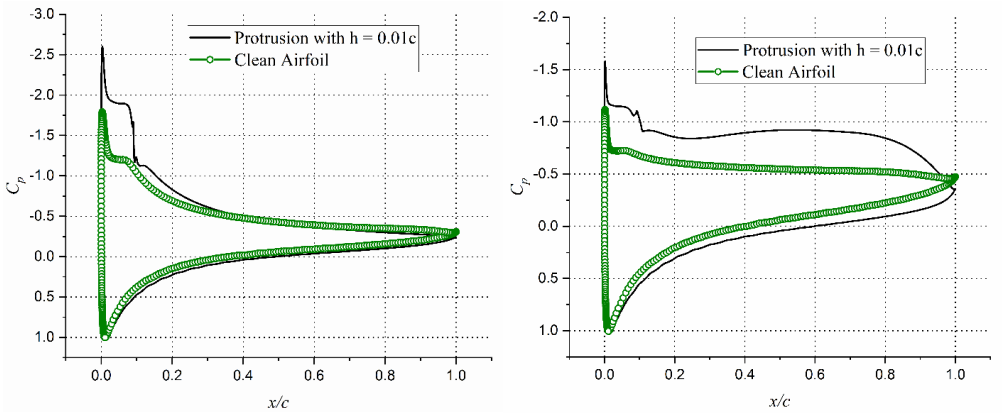

(a) α =12º *(b) α =16º*

Figure 4.14: Instantaneous surface pressure distribution over an airfoil with protrusion of height 0.01c, located at 0.1c

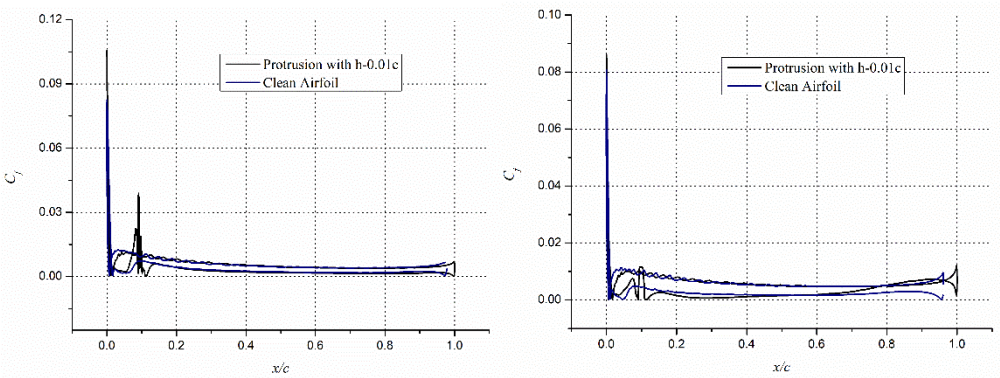

(a) α = 12º *(b) α = 16º*

Figure 4.15: Instantaneous skin friction coefficient over an airfoil with protrusion of height 0.01c, located at 0.1c

The flow, in general, is unsteady for an AOA of 14º and above for all protrusion heights at 0.1c location. The protrusions induce a 125 Hz high frequency, low amplitude oscillations in the lift coefficient at α =14º. As the AOA is increased, the frequency of vortex shedding is reduced to 100 Hz at α=16º and to 86 Hz at α=18º while the amplitude of fluctuation in the lift coefficients surges. At α = 20º, the vortex shedding frequency is unaltered by the presence of protrusions as the flow fully separated, the amplitude of oscillation, however, decreases as the height of the protrusion is increased.

4.1.4 CIRCULAR PROTRUSION AT 0.25C ON SUCTION SURFACE

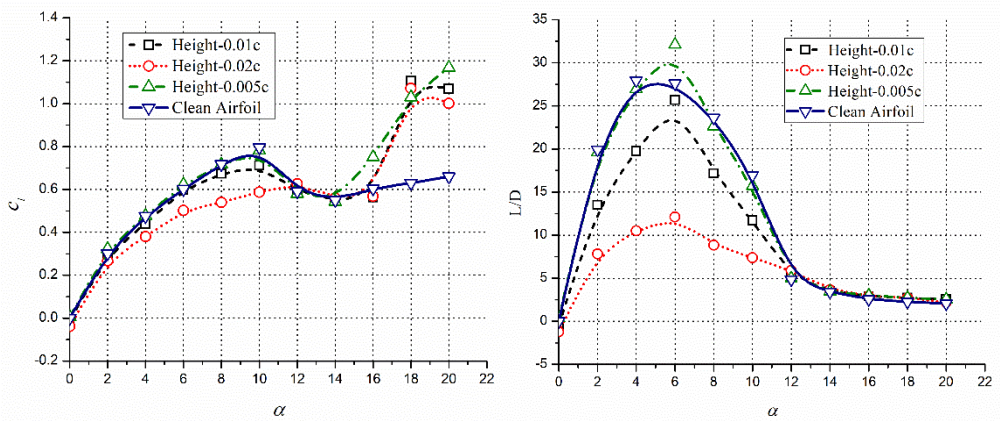

(a) Coefficient of Lift versus α *(b) Time-averaged L/D versus α*

Figure 4.16: Variation of aerodynamic coefficients for an airfoil with a protrusion at 0.25c

Figure 4.16 shows the variation of aerodynamic coefficients for an airfoil with a protrusion at 0.25c on the suction surface. For the smallest protrusion of *h* = 0.005c, the lift and drag coefficients are unaffected in the pre-stall regime, while significant deteriorations in aerodynamic characteristics can be seen for larger protrusions. The lift curve for protrusion of *h* = 0.005c follows the non-linearity of clean airfoil up to α =14º, after which an increase in time-averaged lift value, of about 50% is seen. The drag coefficient also increases slightly from 16º onwards. The *L/D* values are reduced in the pre-stall regime between 3 to 5% except at α = 6º, wherein an increment of 16% is observed. In the post-stall regime, L/D is improving very minutely as compared to the clean airfoil configuration. For the protrusions with *h* = 0.01c, the time-averaged lift in the pre-stall region is slightly less than for the clean airfoil and marginally higher in the post-stall region beyond α=16º. As the height of the protrusion increases, the *L/D* values are decreased in the pre-stall regime.

For *h* =0.01c, the *L/D* in the pre-stall regime degrades by up to 32% whereas for *h* =0.02c it degrades by up to 63%. In the post-stall regime, a slight improvement was detected for both heights. There is a high-frequency oscillation in lift coefficient values for an airfoil with smaller protrusions and at

higher AOAs because of unsteady vortex structure. The instantaneous high lift in the post-stall regime is primarily due to increased suction on the upper surface as can be appreciated in Fig. 4.16 (a). The increase in suction is because of the presence of a single dominant clockwise vortex spanning the entire upper surface, as can be observed in Fig. 4.17 (a). The vortex adds to the downward momentum of the flow hence enhancing circulation besides causing an increase in pressure on the lower side of the airfoil. As the flow rolls up at the trailing edge due to pressure gradient, an anticlockwise vortex builds up at the trailing edge. As this counter-clockwise vortex grows in size, it increases suction near the trailing edge on both suction and pressure surfaces as shown in Fig. 4.17 (b), causing the lift to diminish. When the anticlockwise vortex gains its maximum strength, the clockwise vortex on the suction side becomes elongated and moves farther from the surface as understood in Fig. 4.17 (b), and the lift is reduced to its minimum. After attaining full strength the counter-clockwise vortex is shed away from the surface imparting circulation to the airfoil and the lift increases as the shed vortex moves away from the trailing edge. Fig. 4.18 shows the skin friction over the surface of the airfoil when the primary vortex dominant over the surface of an airfoil.

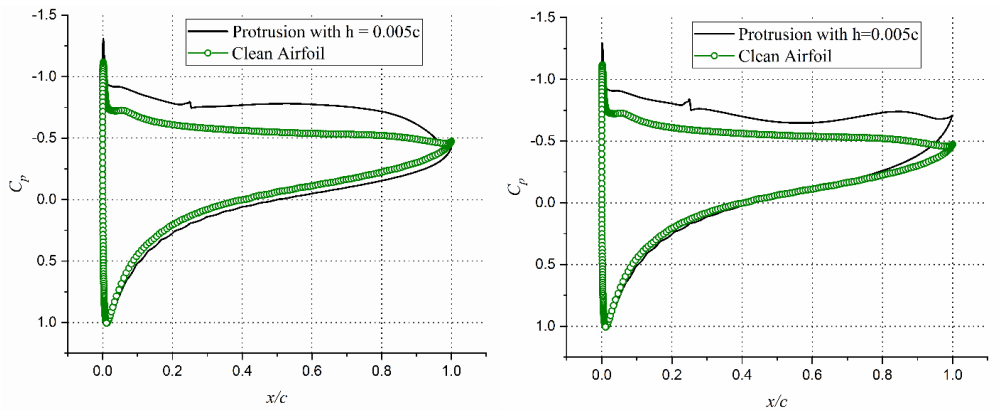

(a) High lift, Cl =0.79 *(b) Low lift, Cl =0.71*

Figure 4.17: Instantaneous surface pressure for an airfoil with a protrusion at 0.25c and α =16º

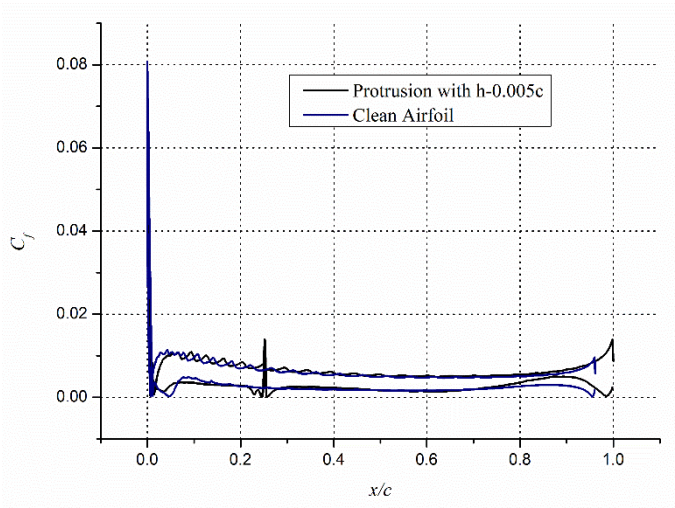

Figure 4.18: Instantaneous skin friction for an airfoil with a protrusion at 0.25c and α =16º

For an airfoil with circular protrusion of height 0.005c, located at 0.25c on the suction surface, the lift coefficient fluctuates between 0.71 and 0.80 at a frequency of 100 Hz, for an AOA of 16°. The instantaneous vortical structures for lift coefficient values of 0.71 and 0.80 are shown in Figs. 4.19 (a) and (b) respectively. At α = 16º, the frequency of oscillation is the same for all protrusion heights while the amplitude of oscillation diminishes for larger protrusions as can be observed in Fig. 4.20. The frequency of oscillations for larger protrusions of *h* = 0.01 and 0.02 is reduced to 90 Hz at α=18º. At α=20º, the lift coefficient fluctuates with a very low fundamental frequency of 40 Hz, the amplitude, however, goes through two intermediate points of inflection during each cycle.

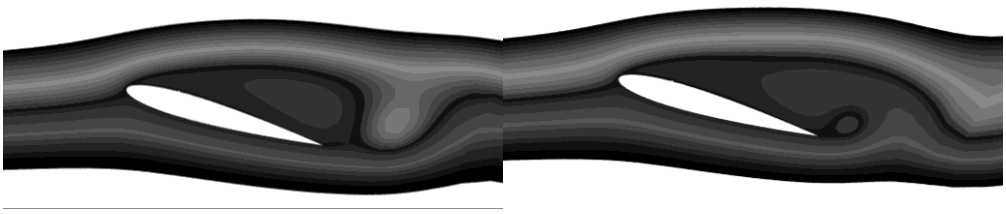

(a) Streamlines for high lift *(b) Streamlines for low lift*

Figure 4.19: Instantaneous vortex structure at α =16º for airfoil with protrusion at 0.25c location and h = 0.005

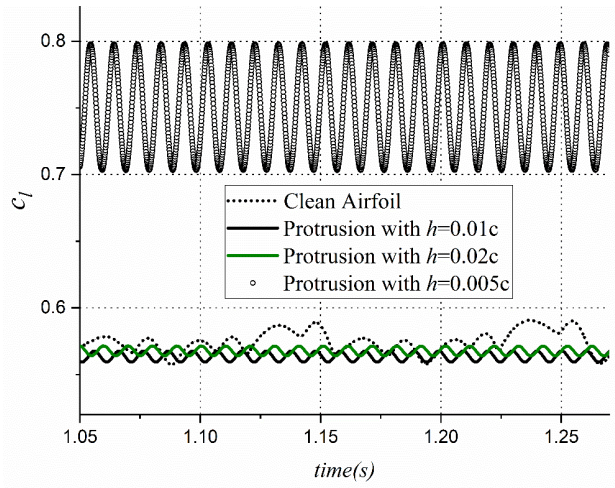

Figure 4.20: Lift history for an airfoil with a protrusion at 0.25c and α = 16º

For a protrusion of height 0.01c, the time-averaged lift coefficient is augmented marginally as compared to the clean airfoil at α = 0º. From α = 2º to 16º, there is no significant change in lift coefficient except at α = 8º and 10º where some reductions can be observed. At both, α = 8º and 10º, the formation of the laminar separation bubble occurs ahead of the protrusion and flow attaches to the protrusion and then separates aft of the protrusion before reattaching again near the trailing edge. Due to this, there is a small fall in the lift coefficient for these AOA's as observed in Fig. 4.16 (a). At α =18º, there is an enhancement in the time-averaged lift coefficient by 13%, which fluctuates between 1.24, when the vortex on the suction surface is strongest, immediately after the vortex is shed and falls to 0.9 as the counter-clockwise vortex becomes strongest at the trailing edge. This increment in time-averaged lift coefficient falls to 6% at α = 20º.

For a protrusion of height 0.02c, located at 0.25c, no significant effect on the lift coefficient is observed at α= 0º and 2º. For AOAs between 4º and 10º however, there is a significant decrement in the lift coefficient as can be appreciated in Fig. 4.16 (a). At α = 6º and 8º, the flow separates ahead of the protrusion forming a short separation bubble, and then separates again from the protrusion forming a long separation bubble aft of the protrusion, which extends up to the trailing edge, as can be seen in Fig. 4.21 (a). The consequence is a significant loss of lift and a small increase in the drag coefficient.

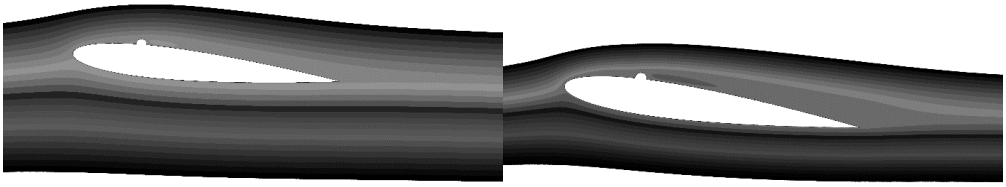

(a) α = 6º *(b) α=8º*

Figure 4.21: Instantaneous streamlines for an airfoil with protrusion of h = 0.02c located at 0.25c

For α = 8º and 10º, the reduction in lift and rise in drag are both amplified as the length of the vortical structure extends beyond the trailing edge forming a hairpin vortex. The coherent structure at α = 8º for an airfoil with protrusion height of 0.02c located at 0.25c on the suction surface is exposed in Fig. 4.21(b). For this configuration of protrusion, the lift curve follows the one for clean configuration up to α =16º, with a slightly higher average lift coefficient as compared to the clean airfoil. At α=18º the vortices are shed from the airfoil at a frequency of 80 Hz and the lift coefficient value fluctuates between 1.242 and 0.96. For α = 20º, the lift coefficient fluctuates between 1.02 to 0.975, as the flow separated from the leading edge remains unaffected by the presence of the protrusion.

4.1.5 CIRCULAR PROTRUSION AT 0.50C ON SUCTION SURFACE

The trends in the lift variations for an airfoil with protrusions located at 0.5c are similar to that for protrusion at 0.25c, for AOAs up to α=14º, as can be observed in Fig. 4.22. The *L/D* ratio, however, has lower values up to α=14º, as compared with clean airfoil configuration. For a protrusion of height *h* = 0.005c, *L/D* is lowered by 11% at an AOA of α =16º as well. In the case of protrusion of *h* = 0.01c, and 0.02c, the values of *L/D* are lowered by 23% and 55% respectively, as shown in Fig. 4.22 (b). The smallest protrusion of *h* = 0.005c does not seem to affect the flow when located at mid-chord, as the lift curve for an airfoil with protrusion overlaps the clean configuration curve up to α=16º. The amplitude of fluctuation of lift coefficient for an airfoil with protrusion is, however, slightly higher than those for the clean airfoil. Also at α=18º and 20º, the time-

averaged lift coefficients for an airfoil with this protrusion height are marginally higher than that for the clean airfoil.

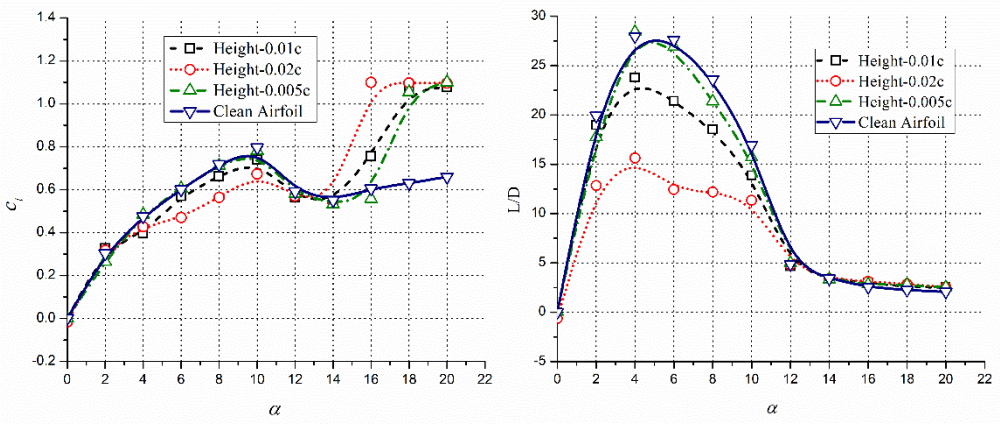

(a) Coefficient of Lift versus α *(b) Time-averaged L/D versus α*

Figure 4.22: Lift Coefficient and Aerodynamic Efficiency for an airfoil with a protrusion at 0.50c

For protrusion with h = 0.01c, the trend in lift variations is similar to those with h = 0.005c, as the protrusion degrades the performance of the airfoil only slightly in the pre-stall regime and improves the lift in the post-stall regime. At α = 16º, the time-averaged lift coefficient is increased by 15%, owing to the coherent vortical lift in the separated flow regime.

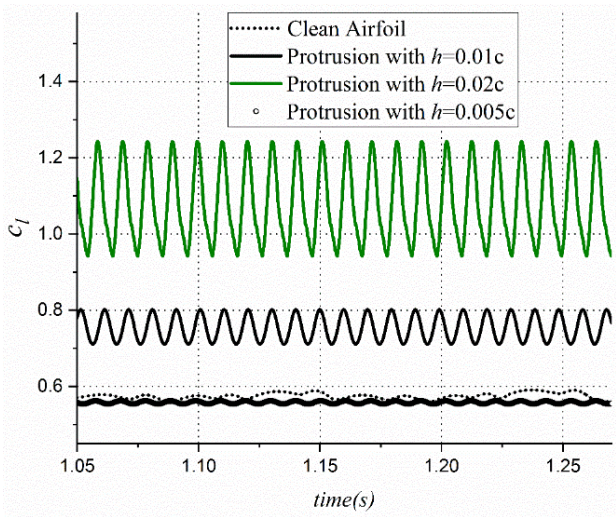

Figure 4.23: Lift history for an airfoil with a protrusion at 0.5c and α=16º

The vortex shedding at this AOA occurs at a frequency of 100 Hz causing the lift coefficient to fluctuate between 0.715 and 0.796, as can be seen in Fig. 4.23. At α =18º and 20º, increments of 43%, and 41% respectively are seen in the time-averaged lift coefficient, with an increased amplitude of fluctuations. At α = 20º, the fundamental frequency of vortex shedding is reduced to 40 Hz for all protrusion heights located at 0.5c. The amplitude of this oscillation, however, goes through three crests and troughs in each cycle.

As the height of protrusion, located at 0.5c, is increased to 0.02c a drastic change in the lift coefficient was observed for α=16º, along with high amplitude fluctuations. A high instantaneous lift for this configuration is caused by a large suction particularly aft of the protrusion as can be observed in Fig. 4.24, which shows the instantaneous surface pressure distribution at α = 16° for an airfoil with circular protrusion of height 0.02c, located at 0.05c on the suction surface. Despite a large suction on the top surface, a strong suction on the lower surface is observed near the trailing edge, in Fig. 4.24 (b). This is the instant when a fully developed anti-clockwise vortex sits on the trailing edge, causing instantaneous decrement in lift coefficient.

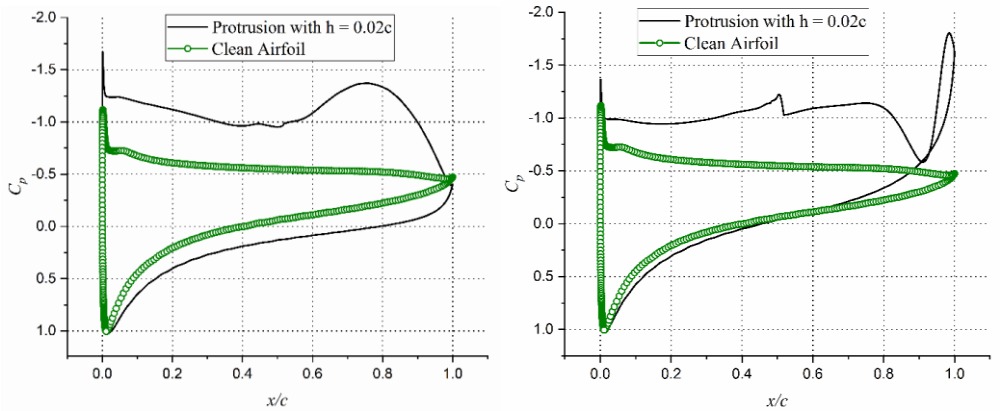

(a) α=16º, C_l =1.23 *(b) α=16º, Cl = 0.96*

Figure 4.24: Instantaneous surface pressure distribution for an airfoil with protrusion of h = 0.02c at 0.5c

A single dominating vortex seen in the cases of smaller protrusions splits into two smaller vortices one centered ahead of the protrusion and the other aft of

the protrusion, as shown in Fig. 4.25 (a). A small anticlockwise vortex can also be seen in front of the protrusion for this high lift vortical system. Due to the suction from this system of vortices, the lift coefficient is increased to 1.23, which diminishes to 0.96, as an anticlockwise vortex gains strength near the trailing edge, as shown in Fig. 4.25 (b). This also forces the two clockwise vortices on the suction surface to merge and as a result, the suction ahead of the protrusion is enhanced.

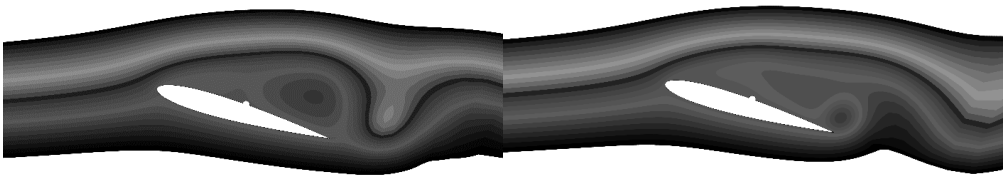

(a) Streamlines for a high lift at α=16º (b) Streamlines for a low lift at α=16º

Figure 4.25: Vortex system for an airfoil with a protrusion at 0.5c on the suction surface with h=0.02c

Despite this, there is a decrement in lift due to enhanced suction on the bottom surface as well can be appreciated in Fig. 4.22 (b). Similar vortex shedding behavior is also observed for α = 18º and 20º, with a slightly smaller increment in the lift coefficient though.

4.1.6 CIRCULAR PROTRUSION AT 0.05C ON PRESSURE SURFACE

Figure 4.26 shows the time-averaged lift coefficients and aerodynamic efficiency variation with AOA for circular protrusions located at 0.05c on the pressure surface. In the pre-stall regime, the time-averaged lift coefficient values are unchanged by the presence of a circular protrusion at 0.05c on the suction surface. In the pre-stall regime, reductions of about 7% in lift coefficient are observed while in the post-stall regime increment of up to 51.2% in lift coefficient is observed. The augmentation in lift coefficient values seen is due to the vortex shedding phenomenon. However, at AOAs of α = 2º and 4º, there is a formation of roll-up vortices resulting in the flow unsteadiness as can be observed in Fig. 4.27.

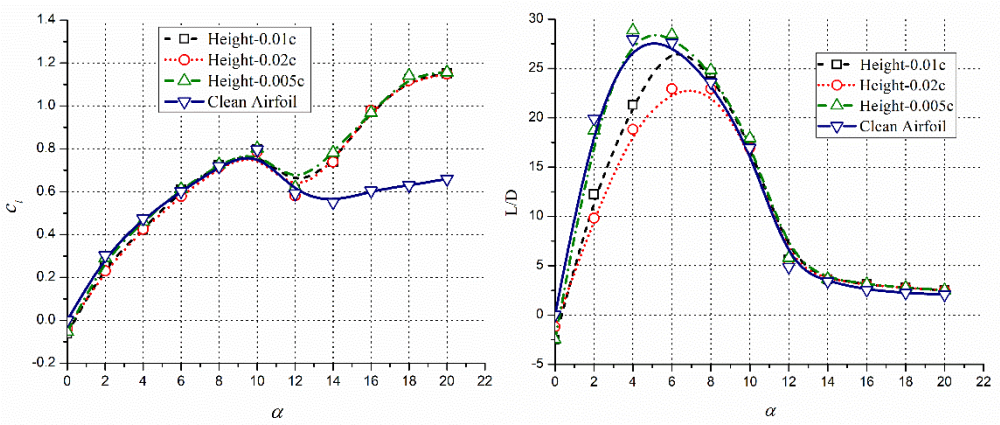

(a) Lift Coefficient versus α *(b) Time-averaged L/D versus α*

Figure 4.26: Aerodynamics characteristic of an airfoil with protrusion located at 0.05c on the Pressure surface

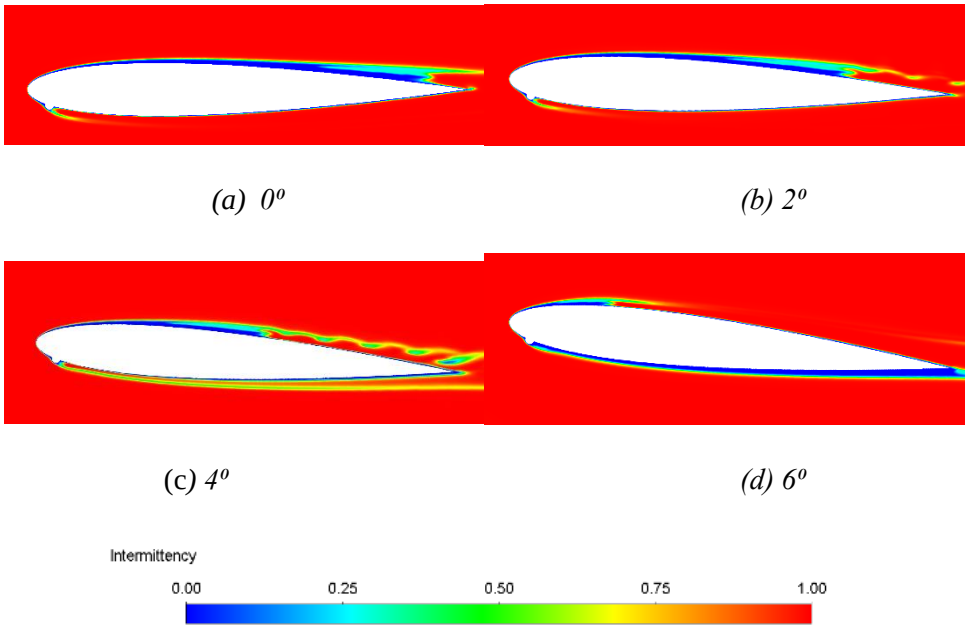

(a) 0° *(b) 2°*

(c) *4°* *(d) 6°*

Figure 4.27: Intermittency of Protrusion with height 0.01c at pressure surface 0.05c location at a different angle of attack

Fig. 4.27 shows the flow transition over an airfoil with protrusion of height 0.01c located at 0.05c on the pressure surface. For α = 0°, the flow transition to turbulent on the suction surface occurs near the trailing edge, whereas on the pressure surface the flow detached at the protrusion reattached as turbulent flow immediately after the protrusion. For all three heights, the flow phenomenon

observed at α = 0º is similar. For the protrusion height 0.005c at α = 2º and 4°, flow transition is visible on both the surfaces of the airfoil. On the upper surface, there is a single laminar separation and multiple turbulent reattachments and separations as can be seen in Fig. 4.27 (b) and (c). As the angle of attack increases, the flow starts separating from the surface, and the separation point moves upstream towards the leading edge as can be seen in Fig. 4.27 (d). In the case of α = 8º, flow separation seen on the suction surface is similar for all protrusion heights. As the height of the protrusion increases, the flow aft of the protrusion starts to turn turbulent on reattachment on the pressure surface as can be observed in Fig. 4.28. The small laminar separation bubble is seen on the suction surface with turbulent reattachment in all cases for these higher angles of attack.

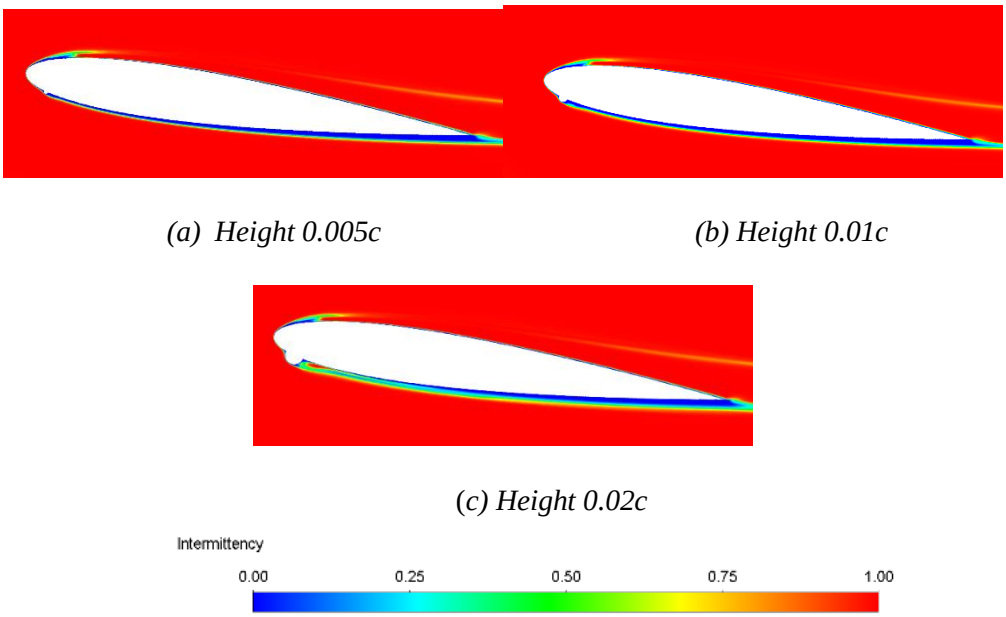

(a) Height 0.005c *(b) Height 0.01c*

(c) Height 0.02c

Figure 4.28: Intermittency for the protrusion location at pressure surface 0.05c location at 8º

Further numerical analysis was investigated to check the effect of the circular protrusion on the pressure surface of the airfoil at the 0.10c, 0.25c, 0.50c, 0.75c location with three heights of the protrusion. Protrusion at none of these locations has shown any significant improvement or degradation in the

aerodynamic efficiency of the airfoil at a Reynolds number of 10^5. However, at the higher angles of attack, there is an improvement in the lift coefficient observed as illustrated in Appendix B.

4.1.7 EFFECT OF CIRCULAR PROTRUSIONS ON STROUHAL NUMBER

The roll-up of separated shear layers and the subsequent shedding of the vortices from the suction side of the airfoil and the shedding of the counterclockwise vortex from the trailing edge results in the oscillations of aerodynamic parameters such as C_l and C_d. The spectrum of lift coefficient is analyzed using a Fast Fourier Transform (FFT) to obtain the fundamental frequencyf_0, of the vortex shedding and therefore the frequency of oscillation in lift coefficient values. These frequencies are converted to non-dimensional Strouhal number *St*, using airfoil chord c as the characteristic length. Thus, $St = {f_0 c}/{U_\infty}$, with U_∞ as the freestream velocity. The clean NACA 0012 does not show any oscillations until α = 16°, for a chord-based freestream Reynolds number of 10^5. From α = 16° onwards, the airfoil behaves similar to a bluff body and the Strouhal number varies from 0.2 at α = 16° to 0.12 at α = 20°. Even for an airfoil with a protrusion at the LE, the oscillations in lift coefficient is seen between α=16° and α=20°. However, for an airfoil with a circular protrusion, the Strouhal number is significantly higher and falls between 0.7 and 0.5, as can be seen in Fig. 4.29 (a). For protrusions of heights 0.005c and 0.01c, located at the LE, the variations in Strouhal number are very similar while for the taller protrusions, it is slightly reduced. In all cases, however, the Strouhal number reduces as the AOA is increased.

For protrusions at 0.05c on either the suction or the pressure surface, the oscillation in C_l values starts at AOA α =14°, as can be seen in Fig. 4.29 (b) and (c). This is primarily due to the early separation of the shear layer from the protrusion and subsequent reattachment for moderate AOAs, leading to vigorous vortex shedding. As compared to the suction surface protrusion, the protrusion on the pressure surface imparts larger flow unsteadiness wherein the

Strouhal number as high as 0.85 is observed, for all heights. The Strouhal number versus AOA curve overlaps for protrusions heights of 0.005c, 0.01c, and 0.02c, irrespective of their location. This suggests that the amount of unsteadiness imparted by three protrusions is similar. For the larger protrusion on the suction surface, the Strouhal number is smaller for AOA less than α=16° and slightly larger for AOA more than α =16°. This implies that the larger protrusion height diminishes the vortex shedding frequency below α = 16°, thereafter the bluff body shedding dominates the flow-field, and the protrusion height becomes ineffective. The Strouhal number, however, continuously diminishes as the AOA is increased.

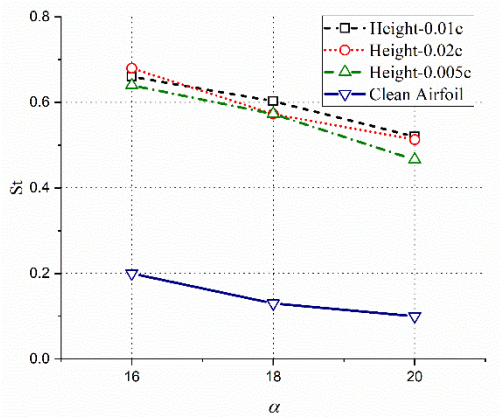

(a) Leading Edge

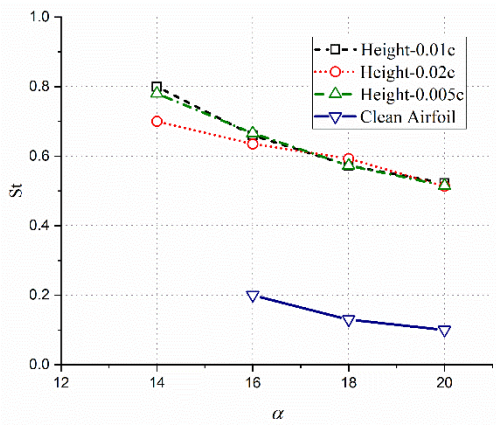

(b) On suction surface at 0.05c

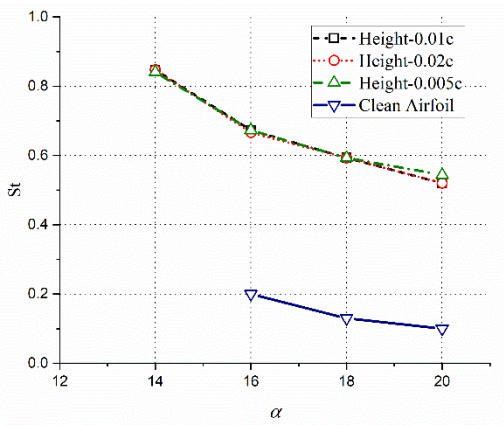

*(c) On pressure surface at 0.*05c

Figure 4.29: Strouhal Number for airfoil with a circular protrusion

4.2 EFFECT OF CIRCULAR PROTRUSION AT Re = 50,000

Numerical simulations are conducted to investigate the effect of circular protrusions located at the leading edge, and at 0.05c on both suction and pressure surfaces for a chord-based Reynolds number of 50,000. The heights of these protrusions are 0.005c, 0.01c, and 0.02c, and locations are chosen based on the experience for Re= 10^5, as the downstream location has little effect on the aerodynamics of the airfoil. The simulations are done at a lower Reynolds number to investigate the sensitivity of the results on the Reynolds number.

4.2.1 EFFECT OF PROTRUSION AT LEADING EDGE

Figure 4.30 illustrates the aerodynamic characteristics of the airfoil with a circular protrusion at the leading edge for a chord-based Reynolds number of 50000. The lift curve for an airfoil with a protrusion at the LE follows the one for the clean airfoil in the pre-stall regime, except at α = 2° and 4°. At these AOAs, the flow becomes highly unsteady due to vigorous vortex shedding, and the time-averaged lift coefficient and *L/D* ratios are enhanced by 6.8% and 23% respectively, at α = 2°.

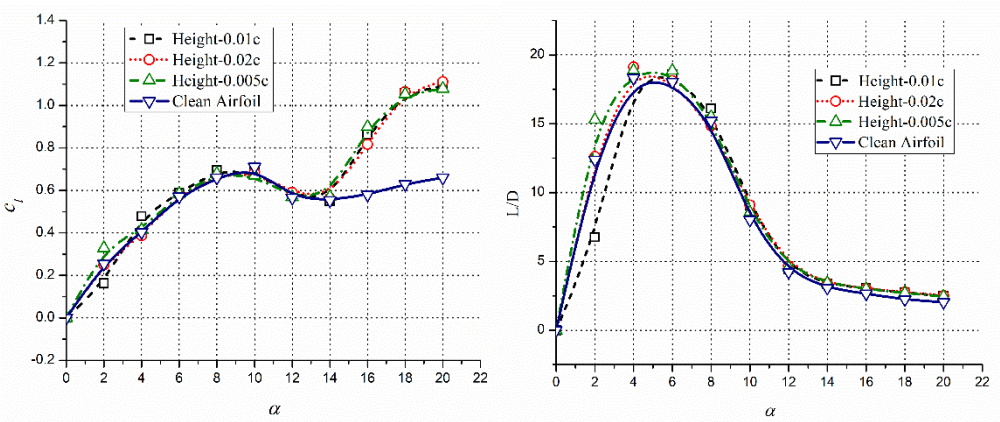

(a) Lift Coefficient versus α *(b) Time-averaged L/D versus α*

Figure 4.30: Aerodynamics characteristic of an airfoil with a protrusion at LE

The flow unsteadiness at α = 2° and 4° is due to the formation of secondary roll-up vortices on the rear portion of the suction surface, especially for larger

protrusion, as can be seen in Fig. 4.31. As can be seen in Fig 4.31, for an AOA of α = 4°, the roll-up vortices move downstream with time and are ultimately shed away causing small-amplitude oscillation the lift of the airfoil.

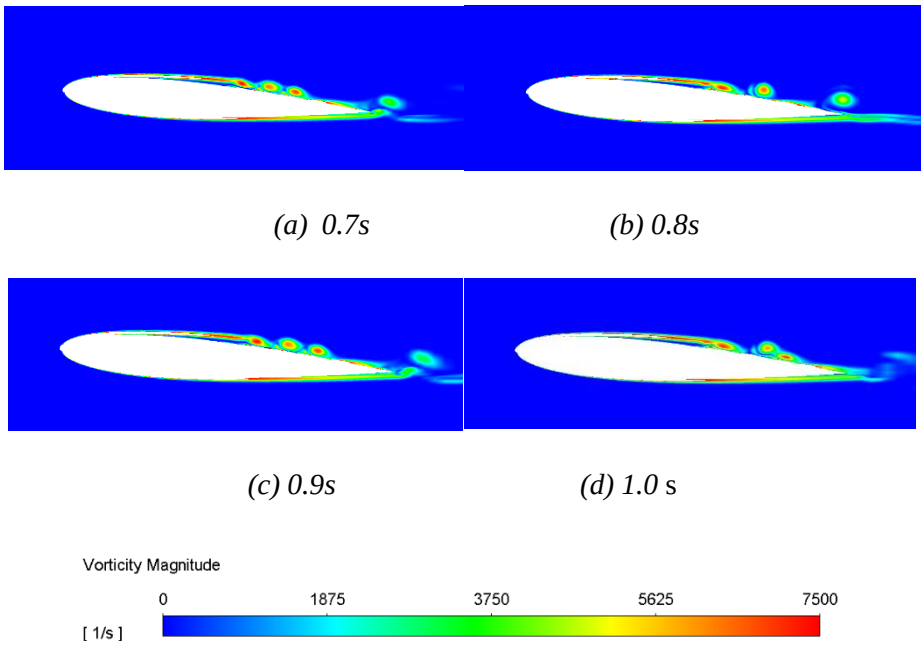

(a) 0.7s *(b) 0.8s*

(c) 0.9s *(d) 1.0* s

Figure 4.31: Vorticity Contours for airfoil at α = 4º, with protrusion of height 0.005c and located at LE

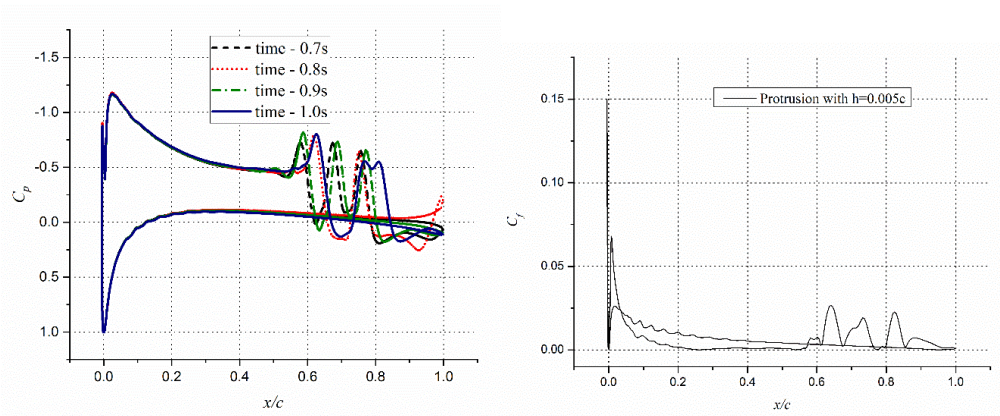

(a) Pressure Coefficient *(b) Skin Friction Coefficient*

Figure 4.32: Pressure distribution and Skin friction over an airfoil with protrusion height 0.005c located at the leading edge, at 4º

As these roll-up vortices drift along the suction surface their strength increases and so does the suction pressure. The drift of these vortices and their increasing

strength can also be visualized through surface pressure distribution for airfoil and corresponding skin friction coefficient for circular protrusion of height 0.005c at the leading edge, as shown in Fig. 4.32.

The roll-up vortices seen for an airfoil with a protrusion height of 0.005c is a result of laminar separations and laminar reattachments as the small size of the protrusion and the chosen freestream turbulence fail to turn the flow turbulent. However, as the height of the protrusion at the leading edge is increased to 0.01c, the flow transitions to turbulent at about 65% of chord, and the reattachment and further separations are turbulent as can be seen in Fig. 4.33. The turbulent separation for the h = 0.01c case makes the flow less unsteady with a very small amplitude of oscillation in lift coefficient. As the height of the protrusion is further increased to 0.02c, a laminar separation bubble is formed aft of the protrusion which reattached much before mid-chord location on the suction surface. The periodic bursting of the laminar separation bubble makes the flow highly unsteady, leaving a trail of small roll-up vortices along the suction surface as can be seen in Fig. 4.33(c).

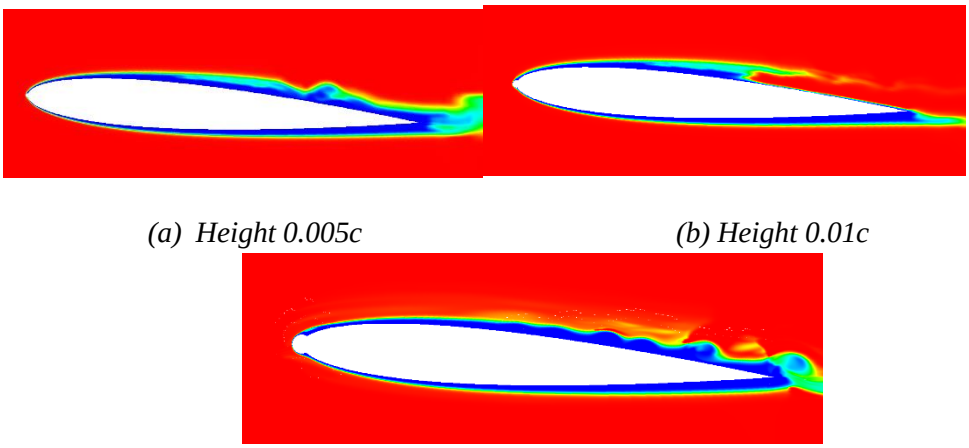

(a) Height 0.005c *(b) Height 0.01c*

(c) Height 0.02c

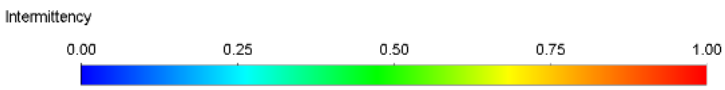

Figure 4.33: Intermittency for an airfoil with a protrusion at the leading edge, α = 4º

The differences between the flow unsteadiness in the case of an airfoil with circular protrusion of heights 0.01c and 0.02c can be illustrated through the transient vorticity contours as shown in Figs. 4.34 and 4.35. As can be seen in Fig 4.34, for an airfoil with a protrusion height of 0.01c, the drift of the vortices on the suction surface is very slow and the roll-up vortices seem to be stationary in the boundary layer. Also, the size of these vortical structures for this configuration is small. On the other hand, for an airfoil with a protrusion height of 0.02c, the flushing away of the roll-up vortices is very fast as can be seen in Fig. 4.35. Besides this, the size of the coherent structures is significantly large which causes a vigorous fluctuation in the lift coefficient for an airfoil with protrusion height of 0.02 c at AOAs of α=2° and 4°. The movement of the trail of roll-up vortices can also be seen in the instantaneous streamlines around the airfoil as has been shown in Fig. 4.36.

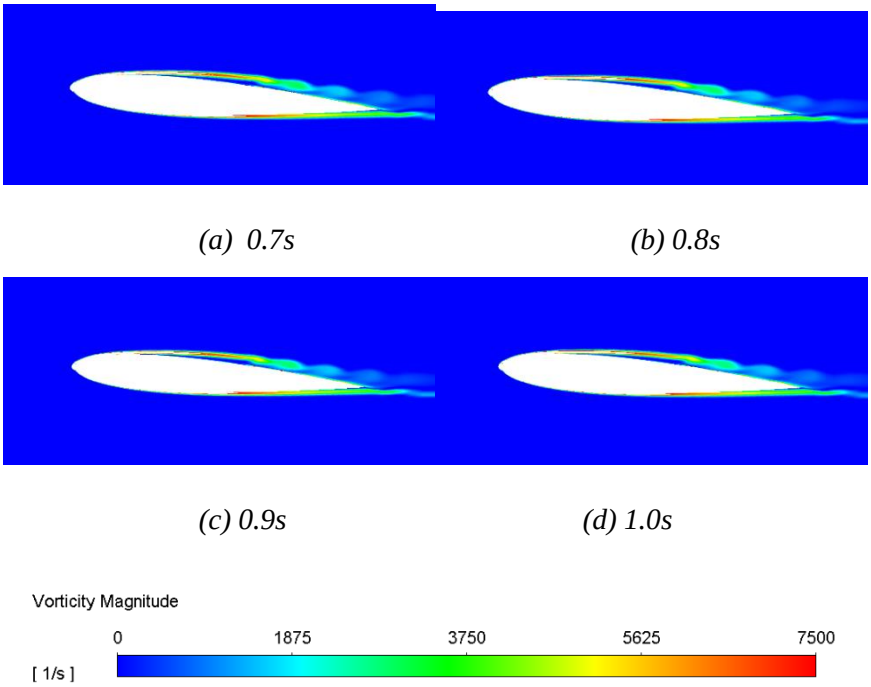

Figure 4.34: Vorticity magnitude over an airfoil protrusion height 0.01c located at the leading edge, at 4º

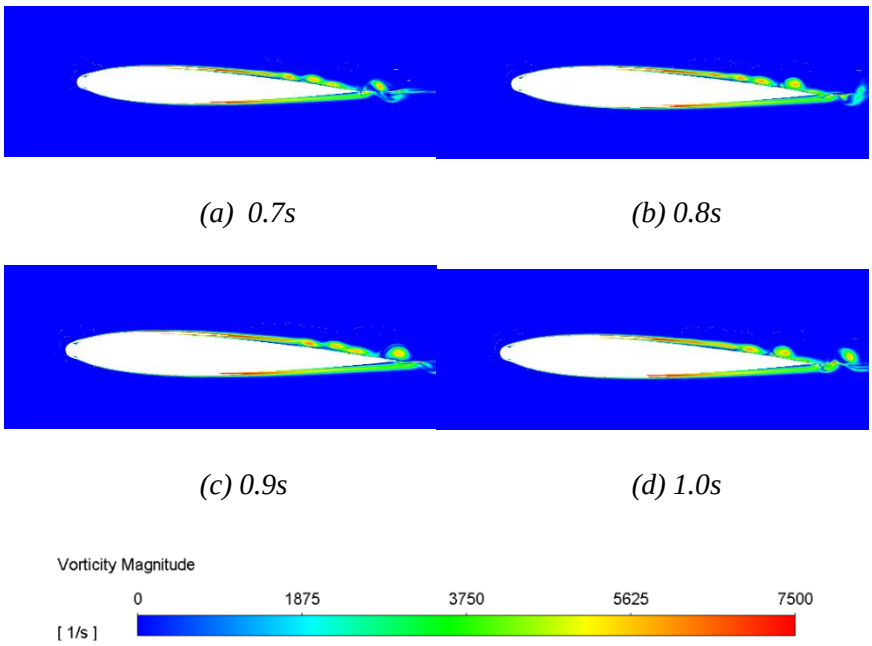

Figure 4.35: Vorticity magnitude over an airfoil protrusion height 0.02c located at the leading edge, at 4º

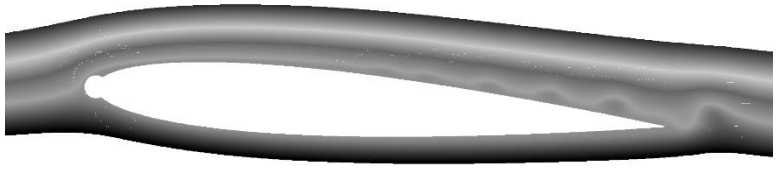

(a) t = 0.7s

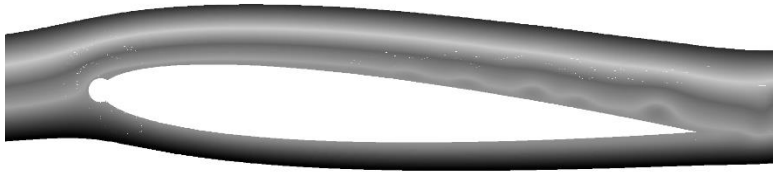

(b) t = 0.8s

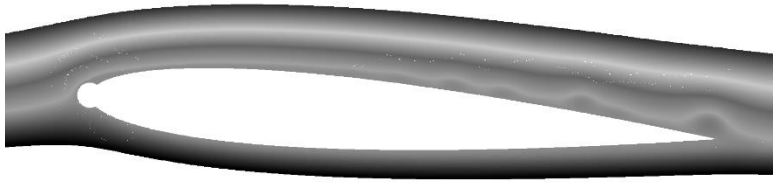

(c)t = 0.9s

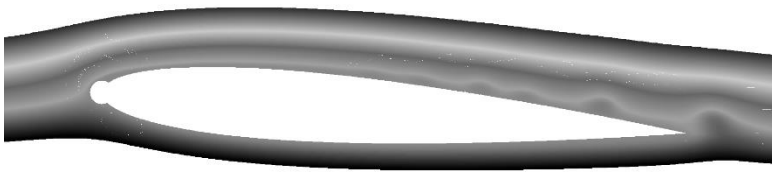

(d)t =1.0s

Figure 4.36*:* Roll up vortices for the protrusion height 0.02c located at the leading edge, at α = 4º

As the angle of attack is increased, there is a negligible increase in the lift coefficient and *L/D* values. Improvements are observed from α = 16º onwards, due to vortex-based lift. The enhancements in the lift coefficient and the *L/D* values were found to be between 2% to 42% and 2% to 21% respectively. For an airfoil with a protrusion height of 0.01c, lift coefficient values are enhanced by 28% to 43% at AOAs between α=16º to 20º. The *L/D* values are also increased by up to 22%. As the height of the protrusion increased to 0.02c, the changes in the lift coefficient are observed very minutely as compared to the clean airfoil configuration with no loss in *L/D* ratio. Similar to the other heights of protrusion, the time-averaged lift coefficient values are almost equal and slight enhancement in the *L/D* is observed. At higher AOAs, increments of up to 45% in the time-averaged lift coefficient and 24% in the *L/D* values are observed, which is due to the periodic shedding of vortices from the surface of the airfoil.

4.2.2 EFFECT OF PROTRUSION ON SUCTION SURFACE AT 0.05C

The aerodynamic characteristics of an airfoil with a circular protrusion at 0.05c on the suction surface are shown in Fig. 4.37. For a protrusion height of 0.005c, a positive lift is observed at α = 0º, even as the base profile is a symmetrical one. But as the AOA is increased, there are significant losses in the time-averaged lift coefficient except for the protrusion height of 0.005c. As compared to the clean configuration, even for a protrusion height of 0.005c, a degradation of 19%, 14%, and 8% in the *L/D* values is observed at α = 4º, 6º, and 8º respectively. In the post-stall regime, improvements in the time-averaged lift

coefficient are observed due to vortex-dominated flowfield, with increments of up to 41% and 22% in C_l and *L/D* values respectively, for a protrusion height of 0.005c. As the protrusion height is increased, there is a severe deterioration in the aerodynamic performance of the airfoil, except at α = 0°. For a protrusion height of 0.01c, decrements of up to 21% and 50% in the lift coefficient value and the aerodynamic efficiency respectively are observed, in the pre-stall regime. As the vortex shedding takes over the flowfield around the airfoil, improvements of up to 45% and 22% are observed in the lift vales and *L/D* values respectively. This degradation in the lift and *L/D* is due to the increased size of the separation bubble length, compared with the clean airfoil.

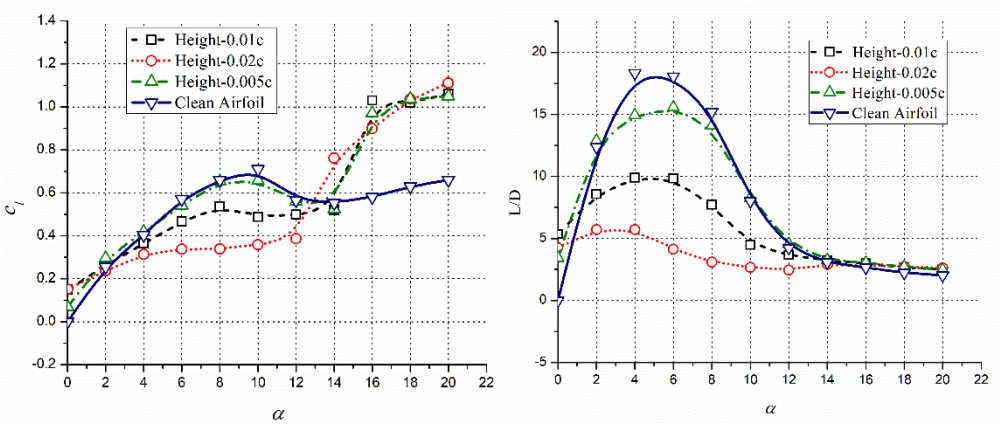

(a) Lift Coefficient versus α *(b) Time-averaged L/D versus α*

Figure 4.37: Aerodynamics characteristic of an airfoil with protrusion located at 0.05c on the Suction surface

The positive lift observed at α = 0°, for the symmetrical airfoil, is due to the enunciation of the unsteadiness in the flow due to the presence of the protrusion. The presence of protrusion on the suction surface causes a laminar separation bubble that reattaches forming a short bubble and a series of roll-up vortices are formed on the rear part of the suction surface, as can be seen in Fig. 4.38. The series of roll-up vortices create an additional suction which makes the flow-field asymmetric producing a positive lift at α = 0°. No such asymmetry is observed for the clean airfoil though.

(a) Airfoil with protrusion of height 0.05c

(b) Clean Airfoil

Figure 4.38: Streamlines over an airfoil with protrusion height 0.005c located at 0.05c and clean configuration at 0º

As the AOA is increased in the pre-stall regime, the deterioration observed in the lift coefficient is due to the inability of the shear layer separated at the protrusion to reattach, especially larger protrusion heights. As can be seen in Fig. 4.39, which shows the intermittency contours for an airfoil with a protrusion at 0.05c, for the protrusion of height 0.005c, the laminar shear layer reattaches aft of the protrusion forming a laminar separation bubble. Even for a protrusion height of 0.01c, the separated shear layer reattaches, this time, however, as turbulent flow, which separates again after covering some distance on the suction surface. For the protrusion height of 0.02c however, the flow separated at the protrusion completely fails to reattach as can be seen in Fig. 4.39 (c). This causes a severe degradation in the aerodynamic performance of the airfoil in the pre-stall regime wherein the lift coefficient and L/D values are reduced by 23% and 78% respectively at α=6°.

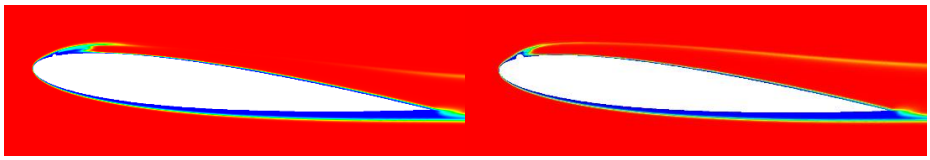

(a) Height 0.005c *(b) Height 0.01c*

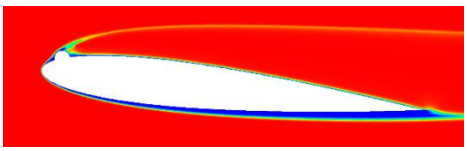

(c)Height 0.02c

Figure 4.39: Intermittency contour for airfoil at α =6º, with a protrusion at 0.05c on the suction surface

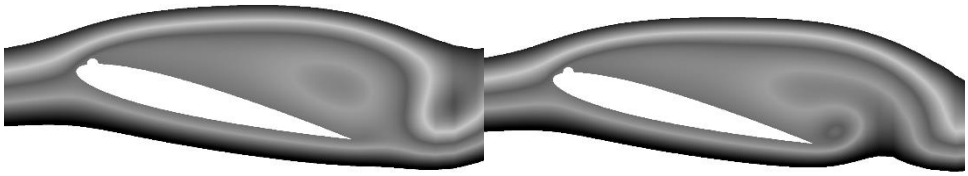

(a)Higher lift *(b) Lower Lift*

Figure 4.40: Instantaneous streamlines over an airfoil at α=14º with protrusion of height 0.02c at 0.05c on the suction surface

In the post-stall regime, the aerodynamics is dominated by vortex dynamics as can be seen in Fig. 4.40. The vortex shedding phenomena creep in AOA as small as α = 14° for an airfoil with a protrusion at 0.05c for a Reynolds number of 50000. For comparison, at Reynolds number of 10^5, the phenomenon starts at α = 16°. As with most vortex shedding cases, the lift coefficient fluctuates between a high and low value caused by instantaneous vortical structures as shown in Figs. 4.40 (a) and (b). In Fig. 4.40 (a), a single primary clockwise vortex is seen which causes a uniform suction, also evident from the surface pressure distribution graph in Fig. 4.41(a), leading to a higher amount of lift. In a contrasting configuration, an anticlockwise vortex build-up at the trailing edge creates a suction on the pressure surface as can be observed in Fig. 4.41 (b), limiting the amount of lift produced. Nevertheless, increments in time-averaged lift coefficient and *L/D* values of 45% and 28%, are observed for α = 14°.

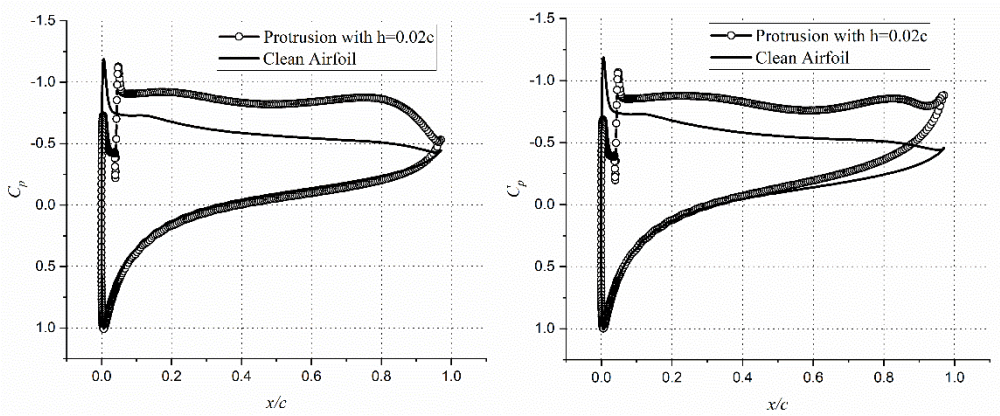

(a) Higher Lift *(b)Lower Lift*

Figure 4.41: Pressure distribution over an airfoil at α=14º with protrusion of height 0.02c at 0.05c on the suction surface

4.2.3 EFFECT OF PROTRUSION ON PRESSURE SURFACE AT 0.05C

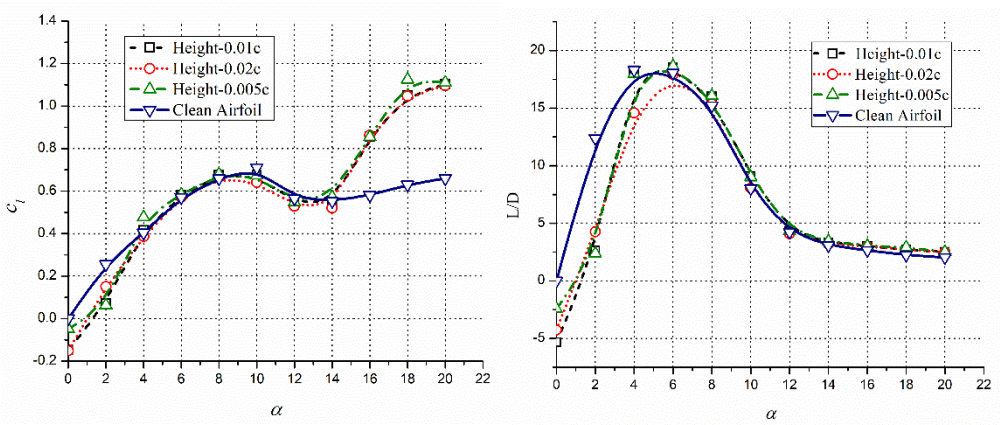

(a) Lift Coefficient versus α *(b) Time-averaged L/D versus α*

Figure 4.42: Aerodynamics characteristic of an airfoil with protrusion located at 0.05c on the pressure surface

The aerodynamic efficiency and the lift of an airfoil are severely degraded in the pre-stall regime, by the presence of a circular protrusion at 0.05c location on the pressure surface, as can be seen in Fig. 4.42. Contrary to the protrusion at 0.05c on the suction surface, a negative lift is observed at α = 0°, for a protrusion on the pressure surface. The flow-field at smaller AOAs viz. α = 0°, 2°, and 4° are highly unsteady resulting in a decrement in the lift coefficient and

L/D values of up to 20% and 80% respectively. This unsteady character and the reduction lift coefficients and the aerodynamic efficiency were not observed for the same configuration at a higher Reynolds number of 10^5. As can be seen in Figs. 4.43 and 4.44, there is a small-scale vortex shedding at $\alpha = 2°$ for an airfoil with protrusion of heights 0.005c and 0.01c, at 0.05c on the pressure surface.

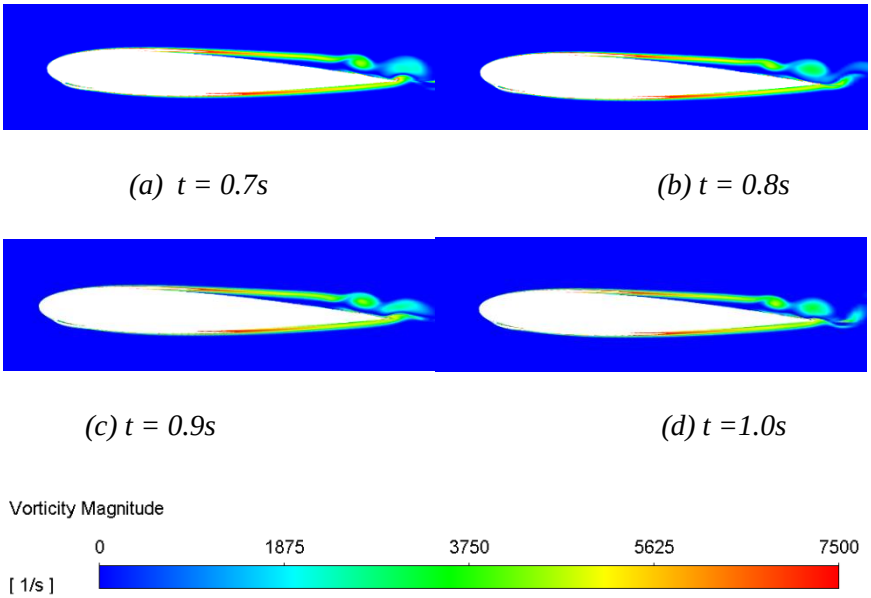

Figure 4.43: Vorticity magnitude for the protrusion height 0.005c located at pressure surface 0.05c, at 2º

Vortices are shed alternately from the suction and the pressure surfaces at these small AOAs, which cause variations in lift and drag coefficients. As the height of the protrusion is increased, the coherent structures on the pressure surface are amplified resulting in more suction on the pressure surface and hence further reduced instantaneous lift coefficients. Also, with an increase in the height of the protrusion, the amplitude of fluctuations in lift coefficient becomes larger due to shedding high strength vortices.

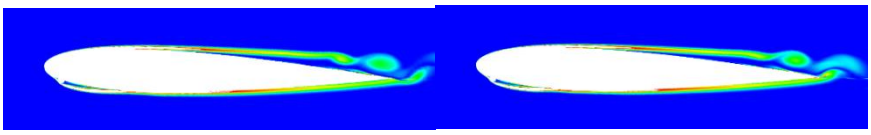

(a) t = 0.7s (b) t = 0.8s

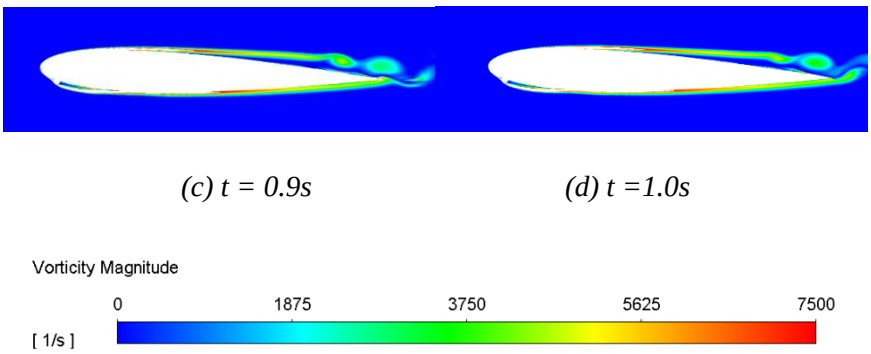

Figure 4.44: Vorticity magnitude for the protrusion height 0.01c located at pressure surface 0.05c, at 2º

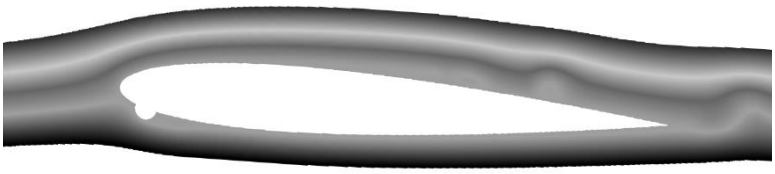

Figure 4.45: Roll up vortices for the protrusion height 0.02c located on the pressure surface, at 4º

For the larger of height 0.02c, a large separation bubble is seen immediately behind the protrusion at these small AOAs, as can be seen in Fig. 4.45. This reduces the unsteadiness on the pressure surface slightly as compared to smaller heights of protrusions. As the AOA is increased, the vortices on the pressure surface are completely washed out and the flow is completely attached with a small separation bubble behind the protrusion. This causes the unsteadiness at small AOAs to die out at α = 8° and higher. This also makes the lift coefficient values regain the values equal to that for a clean configuration. The intermittency contour of the configuration with protrusions of different heights, placed at 0.05c on the pressure surface is shown in Fig. 4.46, for an AOA of α = 8°. As can be seen in Fig, 4.46, for all protrusion heights, a laminar separation bubble of the same length is observed on the suction surface. The flow on the pressure surface remains entirely laminar despite the presence of a protrusion, thus making the flow-field similar to that of a clean airfoil. This is in contrast to

the flow at Reynolds number 10^5 wherein a transition to turbulence was observed for larger protrusions.

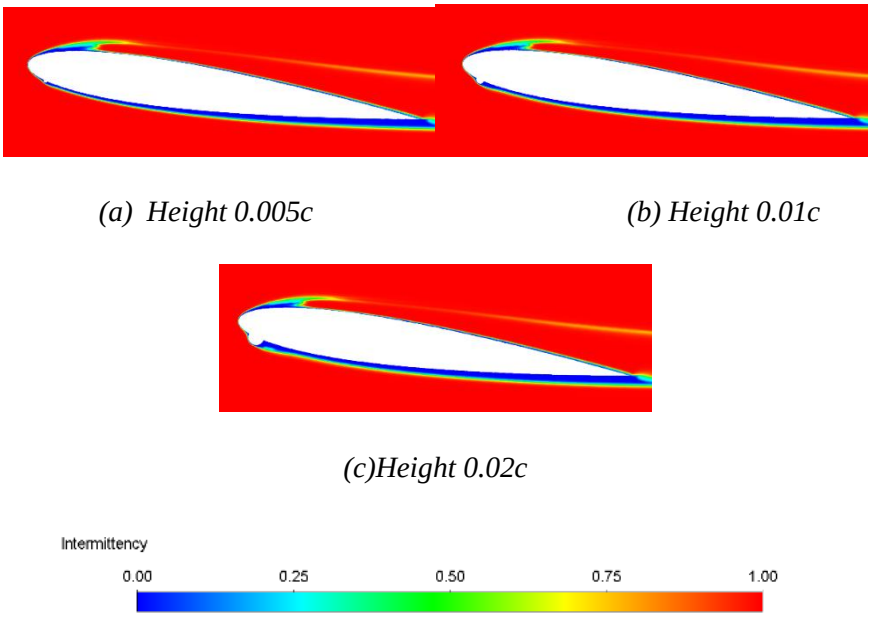

(a) Height 0.005c *(b) Height 0.01c*

(c)Height 0.02c

Figure 4.46: Intermittency contours for airfoil at α = 8º, with a protrusion at 0.05c on the pressure surface

From α =16º onward, as with other protrusion configurations, the vortical interactions take over and improvements in time-averaged lift coefficients are observed. Increments of up to 28% and 23% are observed in the lift and aerodynamic efficiency respectively, at α = 16°, for protrusion height of 0.005c.

4.2.4 EFFECT OF PROTRUSION ON STROUHAL NUMBER

The flow at a Reynolds number of 50000 is highly unsteady due to shear layer instabilities. The roll-up vortices formed especially on the suction surface are shed frequently into the wake causing high-frequency oscillations in the lift values at low AOAs, even for the clean airfoil configuration. The addition of protrusion alters the unsteadiness in the flow significantly depending upon its height and location on the surface as can be seen in Fig. 4.47. A protrusion of height 0.005c located at the leading edge does not affect the magnitude of oscillation but lowers the frequency at which the oscillation in lift values occurs. For a larger protrusion of height 0.01c at the LE, the oscillations in the lift values

almost die out while for a protrusion height of 0.02c, extremely high amplitude and high-frequency oscillation are lift values is observed, as can be seen in Fig 4.47 (a). A small protrusion of h = 0.005c on the pressure surface dampens out the oscillations with a very low amplitude oscillation in the lift values as can be seen in Fig. 4.47 (b). As the height of the protrusion is increased, the oscillations become severe with larger amplitudes of variations in C_l values. The oscillation induced, however, is not as severe as those induced by protrusions on the suction surface.

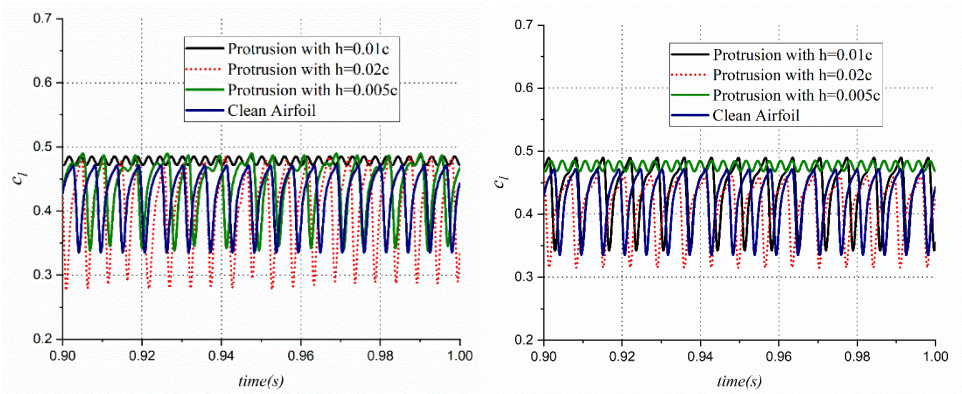

(a) Protrusion at leading edge *(b) Protrusion at 0.05c on pressure surface*

Figure 4.47: Transient oscillations in the lift of airfoil with circular protrusion for Re = 50000, α =4°

On the contrary, the protrusions at 0.05c on the suction surface mitigate the flow unsteadiness at AOAs of α = 2° and 4°. The oscillations in the lift coefficient values observed are primarily because of the periodic flushing of laminar separation bubbles at lower AOAs and vigorous vortex shedding at higher AOAs. These frequencies of these oscillations are presented as chord-based Strouhal numbers for various configurations in Fig. 4.48. As can be seen in Fig. 4.48 (a), the small protrusions at 0.05c on the suction surface do not affect the Strouhal number much at α =0°, but the larger protrusion of height 0.02c eliminates the flow unsteadiness and vortex shedding at this AOA. When located at 0.05c on the suction surface, all protrusions eliminate the flow steadiness and vortex shedding at AOA between α = 2° and 14°. At AOAs of α

= 14° and higher the vortex shedding frequencies are similar to those for the clean configuration. The effect of the protrusions at 0.05c on the suction surface, for higher AOAs, is to increase the Strouhal number slightly.

The smaller protrusion of height 0.005c, located at 0.05c on the suction surface does not affect the vortex shedding frequency at α= 0°, but the larger protrusions diminish the vortex shedding frequency slightly at this AOA. At α = 2°, all protrusions increase the vortex shedding frequency of the airfoil with the smaller protrusions at 0.05c on the pressure surface increasing the Strouhal number by up to 38%. The trend reverses at α =4°, as at this AOA the protrusions diminishing the Strouhal number by up to 40%, as can be seen in Fig. 4.48 (b). Again, the smallest of the protrusion causes a maximum reduction in the vortex shedding frequency. At higher AOAs, the trend is similar to protrusion at the leading edge with the elimination of vortex shedding at α =14°.

The vortex shedding frequency and the Strouhal number pattern for protrusion at the leading edge are slightly different as can be observed in Fig. 4.48 (c). The flow unsteadiness observed for the clean configuration at α = 0°, is eliminated by the presence of protrusion at the LE. The larger protrusion of height 0.02c does not seem to affect the vortex shedding frequency of the airfoil at α = 2° and 4°, but a smaller protrusion of height 0.01c eliminates the vortex shedding at α = 2°. This protrusion, however, exacerbates the vortex shedding at α = 4° with an increase of about 100% in the Strouhal number. The smallest protrusion of height 0.005c at the leading edge has a slightly less effect on the vortex shedding frequency as it dampens the vortex shedding by about 12% at α = 2° and enhancing the Strouhal number by 34% at α = 4°. The trend for higher AOAs is similar to those of other protrusions.

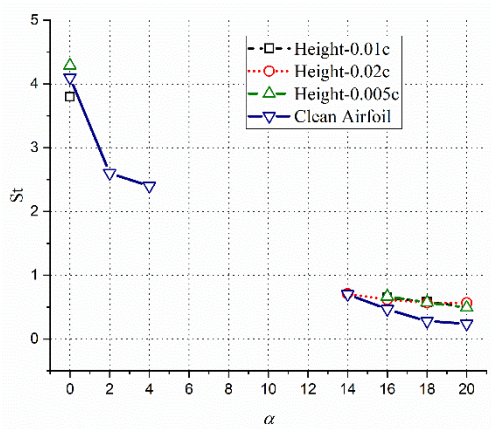

(a)Suction Surface at 0.05c Location

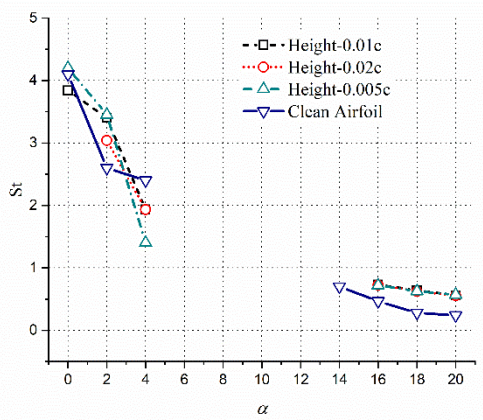

(b) Pressure surface at 0.05c Location

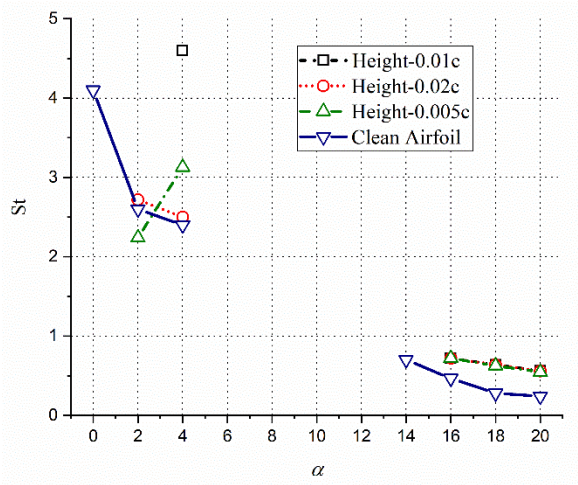

(c)Leading Edge

Figure 4.48: Strouhal Number for various protrusion configurations

4.3 EFFECT OF TRIANGLE SHAPED PROTRUSION AT REYNOLDS NUMBER 10^5

The effect of triangle-shaped protrusions located at the LE, 0.05c on the suction surface, and 0.05c on the pressure surface is investigated at a chord-based Reynolds number of 10^5. These triangles are equilateral in shape with the altitude of the triangle as the height of the protrusion, which is measured normal

to the local airfoil surface. The effect of three different altitudes viz. 0.005c, 0.01c and 0.02c, of these triangles were investigated.

4.3.1 TRIANGLE SHAPED PROTRUSION AT THE LEADING EDGE

The presence of a small triangular protrusion at the leading edge (LE) does not alter the pre-stall aerodynamic characteristics of the airfoil significantly, as can be comprehended in Fig. 4.49. The lift curves for the configurations with protrusion of height h = 0.005c and 0.01c overlaps the ones for clean configuration up to α = 8°. At α = 10°, there is a slight reduction in the C_l values for a larger protrusion, as compared to the clean configuration. Flow unsteadiness, however, is observed for AOAs up to α = 6°, due to the formation of roll-up vortices.

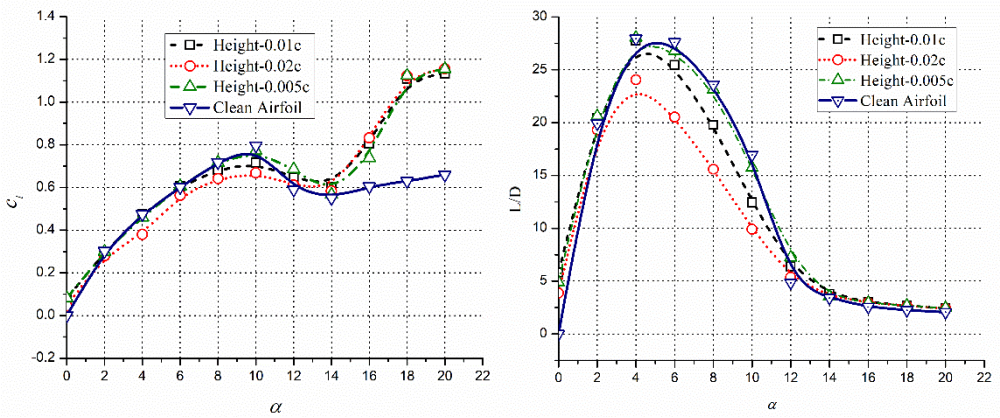

(a) Lift Coefficient versus α *(b) Time-averaged L/D versus α*

Figure 4.49: Aerodynamic characteristics of with Triangular Protrusion at Leading Edge

The roll-up vortices for an airfoil with a triangular protrusion of height h = 0.02c, at the LE, for various instants of time, for α = 0° can be observed in Fig. 4.50. As can be seen in Fig. 4.50, vortices, elongated ellipse in shape shed alternatively from the suction and the pressure surface. The vortices shed from the suction surface are, however, more coherent than those shed from the pressure surface. This makes the vortex shedding asymmetric and a positive time-averaged lift coefficient is observed, even at α = 0°. As the AOA is

increased, is vortices on the suction surface become more coherent and multiple small circular vortices can be seen drifting downstream, as shown in Fig. 4.51. In this figure, multiple coherent structures can be seen on the suction surface of the airfoil at α = 4°, enhancing the vortex shedding from the airfoil, resulting in fluctuations in lift coefficient values.

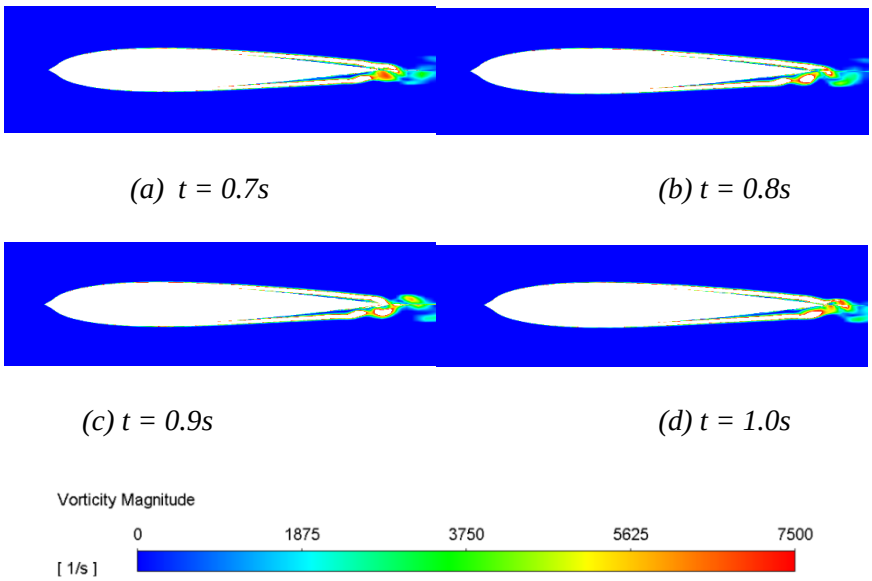

Figure 4.50: Vorticity contour over an airfoil with protrusion of height 0.02c located at the leading edge at α = 0º

As the AOA is further increased, improvements in time-averaged lift coefficients are observed in the post-stall regime. This improvement, however, comes with enhanced flow unsteadiness due to vigorous vortex shedding. The amplitude of fluctuations in the lift coefficient is higher for larger protrusions and higher angles of attack. The unsteadiness in the drag coefficient is seen only for α = 18° and 20°. The time-averaged aerodynamic efficiency (*L/D*) of the airfoil, however, severely deteriorates for larger protrusion at the LE, as can be appreciated in Fig. 4.49 (b). For a smaller protrusion of *h* = 0.005c, the *L/D* ratio is slightly lower than that for a clean configuration.

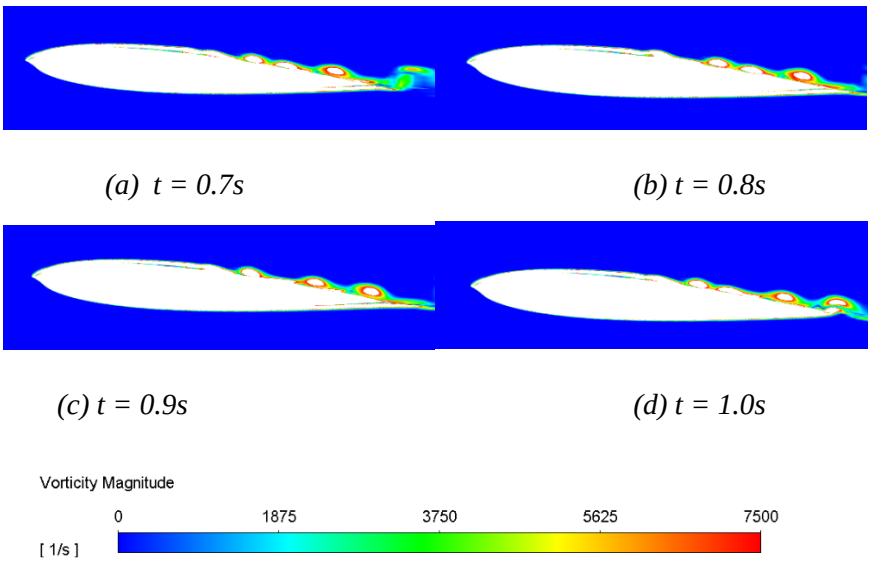

Figure 4.51: Vorticity magnitude over an airfoil with protrusion height 0.02c located at the leading edge at α = 4º

The flow unsteadiness observed at smaller AOAs can be attributed to the character of the separated shear layer and its reattachment. As can be seen in Fig. 4.52 (a), for a smaller protrusion at the LE, the detached shear layer reattaches as a turbulent one and thereafter the flow remains turbulent. The separations and reattachments thereafter are chaotic, no coherent structures are seen, and thus the vortex shedding is absent, making the flow stable. For a larger protrusion, however, the flow remains laminar throughout the suction surface of the airfoil. This aids in the formation of coherent structures aft of mid-section, which are fed into the wake, making the flow highly unsteady, as can be seen in Fig. 4.52 (b).

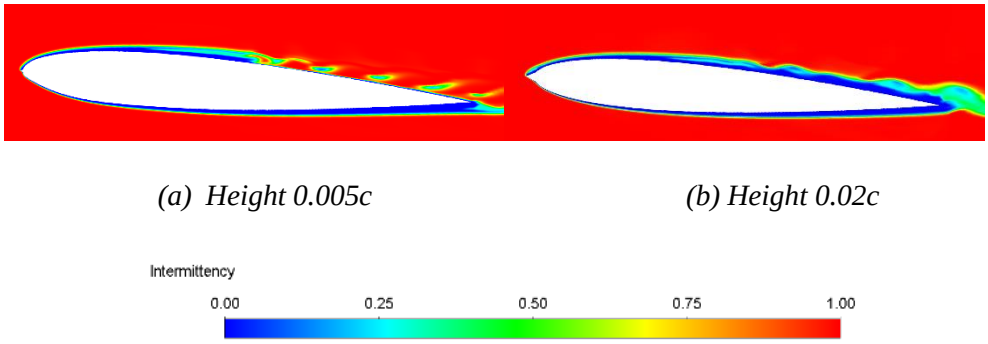

Figure 4.52: Intermittency for the protrusion at the leading edge, at 4º

In the post-stall regime, the *L/D* ratio improves marginally over the clean configuration due to enhancement in vortex lift. An exception can be observed at α = 12°, which is the stalling AOA for the clean configuration. The protrusion of height 0.005c energizes the laminar boundary layer to result in turbulent reattachment resulting in the disappearance of a stall at this AOA. At this AOA, the *L/D* ratio improves by about 49% as compared to the clean configuration. For the taller protrusions investigated, the deteriorations in the L/D ratios in the pre-stall regime are significant. For the protrusions of heights 0.01c and 0.02c, the *L/D* ratios drop by 28% and 42% respectively, at α=10°. The stall at α=12° however, is mitigated for both protrusion heights. In the post-stall regime, all the protrusions show marginal improvements in the *L/D* ratios as can be seen in Fig. 4.49(b).

The details of the frequency and amplitude of oscillations in C_l values at $\alpha=16^0$ are shown in Fig. 4.53. The frequency of oscillation reduces marginally from 100 Hz to 95 Hz as the height of the protrusion is increased from 0.005c to 0.02c. For smaller protrusion of *h*=0.005c, and 0.01c, the frequency of oscillation α=18° and 20° are the same as those at α=16°. For larger protrusion at the leading edge, the frequency of oscillation reduces to 80 Hz and 72 Hz for α=18° and 20° respectively.

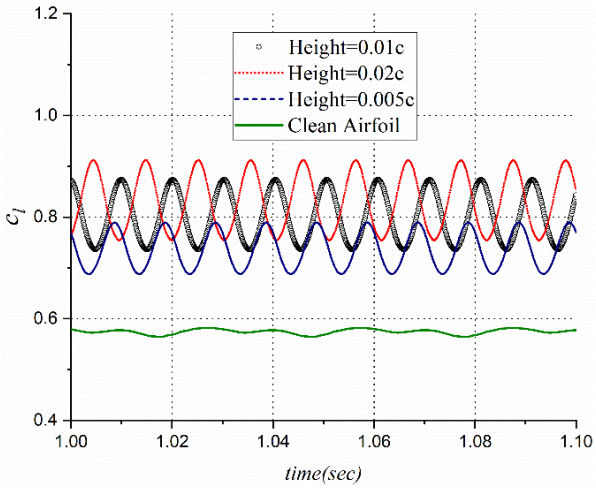

Figure 4.53: Lift coefficient history for an airfoil with a protrusion at the leading edge and α=16°

4.3.2 TRIANGLE SHAPED PROTRUSION AT 0.05C ON THE SUCTION SURFACE

Numerical simulations suggest that a triangular protrusion located at 0.05c on the suction surface of NACA 0012 alters the static aerodynamic characteristics of the airfoil dramatically. As can be seen in Fig. 4.54, protrusion with the height of 0.005c does not degrade the lift coefficient (*Cl*) of the airfoil; the drag coefficient (C_d) however, deteriorates, especially for angles of attack between 0° and 8°. At α=10°, the airfoil with protrusion goes for stall like the original airfoil, the reduction in lift, however, is small as compared to the clean configuration. With only a slight deep at α = 10°, the lift curve recovers immediately from this light stall and shows remarkable enhancements in time-averaged C_l values at all higher AOAs. As shown in Fig. 4.54, enhancements of 13.5%, 24.2%, 30.7%, 52.7%, and 54.3% were observed in the time-averaged C_l values as compared to clean configuration at AOAs of α =12°, 14°, 16°, 18°, and 20° respectively.

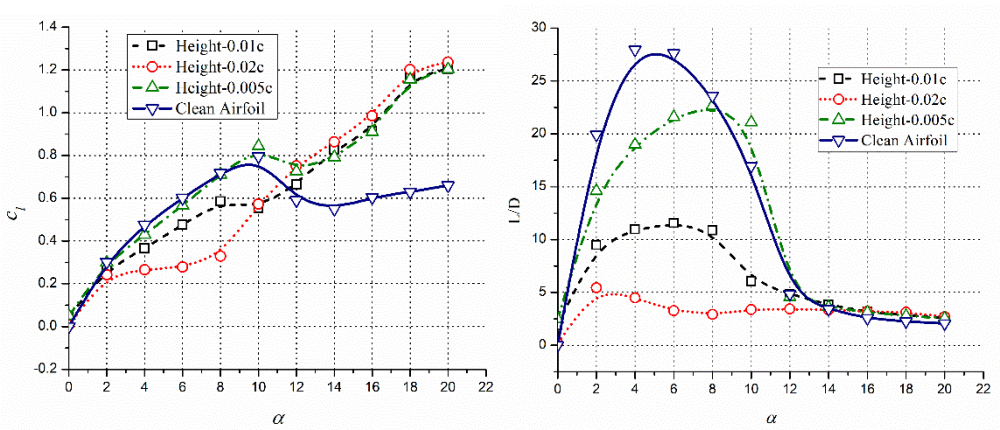

(a)Lift Coefficient versus α *(b) Time-averaged L/D versus α*

Figure 4.54: Aerodynamic characteristics of NACA0012 with a triangular protrusion on the suction surface at 0.05c

Besides a positive *L/D* ratio at α = 0°, a protrusion at 0.05c location on the suction surface severely degrades the aerodynamic efficiency of the airfoil, in the pre-stall regime, as can be seen in Fig. 4.54 (b). Although the stall for an airfoil with protrusion is less severe, the *L/D* ratio reduces by about 23% for a

protrusion height of 0.05c at α = 6°. As the AOA increases, the aerodynamic efficiency improves greatly for this height of protrusion wherein the *L/D* ratio enhances by 23% at α =10°. At higher AOAs, these improvements become smaller. For taller protrusions, the *L/D* ratio diminishes by about 65% for *h* = 0.01c at α=10° and by about 88% for *h* = 0.02c at α = 8°. These deteriorations in the aerodynamic efficiency are due to the reduction in lift coefficients for these configurations. The positive lift seen at α = 0°, is because of the unsteadiness in the flow due to the shedding of vortices as can be seen in Fig. 4.55.

(a) t = 0.7s

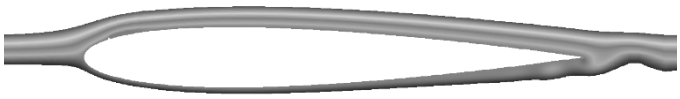

(b) t = 0.8s

(c) t = 0.9s

(d) t =1.0s

Figure 4.55: Streamlines over an airfoil at α = 0°, with protrusion of height 0.01c located at 0.05c on the suction surface

At these small AOAs, a small protrusion on the suction surface results in the formation of a laminar separation bubble, which aggravates laminar instability causing the shedding of small vortices from the airfoil. The suction imparted by

the stationary laminar separation bubble makes the time-averaged lift remain positive. The enhancements in the time-averaged lift coefficients in the post-stall regime are primarily due to the dominance of the vortex lift in this separated regime. As the anticlockwise vortex builds up at the trailing edge, the *Cl* values are less and once the counter-clockwise vortex is shed away, a clockwise circulation is imparted to the airfoil, enhancing the instantaneous lift coefficient. The presence of triangular protrusion at a 5%c location on the suction surface makes the flow highly unsteady with high vortex shedding frequency along with shedding of stronger vortices. The vortex shedding frequency of the airfoil with this protrusion is high at α = 12°, 14° and 16° while at α = 18° and 20° the frequency of the shedding slightly less because of increase in the amplitude of oscillation that is associated with vortex shedding of larger strengths, as can be appreciated in Fig. 4.56.

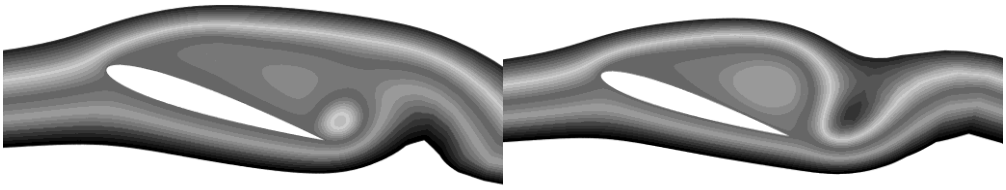

(a) Lower lift coefficient *(b) Higher lift coefficient*

Figure 4.56: Instantaneous vortex structure for airfoil with protrusion at 5%c, h = 0.005c and α =18^0

During the vortex shedding cycle, as a counter-clockwise vortex builds at the trailing edge, the separated flow over the suction surface is pushed further away from the suction surface as can be observed in Fig. 4.56 (a). This results in decreased circulation around the airfoil and hence a reduced lift. The reduction in C_l values continues as the counter-clockwise vortex gains strength. After reaching the peak strength, the vortex at trailing is shed away. As the shed vortex moves away the clockwise vortex on the suction surface gains strength and pulls the separated shear layer downwards as can be detected in Fig. 4.56 (b). This state has a maximum circulation and hence a maximum lift coefficient.

The figure also shows a more circular vortex spanning the entire suction surface thus creating more suction and enhance lift.

As the height of the triangular protrusion located at 0.05c is increased to h = 0.01c, a noticeable reduction in the C_l values is observed from α = 4° to α =10°. This reduction in the lift is because of the flow separation ahead of the protrusion and the large size of the separation bubble, as can be noticed in Fig. 4.57. As shown in Fig. 4.57 (a), for α = 8°, the flow separated from the protrusion attaches to the surface, forming an elongated separation bubble and also can see in Fig. 4.58. For the clean airfoil, however, the separated flow reattaches immediately forming a short separation bubble as revealed in Fig. 4.57 (b).

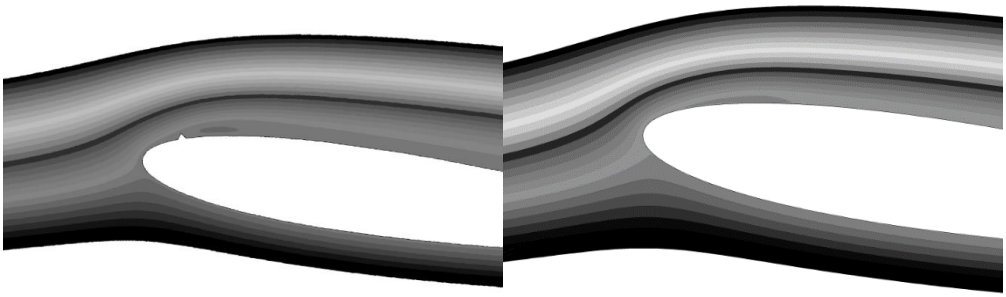

(a) With Protrusion h=0.01c *(b) Clean Airfoil*

Figure 4.57: Laminar separation for bubble at α = 8° for NACA 0012

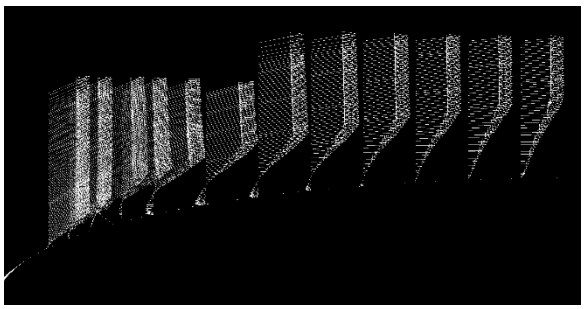

Figure 4.58: Velocity Profile over an airfoil with protrusion height 0.01c located at 0.05c, at 8°

As the AOA is increased to α = 10° and above, the bursting of the separation bubble starts resulting in inflow unsteadiness for an airfoil with this protrusion. The time-averaged lift coefficients for airfoil with protrusion of height h = 0.01c, located at 0.05c is increased by 7.4%, 28%, 31%, 53.4%, and 54.5% at α = 12°, 14°, 16°, 18° and 20^0 respectively. This substantial improvement in the lift coefficient observed at high AOAs is due to vigorous vortex shedding over an airfoil with the protrusion on the suction surface.

As the height of the protrusion increased to 0.02c, there is a drastic reduction in the C_l values, in the pre-stall regime. Even at a low AOA of α = 4°, the flow separated from the protrusion reattaches near the mid-chord location forming a large separation bubble as can be seen in Fig. 4.59 (a). As the AOA increased, the separated flow fails to reattach and the size of the separation vortex grows in size, as is evident from Fig. 4.59 (b) and (c), Fig. 4.61. This results in very low C_l values at α = 6° and 8°. The transition of the flow turbulence can also be established through the contours of intermittency. As can be seen in Fig. 4.60, the separated shear layer reattaches as a turbulent flow aft of the protrusion and the turbulent flow thereafter separates without any reattachment, causing a severe loss in the lift of the airfoil. Although the C_l values are reduced at lower AOAs, the lift curve for an airfoil with protrusion of height h = 0.01c located at 0.05c shows no signs of the stall. This is because the lift for configuration is primarily because of the upper surface vortex. The increment in the lift, however, comes with severe fluctuations due to vortex shedding at angles of attack higher than α = 4°.

(a) Laminar separation bubble formation at α= 4^0

(b) Separated flow at α= 6^0

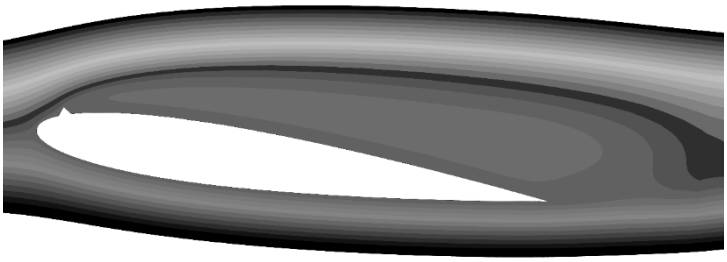

(c) Separated flow at α = 8^0

Figure 4.59: Streamlines for flow over an airfoil with protrusion of height h= 2%c located at 5%c

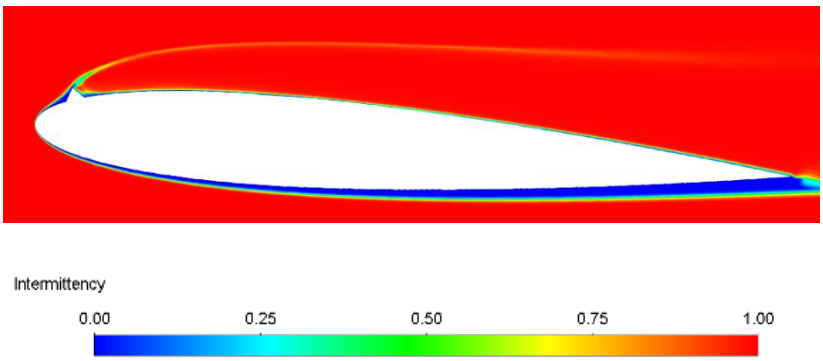

Figure 4.60: Intermittency contour over an airfoil at α=4º, with protrusion of height=0.02c, located at 0.05c

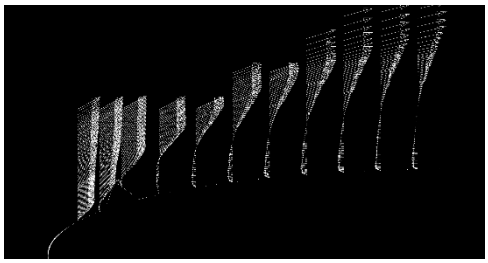

Figure 4.61: Velocity Profile over an airfoil with protrusion height 0.02c located at 0.05c, at 8°

A triangular protrusion located at 0.05c on the suction surface certainly enhances the time-averaged lift coefficients for all heights in the post-stall regime. However, the increase in C_l values is associated with high-frequency vortex shedding, oscillating lift, and drag coefficients. For any protrusion height, the vortex shedding frequency and hence the frequency of oscillation in C_l values decreases as the AOA increased. For a height of h = 0.005c, oscillation frequencies of 147 Hz, 115.6 Hz, 100 Hz, 82 Hz, 75.5 Hz at is observed at α = 12°, 14°, 16°, 18°, and 20° respectively. As the height, the protrusion increased the frequency of oscillation in *Cl* values decreases for the same AOA. For a protrusion of height h = 0.01c the oscillation frequencies reduce to 143 Hz, 115 Hz, 100 Hz, 81.3 Hz, 73 Hz at 12°, 14°, 16°, 18°, and 20° respectively. For the largest protrusion at 0.05c, these frequencies reduce to 116 Hz, 109 Hz, 100 Hz, 87 Hz, and 77 Hz at α = 12°, 14°, 16°, 18°, and 20° respectively. Airfoil with a protrusion at 0.05c shows a frequency of oscillation of 100 Hz at α=16° for all protrusion heights, as can be appreciated in Fig. 4.62. The amplitude of oscillation in C_l values, however, increases as the height of the protrusion is increased.

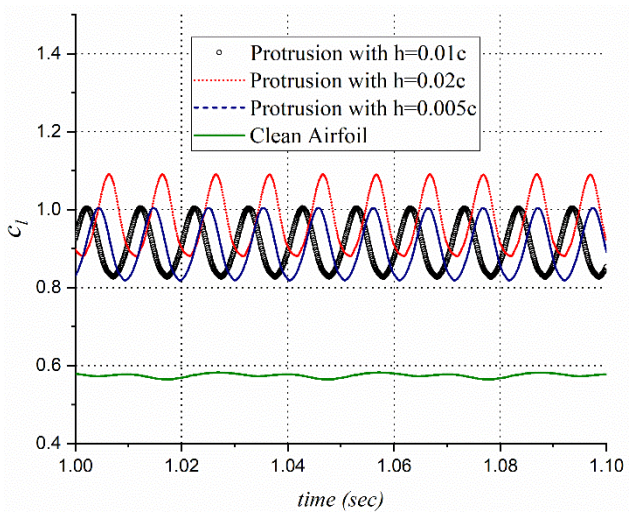

Figure 4.62: Lift coefficient history of triangular protrusion at 0.05c and α = 16°

4.3.3 TRIANGULAR PROTRUSION AT 0.05C ON THE PRESSURE SURFACE

Contrary to protrusion at 0.05c location on the suction surface, a protrusion at 0.05c on the pressure surface does not influence the aerodynamic characteristics of the NACA0012 in the pre-stall regime. Besides a slight drop in C_l value at α = 2^0, the lift curve for an airfoil with this protrusion overlaps the one for clean configuration up to α = 10°, as can be seen in Fig. 4.63. The C_l drop at α = 2° is due to the adverse pressure gradient behind the protrusion caused by the formation of the separation bubble. As the AOA is increased beyond α =10°, the lift and drag curves become vigorously unsteady and the time-averaged curves deviate from the one for the clean airfoil.

Despite the similarity of the lift curve in the pre-stall regime, the *L/D* ratios are highly reduced for protrusions of heights 0.01c and 0.02c as shown in Fig 4.63 (b). For these protrusions the highest reduction in *L/D* values come at α = 2°, with reductions of 50% and 59% respectively for *h* = 0.01c and *h* = 0.02c. The degradation in the aerodynamic efficiency is due to a slight reduction in lift coefficient as well as an increase in the drag coefficient due to the adverse pressure gradient on the lower surface. For the smallest protrusion of height 0.005c however, no degradation in the aerodynamic efficiency is observed.

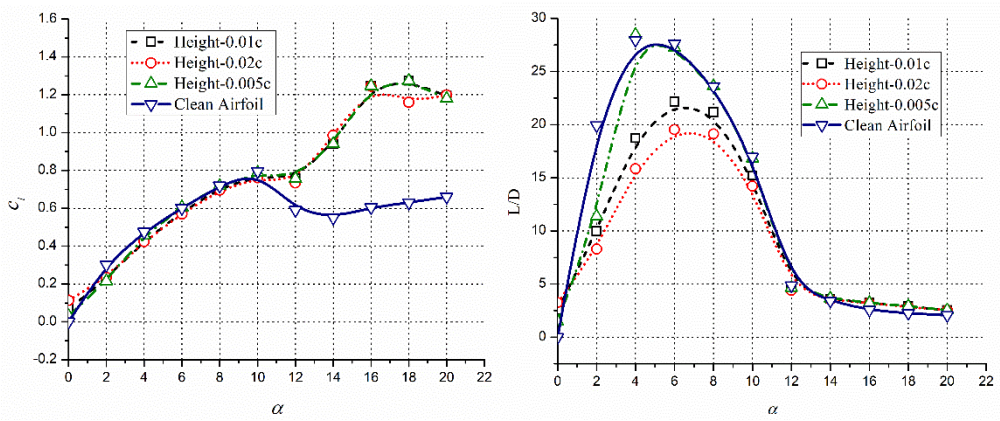

(a)Lift Coefficient versus α *(b) Time-averaged L/D versus α*

Figure 4.63: Lift and drag variations of NACA0012 with a protrusion at 5%c on the pressure surface

The *L/D* versus α curve for this protrusion on the pressure surface almost overlaps the one for the clean airfoil as can be appreciated in Fig. 4.63 (b). An enhancement of up to 16% in the *L/D* ratio is observed for the protrusion of height 0.005c at α = 18°. The increment in time-averaged C_l values is due to the dominance of the vortex lift, as explained earlier. The C_l values are at the trough when a fully developed counter-clockwise vortex is present at the trailing edge, creating a locally high suction at the trailing edge as can be seen in Fig. 4.64(a). The C_l values reach a crest when the counter-clockwise vortex is shed away and the primary vortex on the suction side spans the whole surface creating higher suction as can be detected in Fig 4.64 (b). The skin friction coefficient can see in Fig.65. This is true for triangular protrusion of both heights *h* = 0.005c and *h* = 0.01c. In other words, the presence of two counter-rotating vortices on the suction surface destroys the net suction and decreases the lift coefficient while a single dominating vortex enhances the lift coefficient, with an increase in drag though. The small vortices formed behind the protrusion on the pressure surface create a local downward suction, but the net effect on the lift coefficient is negligible.

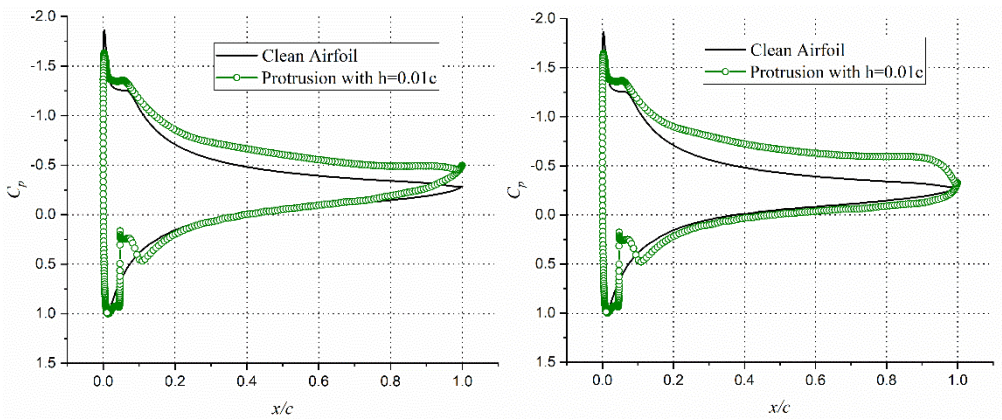

(a) Lower lift coefficient *(b) Higher Lift coefficient*

Figure 4.64: Pressure distribution for minimum and maximum lifts for protrusion with h=0.01c at α = 12°

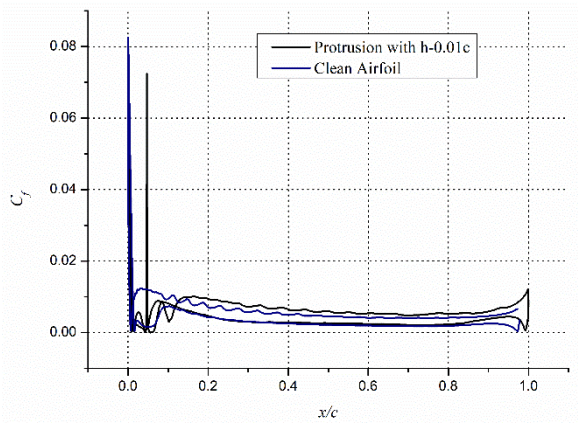

Figure 4.65: Skin Friction coefficient for minimum and maximum lifts for protrusion with h=0.01c at α = 12°

The increments in time-averaged C_l values are 16%, 39%, 64.3%, 64.5%, and 52% at α = 12°, 14°, 16°, 18° and 20° respectively for a protrusion height of 0.005c. As the height of the protrusion is increased to h = 0.01c, there are no drastic fall C_l values at lower AOA in contrary to the results for a protrusion on the suction surface at 0.05c location. In fact, the time-averaged lift coefficient values for protrusion with h = 0.01c improved by 16%, 39%, 64%, 54.4%, and 53% for α =12°, 14°, 16°, 18° and 20° respectively.

(a) t = 0.7s

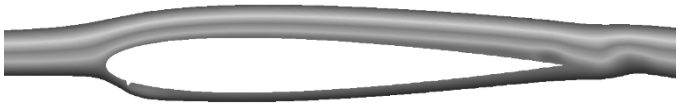

(b) t = 0.8s

(c) t = 0.9s

(d) t =1.0s

Figure 4.66: Streamlines over an airfoil with protrusion height 0.01clocated at suction surface 0.05c, at 0º

As with protrusion on the suction surface, a protrusion at 0.05c on the pressure surface flow unsteadiness at low AOAs resulting in a positive lift at even α = 0°. As can be seen in Fig. 4.66, a protrusion of height 0.01c creates a laminar separation bubble aft of the protrusion imparting instability to the flow. This results in a trail of roll-up vortices on the suction surface. As these vortices leave the surface, the lift coefficient fluctuates. As the AOA is increased, the laminar instability fades away due to the transition of the shear layer to turbulence as can be seen in Fig. 4.67. For a small triangular protrusion of height 0.005c, the boundary layer remains completely laminar on the pressure surface at α = 4°. However, as the protrusion height is increased, the separated shear layer reattaches the pressure surface as a turbulent flow as can be seen in Fig. 4.67 (b) and (c). The shear layer on the suction surface remains laminar for more than 50% of the airfoil surface, forming a long separation bubble for all protrusion heights at α = 4°. After reattachment, a series of turbulent eddies are formed on the latter part of the surface, causing flow unsteadiness as they are shed into the wake. As the angle of attack is increased, the reattachment point moves upstream on the surface of the airfoil, making the flow stable.

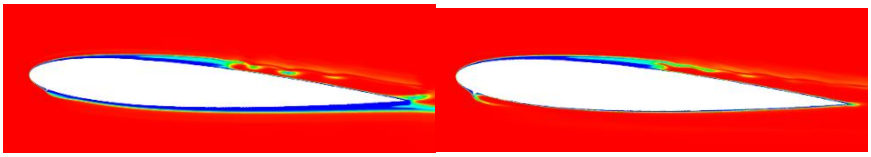

(a) Height 0.005c *(b) Height 0.01c*

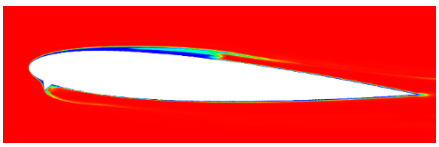

(c)Height 0.02c

Figure 4.67: Intermittency contours for airfoil at α = 4°, with a protrusion at 0.05c on the pressure surface

As with the protrusion at 0.05c on the suction surface and with a protrusion at the leading edge, the augmentation in the lift coefficient values in the post-stall regime comes with highly unsteady vortex shedding cycles. As the AOA is increased in the post-stall regime or α above 10°, the frequency of C_l oscillations for h = 0.005c, and 0.01c is reduced. These frequencies reduce from 93 Hz at α = 12° to 30 Hz at α=20°.

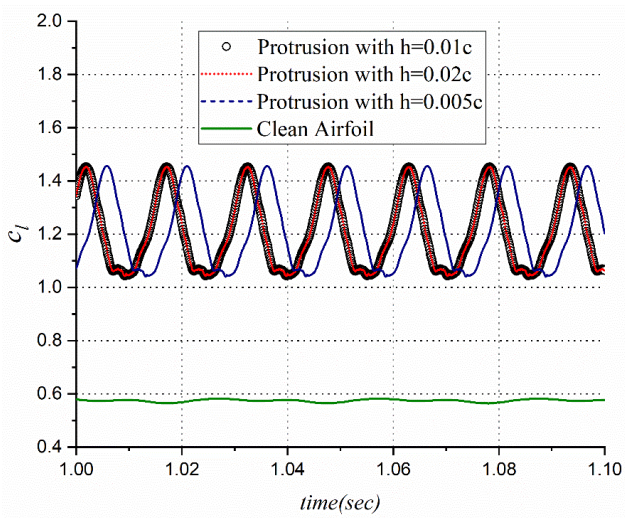

Figure 4.68: Lift coefficient history at α=16^0 on the pressure surface

As seen in Fig. 4.68, at α =16^0, the vortex shedding frequency is the same for all protrusion height with similar C_l values. As the height of the protrusion is increased, the vortex shedding first starts at a lower AOA. As the AOA is increased the frequency of oscillation reduces but not by the magnitudes as with

smaller protrusion heights. Thus for protrusion of height h = 0.01c, at 0.05c on the pressure surface, the lift oscillation frequency decreases from 91 Hz at α = 12° to 58.5 Hz at α=20°.

4.3.4 EFFECT OF TRIANGULAR PROTRUSIONS ON STROUHAL NUMBER

The roll-up of separated shear layers and the subsequent shedding of the vortices from the suction side of the airfoil and the shedding of the counter-clockwise vortex from the trailing edge results in the oscillations of aerodynamic parameters such as C_l and C_d. The spectrum of lift coefficient is analyzed using a Fast Fourier Transform (FFT) to obtain the fundamental frequency f_0, of the vortex shedding and hence the frequency of oscillation in lift coefficient values. These frequencies are converted to non-dimensional Strouhal number St, using airfoil chord c as the characteristic length. Thus, $St = {f_0 c}/{U_\infty}$, with $U\infty$ as the freestream velocity. The clean NACA 0012 does not show any oscillations until α = 16°, for a chord-based freestream Reynolds number of 10^5. From α = 16° onwards, the airfoil behaves similar to a bluff body and the Strouhal varies from 0.2 at α = 16° to 0.12 at α = 20°. Even for an airfoil with a protrusion at the LE, the oscillations in lift coefficient is seen between α =16° and α = 20°. However, for an airfoil with a protrusion, the Strouhal number is significantly higher and falls between 0.5 and 0.6, as can be seen in Fig. 4.69 (a). For protrusions of heights 0.005c and 0.01c, at the LE, the variations of Strouhal number are very similar while for the taller protrusion it is slightly reduced. In all cases, in the post-stall regime, the Strouhal number reduces as the AOA is increased.

For protrusions at 0.05c on either the suction or the pressure surface, the oscillation in C_l values starts at AOA as low as α =12°, as can be seen in Fig. 4. 69 (b) and (c). This is primarily due to the early separation of the shear layer from the protrusion and subsequent reattachment for moderate AOAs, leading to vigorous vortex shedding. As compared to the pressure surface protrusion, the protrusion on the suction surface imparts larger for unsteadiness wherein the Strouhal number as high as 0.98 is observed, for a height of 0.01c. As in the

case of protrusion at the leading edge, the Strouhal number versus AOA curve overlaps for protrusions heights of 0.005c and 0.01c, irrespective of the location. This suggests that the amount of unsteadiness imparted by both protrusions is similar. For the larger protrusion on the suction and pressure surfaces, the Strouhal is smaller for AOA less than α=16° and slightly larger for AOA more than α =16°. This implies that the larger protrusion height diminished the vortex shedding frequency below α =16°, thereafter the bluff body shedding dominates the flowfield, and the protrusion height becomes ineffective. The Strouhal number, however, continuously diminishes as the AOA is increased. The unsteadiness of the flow at low AOAs is completely different from the ones at high AOAs. The clean airfoil itself has very high-frequency oscillations in lift coefficients at α = 0°, 2°, and 4° that increase linearly with AOA. The presence of triangular protrusion at the LE significantly reduces the Strouhal number as can be seen in Fig. 4.69 (a) and (c). A small protrusion of height 0.005c at the LE reduces the Strouhal number by 45% and 30% at α= 0° and 2° respectively, while eliminating the flow unsteadiness at α = 4°. Larger protrusions at LE also substantially reduce the Strouhal number by 22% at α = 0° and up to 36% at α = 2°. The presence of smaller protrusions eliminates the vortex shedding at α = 4°, except for the largest protrusion of 0.02c which reduces the Strouhal number by 70%, but fails to eliminate it.

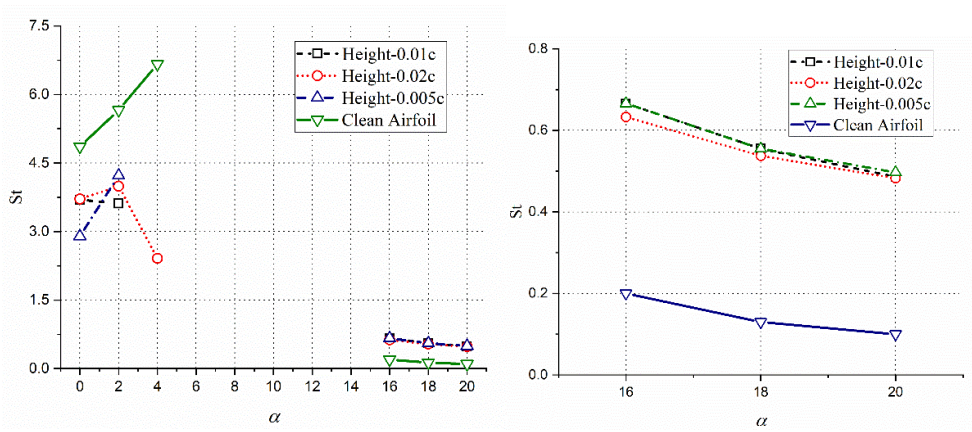

(a) Leading Edge

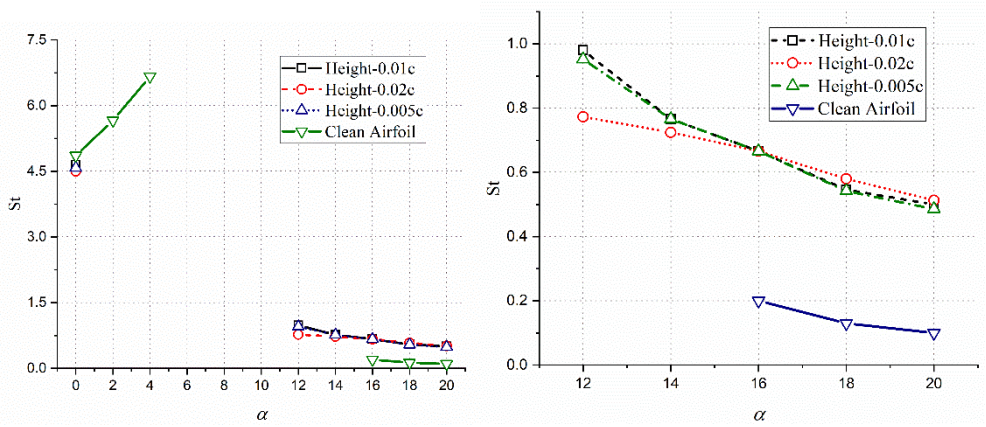

b) On the suction surface at 0.05c

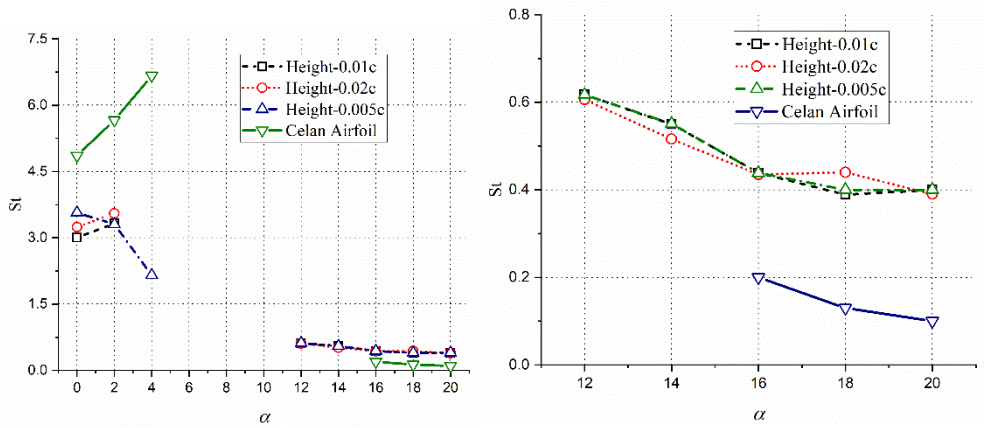

(c) On pressure surface at 0.05c

Figure 4.69: Strouhal Number for different circular protrusion arrangements

The triangular protrusion on the suction surface eliminates the vortex shedding at α = 2° and 4°, for all heights, but the Strouhal number is marginally reduced by these protrusions at α = 0°. Even the protrusions on the pressure surface reduce the vortex shedding and the flow unsteadiness significantly as can be seen in Fig. 4.61 (c). These protrusions can reduce the Strouhal number by up to 38% at α = 0° and 36% at α = 2° while eliminating the vortex shedding at α = 4°. The smallest of protrusions with h= 0.005c however, fails to eliminate the flow unsteadiness at α = 4°, with a Strouhal number of 2.0.

Similar to the circular protrusion, various numerical analyses have been carried out for the triangle-shaped protrusion at 0.25c, 0.50c, 0.75c locations on the

suction surface and pressure surface. The results are not shown here, as these protrusions do not alter the aerodynamics characteristics of the airfoil. The results, however, are included in Appendix B.

4.4 SUMMARY

To examine the effect of protrusion on the aerodynamics of a static airfoil, circular and triangular protrusions are placed at the leading edge, 0.05c, 0.25c, and 0.5c locations on the suction surface and 0.05c location on the pressure surface. The angles of attack (AOA) are varied between $\alpha = 0^o$ and $\alpha = 20^o$ with a 2° interval and the protrusions have heights of 0.005c, 0.01c, and 0.02c. For $Re = 10^5$, the airfoils with circular protrusions of smaller heights at the leading edge show marginal improvements in the C_l, along with significant improvements in *L/D* values. The improvement of up to 8% in *L/D* values in the pre-stall regime is due to a reduction in pressure drag because of the transition of boundary layer into turbulent one by the presence of protrusion. However, for larger protrusions at the leading edge, small reductions in the lift are observed with a significant reduction of 13% to 34% in the *L/D* values, in the pre-stall regime, due to turbulent separation aft of the protrusion. In the post-stall regime, circular protrusions at the leading edge add to the flow unsteadiness as the airfoil undergoes high-frequency vortex shedding, with the enhanced time-averaged lift and frequencies of vortex shedding. Although the time-averaged, C_l is increased by up to 60%, 48.8%, and 48% for the protrusions of heights 0.005c, 0.01c, and 0.02c, no significant improvement in the *L/D* ratio is observed at high AOAs.

A circular protrusion at 5% chord location on suction surface significantly destroys the lift produced in the pre-stall regime, for a Reynolds number of 10^5. Even the smallest protrusion of height 0.005c reduces the lift and L/D values by up to 5% and 29% respectively, at $\alpha = 6°$. The larger protrusions, on the other hand, diminishes the C_l values by up to 39% and the L/D values by up to 87% at $\alpha = 8°$, due to the inability of the shear layer separated at the protrusion to reattach onto the suction surface. Despite the deterioration of aerodynamic

performance in the pre-stall regime, the time-averaged lift curves for larger protrusions at 0.05c location increases monotonically with the AOA, showing no sign of stall. Even the airfoil with the smallest protrusion at 0.05c locations recovers immediately from the stall and displays very high values of time-averaged lift values in the post-stall regime. These increments are, however, associated with vigorous vortex shedding, alternately from the leading and trailing edge, which also increases the drag of the airfoil. Thus, despite increments of up to 63% in the vortical lift, only marginal increments in L/D values are observed in the post-stall regime.

Similar to the protrusion at location 0.05c, the larger protrusions degrades the lift and *L/D* ratio by up to 37% and 85%, respectively, in the pre-stall regime. The smallest protrusion at 0.1c on the other hand significantly improves the aerodynamic performance of the airfoil. With marginal increments in a lift in the pre-stall regime, the aerodynamic efficiency is improved by up to 94% in the pre-stall regime. This increment is realized because of the turbulent reattachment of the shear layer on the suction surface, which reduces the drag by reducing the wake width. In the post-stall regime, as the vortex shedding phenomena takes over the time-averaged C_l values are increased by 9% to 63% for various AOAs between $\alpha = 12°$ to $\alpha = 20°$. Other than the smallest protrusion of h = 0.005c, the larger protrusions at 0.25c location on the suction surface significantly deteriorate the performance of the airfoil in the pre-stall regime. The smallest protrusion enhances the aerodynamic efficiency 16% at $\alpha = 6°$, due to the turbulent reattachment of the boundary layer aft of the protrusion. As the height of the protrusion at 0.25c is increased, the pre-stall L/D ratio values diminish, by up to 64% for the largest protrusion. In the post-stall regime, the time-averaged lift increases at AOA beyond $\alpha = 14°$, for all protrusion height, without a significant increase in the aerodynamic efficiency. These increments come with an increased frequency of vortex shedding, as compared to the clean configurations. The amplitude of oscillation in the lift, however, the largest for the airfoil with the smallest protrusion at these large AOAs. The effect of

circular protrusion at the mid-chord location is also similar with the smallest protrusion providing some improvements in L/D values at small AOAs, while the significant deterioration in the aerodynamic performance is observed for larger protrusions in the pre-stall regime. The reduction in lift and aerodynamic efficiency, however, is reduced as compared to protrusion at 0.25c.

A circular protrusion at 0.05c on the pressure, however, does not affect the lift values in the pre-stall regime at Re = 10^5, with the largest reduction of 7% in C_l values for the largest protrusion. As with protrusions at other locations, the time-averaged lift values are improved in the post-stall regime due to vigorous vortex shedding, without significant improvement in aerodynamic efficiencies though. Protrusions at all locations thus, enhance the flow unsteadiness by increasing the vortex shedding frequency or the Strouhal number. As with the clean airfoil, these Strouhal numbers decrease with increasing AOA, the values of Strouhal numbers for airfoils with circular protrusions are, however, 4 to 5 times higher than the Strouhal numbers for the clean airfoil, in the post-stall regime.

At a Reynolds number of 50000, the effect of a circular protrusion at the leading edge is significantly different from those at a Re = 10^5. The smallest protrusion at the leading edge enhances the lift values marginally while providing significant improvements in the aerodynamic efficiency, in the pre-stall regime at Re = 50000. The time-averaged lift curve for even larger protrusions overlaps the lift curve for the clean airfoil with no major loss of lift in the pre-stall regime. All protrusions at the leading edge, however, show significant improvement in the aerodynamic efficiency, with a 20% increment in L/D ratio for the smallest protrusion and up to 24% increase for larger protrusions. As with the case of Re = 10^5, the aerodynamic performance of the airfoil is significantly degraded with a circular protrusion at 0.05c location in the suction surface. Although there is no significant degradation in aerodynamic performance for the smallest protrusion, a reduction of up to 36% and 78% in C_l and L/D values is observed for the largest protrusion, in the pre-stall regime. These degradations for larger

protrusions are due to the inability of the shear layer detached from the protrusion to reattach onto the suction surface. The protrusion at 0.05c on the suction surface on the other hand makes the flow highly unsteady with degradation in aerodynamic performance similar to those shown by protrusions at 0.05c on the suction surface. The contrast between the protrusions at these two locations being the time-averaged lift at α =0°, wherein a positive lift is observed for a protrusion on the suction surface while a negative lift is observed for a protrusion on the pressure surface.

As with the case of $Re = 10^5$, the protrusion enhances the frequency of vortex shedding in the post-stall regime. The Strouhal number for airfoils with protrusions have similar values in the post-stall regime irrespective of the size and location of the circular protrusion. The protrusion, however, eliminates the vortex shedding at α =14° seen for the clean airfoil at Re = 50000. At α = 0°, the vortex shedding seen for clean airfoil is eliminated by protrusions at the leading edge. The protrusions, however, enhances the vortex shedding frequency at α =2° and 4°. Even the protrusions at 0.05c on the pressure surface enhance the vortex shedding frequency at α =2° while subsiding it at α =4°. The circular protrusion at 0.05c on the suction surface, on the other hand, eliminates the vortex shedding phenomena in the pre-stall regime with some exceptions at α = 0°.

Triangular protrusions offer better aerodynamic performance to an airfoil at a Reynolds number of 10^5, as compared to the circular protrusions. A small triangular protrusion of height h = 0.005c and 0.01c at the leading edge does not alter the pre-stall aerodynamic characteristics of the airfoil, in fact, up to α = 14°. The aerodynamic efficiency, however, diminishes for the larger protrusions, by up to 42% with h = 0.02c, at α = 10°. A small triangular protrusion located at 0.05c on the suction surface, on the other hand, alters the aerodynamic characteristics of the airfoil significantly. The smallest protrusion of height 0.005c, at this location, improves the post-stall Cl of the airfoil without altering the pre-stall characteristics. Although the lift in the post-stall regime is

highly unsteady, the time-averaged C_l values are enhanced by up to 54% for the smallest of protrusion at 0.05c. As the height of the protrusion at this location is increased, the pre-stall aerodynamic characteristics deteriorate, with only marginal improvements in the post-stall Cl values. The aerodynamic efficiency diminishes to values between 65% and 88% for the larger protrusion at 0.5c on the suction surface. The protrusion on the pressure surface does not affect the lift and drag coefficients in the pre-stall regime, but affects the stability of the flow, making the flow inherently unsteady at AOAs of $\alpha = 12°$ or more. The time-averaged C_l values for these unsteady configurations are up to 43% higher than the clean configuration for larger heights of the protrusion. Even the time-averaged L/D do not deteriorate for protrusion of height 0.05c on the pressure surface. For larger protrusions, however, falls of up to 59% in the aerodynamic efficiency are observed, in the pre-stall regime.

Similar to the circular protrusions, the triangular protrusions enhance the flow unsteadiness and vortex shedding that result in the oscillation of Cl values. The triangular protrusion at the LE does not reduce the AOA at which the vortex shedding starts but increases the frequency of vortex shedding and lift oscillation with Strouhal number in between 0.48 and 0.68. For protrusion on the suction surface, the C_l values oscillate between a Strouhal number between 0.5 and 1.0 wherein larger protrusion reduces the Strouhal number for a given AOA in the pre-stall regime. For a protrusion at 0.05c on the pressure surface, the vortex shedding and hence the oscillation in C_l values occur at lower frequencies with a Strouhal number between 0.4 and 0.6. For all triangular protrusions, the Strouhal number reduces as the angle of attack is increased. The triangular protrusions, thus, reduce the AOA at which the vortex shedding starts and increases the vortex shedding frequency as compared to clean NACA 0012.

CHAPTER 5. EFFECT OF CAVITY

Numerical analyses have been carried out over an airfoil with a cavity at three different locations 0.10c, 0.25c, and 0.50c on the suction surface. Two cavity shapes have been chosen viz. circular and triangular with depths of 0.025c and 0.05c, which act as their radii and altitude respectively. The flow analysis conducted at the Reynolds number of 10^5, and 50000, at the AOA between $\alpha = 0^o$ and 20°.

5.1 EFFECT OF CIRCULAR CAVITY AT Re =10^5

5.1.1 CAVITY AT 0.10C LOCATION ON SUCTION SURFACE

A circular cavity of depth 0.025c, located at 0.10c on the suction surface does not affect the aerodynamic lift of a NACA 0012 airfoil, in the pre-stall regime, as can be seen in Fig. 5.1. The aerodynamic efficiency is, however, reduced by up to 20% due to an increase in profile drag of the airfoil. A flow unsteadiness is imparted at $\alpha = 0°$, which makes the time-averaged lift coefficient and the corresponding L/D ratio positive at this AOA. At $\alpha = 10^o$, the *L/D* ratio is similar to that for a clean airfoil, irrespective of the depth of the cavity. At AOAs higher than $\alpha = 10°$, the time-averaged lift coefficient values increase monotonically but the *L/D* ratios remain close to the ones for clean configuration, as can be seen in Fig. 5.1 (a). As the AOA is increased, the increments of 14.3%, 38.4%, 33.5%, and 39% in time-averaged lift coefficient are observed at $\alpha = 14^o$, 16°, 18°, and 20°. For a small depth of 0.025c, even an increment of 17% in L/D value is observed at $\alpha = 8°$. The aerodynamic characteristics, however, deteriorate for a cavity depth of 0.05c, as the drag coefficient rises without any significant increase in lift coefficients, resulting in degradation of aerodynamic efficiency by 8% to 35%.

The augmentation in the lift coefficient in the post-stall regime is due to the periodic vortex shedding from the surface of the airfoil at a higher angle of attack. Various phases of the periodic vortex shedding $\alpha = 16^o$ for an airfoil with a cavity of depth 0.025c are shown in Fig. 5.2. As can be seen in Fig. 5.2 (a), a

single clockwise primary vortex spans the entire suction surface with no other coherent structure near it. At this phase of the vortex shedding cycle, a counter-clockwise vortex has been shed from the trailing edge and the clockwise vortex visible has acquired maximum strength, generating high suction a peak value for the lift coefficient. As time progress, a small anticlockwise vortex can be seen gaining strength at the trailing edge, in Figs. 5.2 (b) to (e). The anticlockwise vortex at the trailing edge seems to gain strength as some vortices as continuously shed from the primary clockwise vortex, which weakens. At ϕ = 0.5, as shown in Fig 5.2 (f), a clockwise vortex has been shed from the primary vortex and the suction on the airfoil is minimum with the lowest lift coefficient values. As the anticlockwise vortex is shed and the primary vortex gains strength, the lift value increases again as can be seen in Fig. 5.2 (g)-(j).

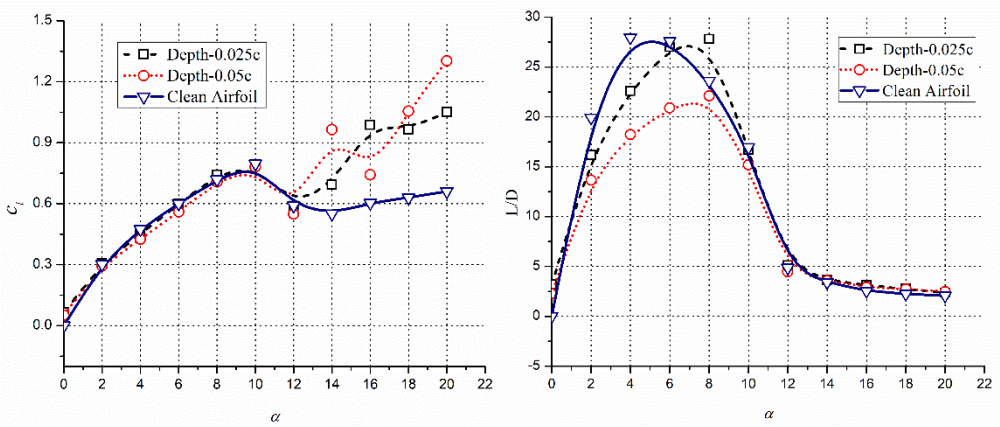

(a) Lift coefficient versus α *(b) Time-averaged L/D versus α*

Figure 5.1: Aerodynamic characteristics of NACA0012 airfoil with a cavity at 0.10c on the suction surface

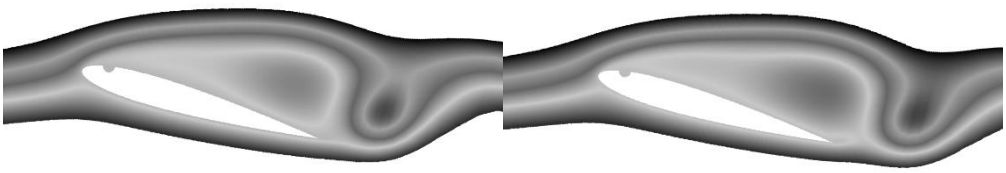

(a) ϕ = 0.1,c_l = 1.074 *(b) ϕ = 0.2, c_l = 1.0725*

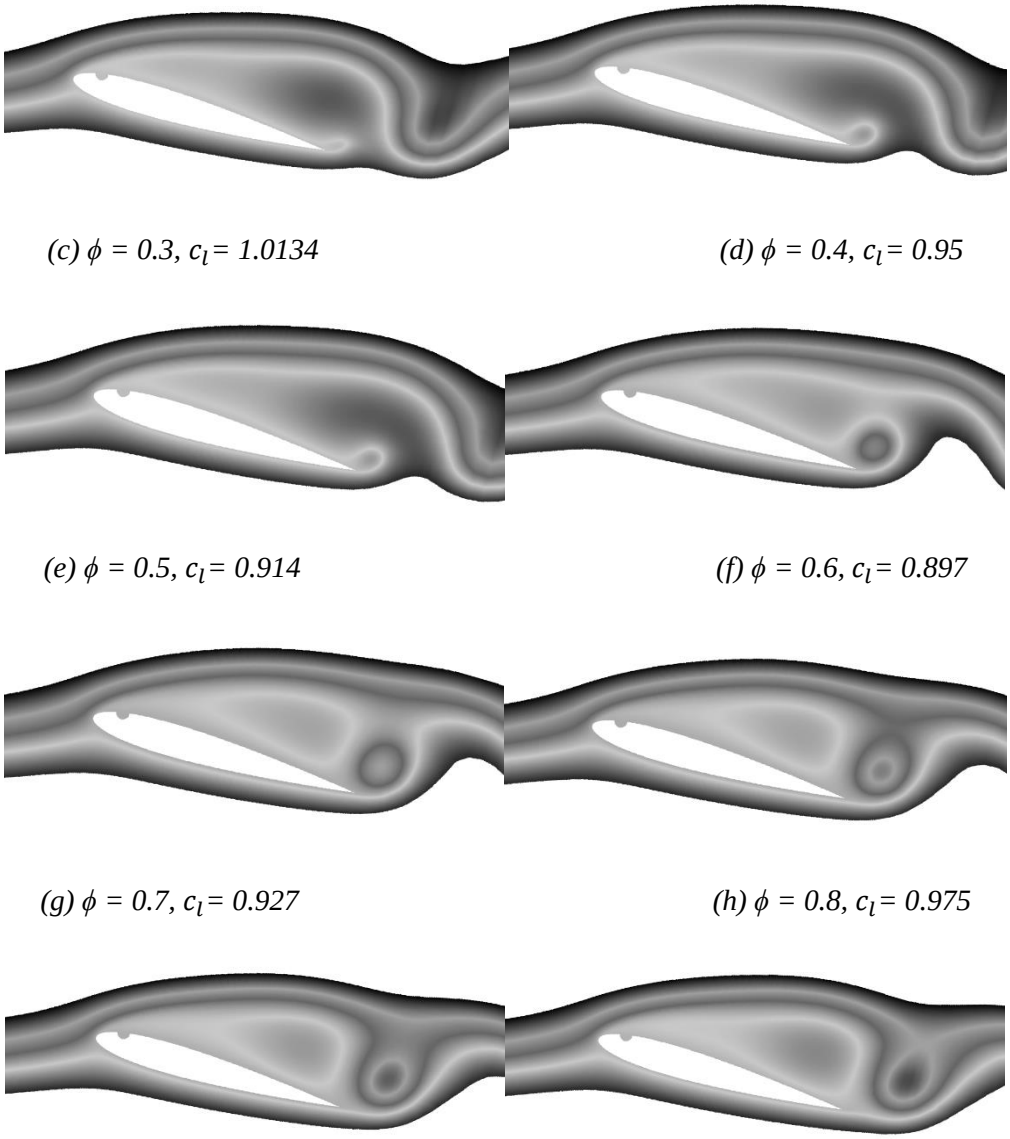

(c) ϕ = 0.3, c_l = 1.0134

(d) ϕ = 0.4, c_l = 0.95

(e) ϕ = 0.5, c_l = 0.914

(f) ϕ = 0.6, c_l = 0.897

(g) ϕ = 0.7, c_l = 0.927

(h) ϕ = 0.8, c_l = 0.975

(i) ϕ = 0.9, c_l = 1.02

(j) ϕ = 1.0, c_l = 1.074

Figure 5.2: Aerodynamic Characteristics of NACA0012 airfoil with cavity depth 0.025c at 0.10c location

Besides a positive lift at α = 0°, caused by flow unsteadiness, the lift-curve does not seems to be affected by the presence of a cavity. This is because the flow separated at the start of the cavity reattaches as a turbulent flow for all AOAs below α= 10°, and both cavity depths, as can be seen in Fig. 5.3. Because of the transition to turbulence, the flow on the suction surface remains attached in the pre-stall regime and the airfoil behaves similarly to the clean configuration. For

a deeper cavity of 0.05c depth, the flow transition occurs inside the cavity as can be seen in Fig.5.3 (c)-(d). For a cavity depth of 0.025c, a reduction in drag coefficient is observed at α = 8°, which makes the *L/D* ratio for the airfoil with a cavity, higher than the one for clean configuration at this AOA. The shifting of maximum L/D towards higher AOAs, as can be seen in Fig. 5.1 (b), for smaller cavity depth, is due to the transition of flow into turbulent, making the flow attached as reducing the wake width. For the deeper cavity, however, the turbulent separation occurs immediately after the cavity as can be seen in Fig. 5.3 (d). This increases the profile drag and hence reduces the aerodynamic efficiency in the pre-stall regime as well.

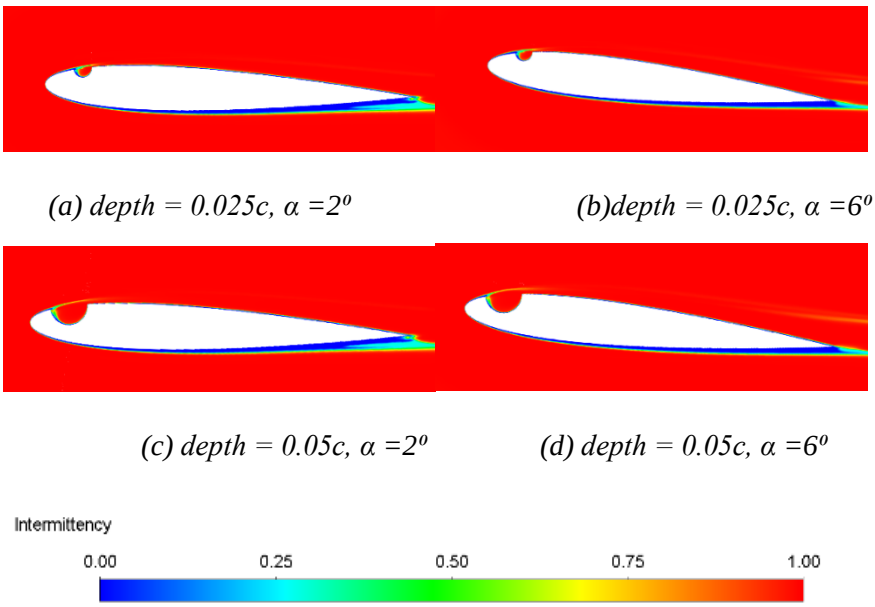

Figure 5.3: Intermittency contours for an airfoil with a circular cavity at 0.1c, on the suction surface.

As the AOA is increased, the vortex shedding creeps in, sooner for the larger cavity of 0.05c depth. The modes of vortex shedding are quite different at different AOAs, based on the nature of the separated shear layer. At α = 14°, the instability is enunciated by the flow emanating from the cavity and the shear layer is transitional, causing the oscillation in the lift of the type shown in Fig. 5.4 (a). As the AOA is increased to α =16°, the flow inside the cavity is turbulent

and so is the shear layer emanating from it. This makes the vortex shedding and the consequent oscillations in the lift completely chaotic, as shown in Fig. 5.4 (b). As the AOA is further increased, the vortex shedding is dominated by the shear layer separated ahead of the cavity, which makes the vortex shedding and the oscillations in the lift to be transitional, as shown in Fig. 5.4 (c) and (d). The amplitude of oscillation, however, for an airfoil with a cavity is larger than for a clean airfoil.

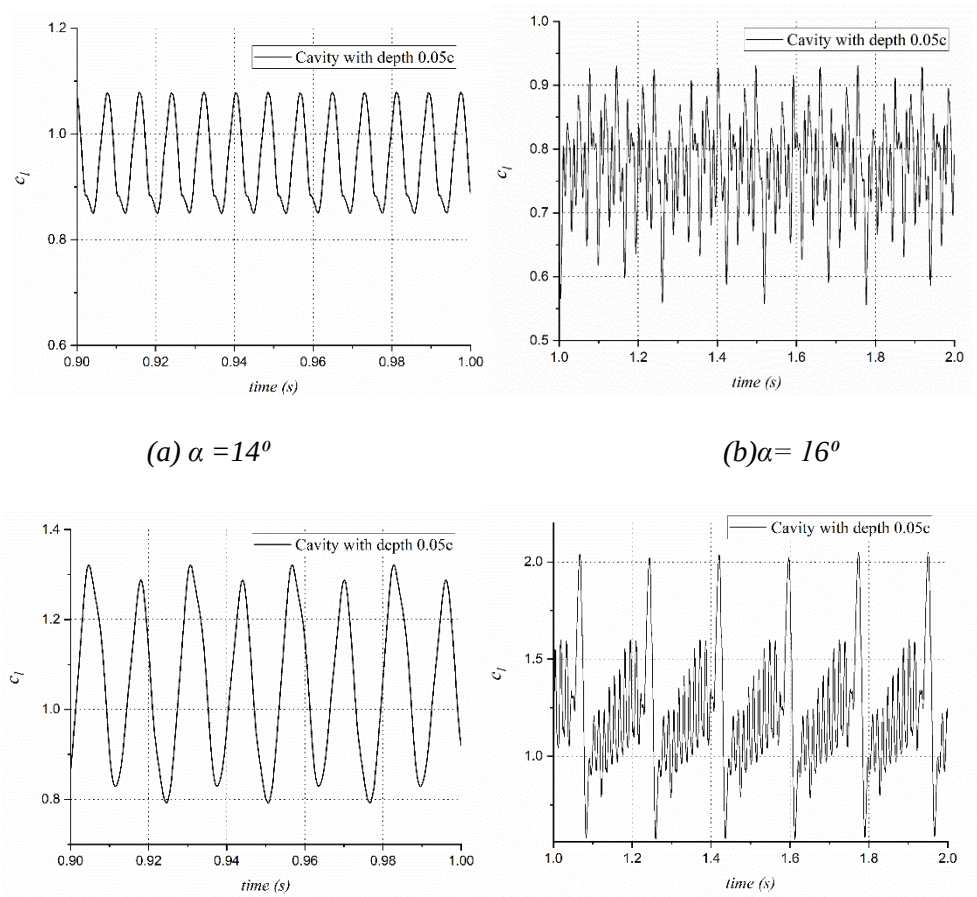

(a) α =14º *(b)α= 16º*

(c) α =18º *(d)α = 20°*

Figure 5.4: Lift coefficient versus time for the cavity depth 0.05c at 0.10c on the suction surface

5.1.2 CAVITY AT 0.25C LOCATION ON THE SUCTION SURFACE

The cavity located at 0.25c on the suction surface slightly degrades the aerodynamic lift of the airfoil small AOAs of α = 0°, 2°, and 4° as shown in Fig.

5.5 (a). The aerodynamic efficiency is, however, severely degraded in the pre-stall regime due to an increase in form drag of the airfoil, as can be seen in Fig. 5.5 (b).

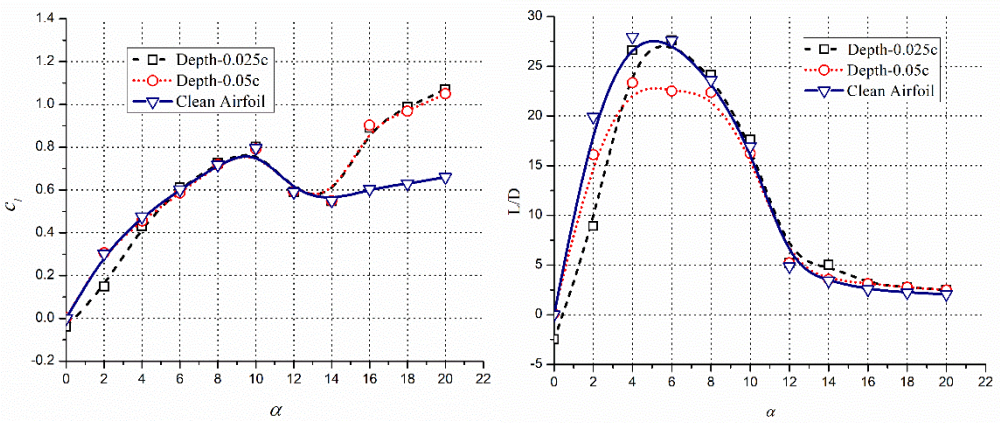

(a) Lift coefficient versus α *(b) Time-averaged L/D versus α*

Figure 5.5: Aerodynamic Characteristics of NACA0012 airfoil with a cavity at 0.25c location

The drop lift coefficient at α = 2° and 4°, due to the formation of tiny roll-up vortices on the suction surface of the airfoil, which causes flow unsteadiness as can be seen in Fig. 5.6. For a cavity of depth 0.025c, a vortex is formed inside the cavity of which is transitional. The flow outside the cavity, however, is largely unaffected by the cavity and remains laminar. The cavity acts as a source of vorticity and releases small roll-up vortices, which are laminar due to the outer laminar shear layer as can be seen in Figs. 5.7 (a) and (c). The periodic oozing out of eddies out the cavity and the subsequent shedding of these vortices makes the flow highly unsteady with the reduced time-averaged lift coefficient at α = 2° and 4°. For a larger cavity depth of 0.05c, at both AOAs, the flow inside the cavity is completely turbulent and the shear layer separated ahead of the cavity has a turbulent reattachment after the cavity as can be seen in Fig. 5.7 (b) and (d). The turbulent flow thereafter remains attached for the full length of the airfoil to give characteristics similar to a clean airfoil. As can be seen in Fig. 5.7 (c), the flow unsteadiness for cavity depth of 0.025c at α=4°, is small as compared to α=2° because of the transition of the boundary layer to turbulent

much before the trailing edge, causing turbulent separation thereafter with turbulent shedding of vortices.

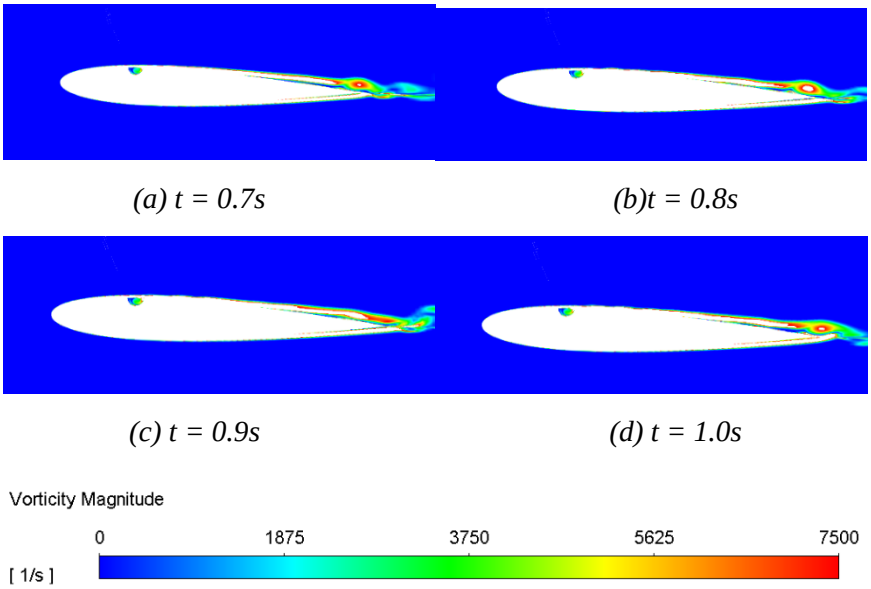

Figure 5.6*:* Vorticity magnitude of the cavity with depth 0.025c at 0.25c location at 2º

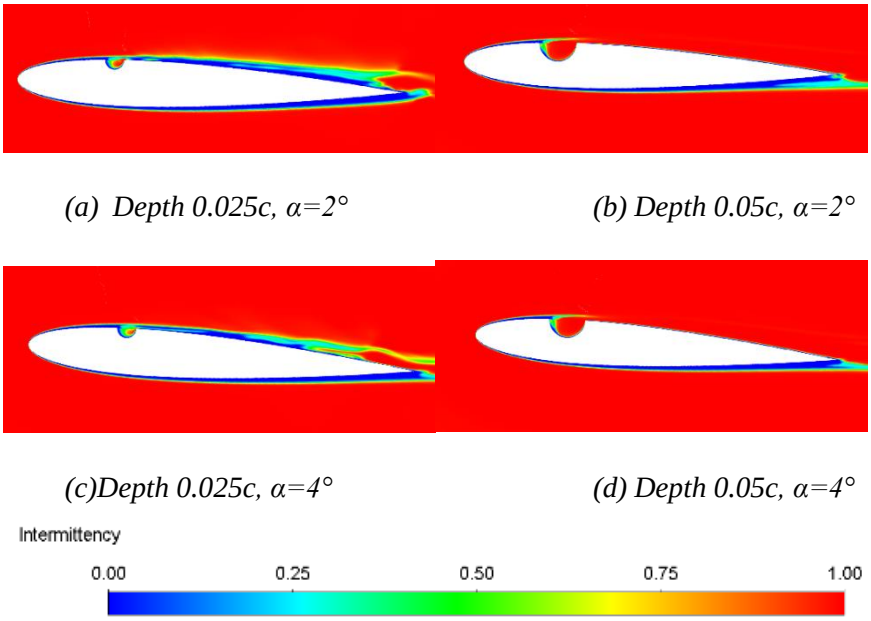

Figure 5.7: Intermittency in the flow for the cavity at 0.25c location

The laminar roll-up vortices for α =2°, for a cavity depth of 0.025c, can also be observed in the surface pressure distribution diagram shown in Fig. 5.8, and the

corresponding skin friction coefficient is observed in Fig. 5.9. Flow is attaching and separating as the roll-up vortices are creating on the surface of the airfoil. As can be seen in Fig. 5.8, the flow-field ahead of the cavity remains steady while the vortex shedding aft of 65% chord on the suction surface is responsible for the flow unsteadiness causing the lift value to dip down. The portion of the airfoil aft of 65%chord contributes to negative lift a considerable instant of time resulting in smaller time-averaged lift coefficient values shown in Fig. 5.5.

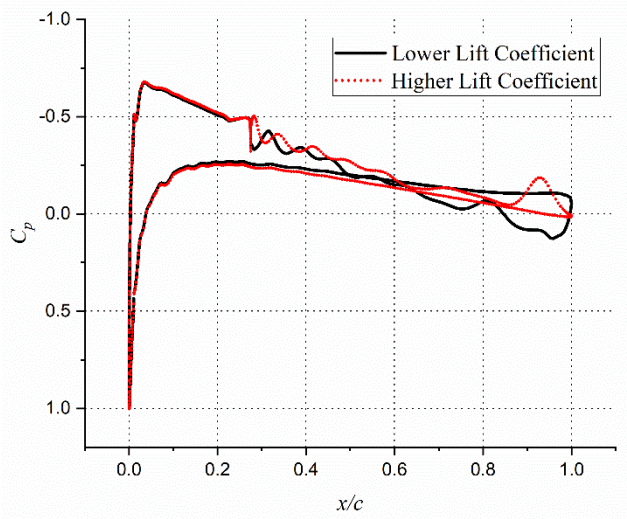

Figure 5.8: Pressure distribution over an airfoil at α= 2º, with the cavity of depth 0.025c, located at 0.25c on the suction surface

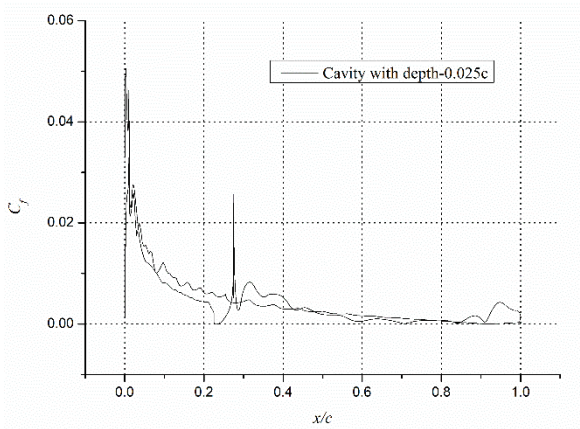

Figure 5.9: Skin friction over an airfoil at α= 2º, with the cavity of depth 0.025c, located at 0.25c on the suction surface

The shallow cavity destroys the lift at small AOAs, but it is the deeper cavity of depth 0.05c that causes an increase in drag coefficient with associated degradation in the aerodynamic efficiency. The lift coefficient and *L/D* values are reduced by 15% and 56% respectively at α =2° while they are reduced only by 4.5% and 5% at α =4°, for a cavity depth of 0.025c. As with other unsteady cases at high AOAs, improvements in time-averaged lift coefficients are observed for vortex-dominated lift regimes with vigorous vortex shedding. In the post-stall regime, the time-averaged lift is augmented by 28.7%, 36%, and 41% at α =16°, 18°, and 20° respectively. Resultant *L/D* ratios are also improved slightly compared with the clean airfoil configuration in the post-stall regime.

As stated above the deeper cavity does not affect the lift much in the pre-stall regime due to transition to turbulence, but the drag rises significantly because of turbulent separation aft of cavity. This causes reductions of up to 20% in the *L/D* values in the pre-stall regime. In the post-stall regime, the flow is chaotic for the deeper cavities resulting in bluff body vortex shedding from the airfoil. The time-averaged lift values are increased by 30%, 34%, and 39% at α = 16°, 18°, and 20°, which the L/D values increased.

5.1.3 CAVITY AT 0.50C LOCATION ON SUCTION PRESSURE

The effect of a circular cavity located at 0.5c, on the aerodynamic efficiency is similar to the effect of a cavity located at 0.25c on the suction surface as can be seen in Fig. 5.10. As with the cavity at 0.25c, severe flow unsteadiness with the reduced time-averaged lift coefficient is observed at α =2°, and 4°, for a cavity depth of 0.025c. The flow unsteadiness observed for these cases is because of the laminar nature of the shear layer up to the trailing edge of the airfoil. The shedding of the laminar roll-up vortices at α = 2° and 4°, causes a reduction of 8% and 10% in lift coefficient and drops 22% and 7% in *L/D* values respectively.

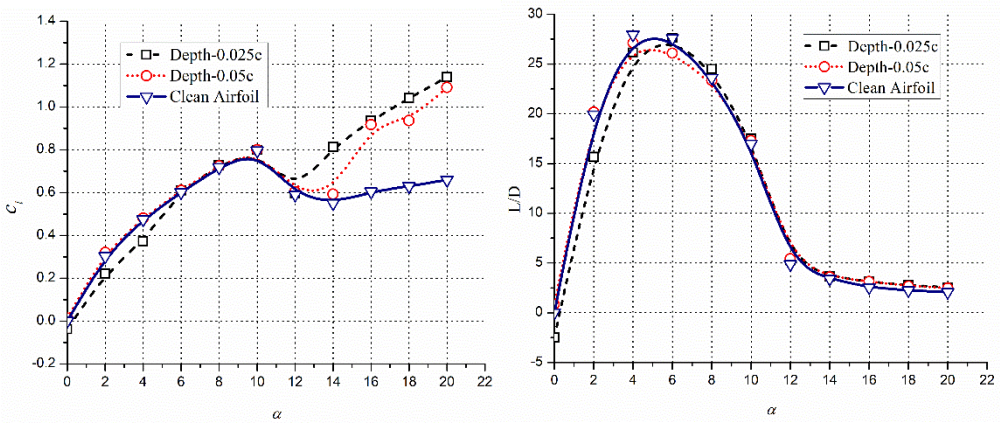

(a) Lift coefficient versus α *(b) Time-averaged L/D versus α*

Figure 5.10: Aerodynamic Characteristics of NACA0012 airfoil with a cavity at 0.50c location

These reductions in lift coefficient are not observed for a cavity depth of 0.05c, as the laminar flow upstream of the cavity transitions to turbulent inside the cavity and continues as turbulent flow aft of the cavity, as can be seen, Fig. 5.11. This reduces the chances of separation at small AOAs, and the aerodynamic characteristics resemble that for a clean airfoil. This turbulent flow, however, separates near the trailing edge, as shown in Fig. 5.11 (b), causing some loss in lift and a corresponding increase in drag. The result is a reduction in aerodynamic efficiency by 3%, 6%, and 2% at α = 4º, 6º, 8º.

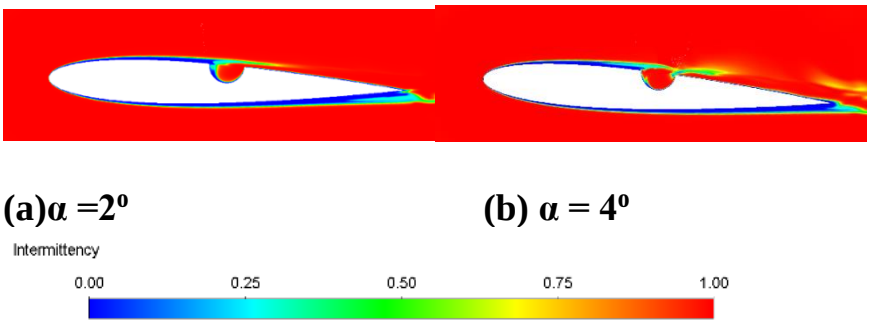

(a)α =2º **(b) α = 4º**

Figure 5.11: Intermittency in the flow for the cavity depth 0.05c at 0.50c location

In the post-stall regime, the vortex shedding and the oscillations in lift coefficient start as early as α = 14°. For a smaller cavity depth of 0.025, the vortex shedding is more conventional and similar to ones at higher AOAs as

can be seen in Figs. 5.12(a) and (b). For the deeper cavity at 0.5c, the vortex shedding is less severe due to the transition of a shear layer to turbulence as can be seen in Fig. 5.12 (c) and (d). For both the cavity depths, however, the flowfield change between two instantaneous configurations; the one for higher instantaneous lift and the other for lower instantaneous lift as shown in Fig. 5.12. When the primary vortex covers the entire suction surface, the suction pressure increases, which results in a higher lift coefficient. As time pass by vortex is shed from the surface of the airfoil and the primary vortex losses its strength resulting in loss of lift. The oscillation in a lift at α = 14° causes an increase of 52% in the time-averaged lift coefficient.

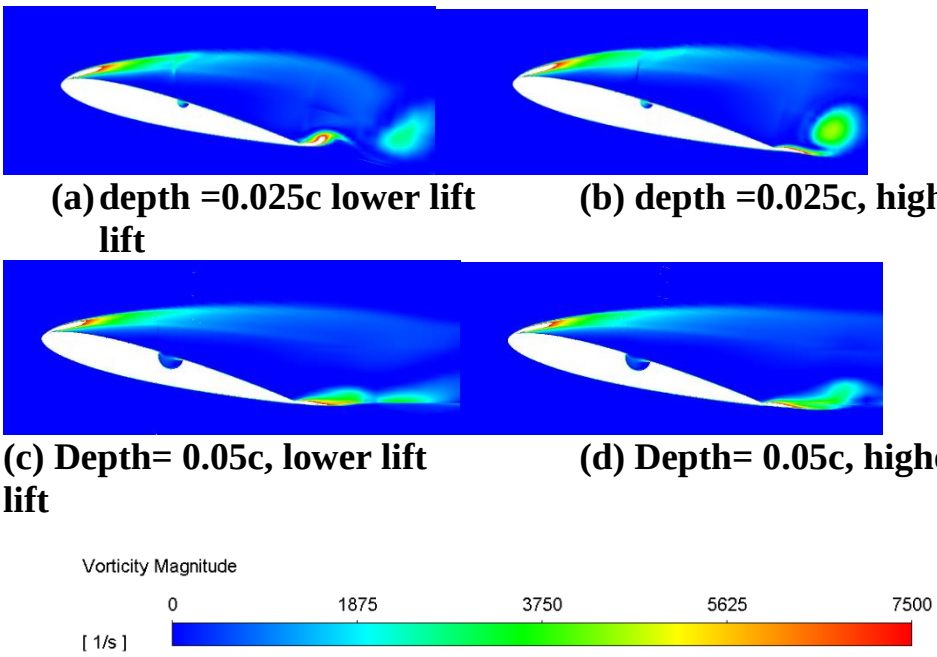

Figure 5.12: Vorticity contour over an airfoil at α = 14°, with a cavity at 0.5c location on the suction surface

5.1.4 EFFECT OF CAVITY ON STROUHAL NUMBER

The clean NACA 0012 also shows vortex shedding and oscillations in lift values at very small AOAs and AOAs higher than α = 16°, for a chord-based freestream Reynolds number of 10^5. From α = 16° onwards, the airfoil behaves similar to a bluff body and the Strouhal number varies from 0.2 at α = 16° to 0.12 at α = 20°, while at AOAs between α =0° and 4°, the vortex shedding occurs at higher

frequencies due to laminar instability with Strouhal number between 4.8 and 6.7. A circular cavity placed at 0.10c on the suction surface stabilizes the flow in the pre-stall regime reducing the vortex shedding the Strouhal number at α = 0° while eliminating oscillations in a lift at α = 2° and 4°, as can be seen in Fig. 5.13 (a). In the post-stall regime, the cavity at 0.01c adds the flow unsteadiness, enunciating the vortex shedding at α = 14°, for both cavity depths. The Strouhal number decreases with the increase in AOA, similar to clean configuration, but the Strouhal number for airfoils with cavity remains higher than the clean configuration at same AOAs, and lie between 0.17 and 0.5 as can be seen in Fig. 5.13 (a). For a deeper cavity of 0.05c depth, the Strouhal does not change with AOA, and the cavity just acts as a resonator.

A cavity located at 0.25c on the suction surface has a similar effect on the vortex shedding frequency, in the post-stall regime, similar to a cavity at 0.1c, as can be seen in Fig. 5.13 (b). The cavity, however, fails to enunciate a vortex shedding at α =14°, and the Strouhal number falls linearly from 0.7 at α =16° to 0.5 at α = 20°. At α = 20°, the shallower cavity, however, does not affect the Strouhal number much. In the pre-stall regime, the cavity at 0.25c location significantly reduces the vortex shedding frequency by assisting flow transition to turbulence. The deeper cavity at 0.25c eliminated the vortex shedding at α =2° and 4°, as can be seen in Fig. 5.13 (b) while reducing the Strouhal to 3.65 at α =0°. The shallower cavity diminishes the vortex shedding frequency significantly, from 3.65 at α = 0° to 1.4 at α =4°

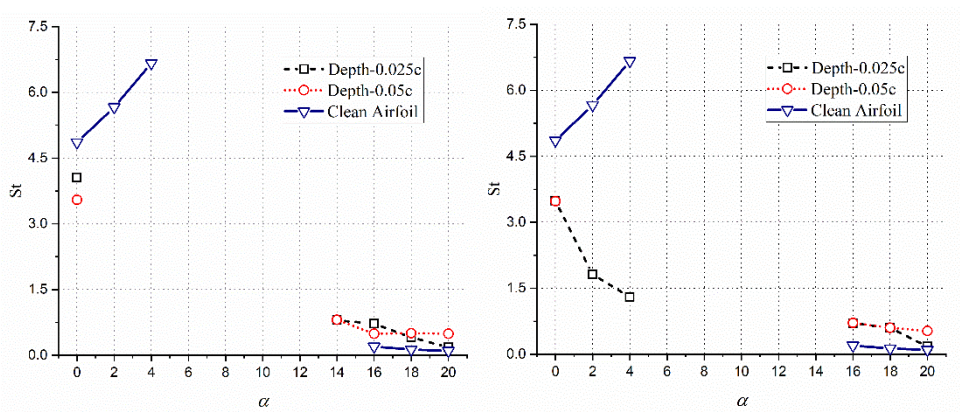

(a)0.10c Location **(b) 0.25c Location**

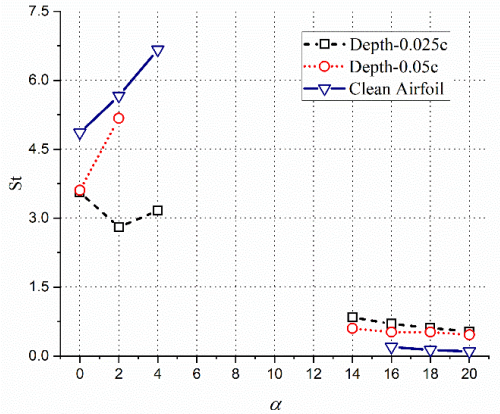

(c)0.50c Location

Figure 5.13: Strouhal Number for an airfoil with various cavities

The effect of the cavity at 0.5c on the suction surface is slightly different from those at 0.25c locations. At very low AOAs of α=0° and 2°, both cavities fail to eliminate vortex shedding, eliminate the vortex shedding at α = 4°, as can be seen in Fig. 5.12 (c). At α = 2°, the Strouhal for an airfoil with a deeper cavity is of the order of the clean configuration and even for shallower cavity the reductions in Strouhal number, observed for cavities at other locations, is not found. In the post-stall regime, the cavity at 0.5c location starts the vortex-shedding phenomenon at α = 14°, with very high Strouhal numbers of 0.84 and 0.6 for depths of 0.025 and 0.05 respectively. Unlike the cavity, at other locations, the shallower cavity at 0.5c location imparts larger flow unsteadiness as compared to a deeper cavity, with Strouhal numbers of 0.57 at α = 20°.

5.2 EFFECT OF CIRCULAR CAVITY AT REYNOLDS NUMBER 50000

5.2.1 EFFECT OF CIRCULAR CAVITY AT 0.10C LOCATION

For a lower Reynolds number of 50000, a circular cavity placed at 0.01c certainly improves the aerodynamic characteristics of NACA 0012 as can be seen in Fig. 5.14. For a cavity of depth 0.025c, vigorous flow unsteadiness is observed at AOAs of up to α = 6°, with marginally reduced time-averaged lift coefficient at α = 2°. For all other AOAs in the pre-stall regime, a slight

improvement in time-averaged lift coefficient is observed for a cavity depth of 0.025c.

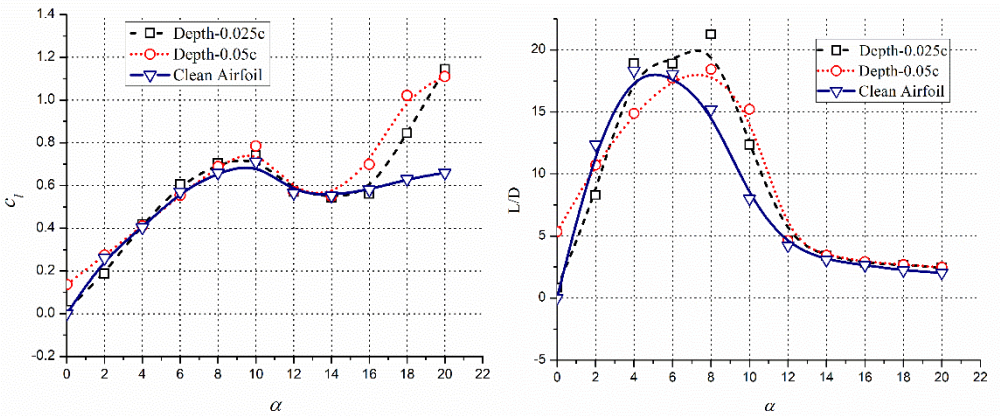

(a) Coefficient of Lift versus AOA *(b) L/D versus AOA*

Figure 5.14: Aerodynamic characteristics of an airfoil with a circular cavity at 0.10c location

The slight drop in lift coefficient value also reduces the aerodynamic efficiency slightly as the drag coefficient is unaffected by the cavity at these small AOAs. The aerodynamic efficiency of an airfoil with shallower cavity depth is, however, improved significantly at α = 6°, 8°, and10°, as can be seen in Fig. 5.14(b). A maximum enhancement of 54% in L/D ratio is observed at α =8° for the airfoil with the cavity of depth 0.025c. At α=12° and 14°, the aerodynamic characteristics of an airfoil with and without cavity at 0.1c are similar, irrespective of the depth of cavity. As the AOA is increased in the post-stall regime, bluff body vortex shedding sets in, with the higher time-averaged lift coefficients at α = 18° and 20°. The aerodynamic efficiency, however, remains unchanged between α=12° and α =20°, due to rise in drag between α =16° and 20°, both cavity depths.

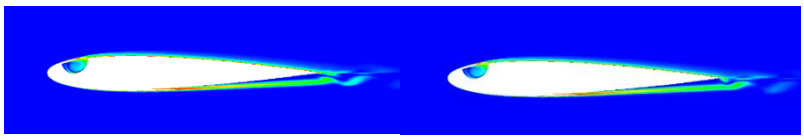

(a) t = 0.7s *(b) t = 0.8s*

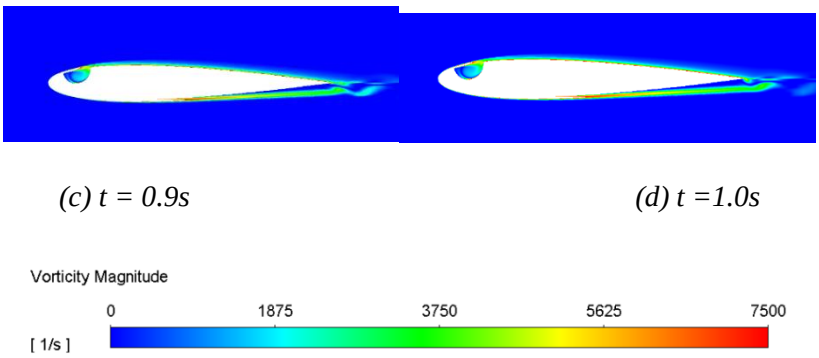

Figure 5.15: Vorticity contours over an airfoil at α = 0°, with a cavity of depth 0.05c, located at 0.10c

For a cavity depth of 0.05c, the significant positive lift is observed at α = 0° for the symmetrical airfoil. The primary reason for this positive lift at zero incidences is the trapped in the cavity as can be seen in Fig. 5.15. Besides having a trapped vortex, the flow on the pressure surface separates near the trailing edge forming roll-up vortices on the pressure side. This makes the flow on the suction surface completely attached up to the trailing edge with enhanced lift coefficient values. The shedding away of vortices from the pressure surface causes some unsteadiness in the flow-field, but a vortex remains trapped inside the cavity for all instances of time.

Despite no loss of lift at α = 4°, a significant loss of 19% in aerodynamic efficiency is observed due to a rise in drag at this AOA, for the deeper cavity. As the AOA is increased, the lift coefficients for an airfoil with a deeper cavity remain similar to those for a clean configuration. This is primarily because of the turbulent nature of the shear layer aft of the cavity, with no laminar instability as can be seen in Fig. 5.16 (b) and (d). For the shallower cavity, however, there is a laminar separation bubble formed aft of the cavity, followed by turbulent reattachment and multiple separations and reattachments downstream, at α=6°. At α = 8°, this unsteadiness reduces slightly due to the transition of a laminar shear layer into turbulent at an upstream location compared to α = 6°, as can be seen in Figs. 5.16 (a) and (c).

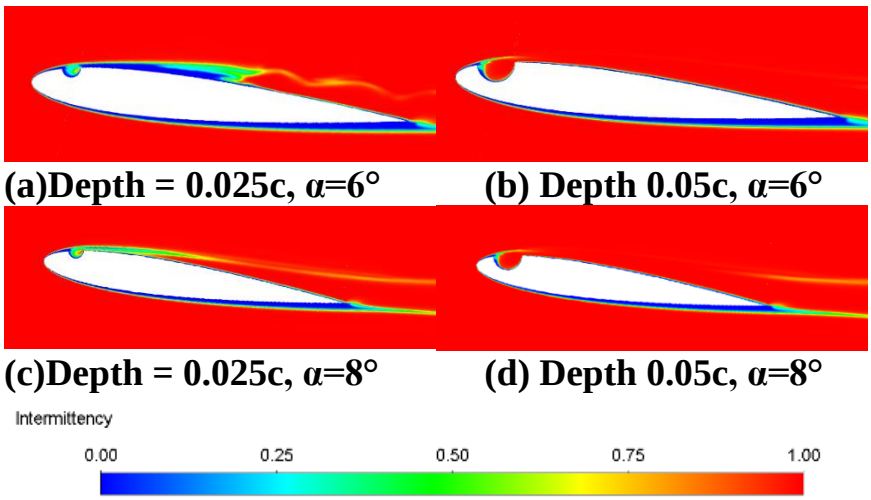

Figure 5.16: Intermittency contour for an airfoil with cavity located at 0.10c

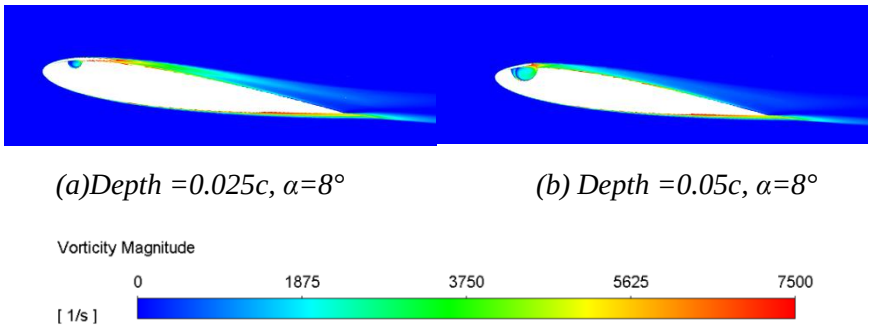

Figure 5.17: Vorticity contour for an airfoil with cavity located at 0.10c

The early transition of a shear layer into a turbulent one at α = 8°, for a shallower cavity, not only makes the flow steady but keeps the flow attached to the suction surface, all along as can be seen in Fig. 5.17 (a). This results in a significant reduction in profile drag with some improvement in a lift as well. The aerodynamic efficiency improves by 54% consequently. For airfoil with a deeper cavity at this AOA however, does not offer such a large improvement in aerodynamic efficiency, due to the early transition of the boundary layer into a turbulent one, increasing the viscous drag of the airfoil. The attached flow over an airfoil with a cavity of depth 0.05c at 0.1c location as can be seen in Fig. 5.17 (b). The trend reverses at α= 10°, wherein the deeper cavity offers improvements of 7.5% and 110% in the lift coefficient and aerodynamic efficiency respectively, while the shallower cavity offers only 54%

improvement in the *L/D* ratio with a marginal improvement in lift coefficient, as compared to the clean configuration. The reason behind these extreme improvements is the reduction in pressure drag of the airfoil due to the turbulent nature of the boundary layer, which remains attached up to the trailing edge. The aerodynamic characteristics of the airfoil do not change with the presence of cavity at 0.1c, for AOs between α= 12° and α=16°. The time-averaged lift coefficient at α = 18º and 20º improves by 26%, and 55%, with up to 20% increase in *L/D* ratio, due to vortex-dominated flow.

5.2.2 EFFECT OF CIRCULAR CAVITY AT 0.25C LOCATION

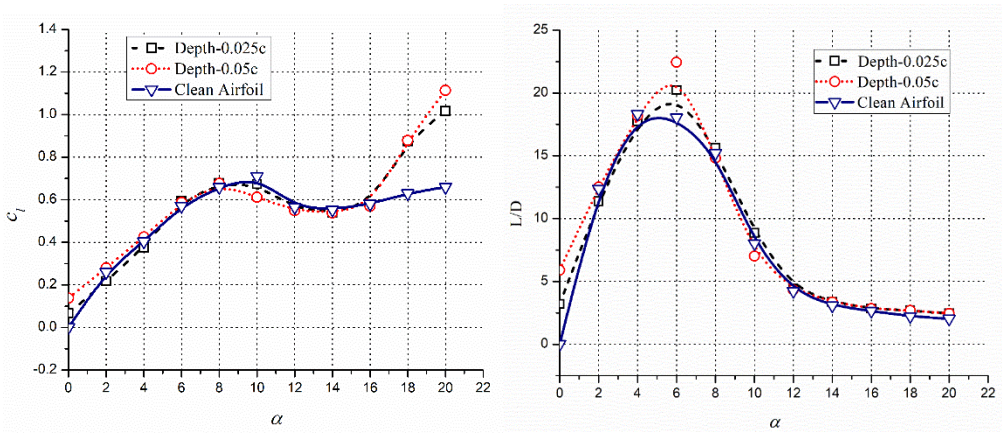

(a)Coefficient of Lift versus AOA *(b) L/D versus AOA*

Figure 5.18: Aerodynamic Characteristics of Circular Cavity at 0.25c location

The aerodynamics characteristics of an airfoil with a circular cavity at 0.25c is very similar to that of an airfoil with a circular cavity at 0.01c, at low AOAs, as can be seen in Fig 5.18. As with the airfoil with a cavity at 0.01c, the airfoil with a cavity at 0.25c also shows a positive time-averaged lift coefficient at α = 0º with increment in *L/D* value as well. The positive lift at α =0°, is a result of the asymmetry of the vortical structures on the suction and pressure surfaces as can be seen in Fig. 5.19. The laminar flow on the pressure surface separates well ahead of the trailing edge, while small roll-up vortices can be seen drifting towards the trailing edge on the suction surface. This creates flow unsteadiness as well for the airfoil with 0.025c depth cavity at α = 0°. For the deeper cavity,

however, there is no unsteadiness in the flow as the roll-up vortices are absent on the suction surface due to the transition of a shear layer into turbulent. The flow on the suction surface is completely attached while the separation can be observed on the pressure surface as shown in Fig. 5.20. This increase in lift comes with no drag penalty and the *L/D* ratio of 3.0 and 6.0 is observed of an airfoil with cavity depths 0.025c and 0.05c respectively, at an AOA of α = 0°.

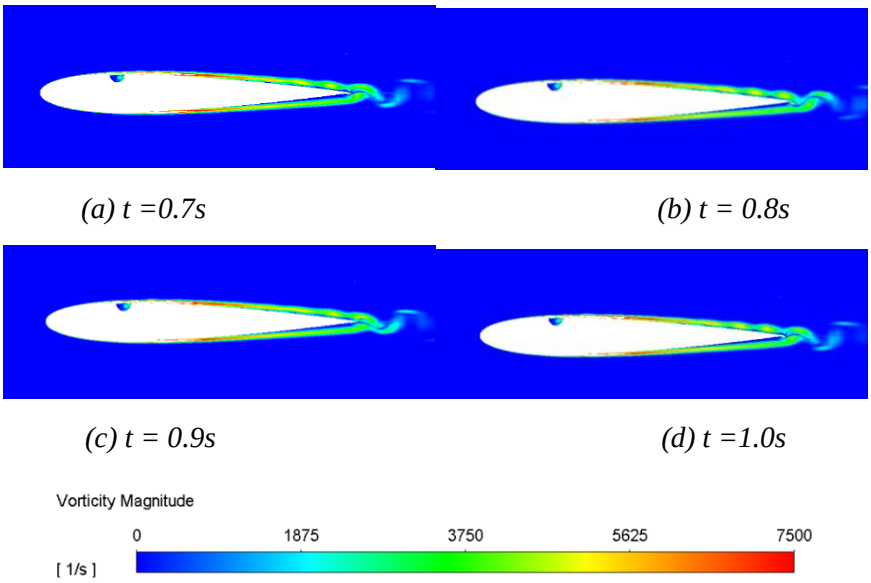

Figure 5.19: Vorticity contour for an airfoil with the cavity of depth 0.025c located at 0.25c, at α= 0°

The unsteadiness in the flow continues for airfoil the cavity of shallower depth, at α =2º, 4º and 6°, resulting in small reductions in time-averaged lift coefficient and L/D values at α = 2° and 4°. The flow unsteadiness seen for these AOAs, for a shallower cavity is because of the laminar nature of the shear layer, extending up to the trailing edge as can be seen in Fig. 5.21 (a) and (b). The presence of roll vortices on the suction surface reduces the viscous drag, and no loss in overall aerodynamic efficiency is observed.

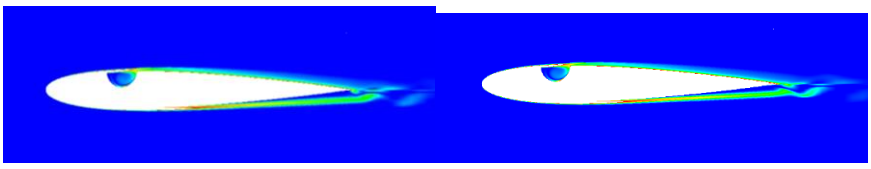

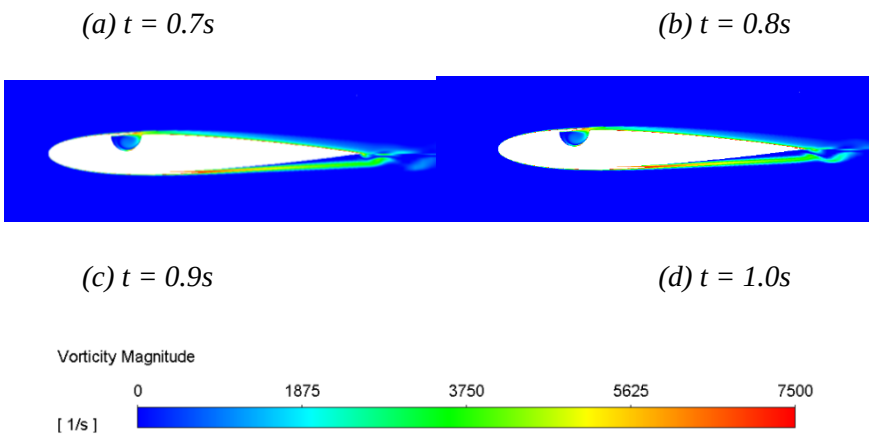

Figure 5.20: Vorticity contours for an airfoil with cavity depth 0.05c located at 0.25c, at α = 0°

As the AOA is increased, the transition of the separated shear layer takes place immediately aft of the cavity at α= 6° and before the cavity for α = 8°, as can be seen in Fig. 5.21 (c) and (d). The length of the laminar separation bubble formed near the leading edge shorten, giving lift coefficients values similar to those for the clean configuration up to α = 16°, except for α =8 °, for the deeper cavity. At α = 6°, the aerodynamic efficiency of the airfoil with a cavity at 0.25c is remarkably improved by 12% and 24% for depths of 0.025c and 0.05c respectively, as can be seen in Fig. 5.18 (b).

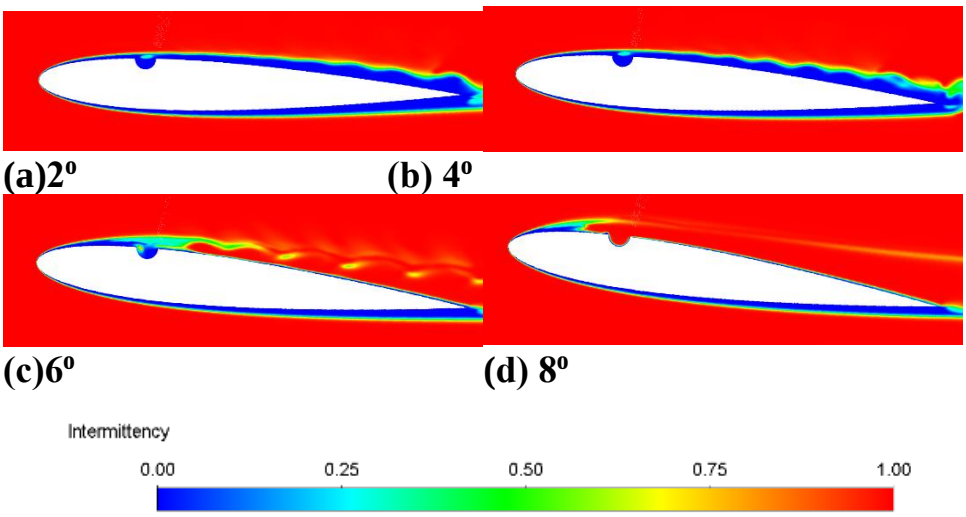

Figure 5.21: Intermittency for the cavity with depth 0.025c located at 0.25c.

These improvements in L/D values come with little increase in the lift coefficient and primarily because of the reduced drag of the configuration. As can be seen in Fig. 5.22, a series of small vortices can be observed rolling along with the suction for an airfoil with a shallower cavity at α = 6°. These roll-up vortices formed aft of the cavity, besides enhancing suction, reduces the skin friction due to multiple separations and reattachment reducing the skin friction drag of the configuration. For the deeper cavity, these roll-up vortices are absent as the transition of the shear layer takes place immediately after the cavity a can be seen in Fig. 5.23. The turbulent boundary layer remains attached to the suction surface all along, reducing the pressure drag significantly, causing an overall enhancement in the L/D ratio.

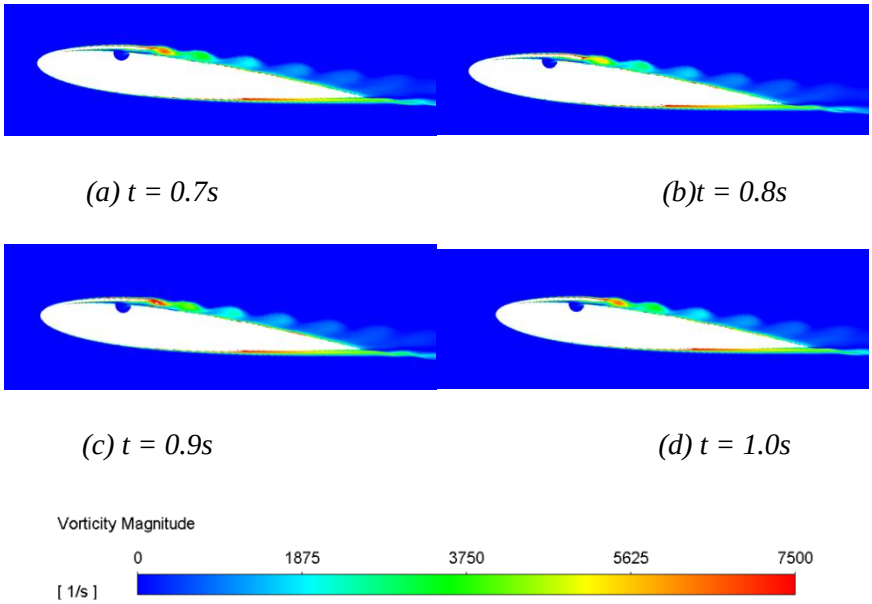

(a) t = 0.7s *(b)t = 0.8s*

(c) t = 0.9s *(d) t = 1.0s*

Figure 5.22: Vorticity magnitude over an airfoil with cavity depth 0.025c located at 0.25c, at 6°

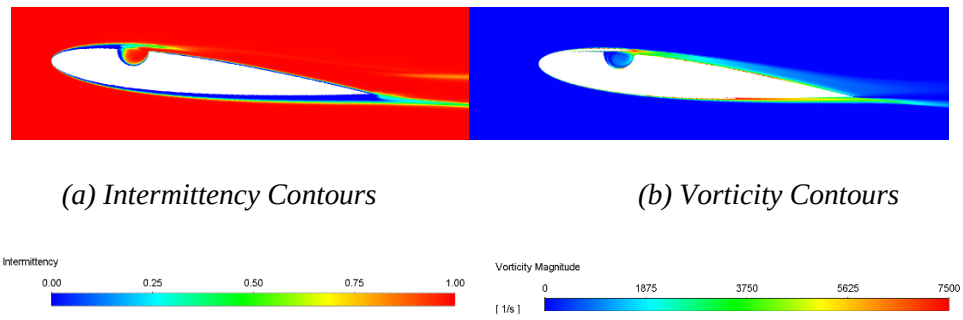

(a) Intermittency Contours *(b) Vorticity Contours*

Figure 5.23: Contours of intermittency and vorticity magnitude over an airfoil with cavity depth 0.05c, located at 0.25c, at α =6°

In the post-stall regime, no major unsteadiness in the flow is observed for AOAs up to α =16°, and the time-averaged lift coefficient values and L/D values for configuration with a cavity of either depth, are similar to those of the clean airfoil. The vorticity contours for an airfoil with a cavity at 0.25c, for an AOA of α = 16° is shown in Fig. 5.24, which clearly shows small-scale vortex shedding. The different contours show instantaneous vortical structure when the lift value is at its peak and minima during the vortex shedding cycle. At α = 18° and 20°, vigorous bluff body vortex shedding is enunciated with enhancements in the lift coefficient values by 24% and 35.7% respectively, for the shallower cavity of depth 0.025c. These increments in lift values become 29%, and 52% respectively, at α=18° and 20°.

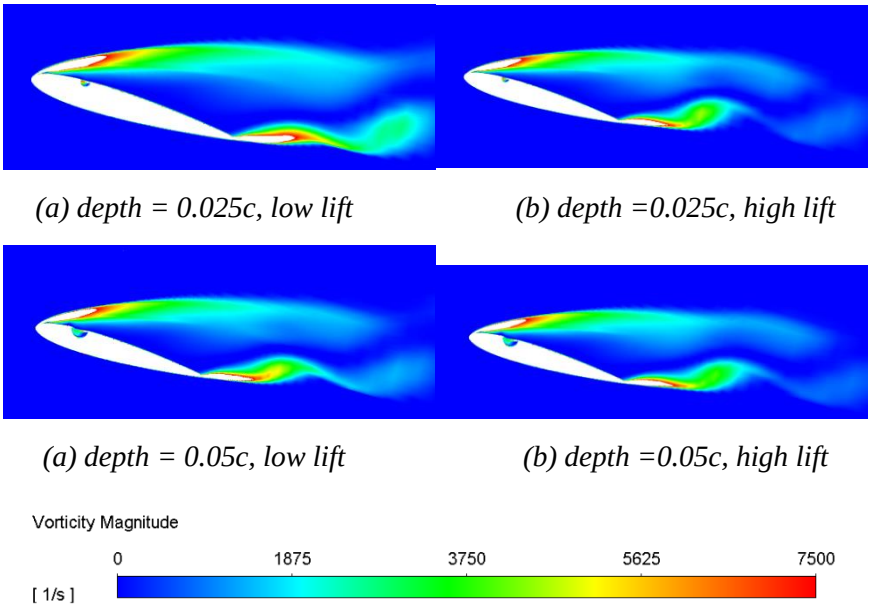

(a) depth = 0.025c, low lift *(b) depth =0.025c, high lift*

(a) depth = 0.05c, low lift *(b) depth =0.05c, high lift*

Figure 5.24: Vorticity contours over an airfoil with a cavity at 0.25c, at α = 16°

5.2.3 EFFECT OF CIRCULAR CAVITY AT 0.50C LOCATION

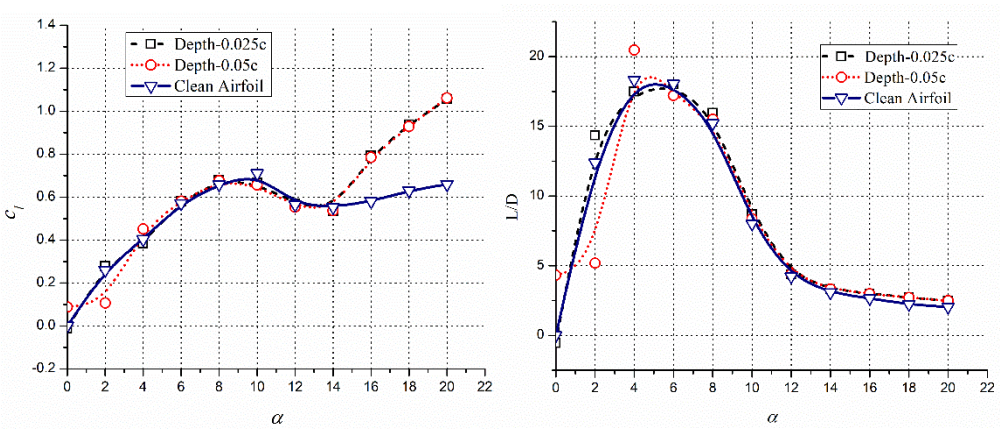

(a) Coefficient of Lift versus AOA *(b) L/D versus AOA*

Figure 5.25: Aerodynamic characteristics of an airfoil with a circular cavity at 0.5c location on the suction surface

The effect of a circular cavity at 0.50c location on the suction surface on the aerodynamic characteristics is similar to the effects of the cavity at 0.25c location as can be seen in Fig. 5.25. As with the former case, the airfoil with a cavity at 0.5c show high degree of unsteadiness at low AOAs of α = 0°, 2°, and 4°, especially for smaller depth. The phenomenon behind this unsteadiness and positive lift at α = 0°, has been discussed earlier. For a cavity depth of 0.025c, the time-averaged lift curve overlaps the time-averaged curve for the clean airfoil up to an AOA of α =14°. For the deeper cavity, however, a severe degradation in a lift and aerodynamic efficiency is observed at α = 2°. The degradation in aerodynamic characteristics at α = 2°, is due to multiple laminar separations and reattachments on the suction aft of the cavity, forming multiple hairpin vortices as can be seen in 5.26.

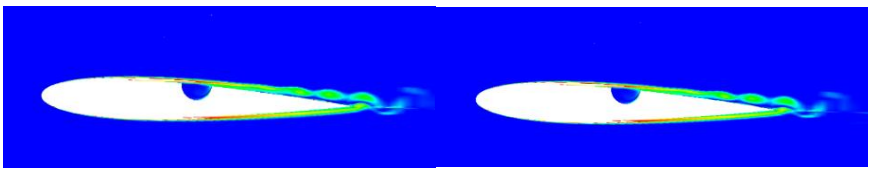

(a) t = 0.7s *(b) t = 0.8s*

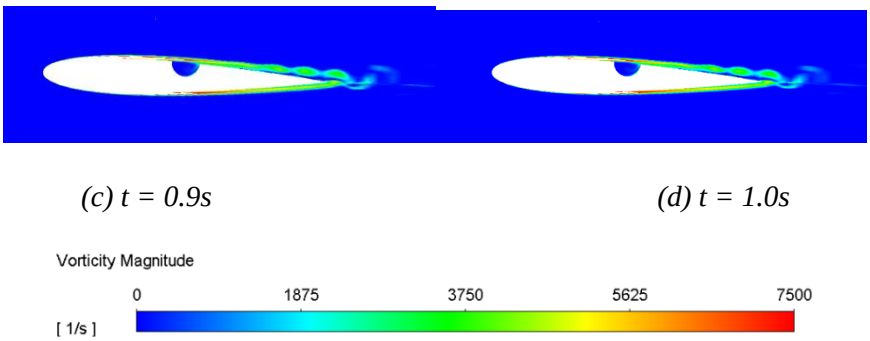

(c) t = 0.9s *(d) t = 1.0s*

Figure 5.26: Vorticity contour over an airfoil with cavity depth 0.05c located at 0.50c, at α =2°

These laminar hairpin vortices, which are separated from the surface, destroys the lift besides augmenting flow unsteadiness. The degradation in the lift coefficient and L/D values are 15% and 59% respectively at α =2º. However, as the AOA is increased to α = 4°, the transition of the shear layer takes place immediately aft of the cavity as can be seen in Fig. 5.27. The separated shear layer aft of the cavity reattaches at a turbulent flow and there multiple turbulent separations and reattachment at α =4°. These turbulent eddies are very close to the surface and more coherent reducing the viscous drag significantly. The result is a favorable enhancement in the aerodynamic efficiency of the airfoil. The vorticity contours for airfoil at α = 4°, with a deeper cavity at 0.5c location, are shown in Fig. 5.28. This figure clearly shows the vortices, very close to the surface for all instances of time, giving enhanced lift and reduced drag, observed.

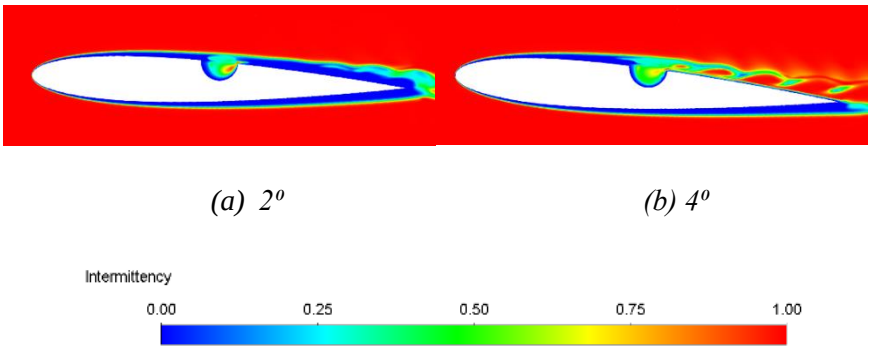

(a) 2º *(b) 4º*

Figure 5.27: Flow intermittency for the cavity depth 0.05c located at 0.50c

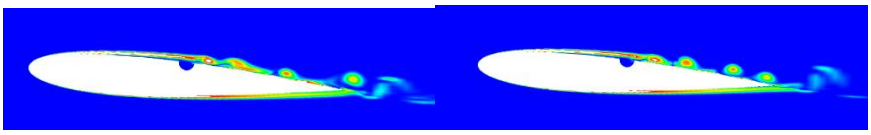

(a) depth = 0.025c, t = 0.7s *(b) depth = 0.025c, t =1s*

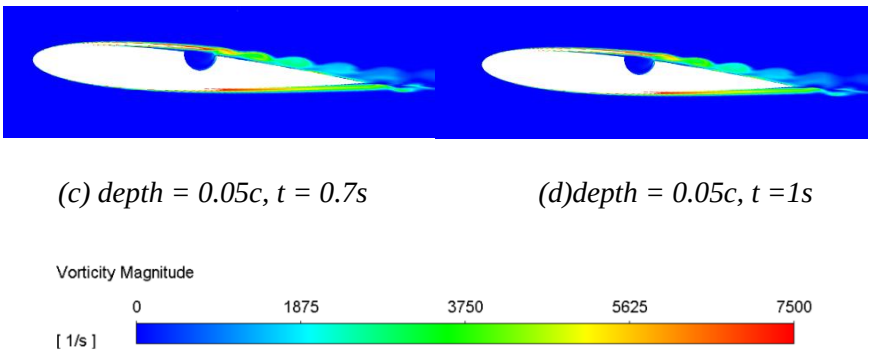

(c) depth = 0.05c, t = 0.7s *(d)depth = 0.05c, t =1s*

Figure 5.28: Vorticity contour for an airfoil with cavity located at 0.50c, at α = 4°

As the AOA is increased beyond α =14°, large-scale vortex shedding starts, and time-averaged lift value is improved, for both cavity depths at 0.5c location on the suction surface. The time-averaged lift coefficient values are improved by up to 40.3% in the post-stall regime, improvement in the aerodynamic efficiency by 22%, at this high AOAs.

5.2.4 EFFECT OF CIRCULAR CAVITY ON STROUHAL NUMBER

The flow around NACA 0012 at a low Reynolds number of 50000 is inherently unsteady at low AOAs due to the formation of laminar separation bubble and roll-up vortices. A cavity of depth 0.025c, located at 0.1c location, enhances the vortex shedding frequencies at α = 0° and 2°, but diminishes the Strouhal number slightly at α = 4°, as can be seen in Fig. 5.29 (a). The cavity, however, enunciates vortex shedding at α = 6°, with a Strouhal number of 2.5, which is not observed for the clean airfoil.

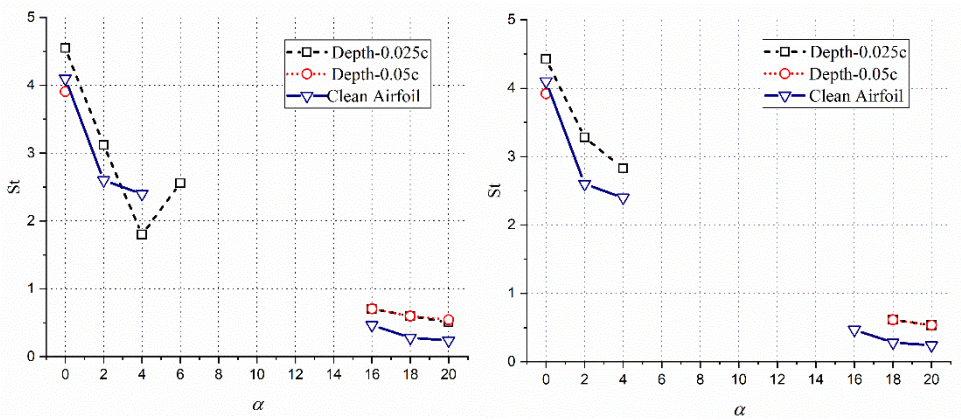

(a) 0.10c location *(b)0.25c location*

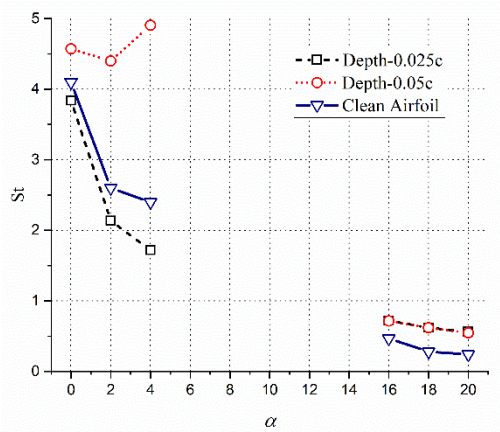

(c)0.50c location

Figure 5.29: Strouhal number for an airfoil with a circular cavity at Re = 50000

The deeper cavity located at 0.1c on the suction surface eliminates the vortex shedding and fluctuations in lift values at all small AOAs other than zero incidences. The deeper cavity eliminates the vortex shedding even when placed at a 0.25c location on the suction surface as can be seen in Fig. 5.29 (b). The reduction in vortex shedding frequencies is because of the transition of the shear layer aft of the cavity. The shallower cavity on the other hand enhances the vortex shedding frequencies at α = 0°, 2°, and 4°, even more, when placed at 0.25c location. The cavities placed at 0.5c location, however, harm the Strouhal numbers as can be seen in Fig. 5.29 (c). As can be seen in Fig. 5.29 (c), the cavity with a depth of 0.025c diminishes the vortex shedding frequencies at AOAs of α= 0°, 2°, and 4°, whereas the deeper cavity enhances the vortex shedding frequencies at these AOAs. At α =4°, the shallower cavity reduces the Strouhal number by 29% while the deeper cavity increases the Strouhal number by 100% when placed at mid-chord location on the suction surface. In the post-stall regime, the cavities affect similar to the protrusions and cavities at 10^5 Reynolds number. The cavities enhance the vortex shedding frequencies by a similar amount at α = 16°, 18°, and 20°, for all depths and locations. An exception is observed for the deeper cavity, which when placed at 0.25c location, eliminates the vortex shedding at α = 16°.

5.3 EFFECT OF TRIANGLE SHAPED CAVITY AT REYNOLDS NUMBER 10^5

The effect of cavities on the aerodynamic characteristics of NACA 0012 is investigated at a Reynolds number of 10^5. These cavities are right-angled triangles in shape and placed at either 0.1c, 0.25c, or 0.5c location on the suction surface. The depth of these cavities, which equal to the altitude of the right triangle, is either 0.025c or 0.05c, where c is the chord of the clean airfoil. The AOA of these configurations is varied between α= 0º to 20º with a 2º interval.

5.3.1 EFFECT OF TRIANGLE SHAPED CAVITY AT 0.10C LOCATION

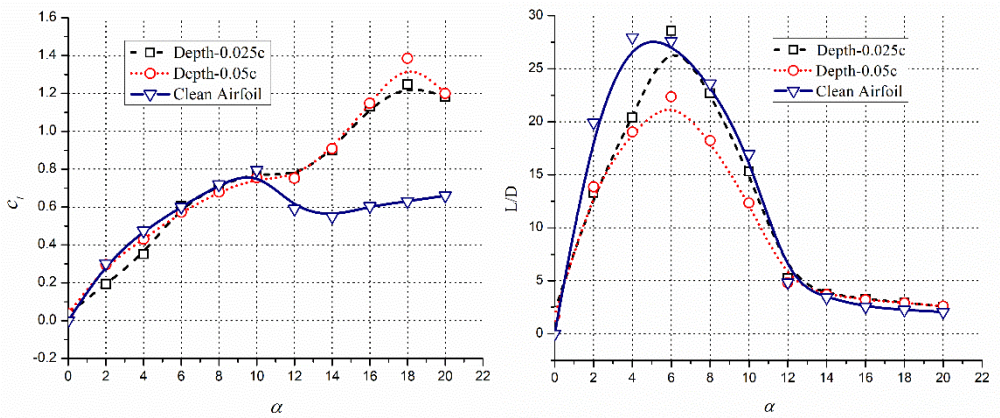

(a) Lift coefficient versus α *(b) Time-averaged L/D versus α*

Figure 5.30: Aerodynamic Characteristics of an airfoil with a triangular cavity at 0.10c location

Unlike a circular cavity at 0.1c location, a shallower triangular cavity of depth 0.025c deteriorates the aerodynamic lift and efficiency of the airfoil at α = 2° and 4°, as can be seen in Fig. 5.30. Besides losses in the time-averaged lift and *L/D* values, the flow at these AOAs is highly unsteady with oozing out of vortices from the cavity at 0.1c location. For AOAs higher than α = 4°, the time-averaged lift value recovers to its clean airfoil values, especially for the shallower cavity. The lift curve for an airfoil with a cavity at 0.1c location, mostly overlaps the curve for clean configuration between α = 6° and 10°, with loss in a lift for deeper cavities. Even the aerodynamic efficiency of an airfoil with a shallower triangular cavity is similar to those for clean configurations in

this AOA range. For the deeper cavity, however, significant reductions in L/D ratio are observed for all AOA below α = 12°, despite only marginal reductions in the lift coefficients, suggesting a drastic rise in drag coefficients.

As the AOA is increased α =12° and beyond, severe vortex shedding sets in, causing a large oscillation of the instantaneous lift coefficient values. The time-averaged values of lift coefficients are, however, much higher than the ones for the clean configuration, for both cavity depths. The aerodynamic efficiency, however, remains unaffected by the presence of cavity at these high AOAs in the post-stall regime, due to an increase in drag. At AOAs of α = 2º and 4°, a vortex is trapped inside the cavity which is blown away periodically along the suction surface as can be seen Fig. 5.31. This causes a series of laminar bubbles on the suction surface for an airfoil with a shallower cavity. Although these bubbles cause local suction, adverse pressure gradient due to these bubbles destroy the overall suction of the upper surface causing a loss of lift along with severe flow unsteadiness. The decrements observed in the lift coefficient values at α =2° and 4° are 10% and 12% respectively while the resultant decrements in L/D values are 34% and 28% respectively at these AOAs.

(a) Small bubbles at time 0.7s

(b) Small bubbles at time 0.8s

(c) Small bubbles at time 0.9s

(d) Small bubbles at time 1.0s

Figure 5.31: Small separation bubbles on the surface of the airfoil with cavity depth 0.025c at 0.10c location, at α = 4º

For a deeper cavity of 0.05c located at 0.1c however, the shear layer separated at the cavity has a turbulent reattachment aft of the cavity. The boundary layer aft of the cavity is thus turbulent and there are no laminar separation bubbles for the airfoil with a deeper cavity, as seen in Fig. 5.31. This destroys the unsteadiness in the flow besides keeping the flow attached to the surface for a longer period. The lift values for the airfoil with a deeper cavity at 0.1c are thus similar to the clean configuration at these small AOAs.

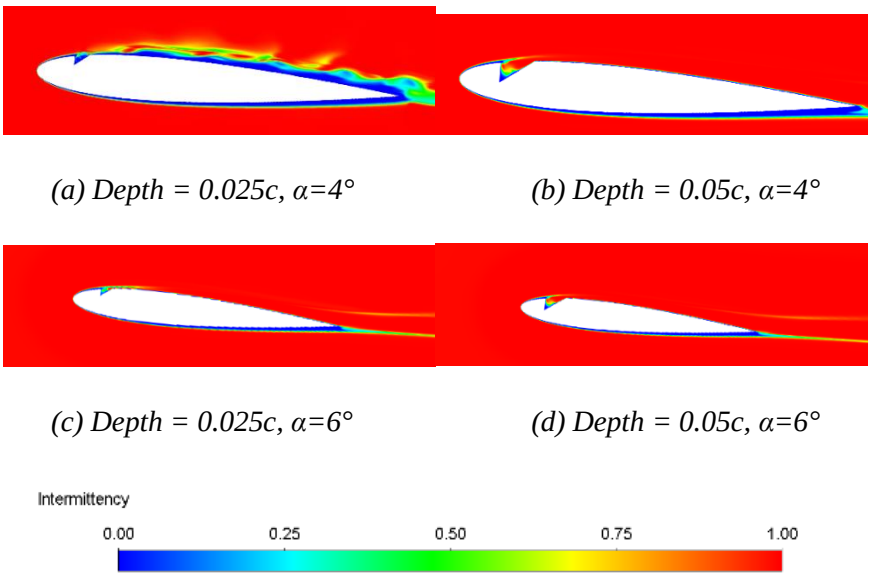

(a) Depth = 0.025c, α=4° *(b) Depth = 0.05c, α=4°*

(c) Depth = 0.025c, α=6° *(d) Depth = 0.05c, α=6°*

Figure 5.32: Intermittency for the cavity at 0.10c location at 4º

As the AOA is increased to α= 6° and beyond, even the shallower cavity turns the shear layer into turbulent. The transition of the shear layer however occurs at some distance aft the cavity as can be seen in Fig. 5.32 (c). For the deeper cavities, the transition occurs inside the cavity and the flow aft of the cavity is

turbulent. Turbulent separation occurs for the deeper cavity at all AOAs other than α =0°, increasing the pressure drag and reducing L/D ratios significantly at all AOAs below α = 12°. For the airfoil with a shallower cavity at α = 6°, however, the turbulent separation occurs very close to the trailing edge as can be seen in Fig. 5.33 (a). This reduces the pressure drag of the airfoil enhancing the L/D ratio, by 3.5%. This trend continues for higher AOAs as well. However, for the deeper cavity, the turbulent separation occurs at an upstream location causing a wider wake as seen in Fig. 5.33 (b). This reduces the aerodynamic efficiency of the airfoil significantly in the range of AOAs between α = 2° and 10°, for the deeper cavity. As the AOA is increased to α =12°, severe vortex shedding is enunciated causing fluctuations in lift coefficient values with the enhanced time-averaged lift coefficient values irrespective of the cavity depth, as can be seen in Fig 5.30 (a). The L/D values are however unchanged due to the corresponding increase in drag of the airfoil.

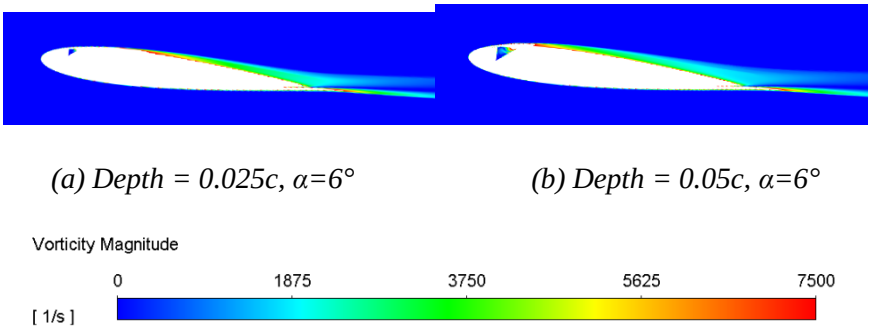

(a) Depth = 0.025c, α=6° *(b) Depth = 0.05c, α=6°*

Figure 5.33: Vorticity contours for an airfoil with a cavity at 0.1c location

Interestingly the conventional stall is not seen for an airfoil with a triangular cavity at 0.1c, due to enhancement of lift at α =12°. At AOAs between α = 12° and 20°, enhancements in the time-averaged lift coefficient values of 35% - 80%, are observed with increments of 2% to 16% in the L/D ratios.

5.3.2 EFFECT OF TRIANGLE SHAPED CAVITY AT 0.25C LOCATION

In the pre-stall regime, the effect of a triangular cavity located at 0.25c, on the airfoil lift and aerodynamic efficiency is similar to the effect of a circular cavity at the same location and Reynolds number, and similar to the triangular cavity

at 0.1c location. The loss in lift seen at α =2°, for circular cavity at 0.25c location and triangular cavity at 0.1c, is not observed for the airfoil with a triangular cavity at 0.25c. As can be seen in Fig. 5.34 (a), for a cavity depth of 0.025c, the time-averaged lift coefficient at α = 2° and 4° are reduced by 2% and 10% respectively due to the formation of laminar bubbles all along the suction surface. The L/D ratios, however, are degraded less as compared to the circular cavity at the same location and even compared to a triangular cavity at 0.1c location, as can be seen in Fig. 5.34 (b).

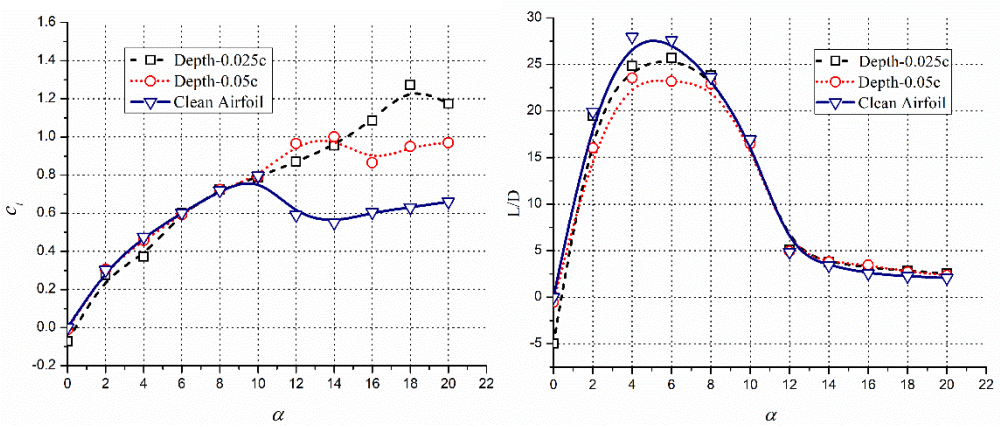

(a) Lift coefficient versus α *(b) Time-averaged L/D versus α*

Figure 5.34: Aerodynamic Characteristics of NACA0012 airfoil with a cavity at 0.25c location

A contrasting difference in the lift curve of an airfoil with a circular cavity at 0.25c and one with a triangular cavity at 0.25 can be observed between α=10° and α =14°. While the lift curve of an airfoil with circular at 0.25c location follows the trend of clean airfoil up to α = 14°, with significant loss of lift at both α=12° and 14°, the lift curve of an airfoil with a triangular cavity at 0.25c shows no stall. The lift for the latter increases almost linearly from its value at α =10° to the values at α=18° especially for the shallower cavity. The increments in lift observed are, however, highly unsteady due to vortex shedding. The magnitude of fluctuations in the lift coefficients for a cavity at 0.25 is higher than observed for a cavity at 0.1c. Nevertheless, the lift coefficients are enhanced by 28% to 64% with a corresponding increase in the

L/D values by 2 % to 13%, in the AOA between α=12° and 20°. For the deeper triangular cavity at 0.25c, there is no reduction in the lift coefficient values in the pre-stall regime but decrements in the L/D values between 5.2% to 27%, are observed. The absence of the stall at α =12º, and the oscillations in the flow from this AOA onwards, increases the lift coefficient without any drop in *L/D* values.

The loss of lift and the flow unsteadiness observed at α = 4°, for a shallower cavity of 0.025c depth is demonstrated through Fig. 5.35. The small size of the cavity is insufficient to cause the transition of the shear layer into turbulence. The flow in the vicinity of the airfoil at α = 4° remains completely laminar for the shallower cavity as can be seen in Fig. 5.36 (a). The instability in the laminar shear layer results in information multiple small separation bubbles aft of the cavity, which destroys the suction on the airfoil. As these vortical structures are pushed downstream and ultimately fed into the wake, the instantaneous flow structure over the airfoil change, as can be seen in Fig. 5.35. This causes the observed unsteadiness in the flow. The presence of these small bubbles, however, reduces the skin friction drag of the airfoil, and the result is a less significant loss in aerodynamic efficiency.

For the deeper cavity at α = 4° however, the transition of the shear layer occurs at the cavity, and flow aft of the cavity is completely turbulent as can be seen in Fig. 5.35 (b). The turbulent boundary layer resists the separation and formation of bubbles and thus there is no loss of lift as compared to the clean configuration. However, the same turbulent boundary layer causes an increase in the skin friction drag of the airfoil deteriorating the aerodynamic efficiency of the airfoil significantly.

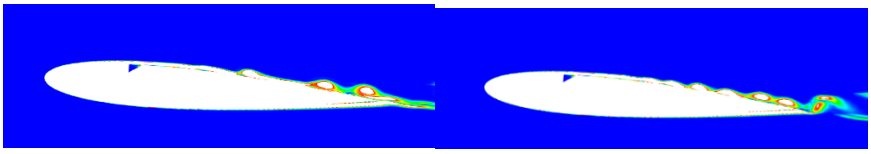

(a) t = 0.7s **(b) t = 0.8s**

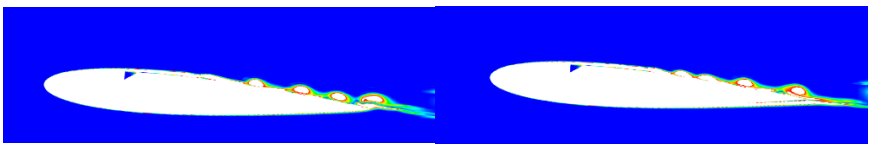

(c) t = 0.9s **(d) t =1.0s**

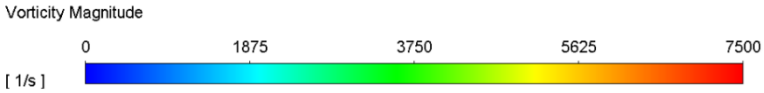

Figure 5.35: Vorticity contours over an airfoil with the cavity of depth 0.025c located at 0.25c, at α = 4°

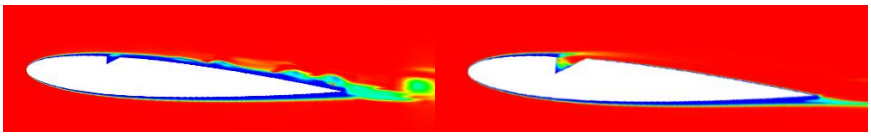

(a) Depth 0.025c *(b) Depth 0.05c*

Figure 5.36: Intermittency over an airfoil with a triangular cavity at 0.25c location, at α = 4°

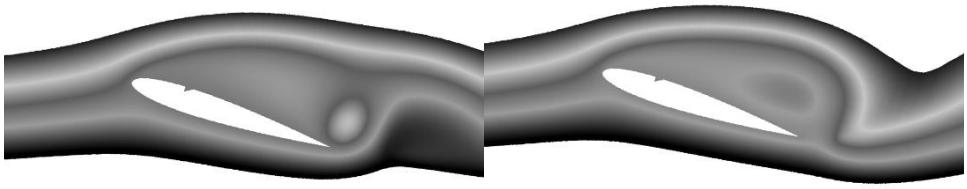

(a) Lower lift *(b) Higher lift*

Figure 5.37: Instantaneous vortex structure for airfoil with cavity depth 0.05c at the location 0.25c at α = 18º

A deeper cavity with depth 0.05c at 0.25c location leads to extreme unsteadiness in the flow due to vigorous vortex shedding. Even at α =12°, the unsteadiness causes an increase of 37.5% in C_l values. For an AOA of α =18°, even the shallower cavity causes a severe vortex shedding enhancing the time-averaged lift coefficient value to 100% more than the peak time-averaged lift for the clean airfoil. Typical instantaneous vortical structures for an airfoil with a triangular cavity of depth 0.05c are shown in Fig 5.37. These two vortical structures are

captured for the instances when the lift is at its minimum and maximum respectively.

5.3.3 EFFECT OF TRIANGLE SHAPED CAVITY AT 0.50C LOCATION

The effect of a triangular cavity located at 0.5c on the suction surface, on the lift values of the airfoil, is very similar to that of a triangular cavity at 0.25c location, in the pre-stall regime. The effects in the post-stall regime, however, are significantly different for the cavities at two different locations at a Reynolds number of 10^5 as can be seen in Fig. 5.38 (a). Unlike the airfoil with a circular cavity at 0.5c or a triangular cavity at a 0.25c location, for an airfoil with a triangular cavity at 0.5c, a positive time-averaged lift is observed. For the shallower cavity of depth 0.025c, the reductions in lift coefficient at $\alpha = 2^o$ and 4° are 3% and 9.8% respectively with consequent reductions of 4% and 6% in the L/D values. The reductions in lift coefficients observed at these AOAs are similar to those for triangular cavity at 0.25c. Even the *L/D* are very similar to those for the clean airfoil, especially for the shallower cavity, as can be seen in Fig. 5.38 (b).

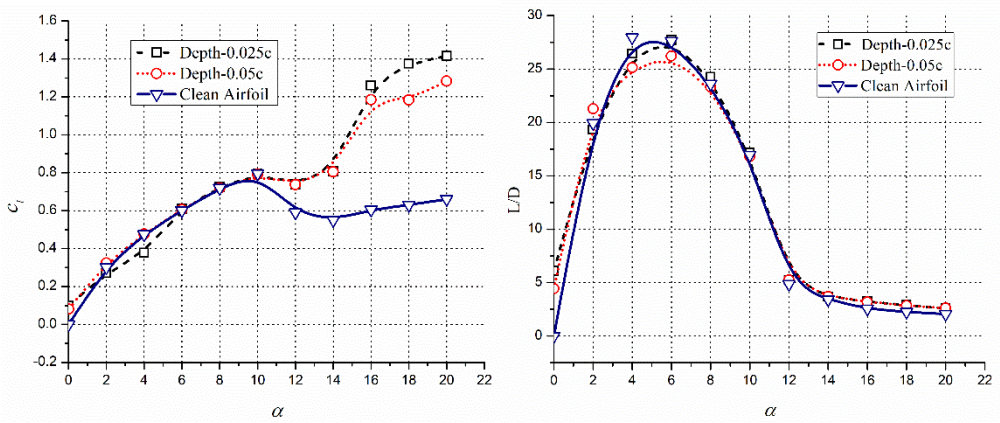

(a) Lift coefficient versus α *(b) Time-averaged L/D versus α*

Figure 5.38: Aerodynamic Characteristics of NACA0012 airfoil with cavity at 0.50c location

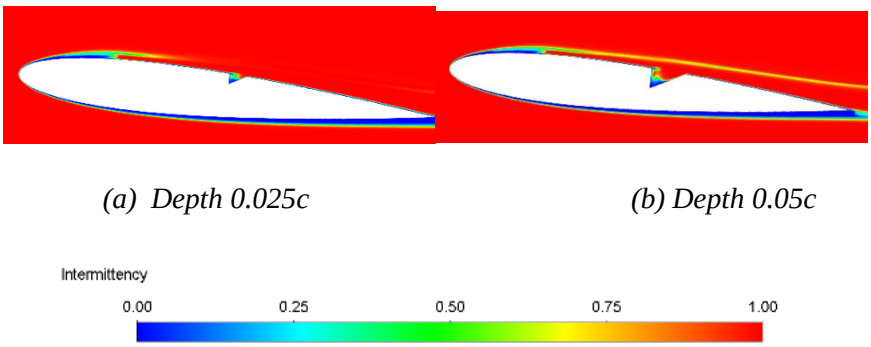

(a) Depth 0.025c *(b) Depth 0.05c*

Figure 5.39: Intermittency for the cavity at 0.50c location, at 6º

The similarity in lift coefficient observed suggests the ineffectiveness of the cavity to influence the size of the laminar separation bubble as can be seen in Figs. 5.39 (a) and (b). For both cavity depths, on the airfoil at α=6°, the shear layer turns turbulent well ahead of the cavity. The turbulent separation for the deeper cavity, however, occurs at an upstream point as compared to the shallower cavity. This makes the pressure drag for the deeper cavity slightly higher with a reduced L/D ratio as observed in Fig. 5.38 (b). As the angle of attack is increased from α = 10°, which is the stalling angle of the clean airfoil, the lift coefficient values diminish marginally at α =12°, for both cavity depths. The typical stall has seen for the clean airfoil, however, is absent and the lift values at α = 12° and 14° are smaller than for airfoil with a triangular cavity at 0.25c. Nevertheless, the lift coefficient values increase monotonically from α = 12° to α =20°. Another contrasting result as compared to an airfoil with a triangular cavity at 0.25c, is the absence of severe flow unsteadiness, at α = 12° and α = 14°. As can be seen in Fig. 5.40, the vortex shedding phenomenon is observed for α =12°, for both cavity depths. The size of the vortices shed, however, is very small with a smaller amplitude of fluctuations in lift values, especially for the shallower cavity at 0.5c location.

(a) Lower lift, depth = 0.025c *(b) Higher lift, depth = 0.025*

(a) Lower lift, depth = 0.05c *(b) Higher lift, depth = 0.05c*

Figure 5.40: Instantaneous vortical structures over an airfoil with cavity located at 0.50c, at α = 12°

For the deeper cavity, the size of the vortices shed from the airfoil increase slightly cause a larger fluctuation in lift coefficient values. The increment in time-averaged lift coefficient values seen at α = 12° and 14°, is due to the smaller size of the separation bubble near the leading edge, and the formation of a primary clockwise vortex, aft of the cavity, which enhances the suction all along the suction surface as can be seen in Fig. 5.41. The distribution of the skin friction coefficient is similar to the for clean airfoil ahead of the cavity inside the cavity, flow is separated as seen in Fig. 5.42 (a). The smaller size of the laminar separation bubble observed is due to the early transition of the shear into turbulent because of the cavity. At AOAs between α = 14º to α = 20º, improvements in the time-averaged lift values of 26% to 75.5% are observed. The increment in time-averaged C_l values is due to the dominance of vortex lift, as explained earlier. The C_l values are at low when a fully developed counter-clockwise vortex sits on the trailing edge, generating a locally high suction at the trailing edge as can be seen in Fig. 5.43 (a). The C_l value becomes extremely high when the counter-clockwise vortex is shed away and the primary vortex on the suction side spans the whole surface producing higher suction as can be seen in Fig. 5.43(b). In Fig 5.42 (b), skin friction coeffient over an airfoil has been seen, separated flow is visible near the trailing edge as the vortex is shedding from the surface. For the deeper cavity at 0.5c, the time-averaged lift coefficient values are also improved by 14.8%, 26%, 58%, 55.4%, 62.3% at the AOAs of α = 12º, 14º, 16º, 18º and 20º respectively, due to vortex dominated flow-field.

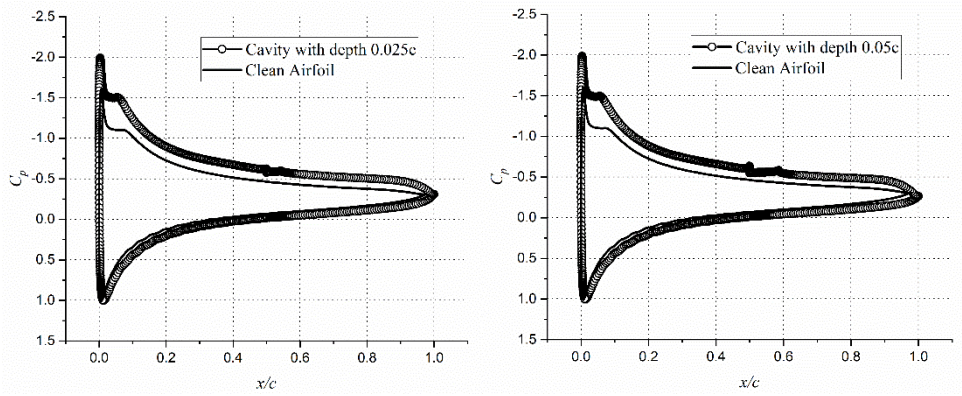

(a) Cavity depth = 0.025c *(b) Cavity depth = 0.05c*

Figure 5.41: Pressure distribution over an airfoil with cavity located at 0.50c, at α = 12°

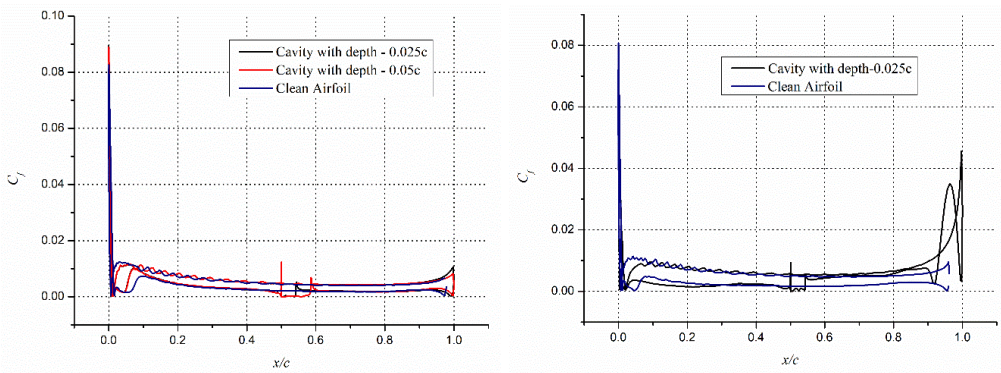

(a) α = 12° *(b) α = 16°*

Figure 5.42: Skin friction over an airfoil with cavity located at 0.50c, at α = 12°

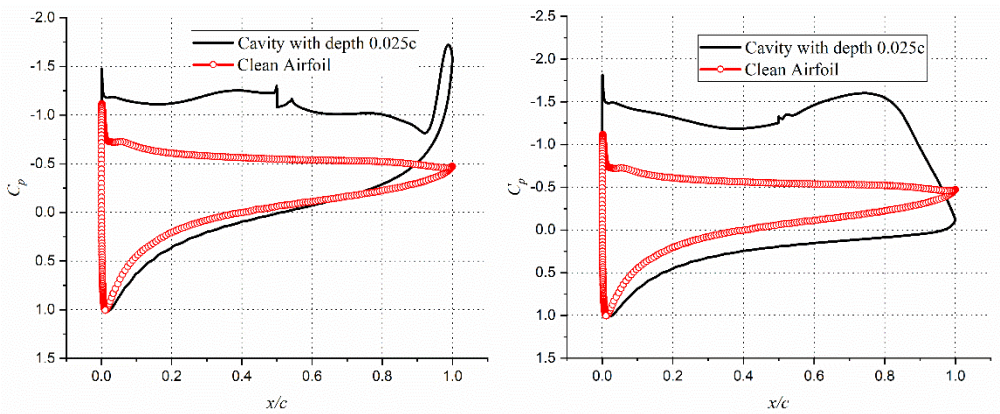

(a) Lower lift coefficient *(b) Higher Lift coefficient*

Figure 5.43: Pressure distribution for minimum and maximum lifts by airfoil cavity with depth = 0.025c, at α = 16º

5.3.4 EFFECT OF TRIANGULAR CAVITY ON STROUHAL NUMBER

Flow over NACA 0012 at Re = 10^5 is inherently unsteady, at low AOAs due to laminar separation bubble and at high AOAs due to vortex shedding. In the pre-stall regime, the frequency of oscillations in lift values increases with increasing AOA while in the post-stall regime, the frequency of oscillations decreases with AOA. A triangular cavity at 0.1c location reduces the unsteady oscillations in lift coefficient values, but not as effective as a circular cavity at the same location on the airfoil. Both cavities at 0.1c location, fail to eliminate the severe flow unsteadiness at α = 0°. The deeper cavity, however, reduces the frequency of oscillations by 16% and can eliminate the vortex shedding at α = 2° and 4°, as can be seen in Fig. 5.44 (a). The shallower cavity at 0.1c on the other hand reduced the frequency of oscillations at α=2° and 4° significantly. In the post-stall regime, the presence of a triangular cavity at 0.1c enunciates a high-frequency vortex shedding at AOA as early as α = 12°. The Strouhal number at α = 12° and 14° remain equal to 0.7, for both depths. As the AOA is further increased, the frequency of oscillation reduces but the Strouhal numbers, which is much than those for the clean airfoil, remain independent of the cavity depth, as can be seen in Fig. 5.44 (b).

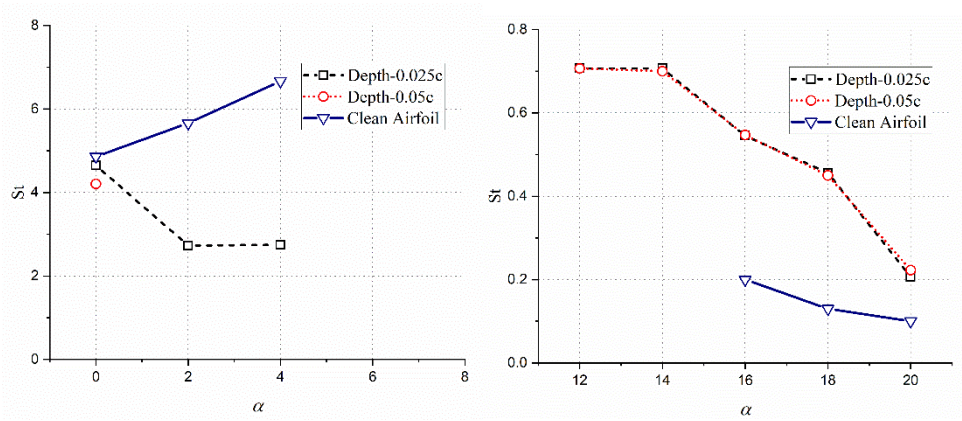

(a) 0.10c location, pre-stall AOAs *(b) 0.10c location, post-stall AOAs*

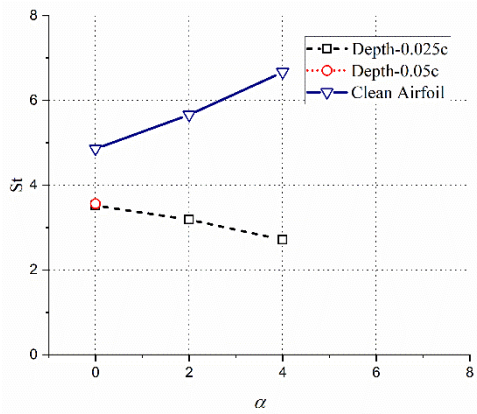

(c) 0.25c location, pre-stall AOAs

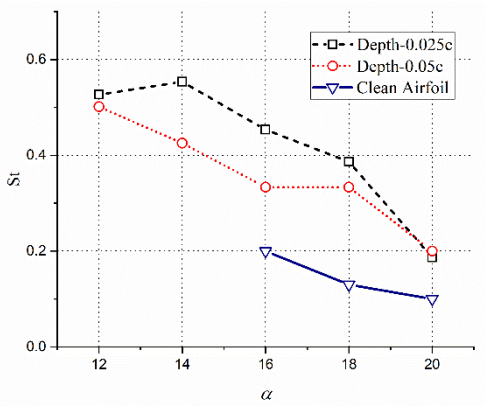

(d) 0.25c location, post-stall AOAs

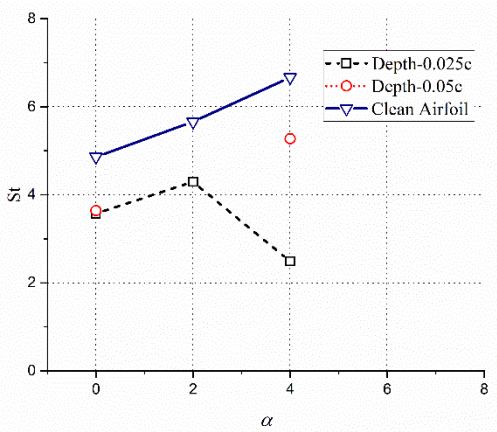

(e) 0.5c location, pre-stall AOAs

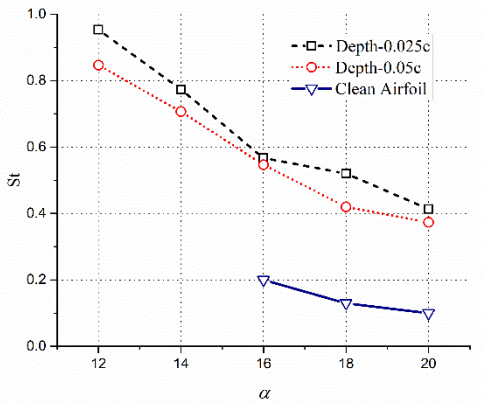

(f) 0.5c location, post-stall AOAs

Figure 5.44*:* Strouhal Number for various cavity configurations

The triangular cavity at 0.25c also has a similar effect on the Strouhal number at low AOAs as for the triangular cavity at 0.1c. The reduction in the frequency of oscillation in lift coefficient is however larger for both triangular cavities at α = 0°. For both cavity depths, the Strouhal number at α = 0°, is reduced by 24%. At α = 2° and 4°, the fluctuations are eliminated by the presence of a deeper triangular cavity at 0.25c while the shallower cavity reduces the Strouhal number by up to 58% at α = 4°, as can be seen in Fig. 5.44 (c). These reductions are, however, very less compared to those by a circular cavity, at the same location on the airfoil. As with cavity at 0.1c location, the triangular cavity at 0.25c also induces vortex shedding at α= 12°, and the frequencies of these

oscillation decrease with AOAs, except for the shallower cavity at α =14°. The other exception from the cavity at 0.1c is that the deeper cavity reduces the frequency of oscillations more as compared to the shallower triangular cavity, in the post-stall regime. The triangular cavity located at 0.5c reduces the frequency of oscillation at low AOAs, but only slightly. Even the deeper cavity of 0.05c depth is unable to eliminate the oscillation in a lift at α =4°, as can be seen in Fig. 5.42(e). The reduction in Strouhal number, however, is higher at α = 4°, as compared to the circular cavity at the same location but similar to the reduction by shallower cavity at 0.25c location. At higher AOAs, the Strouhal numbers are enhanced and the shallower cavity causes oscillations of higher frequency but lower amplitudes as compared to the deeper cavity at 0.5c location, as can be seen in Fig. 5.44 (f).

5.4 EFFECT OF TRIANGLE SHAPED CAVITY AT REYNOLDS NUMBER 50000

The effect of cavities on the aerodynamic characteristics of NACA 0012 is investigated at a Reynolds number of 50000. These cavities are right-angled triangles in shape and placed at either 0.1c, 0.25c, or 0.5c location on the suction surface. The depth of these cavities, which equal to the altitude of the right triangle, is either 0.025c or 0.05c, where c is the chord of the clean airfoil. The AOA of these configurations is varied between α = 0º to 20º with a 2º interval.

5.4.1 EFFECT OF TRIANGLE SHAPED CAVITY AT 0.10C LOCATION

The aerodynamic characteristics of NACA 0012 are significantly improved by the presence of a triangular cavity at 0.1c on the suction surface for a Reynolds number of 50000, as can be seen in Fig. 5.45. At α = 0º, the shallower cavity does not seem to affect the flow much and a marginally negative lift is observed due to flow unsteadiness. The deeper cavity, however, affects a significant improvement in the lift coefficient values with greatly reduced flow unsteadiness. As with the circular cavity at this location, a highly positive lift

observed for the deeper triangular cavity is due to the trapping of a vortex inside the cavity, which enhances the suction on the upper surface as can be seen in Fig. 5.46.

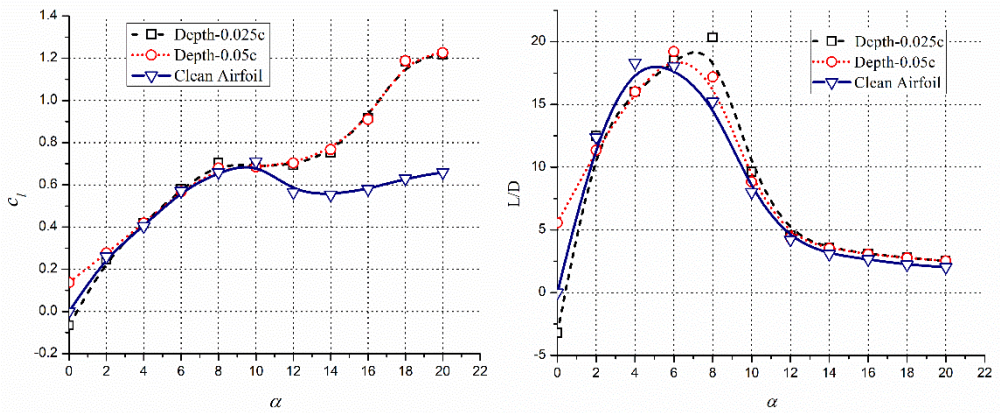

(a) Coefficient of Lift versus AOA *(b) L/D versus AOA*

Figure 5.45: Aerodynamic Characteristics of Circular Cavity at 0.10c location

Fig. 5.46 also shows the laminar separation of the shear layer on the pressure side that destroys the suction on the pressure side thus creating a high lift at zero incidences. The unsteadiness of the flow however is not eliminated, but a very low amplitude high-frequency oscillation in lift coefficients is observed due to the shedding away of roll-up vortices. As the AOA is increased, the flow unsteadiness remains persistent α = 2º and 4° for the shallower cavity due to shedding away small roll-up vortices. The time-averaged lift coefficient values, however, are the same as those for the clean airfoil as can be seen in Fig. 5.45 (a). As with the deeper circular cavity at 0.1c location, for a deeper triangular cavity at this location the flow transitions to the turbulent aft of the cavity, making the flow steady with no oscillations in lift values. The turbulent nature of the boundary layer increases the shear stress and the viscous drag causing a significant reduction *L/D* ratio, despite no loss in a lift at α = 4°. The reduction in the aerodynamic efficiency at this AOA for the deeper cavity is 13% as can be seen in Fig 5.45 (b).

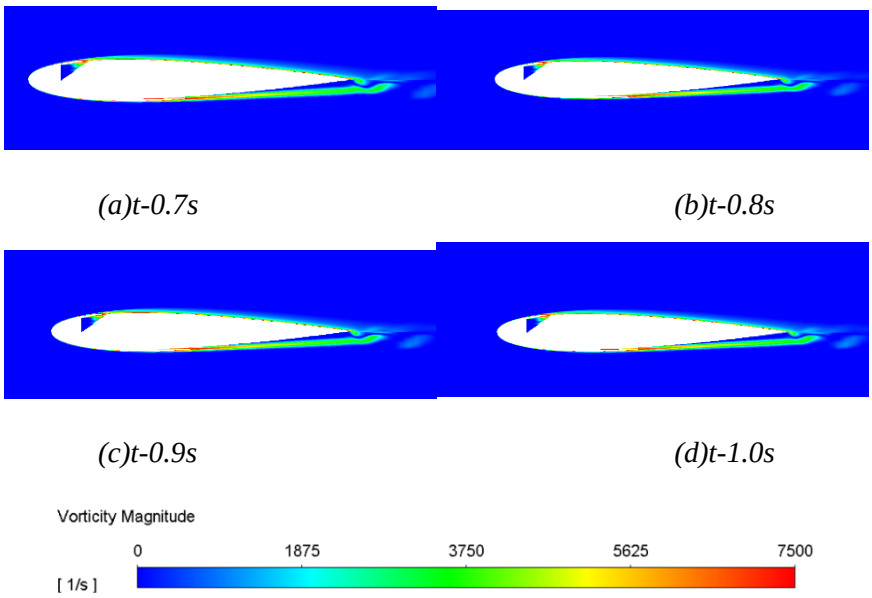

Figure 5.46: Vorticity contour over an airfoil with cavity depth 0.05c located at 0.10c, at α =0°

As the AOA is increased further, there are slight improvements in the lift coefficient values but with significant improvement in *L/D* values due to reduction in pressure drag. As can be seen in Fig. 5.45 (b), an enhancement of 33% in the *L/D* value is observed for an airfoil with a shallower cavity at α = 8°. The reduction in drag observed at α = 8° is due to the transition of the boundary layer due to the presence of the cavity. As can be seen in Fig. 5.47, for the shallower cavity, the boundary layer turns turbulent just aft of the cavity while for the deeper cavity, the boundary layer transitions to turbulent inside the cavity itself. In both cases, the flow is attached aft of the cavity, but the turbulent separation for the configuration with a deeper cavity occurs at an upstream location as compared to the configuration with a shallower cavity. This results in a larger pressure drag for the former case while having a similar lift coefficient because of the same size of the laminar separation bubble. The result is a significantly higher L/D ratio for the airfoil with a shallower cavity at α = 8°. The wider wake due to the early separation of the turbulent flow on the suction surface for this AOA is also visible in the vorticity contours as shown in Fig. 5.48.

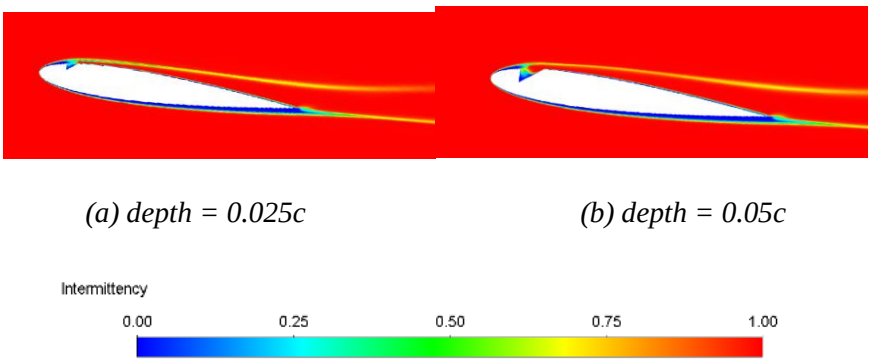

(a) depth = 0.025c *(b) depth = 0.05c*

Figure 5.47: Intermittency contour over an airfoil with triangular cavity located at 0.10c, at α =8°

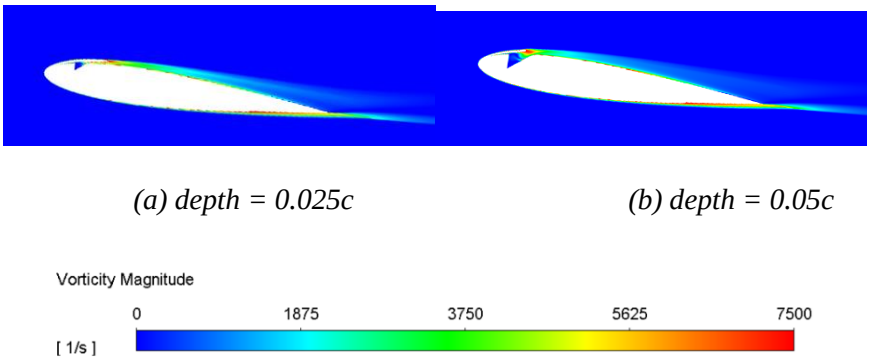

(a) depth = 0.025c *(b) depth = 0.05c*

Figure 5.48: Vorticity contour over an airfoil with triangular cavity located at 0.10c, at α = 8°

As the AOA is increased to 10º, the enhancement in L/D ratio falls to 11%. As the AOA is further increased to α = 12° and beyond the vortex shedding sets in, as with the airfoil with a triangular cavity at *Re* = 10^5, but the increments in time-averaged lift coefficients is smaller for *Re* = 50000 case. The flow unsteadiness and increments in lift values seen at α = 12° and 14° are in contrast to the airfoil with a circular cavity at the same Reynolds number and location, wherein no increases in lift coefficients are observed. Along with the improvement of the lift coefficient values, marginal improvements in *L/D* values are also observed at these AOAs. The enhancements in lift coefficients observed at α = 12° and 14° are due to the enhanced suction created by the vortical structures on the suction surface as can be seen in Fig. 5.49. As can be seen in Fig. 5.49, the reduction in suction due to the laminar separation bubble

seen for the clean configuration is eliminated by the presence of a triangular cavity at 0.1c location. The cavity itself creates suction and induces vortex shedding with enhanced suction on the rear part of the airfoil. The surface pressures, however, are not dependent much on the cavity depth as can be seen in Figs. 5.49 (a) and (c). However, the increase of AOA increases the size of the vortex and the suction on the rear portion of the airfoil, as can be seen in Figs. 5.49 (b) and (d). The variation in the skin friction coefficient is shown in Fig. 5.50. The results increments of 13% and 21% in the lift coefficient values at α=12° and 14° respectively.

As the AOA is increased in the range of α =16° to 20°, the bluff body vortex sets in with high amplitude, low-frequency oscillation in lift values. The instantaneous flowfield is similar to an airfoil with cavities of circular shape as can be seen in Fig. 5.51. When the primary vortex gains the entire strength on the surface of the airfoil the suction is enhanced leading to a higher lift coefficient. The build-up of the counter-clockwise vortex at the trailing edge destroys this suction and enhances suction on the pressure side leading to the destruction of lift. A similar phenomenon is observed at all AOAs higher than α = 16°, increasing the time-averaged values of lift coefficient by up to 56.6%, nevertheless. These increments at high AOAs are independent of the cavity depth as can be seen in Fig. 5.45 (a).

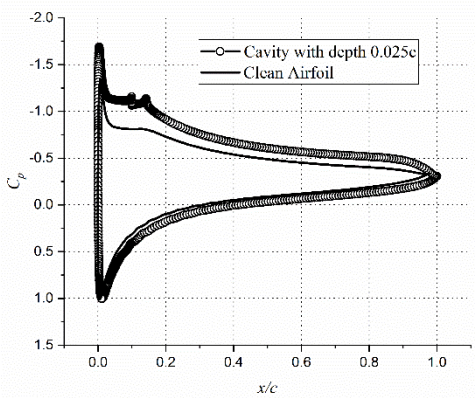

(a) α = 12°, depth = 0.025c

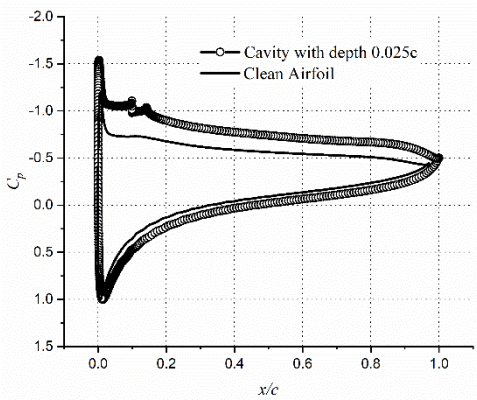

(b) α = 14°, depth = 0.025c

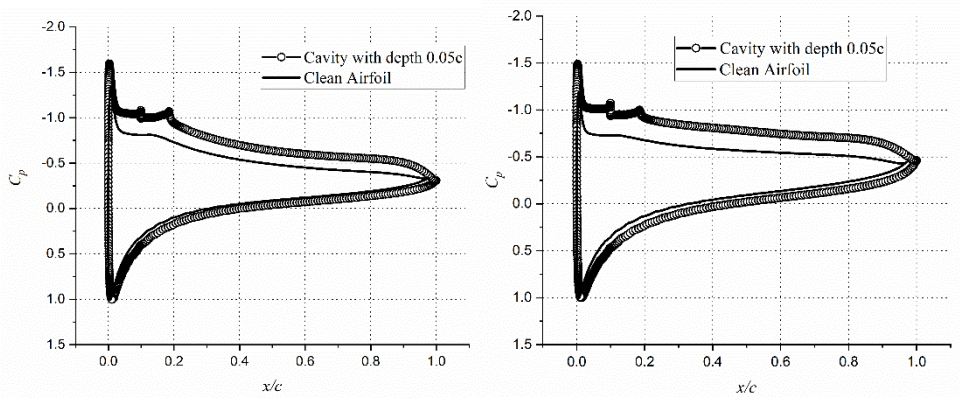

(c) α = 12°, depth = 0.05c *(d) α = 14°, depth = 0.05c*

Figure 5.49: Pressure distribution over an airfoil with triangular cavity located at 0.10c

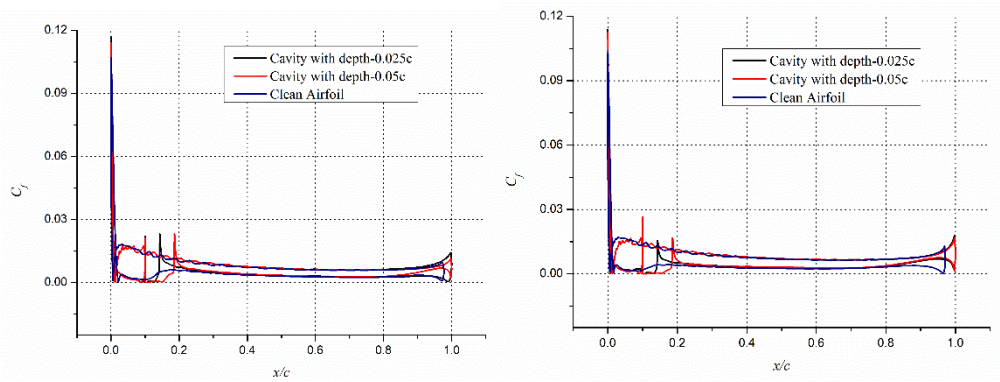

(a) α = 12° *(b) α = 14°*

Figure 5.50: Skin friction over an airfoil with triangular cavity located at 0.10c

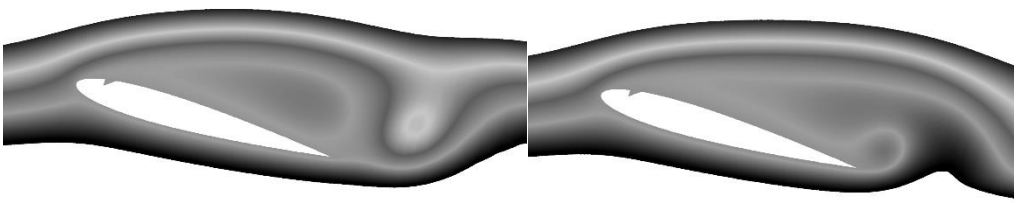

(a) *Higher Coefficient of Lift* *(b) Lower Coefficient of Lift*

Figure 5.51: Vortex structure for the cavity with depth 0.025c at 0.10c location, at 16º

5.4.2 EFFECT OF TRIANGLE SHAPED CAVITY AT 0.25C LOCATION

The effect of a triangular cavity located at 0.25c, on the aerodynamic characteristics of an airfoil significantly different from the effect of a circular cavity located at the same position on the suction surface. Unlike the circular cavity, high amplitude oscillations in lift values are observed even for deeper triangular cavity located at 0.25c, when the AOA is α = 0°, 2° or 4°. As can be seen in Fig. 5.52 (a), a positive time-averaged lift coefficient is observed for the deeper cavity at α = 0°. The aerodynamic characteristics of the airfoil with a deeper cavity, however, are severely deteriorated at α = 2°, as can be seen in Fig. 5.52. This deterioration of lift is not observed for the deeper circular cavity at Re = 50000. At a Reynolds number of 10^5 however, a similar deterioration in the time-averaged lift is observed for the shallower cavity at 0.025c location. The airfoil with a shallower cavity on the other hand shows time-averaged aerodynamic characteristics similar to those for the clean airfoil in the pre-stall regime. Some improvements in aerodynamic efficiency are observed at α = 6° and 8° due to the reduction of the pressure drag because of the transition of the laminar boundary layer into turbulent.

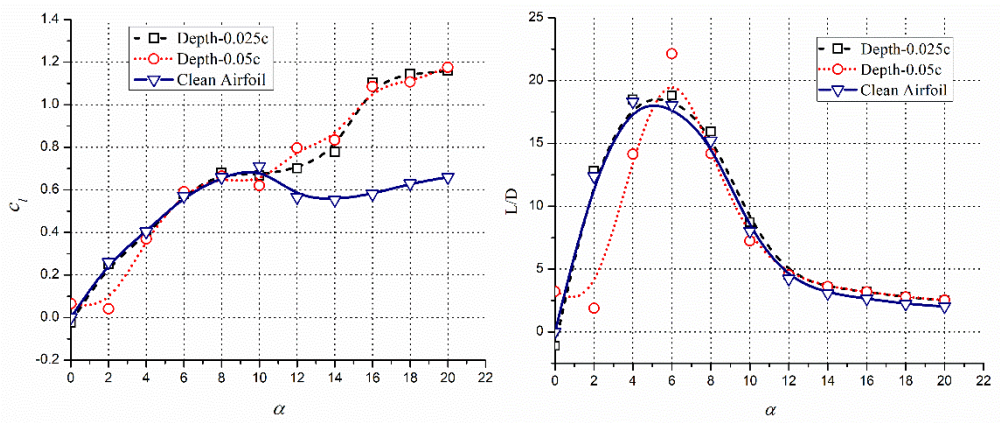

(a)Coefficient of Lift versus AOA *(b) L/D versus AOA*

Figure 5.52: Aerodynamic Characteristics of Triangle shaped Cavity at 0.25c location

The deterioration in the aerodynamic lift and efficiency of the airfoil at α =2° is because of the inability of the shear layer separated at the cavity to reattach

because of the laminar nature of the boundary layer as can be seen in Fig. 5.53. The lift at this AOA is reduced by over 22% while the aerodynamic efficiency is deteriorated by 85%, due to enhancement in pressure drag. The reattachment that occurs instantaneously near the trailing edge makes the flow highly unsteady and with destroyed suction and increased drag. As the AOA is increased, the reattachment point on the suction surface moves upstream on the suction surface, reducing the destruction of lift. At an AOA of α = 6°, the boundary layer turns turbulent at the cavity for 0.05c depth as can be seen in Fig. 5.54 (a). This makes the attached for a larger section of airfoil surface aft of the cavity and the turbulent separation occurs at a downstream location as can be seen in Fig. 5.54(b). This makes the wakeless wide with reduced pressure drag and enhanced suction increasing the aerodynamic efficiency by 22% at α = 6°. For the shallower cavity at this AOA however, no such transition is observed, the values of lift and drag are similar to those for the clean airfoil.

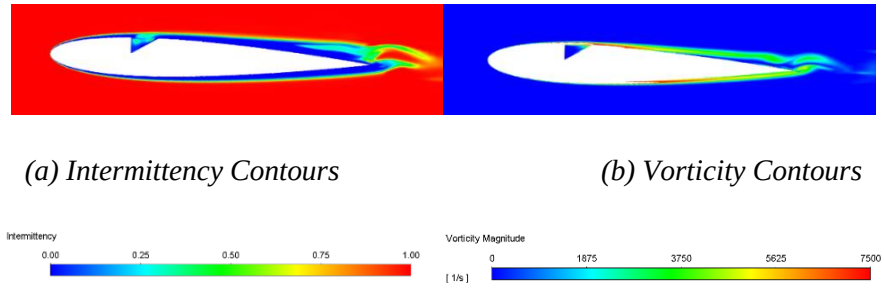

(a) Intermittency Contours *(b) Vorticity Contours*

Figure 5.53: Flow-field around an airfoil at α = 2°, with a triangular cavity of depth 0.05c at 0.25c

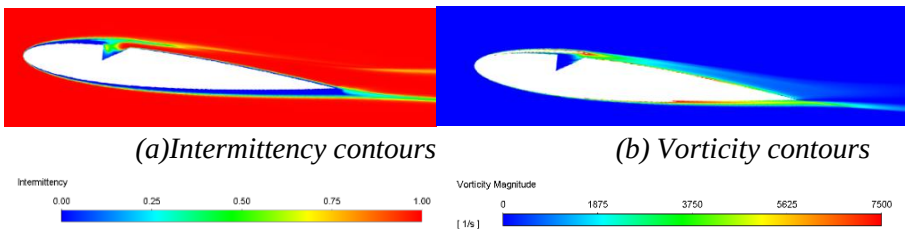

(a)Intermittency contours *(b) Vorticity contours*

Figure 5.54: Flow-field around an airfoil at α = 6°, with a triangular cavity of depth 0.05c at 0.25c

As the AOA is further increased, some deterioration in the performance of the airfoil is observed at α = 10° for the deeper cavity, due to turbulent separation

of the flow aft of the cavity. But for AOAs of α =12° and 14°, significant improvements in the time-averaged lift coefficient are observed for both depths of the triangular cavity at 0.25c, as can be seen in Fig 5.52. These enhancements are due to the vortical source of the lift and are higher for the deeper cavity. Besides, these enhancements are not observed for the circular cavity at the same location, but airfoil with a triangular cavity at this location exhibits vigorous vortex shedding and even higher enhancements in lift values at Re = 10^5. Nevertheless, enhancements of 14%, 23%, and 52% are observed in the time-averaged lift coefficient values for AOAs of α = 12º, 14° and 16° respectively with associated enhancements in L/D values of 7.2%, 16%, and 20%.

5.4.3 EFFECT OF TRIANGLE SHAPED CAVITY AT 0.50C LOCATION

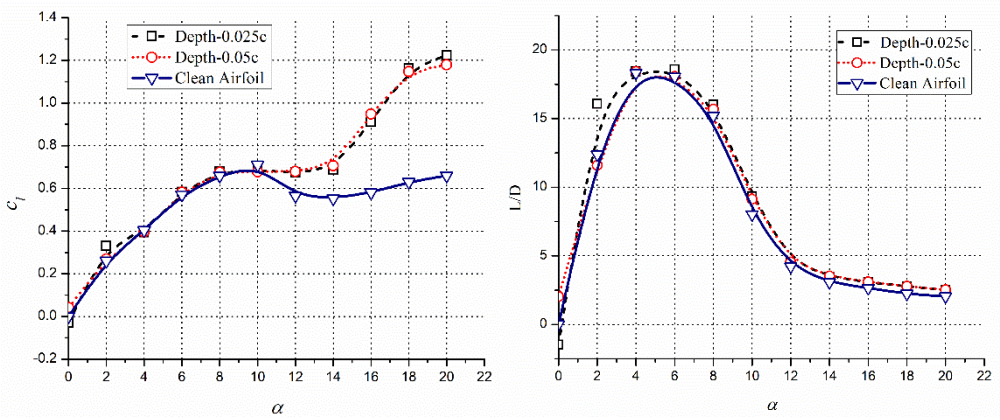

(a) Coefficient of Lift versus AOA *(b) L/D versus AOA*

Figure 5.55: Aerodynamic Characteristics of Circular Cavity at 0.50c location

The effect of the triangular cavity located at 0.5c on the surface is negligible on the aerodynamic lift of the airfoil in the pre-stall regime as can be seen in Fig. 5.55 (a). This is in contrast to the circular cavity at the same location, which results in some deterioration of the aerodynamic lift at low AOAs, especially for the deeper cavity. The cavity at 0.5c location fails to cease the flow unsteadiness at α =0°, 2°, and 4°, especially with the shallower cavity. The deeper cavity, however, reduces the amplitude of oscillations in lift values by inducing transition to turbulence. The result is a negative time-averaged lift

coefficient for the shallower cavity and a positive time-averaged lift coefficient for the deeper cavity, as can be seen in Fig. 5.55 (a). The vigorous vortex shedding induced by the shallower cavity at 0.5c location reduces the skin friction drag due to laminar bubbles aft of the cavity. This results in an enhancement in the aerodynamic efficiency of the airfoil at α =2° by up to 29%, as can be seen in Fig. 5.55 (b). Despite time-averaged lift coefficient values being similar to those for the clean configuration, the shallower cavity at 0.5c offers marginal reductions in drag at all AOAs in the pre-stall regime, due to reduction in skin friction aft of the cavity. The trend of small gains in the aerodynamic efficiency continues even in the post-stall regime as can be seen in Fig. 5.55 (b). As the AOA is increased beyond the stalling angle of α =10°, significant improvements in the time-averaged lift coefficient values are observed. This is in contrast to the circular cavity case wherein no improvement in lift values is observed at α = 12° and 14°. Similar improvements were also observed for a Reynolds number of 10^5. The reason behind the improvement in lift values is a sustained primary vortex on the suction surface as can be seen in Fig. 5.56 (a) and (b). The small unsteadiness observed is due to the vortex shedding of smaller scales for both cavity depths as can be seen in Fig. 5.56.

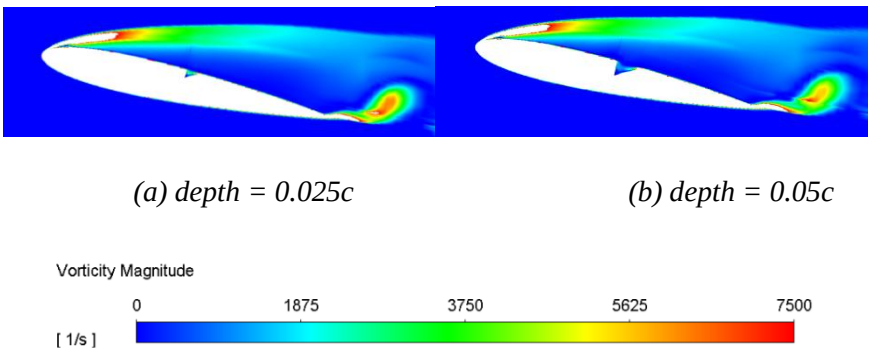

(a) depth = 0.025c *(b) depth = 0.05c*

Figure 5.56: Vorticity contours over an airfoil with cavity located at 0.50c, at α = 12°

A small laminar separation bubble, near the LE, as can be seen in Figs. 5.57 (a) and (b), also characterizes the sustained steady nature of the flowfield. The turbulent shear layer that separates well ahead of the cavity, fails to reattach to the suction surface causing larger wake and pressure drag. The enhancement in the lift is thus, not

translated into an improvement in aerodynamic efficiency. A similar flow-field is observed at α =14°, with enhanced lift coefficient without much oscillations in the lift values for both cavity depths. The suction aft of the separation bubble is significant for the airfoil with a cavity, as can be seen in Fig. 5.58. Skin friction variation is shown in Fig. 5.59, similar to the clean airfoil configuration except inside the cavity. Small vortices oozing out the cavity at 0.5c location also enhance the suction slightly, aft of the cavity. The suction aft of the cavity, however, is instantaneous and not sustained causing some oscillation in the lift coefficient values observed at α =12° and 14°. As the AOA is further increased, high amplitude vortex shedding sets in and the cavity just acts as induced of the flow unsteadiness. Nevertheless, improvements of 11% to 56.3% in the lift coefficient values and improvements of 7.2% to 24% are observed in L/D values at these high AOAs.

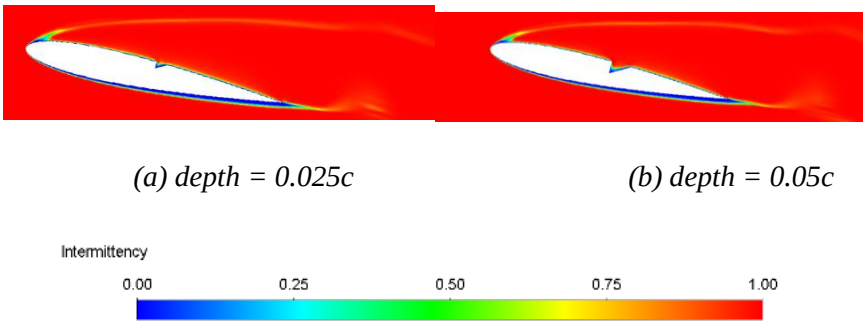

(a) depth = 0.025c *(b) depth = 0.05c*

Figure 5.57: Intermittency over an airfoil with cavity located at 0.50c, at α = 12°

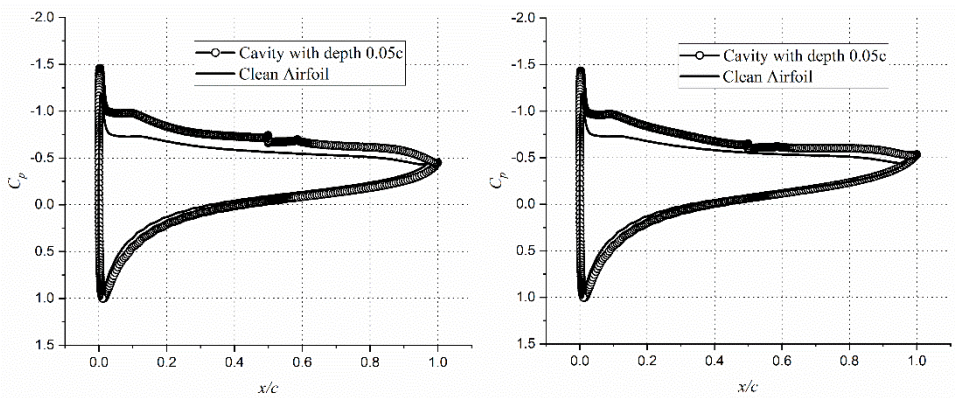

(a) Higher lift coefficient *(b) lower Lift coefficient*

Figure 5.58: Pressure variation over an airfoil with cavity located at 0.50c, at α = 14°

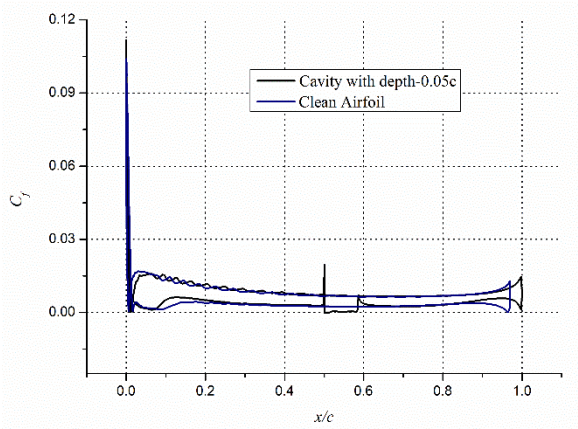

Figure 5.59: Skin friction over an airfoil with cavity located at 0.50c, at α = 14°

5.4.4. EFFECT OF TRIANGULAR CAVITY ON STROUHAL NUMBER

The Strouhal numbers derived from the FFT of the unsteady lift spectrum show a significant effect of the triangular cavity on the vortex shedding frequency and amplitude of oscillations in lift coefficients. A shallower cavity at 0.1c location reduces the frequency of oscillation lift slightly at α = 0° but enhances the vortex shedding and the oscillations in a lift as compared to the clean configuration at α = 2° while eliminating it at α = 4°. The deeper cavity at 0.01c location on the other hand inhibits the vortex shedding at α =2° and 4°, as can be seen in Fig. 5.60(a). In the post-stall regime, a triangular cavity located at 0.1c induces vortex shedding at AOA as early as α = 12°, irrespective of its depth, as can be seen in Fig. 5.60 (b). The frequencies of these vortex shedding induced by cavities at 0.1c location, fall linearly with increasing AOAs but remain significantly higher than the vortex shedding frequencies for the clean airfoil. As the location of the cavity is moves downstream on the surface of the airfoil at 0.25c, their effect on the vortex shedding is significantly reduced in the pre-stall regime, as can be seen in Fig. 5.60(c). At α = 0°, the shallower cavity of depth 0.025c reduces the vortex shedding frequency by 22% while the deeper cavity of 0.05c depth enhances the vortex shedding frequency by 12%.

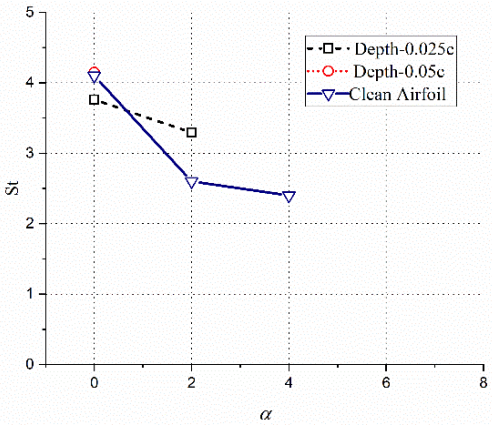

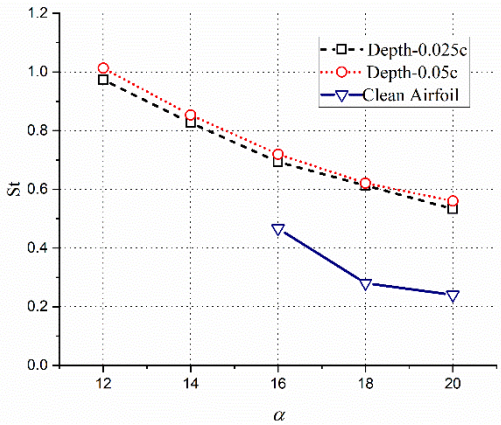

(a) Pre-stall AOAs, location = 0.10c *(b) Post-stall AOAs, location = 0.10c*

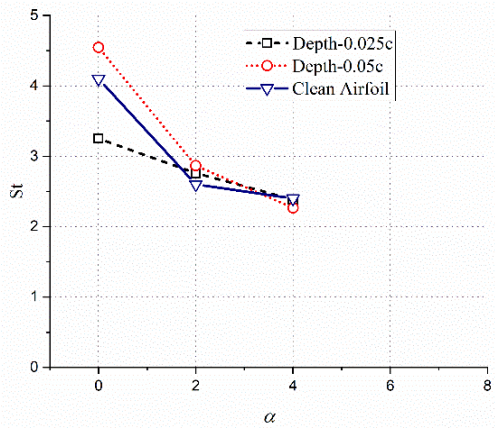

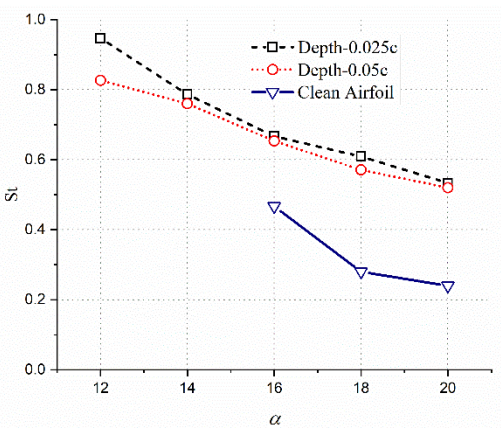

(c) Pre-stall AOAs, location = 0.25c *(d) Post-stall AOAs, location = 0.25c*

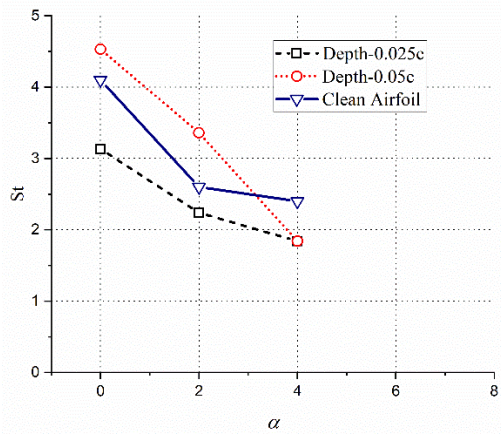

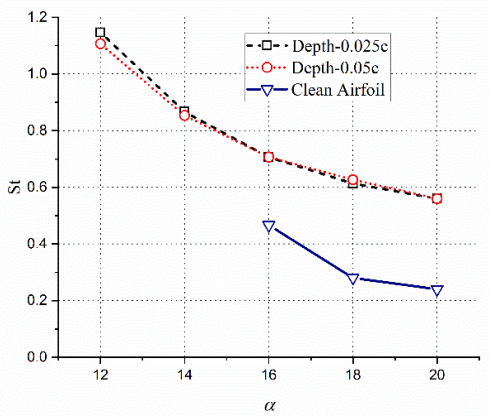

(e) Pre-stall AOAs, location = 0.5c *(f) Post-stall AOAs, location = 0.5c*

Figure 5.60: Strouhal number for an airfoil with a triangular cavity

At AOAs other than α = 0° the Strouhal number for an airfoil with a cavity is similar to those for the clean configuration. In the post-stall regime, the effect of a triangular cavity at a 0.25c location is similar to those located at 0.1c, as can be seen in Fig. 5.60 (d). The cavity induces a vortex shedding at α = 12° and above with shallower cavity-causing higher frequency oscillation, especially at α =12°, as compared to the shallower cavity. For a triangular cavity located at 0.5c on the suction surface, the shallower cavity reduced the frequency of vortex shedding at α = 0°, 2°, and 4°, with highest reduction of about 25% at α = 0°, as can be seen in Fig. 5.60 (e). The deeper cavity, however, enhances the vortex shedding at α = 0° and 2° while reducing the frequency by an amount similar to that by the shallower cavity, at α = 4°. In the post-stall regime, the triangular cavity at 0.5c has a similar effect of inducing very high-frequency vortex shedding at α = 12° and above. The frequencies of oscillations as observed in Fig. 5.60(f), is higher than caused by cavities at upstream locations. These frequencies are, however, independent of the depth of the cavity and reduce with increasing AOAs.

5.5 SUMMARY

A circular cavity of depth 0.025c, located at 0.1c on the suction surface does not affect the aerodynamic lift of a NACA 0012 airfoil, in the pre-stall regime, for a Reynolds number of 10^5. This is because the flow separated at the start of the cavity reattaches as a turbulent flow for all AOAs below α = 10°, and both cavity depths. Because of the transition to turbulence, the flow on the suction surface remains attached in the pre-stall regime and the airfoil behaves similarly to the clean configuration. The aerodynamic efficiency is, however, reduced by up to 20% due to an increase in profile drag of the airfoil. At AOAs higher than α = 10° however, the time-averaged C_l values increase monotonically but the *L/D* ratios remain close to the ones for clean configuration. An increment of 17% in *L/D* value is observed at α =8° for the shallower cavity. The aerodynamic characteristics, however, deteriorate for a cavity depth of 0.05c,

as the drag coefficient rises without any significant increase in Cls, resulting in degradation of aerodynamic efficiency by 7 % to 35%. For a circular cavity at 0.1c location, the maxima in *L/D* shifts towards higher AOAs, for smaller depths due to the transition of flow into turbulent, making the flow attached as reducing the wake width. For a deeper cavity, however, the turbulent separation occurs immediately after the cavity increasing the profile drag and hence reducing the aerodynamic efficiency in the pre-stall regime as well.

A shallow circular cavity at 0.25c location on the suctions surface degrades the performance of the airfoil due to the formation of tiny roll-up vortices formation on a surface with reductions of 15% and 56% in the lift and *L/D* values respectively at $\alpha = 2°$. At other AOAs in the pre-stall regime, the transition of boundary layer into turbulent reduced the pressure drag significantly, improving the aerodynamic efficiency significantly by up to 10%, without any increase in lift. Deeper cavity does not affect the lift much in the pre-stall regime due to transition to turbulence, but the drag rises significantly because of turbulent separation aft of cavity, which leads to a reduction in L/D values. In the post-stall regime, the flow is chaotic for the deeper cavities resulting in bluff body vortex shedding from the airfoil. The time-averaged lift values are increased by up to 39%, and the L/D values are increased by up to 23%.

The effect of a circular cavity located at 0.5c, on the aerodynamic efficiency is similar to those at 0.25c for a Reynolds number of 10^5. The shedding of the laminar roll-up vortices at $\alpha = 2°$ causes a reduction of 8% in C_l and 22% in *L/D* values. The reductions in C_l, at $\alpha = 2°$, are not observed for a cavity depth of 0.05c, as the laminar flow upstream of the cavity transitions to turbulent inside the cavity and continues as turbulent flow aft of the cavity. In the post-stall regime, the vortex shedding and the oscillations in Cl start as early as $\alpha = 14°$. For deeper cavity at 0.5c however, the vortex shedding is less severe due to the transition of the shear layer to turbulence. The oscillation in the lift at $\alpha = 14°$ causes an increase of 26% in the time-averaged C_l, with higher increments for higher AOAs, for both cavity depths.

For a Reynolds number of 10^5, a circular cavity placed at 0.10c on the suction surface stabilizes the flow in the pre-stall regime, eliminating oscillations in a lift at α = 2° and 4°. In the post-stall regime, however, this cavity adds to the flow unsteadiness, enunciating the vortex shedding at α = 14°, for both cavity depths. In the pre-stall regime, the Strouhal number (St) decreases with the increase in AOA, similar to clean configuration, but the St for airfoils with cavity remains higher than the clean configuration at same AOAs. A cavity located at 0.25c on the suction surface has a similar effect on the vortex shedding frequency, in the post-stall regime, however, it fails to enunciate a vortex shedding at α =14°. In the pre-stall regime, the cavity at 0.25c location significantly reduces the vortex shedding frequency by assisting flow transition to turbulence. The deeper cavity at 0.25c eliminates the vortex shedding at α =2° and 4° while reducing the Strouhal to 3.65 at α =0°. The effect of the circular cavity at 0.5c is slightly different from those at other locations as it fails to contain vortex shedding at small AOAs. In the post-stall regime, the cavity at 0.5c location imparts a larger flow unsteadiness as compared to other cavity locations, with very high Strouhal numbers of 0.84 and 0.6 for depths of 0.025 and 0.05 respectively at α =14°.

For a lower Reynolds number of 50000, a circular cavity placed at 0.1c significantly improves the aerodynamic characteristics of NACA 0012. The shallower cavity depth cavity at 0.1c improves the aerodynamic efficiency significantly in the pre-stall regime, other than α = 2°, with 54% enhancement in *L/D* ratio at α =10°. These improvements come from the reductions in drag due to the transition of the boundary layer at the cavity. For the deeper circular cavity at 0.1c, a vortex is trapped inside the cavity, with the flow transitioning to turbulent at the cavity, resulting in an attached flow aft of the cavity on the suction surface. This enhances the C_l values for a deeper cavity, in the pre-stall regime, with a 7.5% increment at α = 10°. The corresponding enhancement in the aerodynamic efficiency is 110%, due to further reduction in drag. The time-averaged aerodynamic characteristics of the airfoil with a cavity at 0.1c is

similar to those for a clean airfoil at AOAs between α = 12° and α =16°. In the post-stall regime, the time-averaged C_l and *L/D* values improve by up to 48% and 22% respectively due to vortex-dominated flow.

The aerodynamics characteristics of an airfoil with a circular cavity at 0.25c is very similar to that of an airfoil with a circular cavity at 0.01c, for a Reynolds number of 50000, especially at low AOAs. The airfoil with a cavity at 0.25c also shows a positive time-averaged C_l at α = 0º with increment in *L/D* value as well. For the deeper cavity, however, there is no unsteadiness in the flow as the roll-up vortices are absent on the suction surface due to the transition of the shear layer into turbulent. This increase in lift comes with no drag penalty and the *L/D* ratio of 3.0 and 6.0 is observed of an airfoil with cavity depths 0.025c and 0.05c respectively, at an AOA of α = 0°. The lift curve for an airfoil with a cavity at 0.25c is similar to that for the clean configuration in the pre-stall regime, except for α = 8 °, for the deeper cavity. At α = 6°, the aerodynamic efficiency of the airfoil with a cavity at 0.25c is remarkably improved by 12% and 24% for depths of 0.025c and 0.05c respectively, due to a reduction in drag. In the post-stall regime, no major unsteadiness in flow is observed for AOAs up to α = 16° and the time-averaged C_l values and *L/D* values for configuration with a cavity of either depth, are similar to those of the clean airfoil. At high AOAs, improvements of up to 45.4% in C_l values are observed due to vortex-dominated lift.

As the location of the circular cavity is changed to a 0.50c location, no significant change in the aerodynamic characteristics is observed. Similar to the cavity at upstream locations, the airfoil with a cavity at 0.5c shows a high degree of unsteadiness at low AOAs small AOAs, especially for smaller depth. For a cavity depth of 0.025c, the time-averaged lift curve overlaps the time-averaged curve for the clean airfoil up to an AOA of α =14°. For the deeper cavity, however, a severe degradation in a lift and aerodynamic efficiency of about 15% and 59% respectively, at α = 2º, is observed. In the post-stall regime, the time-

averaged C_l values are improved by up to 40.3%, without any improvement in the aerodynamic efficiency.

The flow around NACA 0012 at a low Reynolds number of 50000 is inherently unsteady at low AOAs and a cavity of depth 0.025c, located at 0.1c location, enhances the vortex shedding frequencies at α = 0° and 2°, but diminishes the Strouhal number slightly at α = 4°while inducing vortex shedding at α = 6°. The deeper cavity located at 0.1c on the suction surface eliminates the vortex shedding and fluctuations in lift values at all small AOAs other than zero incidences. The deeper cavity eliminates the vortex shedding even when placed at a 0.25c location on the suction surface. The reduction in vortex shedding frequencies is because of the transition of the shear layer aft of the cavity. The cavity with the depth of 0.025c diminishes the vortex shedding frequencies at AOAs of α= 0°, 2°, and 4°, whereas the deeper cavity enhances the vortex shedding frequencies at these AOAs. At α = 4°, the shallower cavity reduces the Strouhal number by 29% while the deeper cavity increases the Strouhal number by 100% when placed at mid-chord location on the suction surface. In the post-stall regime, the cavities affect similar to the protrusions and cavities at 10^5 Reynolds number. The cavities enhance the vortex shedding frequencies by a similar amount for all depths and locations except for a deeper cavity at 0.25c location which eliminates the vortex shedding at α = 16°.

Unlike a circular cavity at 0.1c location, a shallower triangular cavity of depth 0.025c deteriorates the performance of the airfoil at α = 2° and 4° with reductions of up to 12% and 34% in C_l values and L/D values respectively. The C_l and L/D values for an airfoil with a cavity at 0.1c location, are similar to those for clean configuration between α = 6° and 10°, with loss in a lift for deeper cavities. For the deeper cavity, however, significant reductions in L/D ratio are observed for all AOA below α = 12°, despite only marginal reductions in the C_l, suggesting a drastic rise in drag coefficients. As the AOA is increased to α =12°, severe vortex shedding is enunciated causing fluctuations in lift coefficient values with the enhanced time-averaged C_l values irrespective of the

cavity depth. Interestingly, the conventional stall is not seen for an airfoil with a triangular cavity at 0.1c, due to enhancement of lift at α = 12°. At AOAs between α = 12° and 20°, enhancements in the time-averaged C_l values of 16% - 75.5%, are observed with increments of 8.5% to 31% in the L/D ratios.

In the pre-stall regime, the effect of a triangular cavity located at 0.25c is similar to those of a circular cavity at the same location and Reynolds number and similar to the triangular cavity at 0.1c location. The loss in lift seen at α =2°, for circular cavity at 0.25c location and triangular cavity at 0.1c, is not observed for the airfoil with a triangular cavity at 0.25c. Another contrasting difference in the lift curve of an airfoil with a circular cavity at 0.25c and one with a triangular cavity at 0.25 can be observed between α=10° and α =14°. While the lift curve of an airfoil with circular at 0.25c location follows the trend of clean airfoil up to α = 14°, with significant loss of lift at both α=12° and 14°, the lift curve of an airfoil with a triangular cavity at 0.25c shows no stall. Nevertheless, the lift coefficients are enhanced by 28% to 64% with a corresponding increase in the L/D values by 5.2 % to 27%, in the AOA between α=12° and 20°. Even for the deeper cavity absence of stall is observed with an increment of 37.5% at α =12°. There is also no reduction in the C_l values in the pre-stall regime but decrements in the L/D values between 2% to 36%, are observed.

The effects of the triangular cavity at 0.5c, are significantly different from those for cavities at different locations at a Reynolds number of 10^5, in the post-stall regime. The typical stall seen for the clean airfoil is absent but the C_l values at α = 12° and 14° are smaller than for airfoil with a triangular cavity at 0.25c. Nevertheless, the lift coefficient values increase monotonically from α = 12° to α =20°. Another contrasting result as compared to an airfoil with a triangular cavity at 0.25c, is the absence of severe flow unsteadiness, at α = 12° and α = 14°. At AOAs between α = 12º to α = 20º, improvements in the time-averaged C_l values of 15% to 75.5% are observed. In the pre-stall regime, for both cavity depths, at α=6°, the shear layer turns turbulent well ahead of the cavity. The turbulent separation for the deeper cavity, however, occurs at an upstream point

as compared to the shallower cavity. This makes the pressure drag for the deeper cavity slightly higher with a reduced *L/D* ratio.

A triangular cavity at 0.1c location reduces the unsteady oscillations in C_l values, but not as effective as a circular cavity at the same location on the airfoil, for Re $=10^5$. Triangular cavities at 0.1c location, fail to eliminate the severe flow unsteadiness at α = 0°. The deeper cavity, however, reduces the frequency of oscillations by 16% and can eliminate the vortex shedding at α = 2° and 4°. The shallower cavity at 0.1c on the other hand reduced the frequency of oscillations at α=2° and 4° significantly. In the post-stall regime, the presence of a triangular cavity at 0.1c enunciates a high-frequency vortex shedding at AOA as early as α = 12°, with *St* = 0.7, for both depths. As the AOA is further increased, *St* reduces, but remains, significantly higher than clean airfoil. The triangular cavity at 0.25c also has a similar effect on the Strouhal number at low AOAs as for the triangular cavity at 0.1c. For both cavity depths, the Strouhal number at α = 0°, is reduced by 24%. At α = 2° and 4°, the fluctuations are eliminated by the presence of a deeper triangular cavity at 0.25c while the shallower cavity reduces the Strouhal number by up to 58% at α = 4°. These reductions are, however, very less compared to those by a circular cavity, at the same location on the airfoil. The triangular cavity located at 0.5c on the contrary reduces *St* only slightly. Even the deeper cavity of 0.05c depth is unable to eliminate the oscillation in a lift at α =4°.

The aerodynamic characteristics of an airfoil are highly improved by the presence of a triangular cavity at 0.1c for a Reynolds number of 50000. The deeper cavity affects a significant improvement in the C_l values with greatly reduced flow unsteadiness. As with the circular cavity at this location, a highly positive lift observed for the deeper triangular cavity is due to the trapping of a vortex inside the cavity. A deeper triangular cavity at 0.1c, making the flow steady by transitioning the flow turbulent, aft of the cavity. The turbulent nature of the boundary layer increases the viscous drag causing a significant reduction *L/D* ratio at small AOAs. At moderate AOAs, an enhancement of up to 33% in

the *L/D* value is observed due to a reduction in pressure drag. At α = 12° and higher, the vortex shedding sets in, with increments of 13% and 21% in C_l values at α=12° and 14° respectively, but these increments in time-averaged C_l are smaller, as compared to $Re = 10^5$ cases. These increments are also in contrast to the circular cavity at 0.1c, wherein no increases in C_l are observed for Re = 50000. At higher AOAs the times averaged C_l values are increased by 57%.

For a Reynolds number of 50000, a triangular cavity located at 0.25c causes high amplitude oscillations in C_l values is observed at α = 0°, 2° or 4°, irrespective of cavity depth. Unlike the circular cavity, this unsteadiness results in a positive C_l at α = 0° for the larger depth. The aerodynamic characteristics of the airfoil with a deeper cavity, however, are severely deteriorated at α = 2° with reductions of 22% and 85%, in C_l and *L/D* values respectively, due to enhancement in pressure drag. This deterioration of lift was not observed for the deeper circular cavity at Re = 50000. At a Reynolds number of 10^5 however, a similar deterioration in time-averaged C_l was observed for the shallower cavity at 0.025c location. The aerodynamic efficiency however improves by 22% at α = 6°, as the cavity turns the flow into turbulent. As with triangular cavity 0.1c, significant improvements of 14%, 23%, and 52% in the time-averaged C_l at α = 12°, 14° and 16° respectively, for a cavity at 0.25c, due to vortex dominated lift enhancement. The corresponding enhancements are *L/D* values are 7.2%, 16%, and 20% respectively.

In contrast to a circular cavity at 0.05c location, a triangular cavity does not affect the C_l values in the pre-stall regime, for Re = 50000. The deeper cavity, however, reduces the amplitude of oscillations in lift values by inducing transition to turbulence. Despite time-averaged C_l values being similar to those for the clean configuration, the shallower cavity at 0.5c offers marginal reductions in drag at all AOAs in the pre-stall regime, due to reduction in skin friction aft of the cavity resulting in enhancements of up to 29% in *L/D* values in the pre-stall regime. As the AOA is increased beyond α =10°, significant improvements in the time-averaged C_l values are observed, similar to those

observed for a Reynolds number of 10^5. Improvements of up to 56.3% in the C_l values and up to 24% in *L/D* values are observed at these high AOAs.

For *Re* = 50000, a shallower triangular cavity at 0.1c location reduces the frequency of oscillations in lift slightly at α = 0° but enhances *St* at α = 2°, while eliminating it at α = 4°. The deeper cavity on the other hand inhibits the vortex shedding at α =2° and 4°. In the post-stall regime, the triangular cavity induces vortex shedding at AOA as early as α = 12°, irrespective of its depth. The St, however, fall linearly with AOAs but, remain significantly higher than those for a clean airfoil. As the cavity moves downstream to 0.25c, its effect on St in the pre-stall regime, diminishes, with the cavity affecting the St values at α = 0° only. At α = 0°, the shallower cavity reduces *St* by 22% while the deeper cavity enhances *St* by 12%. As the triangular moves further downstream to 0.5c, the shallower cavity reduces the *St* at low AOAs, with the highest reduction of about 25% at α = 0°. The deeper cavity, however, enhances the St at α = 0° and 2°. In the post-stall regime, the effect of all triangular cavities is similar as they enhance the *St* values for α = 12° and above.

CHAPTER 6. EFFECT OF PROTRUSION AND CAVITY ON DYNAMIC STALL

Dynamic stall is one of the most crucial and fascinating aerodynamic phenomena, it is a very practical problem and at the same phase very interesting one as well. It occurs when the lifting surface is promptly pitched further than its static stall angle, a follow-on to a primary lift enhancement, and its consequent loss in an extremely non-linear manner. The effect of cavities or surface depressions, on the dynamic stall characteristics of an airfoil, has not been presented in the open literature. The current chapter presents the results of the numerical analysis carried over a NACA 0012 airfoil with triangular and circular cavities at a Reynolds number of 135000. The reason to choose this particular Reynolds number is the availability of the experimental data for validating the present numerical analysis.

6.1 EFFECT OF TRIANGLE SHAPED CAVITY ON DYNAMIC STALL

Numerical analysis was carried out to check the effect of the triangular cavity on dynamic stall characteristics of NACA 0012 airfoil. The cavity is placed at one of the three locations viz. 0.10c, 0.25c and 0.50c on the suction surface. The cavities are of two depths of altitude with the shallower cavity having a depth of 0.025c and the deeper cavity having a depth of 0.05c.

6.1.1 EFFECT OF TRIANGLE SHAPED CAVITY AT 0.10C LOCATION

The dynamic aerodynamic characteristics of the NACA 0012 airfoil without and with a cavity at 0.1c location are illustrated in Fig. 6.1. As can be seen in Fig. 6.1(a), the stalling angle and the maximum lift coefficient are both reduced for the airfoil with the cavity at 0.1c location. The stalling angle for the clean airfoil is 23.5° while for the airfoil with cavity stalls at $\alpha = 22°$, for a cavity depth of 0.05c. The losses in the maximum lift and the stalling are bigger for the deeper cavity. At low and moderate AOAs however, the small-scale oscillations observed during the upstroke, for the clean airfoil is eliminated for

both cavities at this location. During the down-stroke, the non-linearity in the lift curve is highly oscillatory. Besides, at AOAs between α = 20° to 15°, these oscillations are at different phases for the clean airfoil and the airfoil with cavities. Other than the minima between α =18° and 20°, the range of Cl remains similar for airfoils with and without cavity between AOAs of α = 25° to 13°, during the down-stroke. Below α = 13°, significant improvement in the lift is observed for the airfoil cavity at 0.1c location for both depths. The lift for the clean configuration turns negative below α = 6.5°, while for configurations with a cavity at 0.1c location lift becomes negative below α = 5°.

The drag curve behaves slightly differently with the cavities adding to the drag coefficient during the upstroke motion as can be seen in Fig. 6.1(b). The oscillations in the drag values at lower AOAs are eliminated by the presence of cavity at 0.1c and the drag coefficient for all the three configurations are similar for AOAs of up to α =14°. Beyond α =14°, a detrimental increment in drag is observed for an airfoil with a cavity at 0.1c location. The increase in drag continues until the stalling angle and the increments are higher for the deeper cavity of 0.05c depth. The increments in drag at higher AOAs, observed during the upstroke are viscous due to the earlier transition of boundary layer into turbulent one because of the cavity.

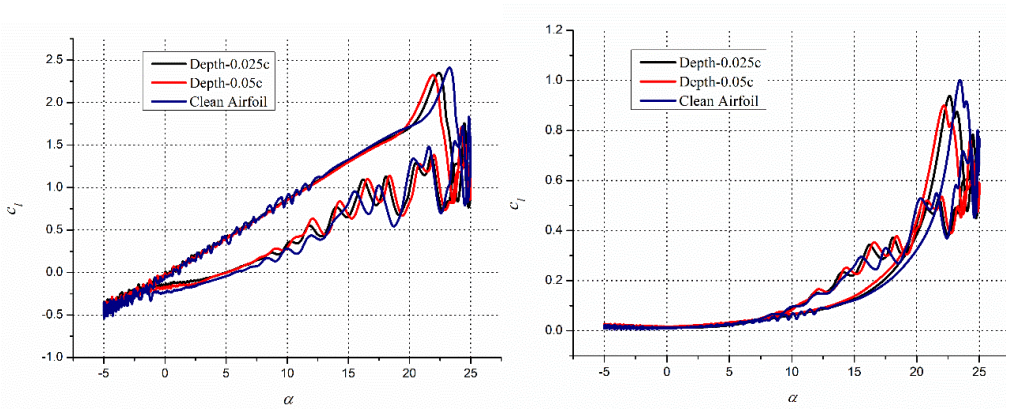

(a) Coefficient of Lift versus α *(b) Coefficient of Drag versus α*

Figure 6.1: Aerodynamic characteristics of the Cavity at 0.10c Location

As the stall occurs earlier than the airfoil with the cavity, the peak drag coefficient is much smaller than the clean airfoil. During the downstroke, oscillations in drag coefficient are observed due to vortex shedding for clean airfoil as well as for airfoil with a cavity. The time-averaged drag coefficient, however, is higher for the airfoil with the cavity for AOAs above $\alpha = 16°$, as can be seen in Fig. 6.1(b). Below $\alpha = 15°$, however, all configurations show similar drag coefficients. The variation of lift and drag observed is due to the dominance of vortex dynamics around the airfoil as shown in Fig. 6.2.

During the upstroke, at AOA close $\alpha = 1.38°$, small vortical structures are seen on the pressure side for airfoils with and without a cavity. These vortices are continuously fed into the wake causing flow unsteadiness. On the suction side, however, these roll-up vortices are not observed for the airfoils with the cavity due to the transition of the boundary layer into a turbulent one. This reduces the unsteadiness of flow around the airfoil with both cavity depths. As the AOA increases during the upstroke, for $\alpha = 4.73°$, the extent of the region of roll-up vortices on the suction side increases on the clean airfoil. For the airfoils with a cavity, the flow remains largely attached on the suction surface, with turbulent separation occurring near the trailing edge. This enhances the lift coefficient of an airfoil in upstroke motion, as compared to the clean configuration. The turbulent boundary layer on the other hand increases the skin friction increasing drag as well as shown in Fig.6.3(b).

As the AOA further increases to $\alpha = 7.32°$, the lift for the clean configuration increases due to enhanced suction near the minimum pressure point and so does it happen for the airfoils with a cavity. The lift for the clean configuration is oscillatory due to the presence of roll-up vortices on the suction surface. For the airfoil with the shallower cavity, some enhancement is observed due to the turbulent nature of the flow on the suction side. For the deeper cavity, however, movement of turbulent separation point to an upstream location diminishes the lift produced, and the lift values are similar to those for the clean airfoil.

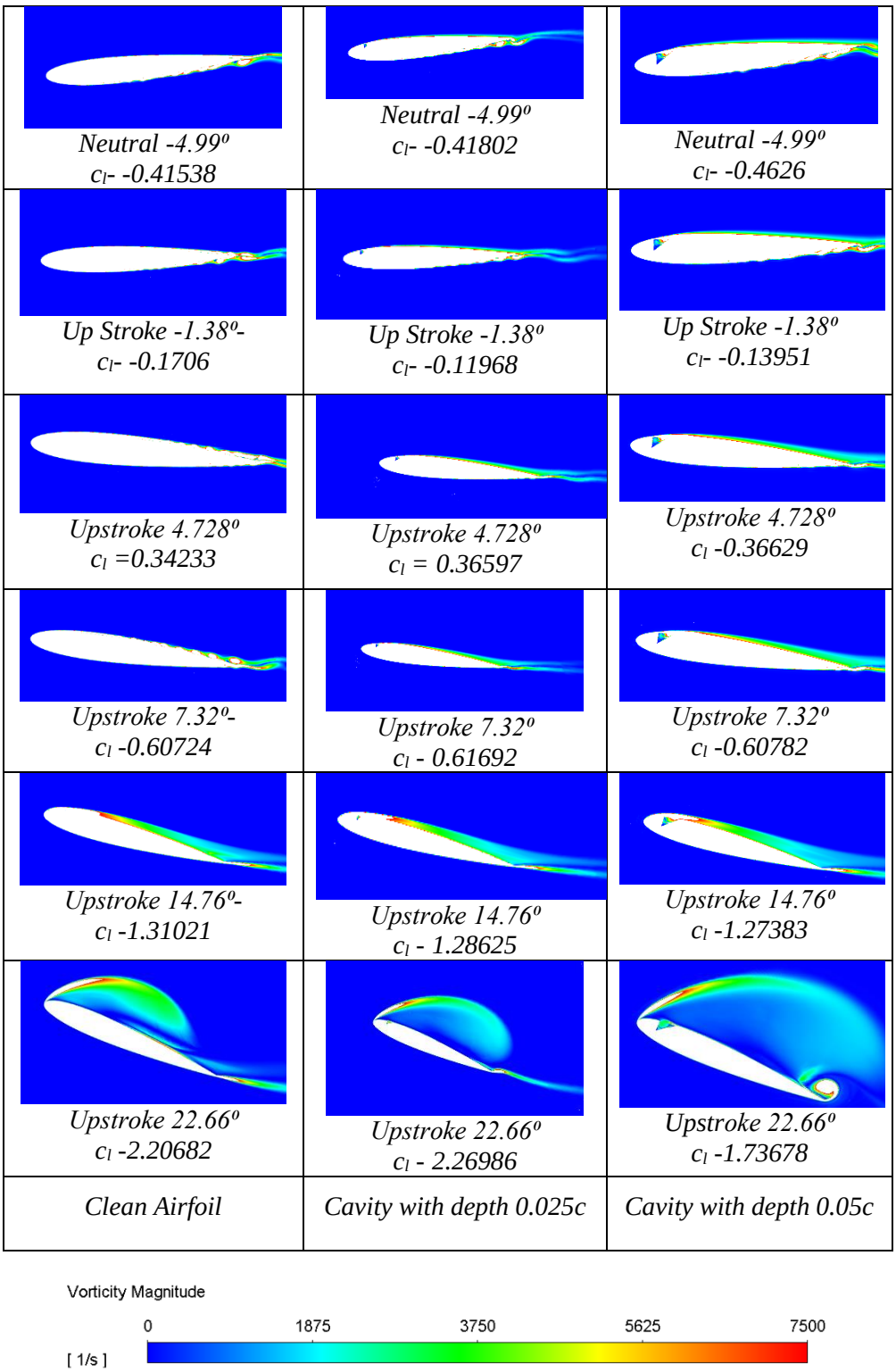

Figure 6.2: Vorticity Magnitude for the airfoil with cavity located at 0.10c during upstroke motion

As the AOA increases further during the upstroke motion, boundary layer transitions on the suction surface of the clean airfoil occur and the transition point moves forward with increasing AOA. This results in an attached flow on the suction surface of the clean airfoil with increasing lift values. For the airfoils with a cavity, on the other hand, the turbulent separation point moves upstream with increasing AOAs. In the range of AOA between $\alpha = 10°$ and 20°, the turbulent separation point for the clean airfoil is at the most backward position while for the airfoil with a deeper cavity; it is at the forward-most position, for the same AOA. This causes a slight reduction in the lift of the airfoil with the cavity (not visible in Fig. 6.1) as compared to the clean configuration.

As the AOA further increases during the upstrokes motion, the flow separates near the leading edge and reattaches at a downstream location forming a dominant clockwise vortex on the suction surface. This causes a sudden enhancement in the lift of the airfoil due to the strong suction caused by the vortex. This phenomenon of formation of a vortex, occur at $\alpha = 19°$ for the airfoil with the deeper cavity, while at $\alpha = 21°$ for an airfoil with a shallower cavity and $\alpha = 22.5°$ for the clean airfoil. As the vortex gains strength the lift curve of the airfoil with a deeper cavity moves higher followed by the lift curve of the airfoil with a shallower cavity and the one for the clean airfoil. After attaining full strength, the vortex is unable to sustain itself and is shed away causing stall to the airfoil. As can be seen in Fig 6.2, at $\alpha = 22.66°$, the vortex on the clean airfoil is still building up its strength, while the airfoil with a shallower cavity has its vortex at full strength and the vortex on the airfoil with a deeper cavity has just been shed away. As the clockwise vortex is shed away, an anticlockwise vortex builds upon the suction surface, near the trailing edge, which brings some suction for lift. A clear difference in vortex structure of the airfoil with and without cavity can be observed in the pressure distribution graph, which clearly shows higher suction aft of the cavity for an airfoil with the cavity. As can be seen in Fig. 6.3 (g), even though the suction is higher on the forward half for the clean configuration at $\alpha = 22.66°$, strong suction on the rear half of the airfoil

with shallower cavity makes lift higher. Corresponding skin friction variation is given in Fig.6.3 (h). This clearly shows the effect of the cavity that shifts the center of vortex aft of the cavity distributing the suction evenly. For the deeper cavity, the suction is significantly diminished at this AOA, but the strong suction from an anticlockwise vortex is visible. The clean airfoil also stalls at a later AOA of α = 23.5°.

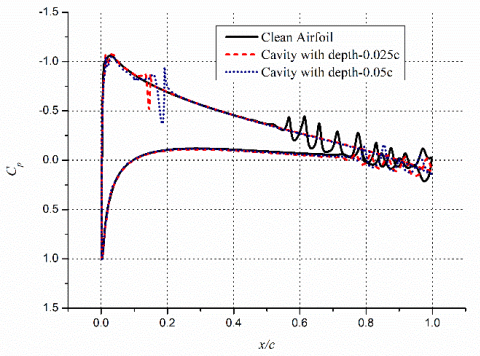

(a) Upstroke 4.728⁰ -Pressure

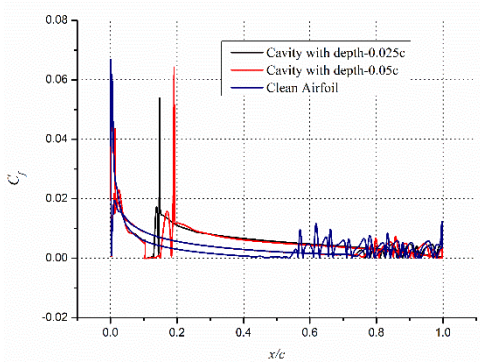

(b) Upstroke 4.728⁰-Skin Friction

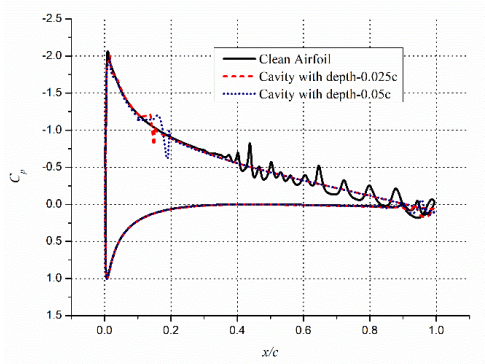

(c) Up stroke 7.32⁰-Pressure

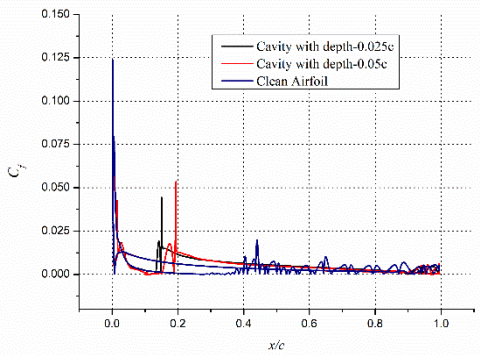

(d) Up stroke 7.32⁰-Skin Friction

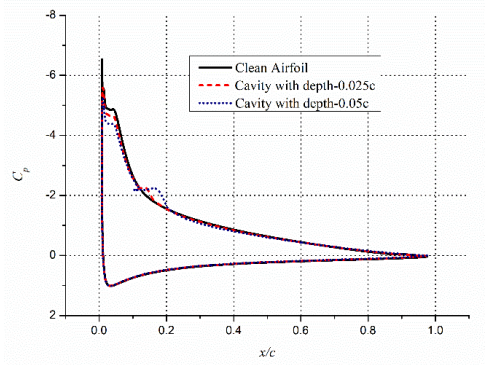

(e) Up stroke 14.76⁰-Pressure

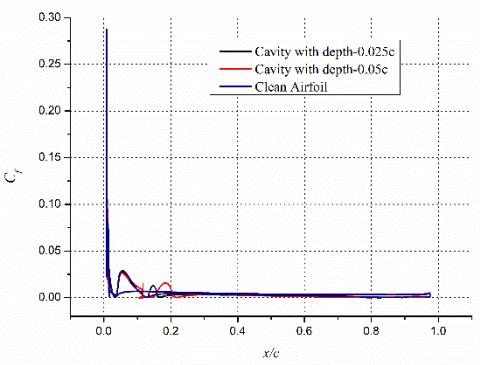

(f) Up stroke 14.76⁰-Skin Friction

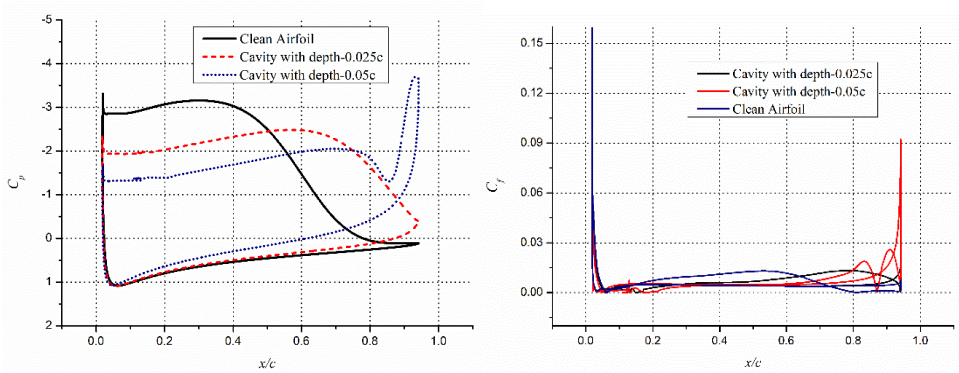

(g) Upstroke 22.66⁰-Pressure *(h) Upstroke 22.66⁰-Skin Friction*

Figure 6.3: Surface pressure and skin friction distribution during upstroke motion

At α = 24.89°, immediately after the start of the downstroke motion, all the airfoils are in a fully stalled condition. A strong anticlockwise vortex, on the suction surface near the trailing, however, keeps the lift values moderately high. During the downstroke, as the AOA decreases, the lift is entirely dependent on the vortex dynamics on the suction surface, as the shedding of vortices starts, shedding from the trailing and leading edge alternately. This shedding of vortices alternately from the leading and trailing edge causes severe oscillations in both lift and drag of the airfoils with and without cavity at 0.1c location. As can be seen in Fig. 6.4, at α = 22.21°, the counter-clockwise vortex near the trailing edge has just left the surface for the clean airfoil while the airfoils with the shallower and deeper cavity, the shed vortex has moved progressively downstream. The strength of the primary clockwise vortex has thus, a maximum strength for the airfoil with a deeper cavity while the one for clean configuration has the least strength. This is reflected in the lift produced by the airfoils with the airfoil having a deeper cavity showing the maximum lift at this AOA.

As the AOA further decreases, this vortex shedding phenomenon continues for all configurations, the phases of these vortex shedding cycles are, however, different for the three configurations causing alternate maxima and minima in the lift and drag values. At AOAs below α = 19° however, the mean lift and drag values for airfoils with cavity are higher due to suction induced by the trapped vortex inside the cavity. This trend of oscillating lift and drag

coefficients continues as the AOA decreases during the downstroke, and mean lift and drag values fall with decreasing AOA. The vortical nature of the lift during the downstroke is confirmed by the surface pressure distribution, as shown in Fig. 6.5. As can be seen in Fig. 6.5(c), at α = 13. 99°, the suction near the leading edge is highly diminished for the clean airfoil; however, small suction can be observed near the leading edge for the airfoils with a cavity. Even the suction near the trailing edge is higher for the airfoils with cavity due to more coherent and stable anticlockwise vortex aft of the cavity. The increased mean lift for the airfoils with the cavity is observed at all AOAs during the downstroke, as the airfoil further plunges to lower AOAs. As the AOA reduces the separation point on the suction surface, near the leading edge moves downstream, with some recovery in the leeward surface suction as shown in Fig.6.5 (b), (d), (e), (f) in the skin friction variation. The turbulent separation point on the leeward surface during the downstroke is at the most downstream location for an airfoil with a deeper cavity and most upstream location for the clean airfoil. As the flow separation point moves downstream, the vortex shedding and the oscillations in lift and drag ceases below α = 9°, for the airfoil with the deeper cavity, while at smaller AOA for the clean airfoil.

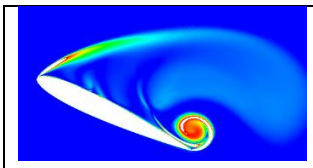 *Down-Stroke 24.89⁰- c_l -1.0618*	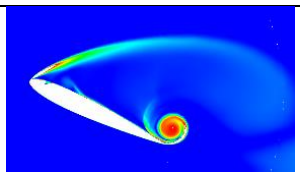 *Down-Stroke 24.89⁰ c_l - 0.79534*	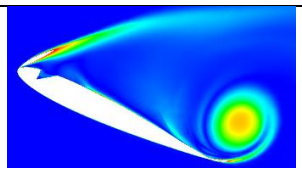 *Down-Stroke 24.89⁰ c_l -0.88554*
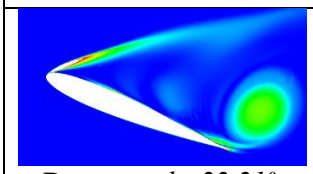 *Down-stroke 22.21⁰- c_l -0.90879*	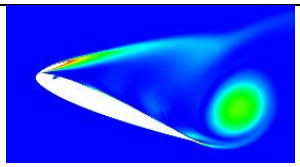 *Down-stroke 22.21⁰ c_l - 1.02054*	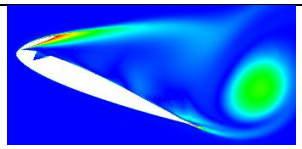 *Down-stroke 22.21⁰ c_l -1.25147*
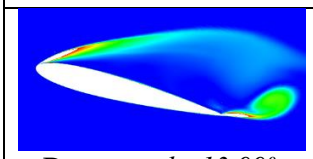 *Down-stroke 13.99⁰- c_l -0.64025*	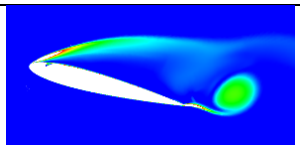 *Down-stroke 13.99⁰ c_l - 0.76935*	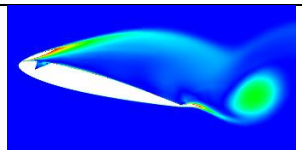 *Down-stroke 13.99⁰ c_l -0.77076*

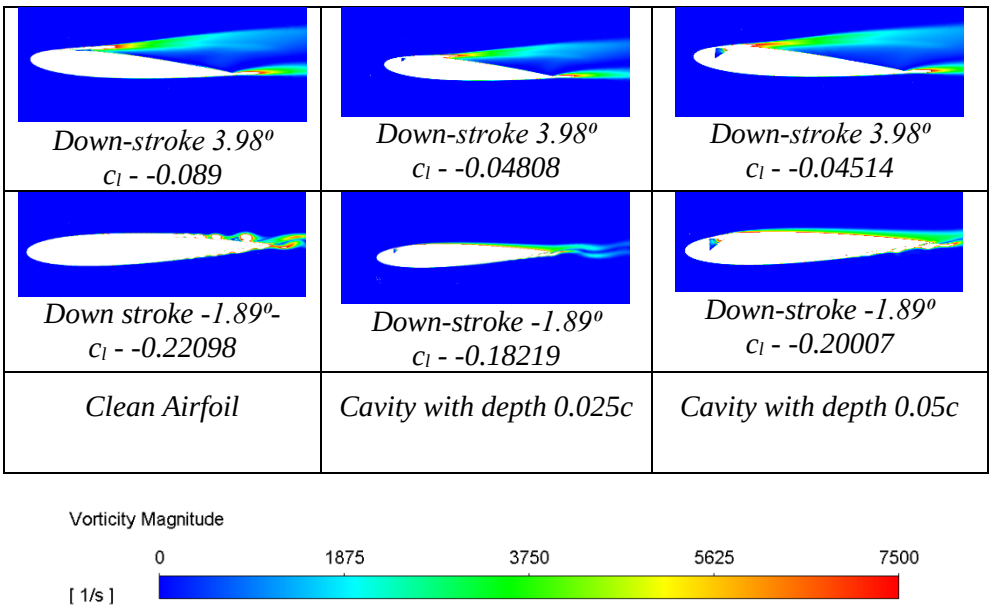

Figure 6.4: Vorticity Magnitude for the airfoil with cavity located at 0.10c during down-stroke motion

As the AOA reduces, the suction on the windward surface also increases, making the lift much smaller than the values during upstroke at the same AOA. At low AOAs, the suction on the windward becomes higher than the suction produced by the leeward surface as can be seen in Fig. 6.5 (d). The consequence is a negative lift produced by airfoils below α = 7° and α = 5°, for clean configuration and configurations with the cavity, respectively.

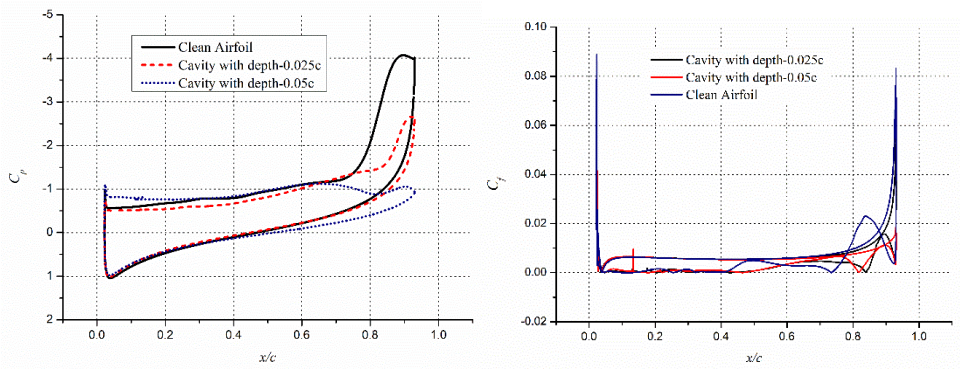

(a) Down-Stroke 24.89⁰-Pressure *(b) Down-Stroke 24.89⁰-Skin Friction*

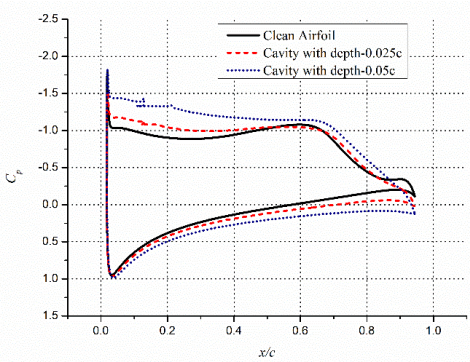

(c) Down-stroke 22.21⁰-Pressure

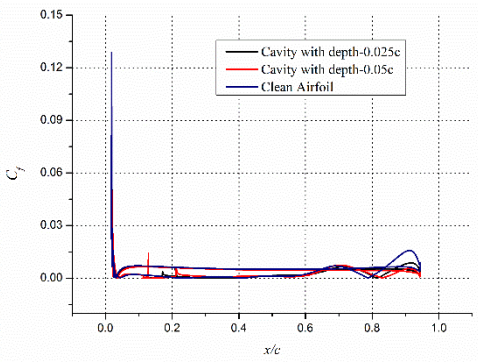

(d) Down-stroke 22.21⁰-Skin Friction

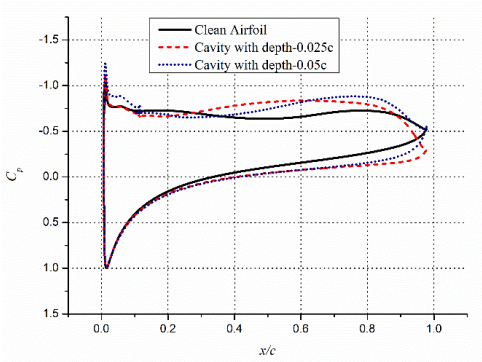

(e) Down-stroke 13.99⁰-Pressure

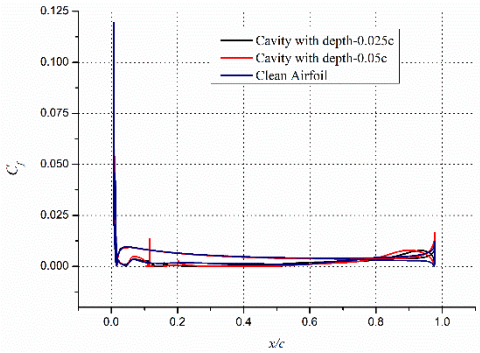

(f) Down-stroke 13.99⁰-Skin Friction

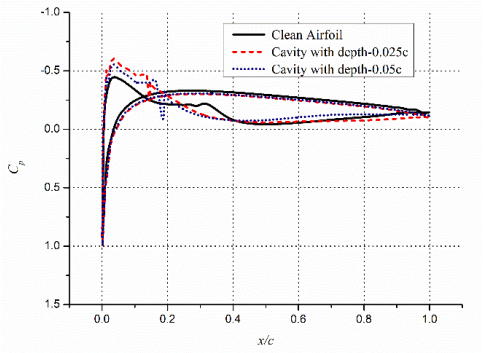

(g) Down-stroke 3.98⁰-Pressure

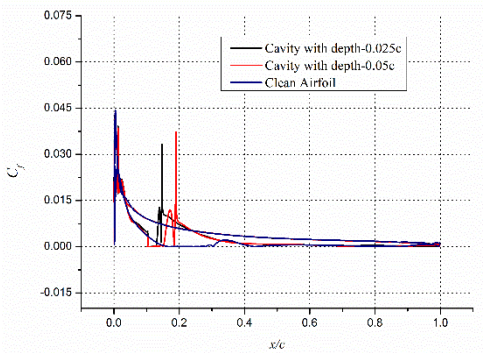

(h) Down-stroke 3.98⁰-Skin Friction

Figure 6.5: Surface pressure distribution during upstroke motion

The negative lift at small AOAs can also be explained through the intermittency contours as shown in Fig. 6.6. As can be seen in Fig. 6.6, a small laminar separation bubble is observed for the configurations at α = 3.99°. The flow aft of the bubble is detached for the clean airfoil whereas flow separation happens aft of the cavity for the airfoil with the cavity, as can be seen in Figs. 6.6 (b) and (c). There is thus an enhanced suction ahead of the cavity, which causes an

increase in the lift for an airfoil with the cavity. Figure 6.6 also shows similar suction on the windward surface for all configurations.

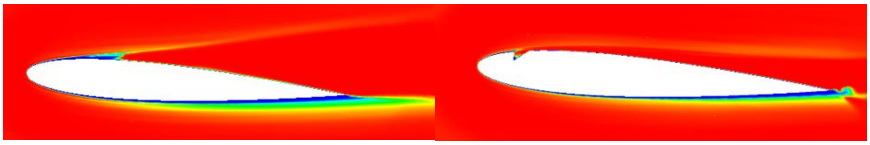

(a) Clean Airfoil (b) *Depth 0.025c*

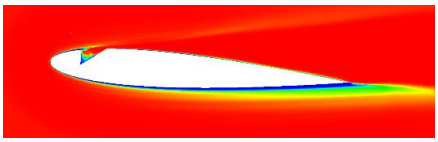

(c)Depth 0.05c

Figure 6.6: Flow Intermittency for various airfoil configurations α = 3.98º, during down-stroke

6.1.2 EFFECT OF TRIANGLE SHAPED CAVITY AT 0.25C LOCATION

The effect of the triangular cavity, especially with depth 0.05c, located at 0.25c on the suction surface is significantly different from cavities located at 0.1c location, as can be seen in Fig. 6.7. The airfoils with cavity of depths 0.025c and 0.05c, located at 0.25c, stall at α = 22.5° and α = 20°, respectively. Similar to the airfoils with a cavity at 0.1c, the oscillations in lift and drag are significantly diminished by the presence of cavity and the lift values are similar to those for the clean configuration during the upstroke, as can be seen in Fig. 6.7 (a). The drag rise is also severe from α = 15° onwards, as compared to the clean configuration and the airfoils with the cavity at 0.1c location, as can be seen in Fig. 6.7 (b). Also unlike the airfoil with a cavity at 0.1c location, the lift produced by the airfoil with the shallower cavity is oscillatory up to moderate AOAs, due to the formation of roll-up vortices on the suction surface during the upstroke, as can be seen in the vorticity contours in Fig. 6.8. The vortices on the airfoil with the cavity of 0.025c depth have however stronger vortices,

causing deeper oscillations and higher time-averaged lift values at moderate AOAs, as compared to the clean configuration. Even the drag coefficient values for the airfoil with the shallower cavity are highly oscillatory, during the upstroke motion as can be seen in Fig. 6.7. The time-averaged values of the drag coefficients for an airfoil with the shallower cavity are higher than both the clean airfoil and the airfoil with a deeper cavity at AOAs between α =12° and 18°.

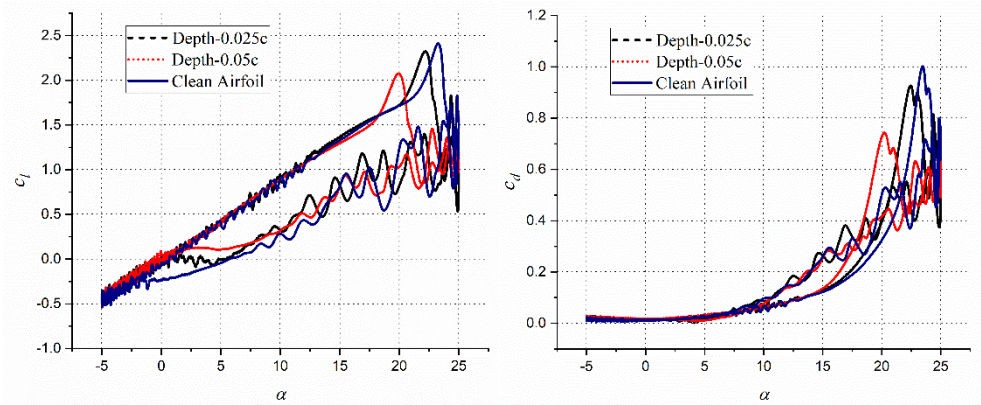

(a) Coefficient of Lift versus α *(b) Coefficient of Drag versus α*

Figure 6.7: Aerodynamic characteristics of the cavity at 0.25c Location

For the airfoils with a deeper cavity at 0.25c location, the transition of boundary to turbulent takes place at the cavity, at smaller AOAs, making the flow attached and stable, with no roll up vortices as can be seen in Fig. 6.8. The attached turbulent flow produces significant suction on the upper surface resulting in enhanced lift up to moderate AOAs. Even the drag is relatively low at small and moderate AOAs due to reduced wake size, although the skin friction increases. As the AOA increases beyond α =13°, the flow unsteadiness dies out for both the clean airfoil and the airfoil with shallower cavity due to the transition of the boundary layer into a turbulent one. The pressure distribution is similar for all configurations in the AOA in the range of α =13° to α = 18°, as can be seen in Fig. 6.9 (e), which shows surface pressure distribution at α = 14.76°. In Fig. 6.9 (e), a small reduction in the upper surface suction can be seen at the cavity location. This causes the lift produced by the airfoil with the deeper cavity to be

slightly lesser than that for the clean and the airfoil with the shallower cavity. The surface pressure distribution curves at AOAs less than α =13°, during upstroke motion, viz. Figs. 6.9 (a), (b), (c), and (d), clearly show the presence of multiple rolls vortices on both suction and pressure surfaces for clean airfoil and the airfoil with the shallower cavity. The skin friction coefficient explains the reattachment and separation in Fig. 6.10 (a), (b), (c).

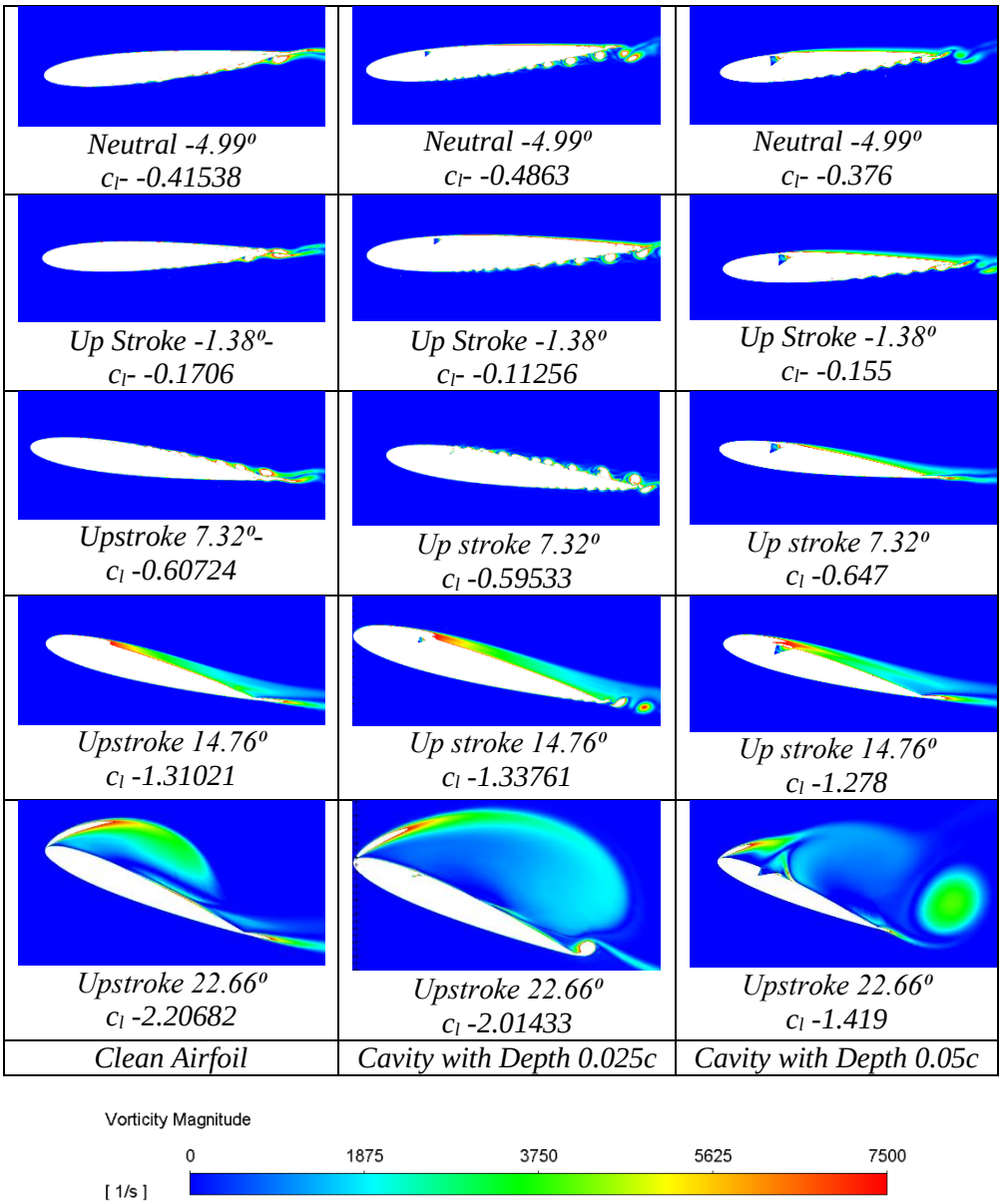

Figure 6.8: Vorticity magnitude at the Triangle shaped cavity with depth at 0.25 location

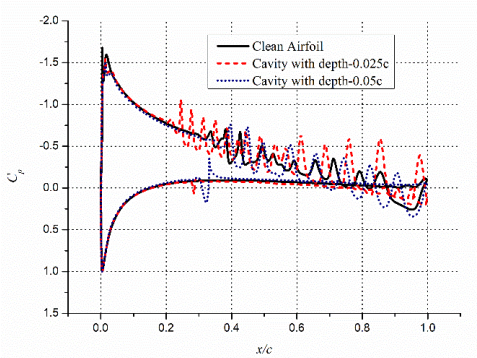

(a) Neutral -4.99º

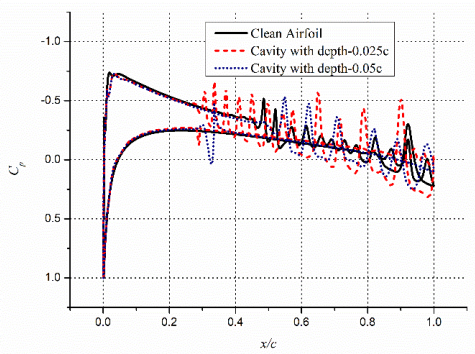

(b)Up Stroke -1.38º

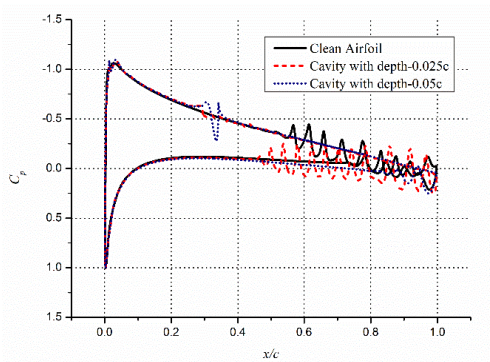

(c) Upstroke 4.728º

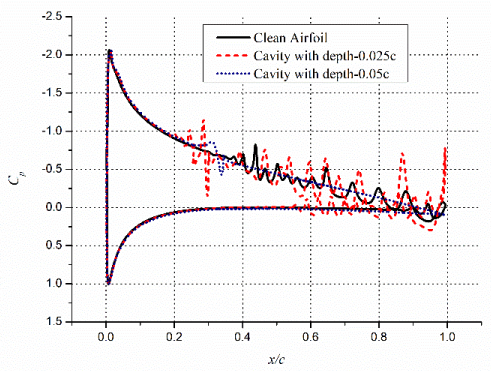

(d) Up stroke 7.32º

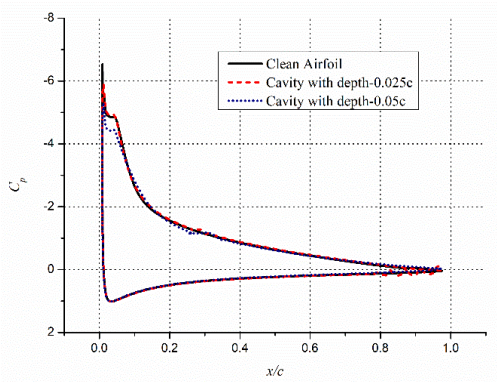

(e) Up stroke 14.76º

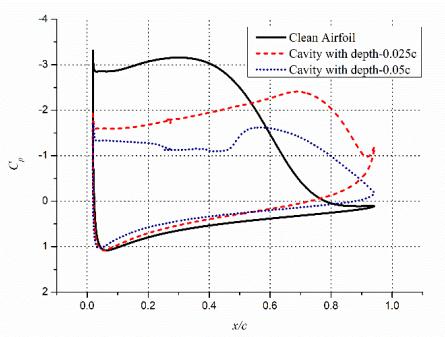

(f) Upstroke 22.66º

Figure 6.9: Surface pressure distribution during upstroke motion

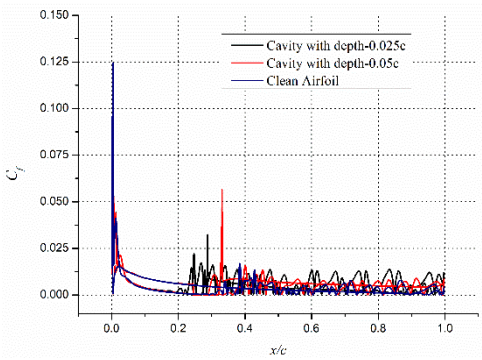

(a) Neutral -4.99º

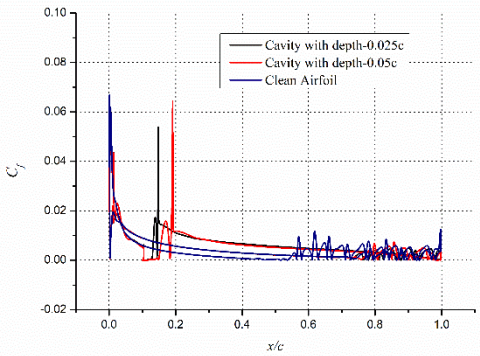

(b)Up Stroke -4.728º

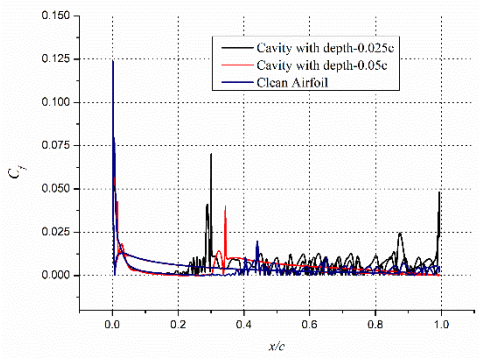

(c)Up stroke 7.32º

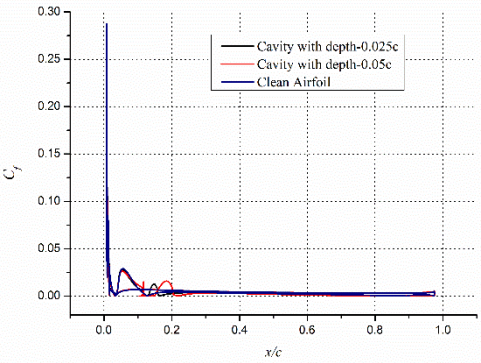

(d) Up stroke 14.76º

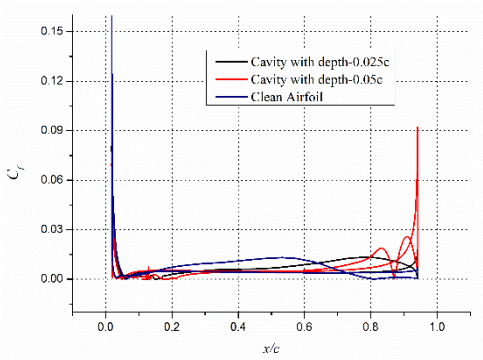

(e) Upstroke 22.66º

Figure 6.10: Skin Friction variation during upstroke motion

As the AOA is further increased, during the upstroke motion, the airfoil with the deeper cavity stalls at α =20°, with flow separation near the leading on the upper surface. A dominant anticlockwise vortex, however, forms near the trailing as can be seen in the vorticity contours at α = 22. 66°, in Fig. 6.8, which provides some lift to the airfoil. At this AOA, the clean airfoil has a dominant clockwise vortex near the leading providing significant suction, as can be seen

in Fig. 6.9 (f). The airfoil with the shallower cavity, however, has stalled at 22.5°, with significant suction from the primary clockwise vortex, as seen in Fig. 6.8.

As the AOA is further increased after stall, vigorous vortex shedding from both the leading edge and the trailing edge starts, causing oscillations in lift and drag values. This vortex shedding phenomena continue as the AOA is reduced during the downstroke motion as can be seen in Fig. 6.11, causing oscillations in lift and drag values. As can be seen in Fig. 6.11, this vortex shedding phenomena is progressively weaker in airfoils with a shallower and deeper cavity as compared to the clean airfoil. Moreover, as with the cavity at 0.1c location, this cyclic phenomenon is out of phase of each configuration. Nevertheless, the strength of the vortices shed from the airfoil is highest for the clean airfoil and thus the amplitudes of oscillations in lift and drag are the largest for the clean configuration. The strength of these vortex shedding reduces as the AOA decreases during the downstroke motion, for all configurations. In fact at AOAs below $\alpha = 15°$, the clean configuration shows minimal oscillation in the lift as it reduces with AOA. The airfoil with the shallower cavity, however, shows significant oscillations even below $\alpha = 15°$, during the downstroke motion as can be observed in Fig. 6.11. During the downstroke, the suction from the leading half of the upper surface is significantly diminished while some suction is provided by the vortices at the trailing edge, as can be seen in Fig. 6.13.

The vortex shedding and the oscillations in lift finally die out at AOAs below $\alpha = 8°$ for both clean airfoil and the airfoil with a shallower cavity as the shear layer attaches on the leeward surface during the downstroke motion. However, at AOAs below $\alpha = 5°$, the airfoil with the shallower cavity shows significant oscillation due to the shedding of roll-up vortices. These vortices are formed on the airfoil with a shallower cavity due to the presence of cavity at 0.25c and the existence of a laminar boundary layer as can be seen in Fig. 6.12. As can be seen in the surface pressure distribution graphs viz. Fig. 6.13, at AOA below $\alpha = 6°$, the suction on the windward surface exceeds the suction on the leeward

surface during the downstroke motion. This causes a negative lift at these small AOAs as observed in Fig. 6.7 (a). For smaller AOAs, the roll-up vortices are seen on the windward surface for all configurations, but the airfoil with a shallower cavity produces these vortices excessively as can be seen in Fig. 6.11 and as also reflected in the surface pressure distribution graphs in Fig 6.13 and skin friction coefficient variation in Fig. 6.14.

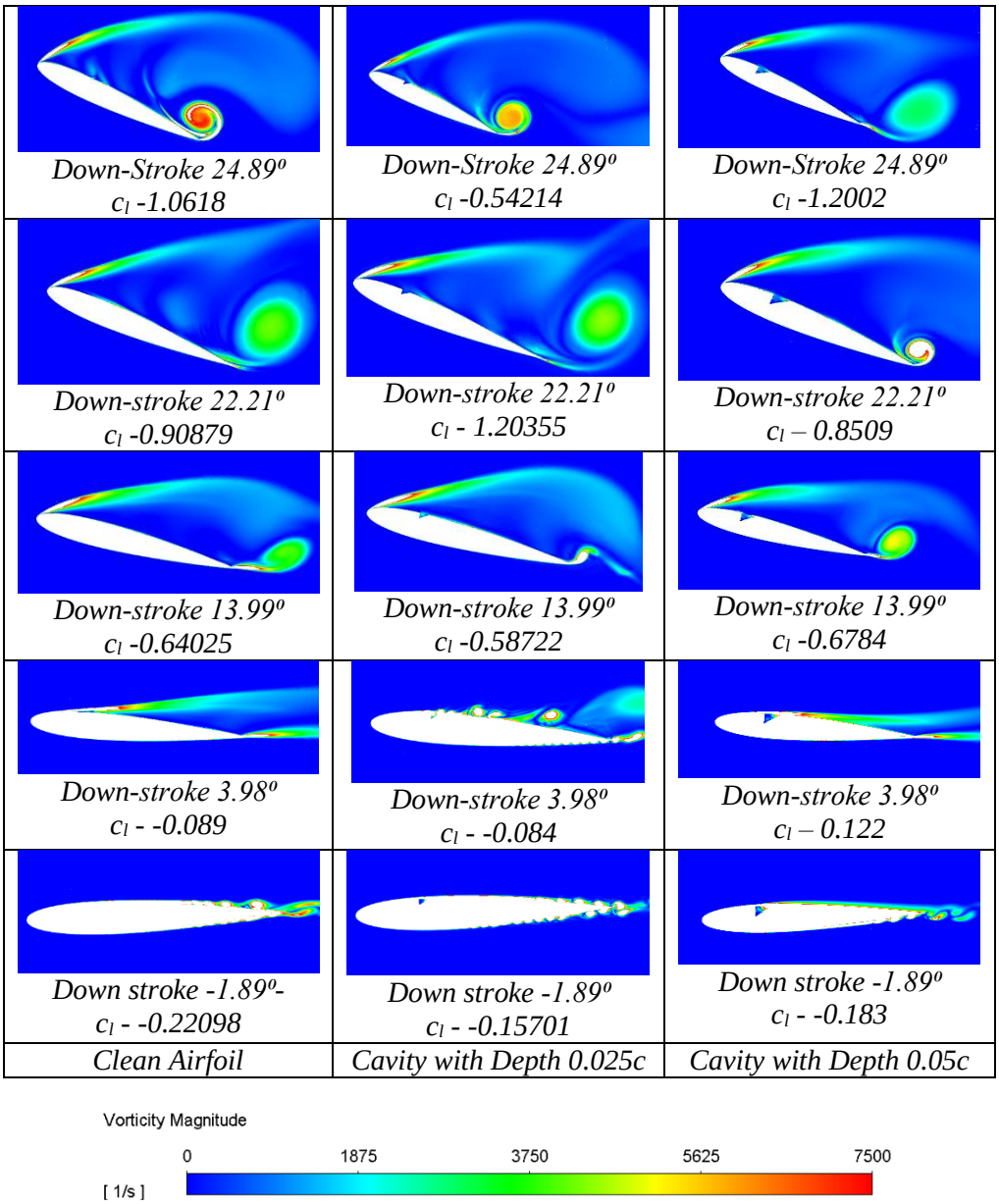

Figure 6.11: Vorticity magnitude at the Triangle shaped cavity with depth at 0.25 location

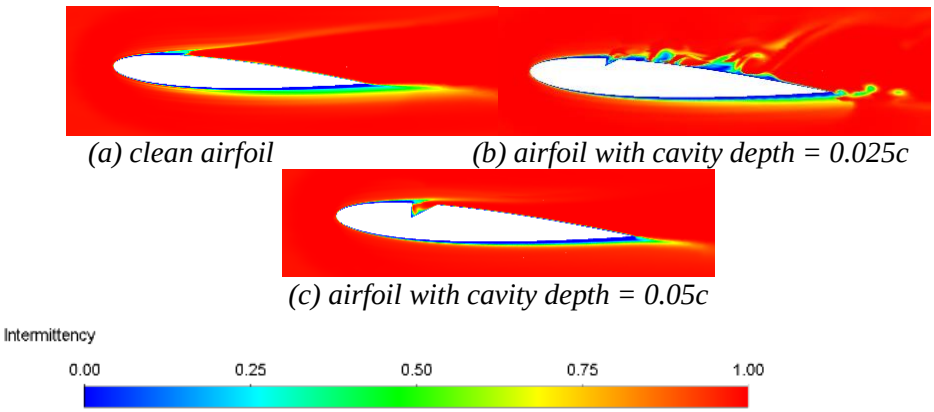

Figure 6.12: Intermittency Contours for airfoil with cavity at 0.25 location, α = 3.98°

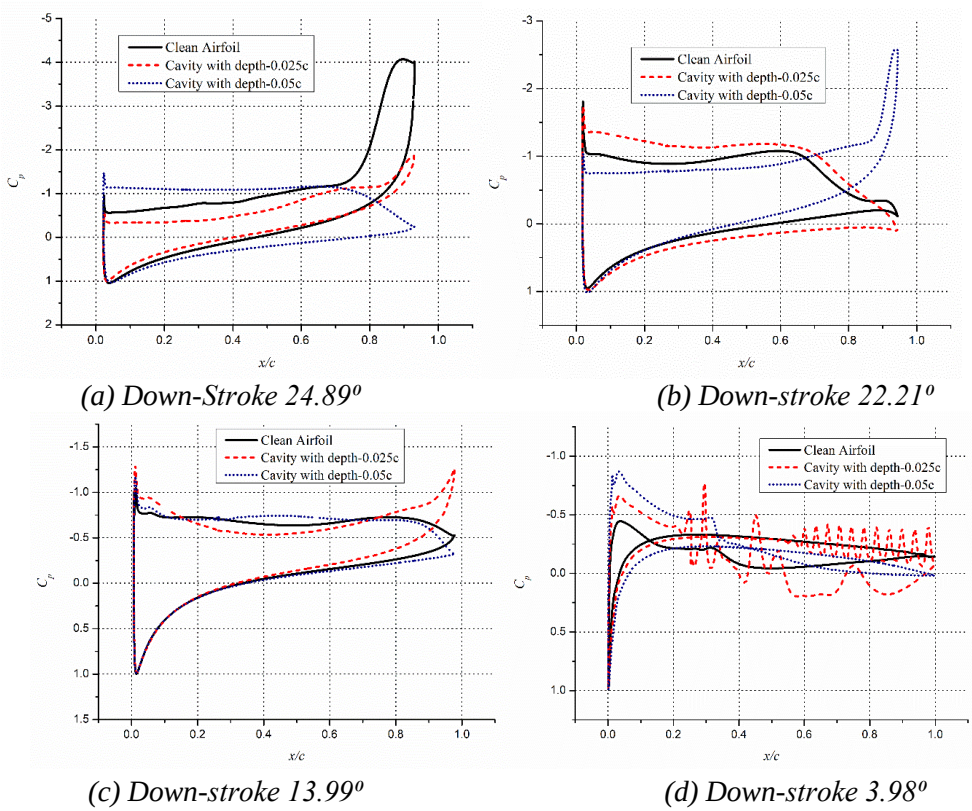

Figure 6.13: Surface pressure distribution during down-stroke motion

Unlike the airfoil with a cavity at 0.1c location, the airfoil with a deeper cavity show significantly improved lift at very low AOAs during the downstroke motion. As other configurations yield negative lift, the airfoil with a deeper cavity at 0.25c provides positive lift due to improved suction ahead of the cavity and a turbulent boundary layer aft of the cavity that keeps flow oscillations at

bay. This positive lift continues up to zero incidences, below which small-scale oscillations start even for the deeper cavity.

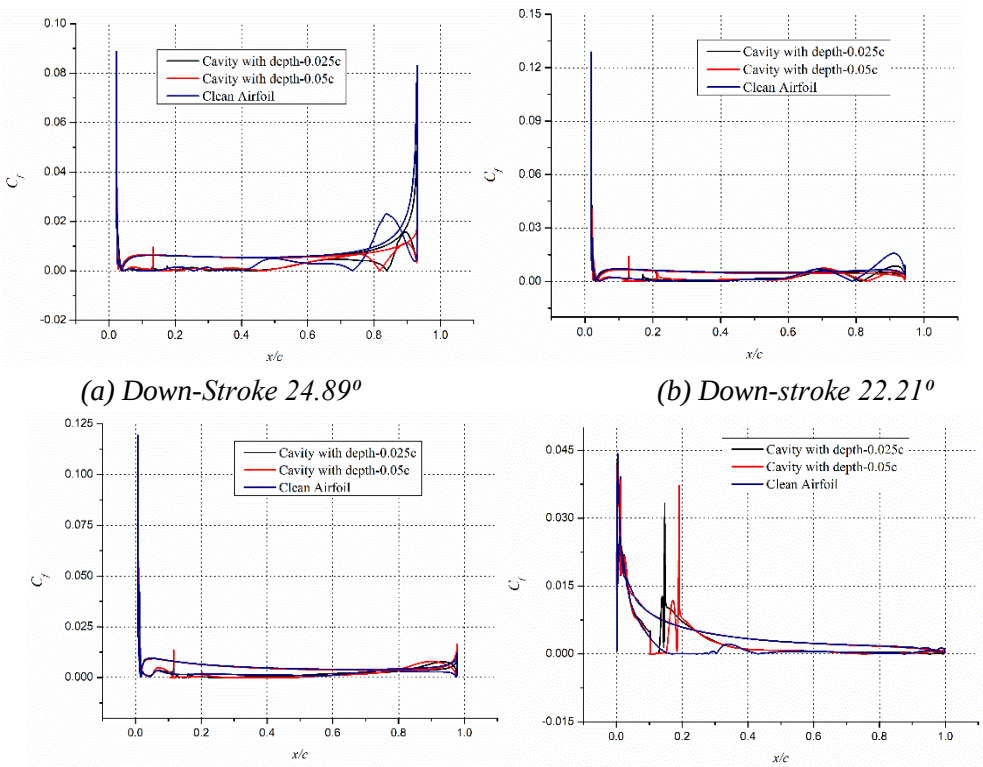

(a) Down-Stroke 24.89⁰ *(b) Down-stroke 22.21⁰*

(c) Down-stroke 13.99⁰ *(d) Down-stroke 3.98⁰*

Figure 6.14: Skin Friction distribution during down-stroke motion

6.1.3 EFFECT OF TRIANGLE SHAPED CAVITY AT 0.50C LOCATION

The aerodynamic characteristics of airfoils with a cavity at 0.5c on the suction surface are again significantly different from the aerodynamic characteristics of airfoils with a cavity at other locations investigated. As can be seen in Fig. 6.15, the airfoil with the cavity of depth 0.05c shows no stall up to α = 25°, which the upper limit of the AOA during the upstroke motion. Even the drag is significantly reduced during the upstroke motion for the airfoil with a deeper cavity at 0.5c, as compared to the clean airfoil and airfoil with cavity at other locations and depth, as can be seen in Fig. 6.15 (b).

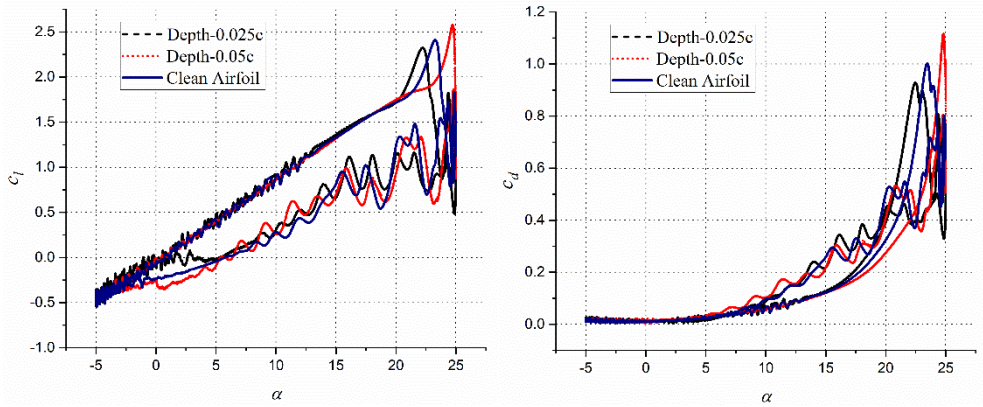

(a) Coefficient of Lift versus α *(b) Coefficient of Drag versus α*

Figure 6.15: Aerodynamic characteristics of the circular protrusion at 0.50c location

At low and moderated AOAs during the upstroke motion, the lift curve for the airfoil with a cavity at 0.5c location is similar to those for cavity at other locations with smaller cavity producing oscillations in lift and drag coefficient like the clean airfoil. Even the vorticity contours for an airfoil with a shallower cavity at 0.5c, as shown in Fig. 6.16, are similar to those of airfoils with a shallower cavity at other locations. As with other locations, the deeper cavity offers steady lift even at low AOAs due to the transition of the boundary layer into a turbulent one, on the suction surface. Some unsteadiness observed for the airfoil with a deeper cavity at 0.5c location is due to the formation of roll-up vortices on the pressure side of the airfoil, especially at low positive AOAs, because of the laminar nature of the airfoil. As the AOA is increased beyond α =13°, the boundary layer for the clean as well as the airfoil with shallower cavity turns turbulent very close to the leading edge, with the attached flow all along, separating near the trailing edge in all cases as can be seen in Fig 6.17. This makes the lift and the drag steady, of similar values for an airfoil with a cavity at 0.5c and for an airfoil without a cavity. This similarity in lift values is observed until α = 21°. The drag coefficients, however, behave differently. Beyond α =16°, during the upstroke, the drag coefficient for an airfoil with the shallower cavity is increased, whereas, for airfoil with the deeper cavity, it decreases as compared to the clean configuration.

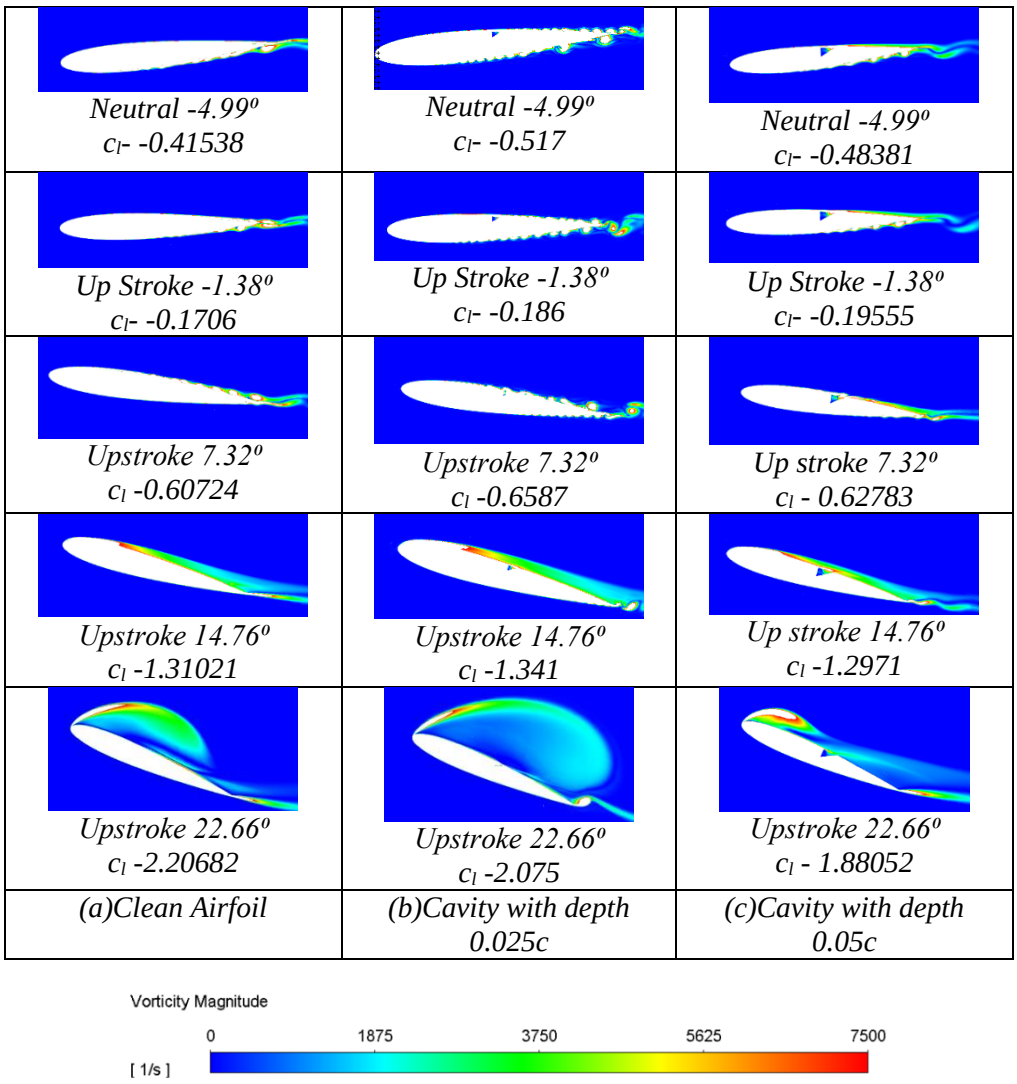

Figure 6.16: Vorticity contours for airfoils with cavity at 0.50c location, during upstroke motion

The decrement in the drag, observed for an airfoil with a deeper cavity at 0.5c, beyond α =16°, is because of the action of the deeper cavity that reduces the extent of the primary clockwise vortex, as can be seen in Fig. 6.16, for α = 22.66°. The smaller size of the clockwise vortex, ahead of the cavity, remains attached to the surface for a longer period creating significant lift. The drag, however, is less as compared to the clean airfoil as the clean configuration has a bigger primary clockwise vortex, which creates a wider wake and increased pressure drag. The same is true for the airfoil with the shallower cavity, which has an even bigger vortex than the clean configuration as can be seen in Fig.

6.16. The turbulent flow detaches aft of the cavity, for the airfoil with a deeper cavity at 0.5c as can be seen in Fig. 6.16 as well, which shows the intermittency contours at α = 22.66°.

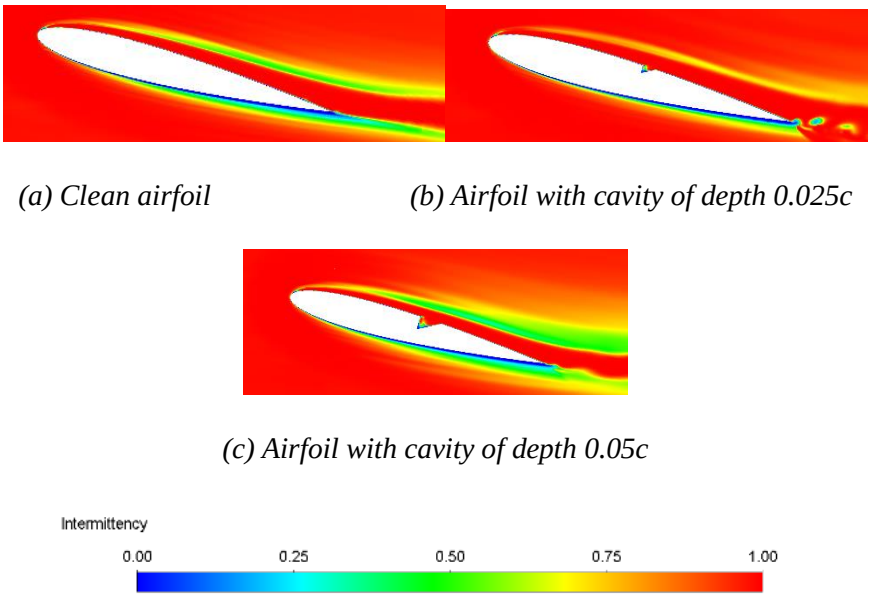

(a) Clean airfoil *(b) Airfoil with cavity of depth 0.025c*

(c) Airfoil with cavity of depth 0.05c

Figure 6.17: Intermittency Contours for airfoil with cavity at 0.5c location, α = 14.76°, during upstroke

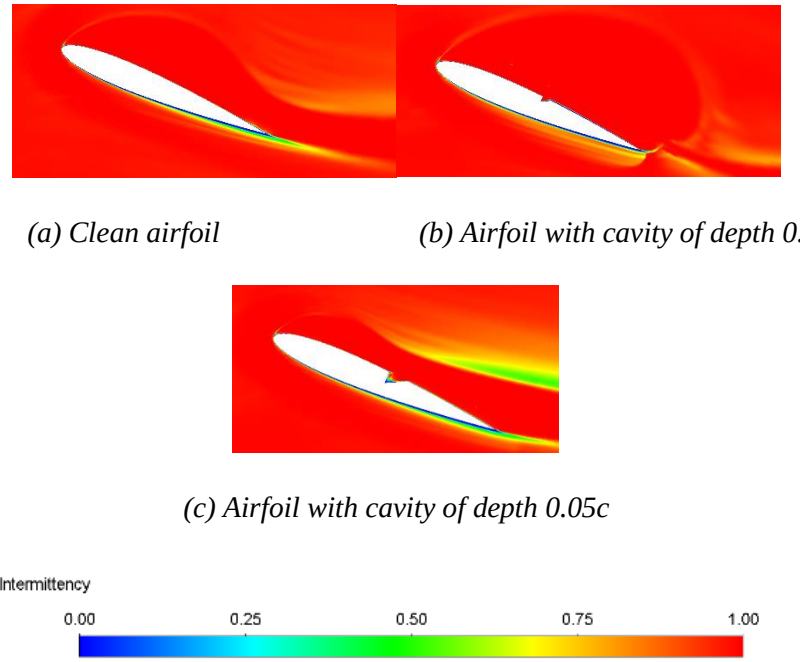

(a) Clean airfoil *(b) Airfoil with cavity of depth 0.025c*

(c) Airfoil with cavity of depth 0.05c

Figure 6.18: Intermittency Contours for airfoil with cavity at 0.5c location, α = 22.66°, during upstroke

The surface pressure distribution for airfoils with and without cavity at selected AOAs, during the upstroke motion, is illustrated in Fig. 6.19. These figures clearly show the presence of roll-up vortices on the rear half of airfoil for clean airfoil and configuration with the shallower cavity, at low AOAs as visible in Figs. 6.19 (a) and (b). At α = 14.76°, a similarity in pressure distribution is observed as shown in Fig. 6.19 (c). This suggests a steady and equivalent lift at this AOA for all configurations with and without cavity at 0.5c. A strong suction created by a relatively smaller vortex ahead of the cavity at higher AOAs is seen in Fig. 6.19(d), for the airfoil with a deeper cavity at 0.5c location. The same figure also demonstrates the destruction of suction ahead of the cavity for the airfoil with shallower cavity while a mid-chord suction for the clean configuration at α = 22.66°, just before the stalling for the clean airfoil.

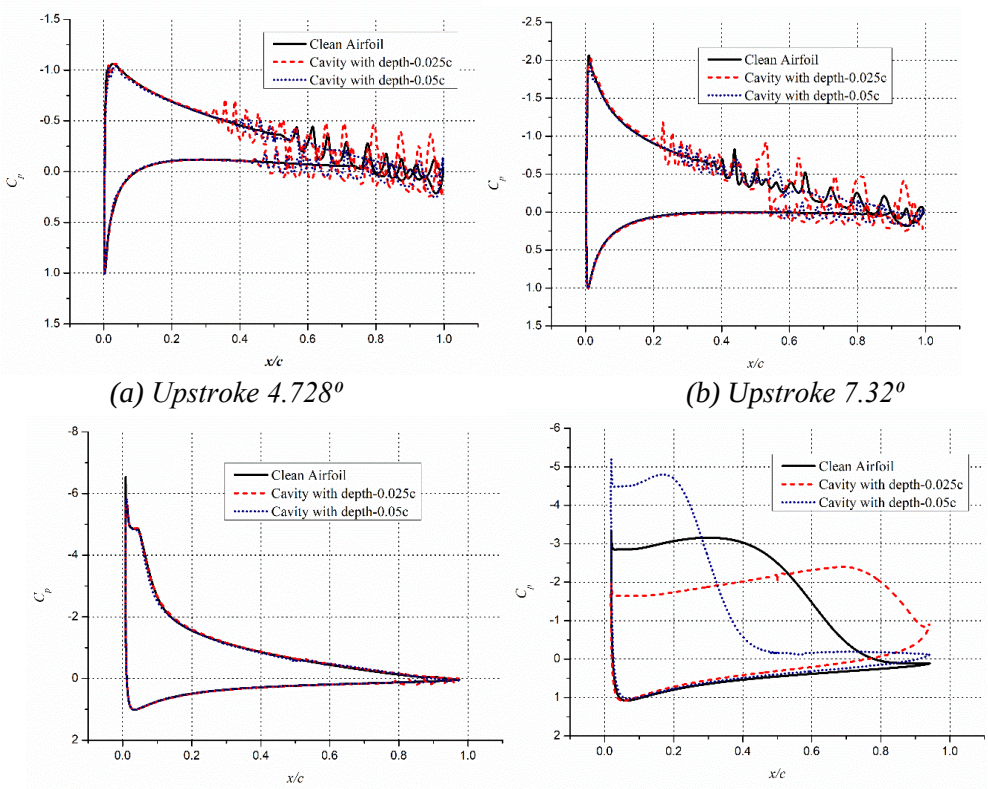

(a) Upstroke 4.728º *(b) Upstroke 7.32º*

(c) Upstroke 14.76º *(d) Upstroke 22.66º*

Figure 6.19: Surface pressure distribution over airfoil with cavity located at 0.50c, during upstroke motion

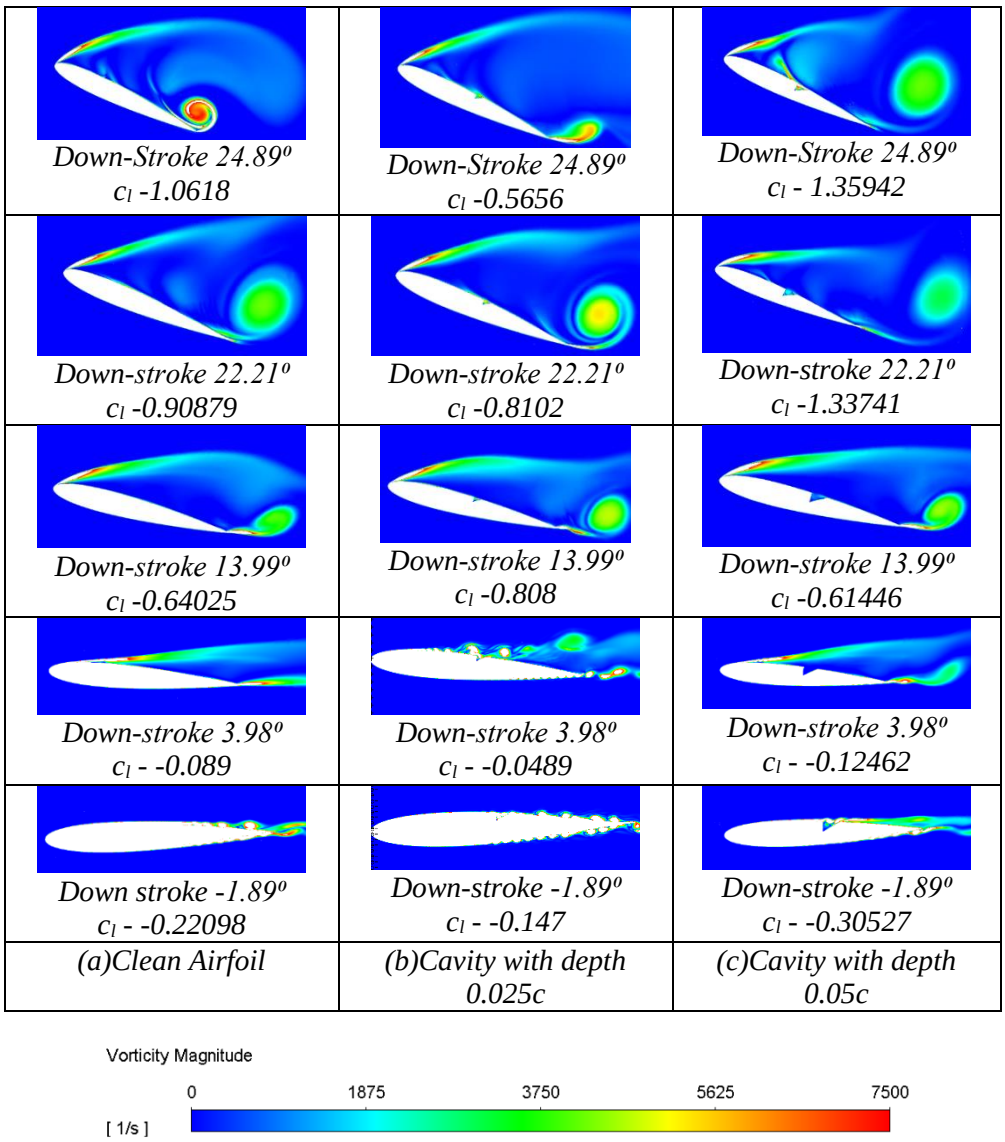

Figure 6.20: Vorticity contours for airfoils with cavity at 0.50c location, during down-stroke motion

During the downstroke, the lift is highly oscillatory due to the vortical nature of the lift generated. Unlike the airfoils with a cavity at 0.1c and 0.25c locations, the lift curve for an airfoil with a cavity at 0.5c locations shows no respite from oscillations even at low AOAs, even for the airfoil with the deeper cavity, as can be seen in Fig. 6.15 (a). The oscillations in the lift are higher for the airfoil with a deeper cavity at 0.5c, at moderate and low AOAs, during the downstroke. This is because of the large-scale vortex shedding caused by the deeper cavity, which oozes out small vortices trapped inside it, periodically, causing flow

unsteadiness, as can be seen in Fig. 6.20. Even though the flow is attached to the surface at low AOAs, the oozing out of vortices from the cavity, as can be seen in Fig. 6.20, makes the flow unsteady for airfoils with a cavity at 0.5c location. As the flow is detached before the cavity during the down-stroke motion, the turbulence fails to stabilize the unsteadiness caused by the cavity itself. The lift values thus, for an airfoil with a deeper cavity go significantly negative, while for an airfoil with a shallower cavity oscillate around zero due to vortex shedding from both upper and lower surfaces as can be seen in Fig. 6.19 (b). As far as the drag behavior is concerned, it is oscillatory for all configurations and the average drag decreases with reducing AOA, like for airfoils with a cavity at other locations. The drag curve for the down-stroke motion merges with that for the upstroke motion at $\alpha = 5°$. The oscillatory nature of the lift and drag during the down-stroke motion is emphasized by the signs of vortices in the surface pressure distribution curves, shown in Fig. 6.20.

A can be seen in Fig. 6.21 (a), at the start of the down-stroke motion, the lift of clean configuration is entirely due to an anticlockwise vortex at the trailing edge while the airfoil with shallower cavity remains stalled with little suction; the airfoil with a deeper cavity, however, shows significant suction both ahead and aft of cavity. As the anticlockwise vortex is shed away, the clean airfoil loses the suction coming from the latter half of the suction surface, while the airfoil with a deeper cavity continues to enjoy enhanced suction due to a smaller vortex ahead of the cavity, as can be seen in Fig. 6.21 (b). At further smaller AOAs, as the clockwise vortex is shed away and anticlockwise vortex gains strength at the trailing edge, the lift and drag values oscillate. As shown in Fig. 6.21 (c), all configurations seem to be in the same phase after shedding the clockwise vortex near the leading edge. At very low AOAs, as shown in Fig. 6.21(d), the suction on the pressure surface exceeds the suction on the suction surface giving a negative lift for clean airfoil as well as the airfoil with a deeper cavity. The pressure distribution on the airfoil with a shallower cavity on the other hand shows the presence of multiple vortices on the suction surface at $\alpha = 3.98°$. This

makes the lift coefficient values highly oscillatory during the down-stroke, for this configuration. Fig. 6.22 expresses the skin friction variation over an airfoil during up and down stroke where the roll-up vortices shed from the surface of the airfoil.

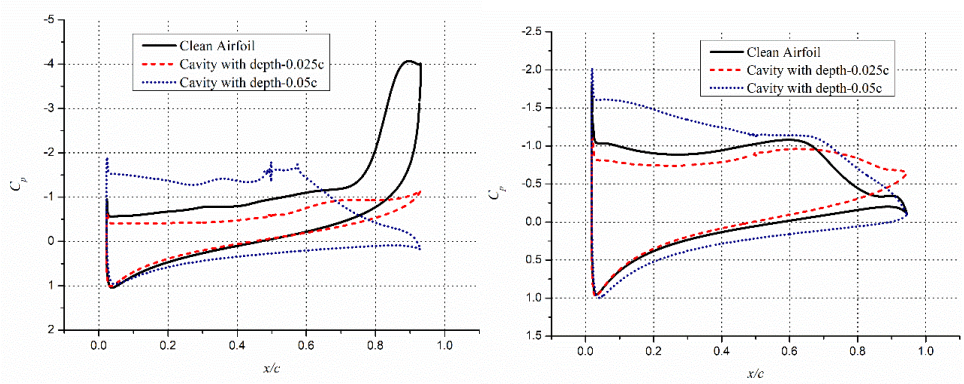

(a) Down-Stroke 24.89º *(b) Down-stroke 22.21º*

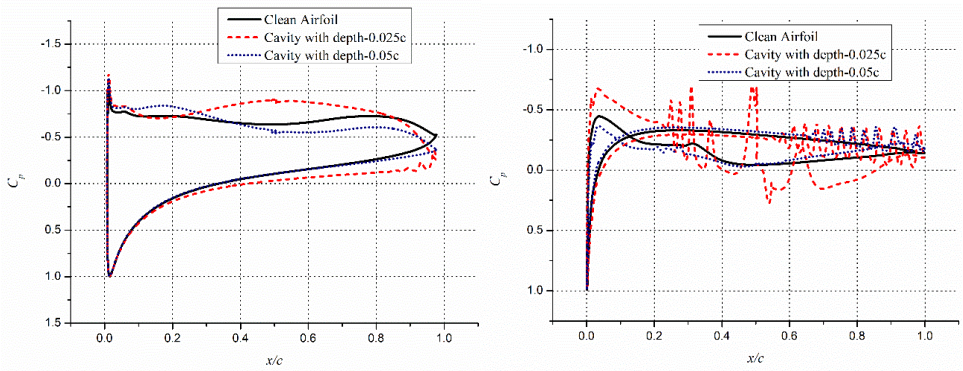

(c) Down-stroke 13.99º *(d) Down-stroke 3.98º*

Figure 6.21: Surface pressure distribution over airfoil with cavity located at 0.50c, during down-stroke motion

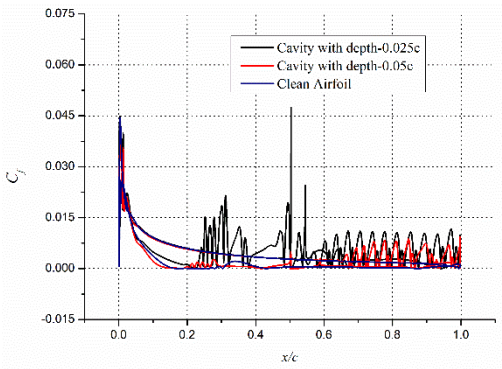

(a) Down-stroke 3.981º

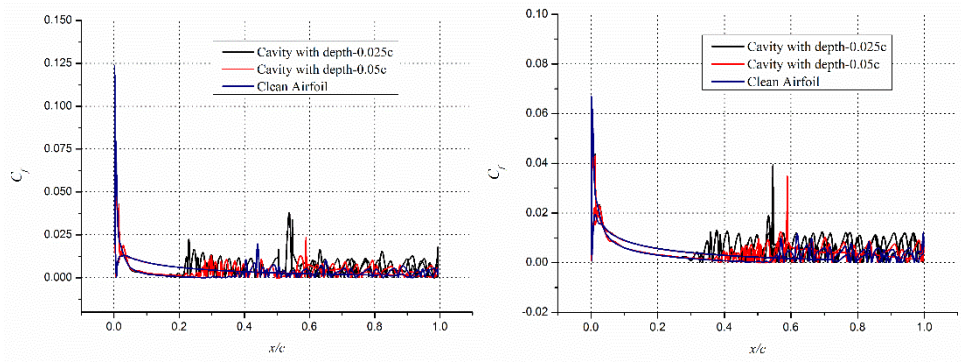

(c) Up-stroke 7.32º *(d) Up-stroke 4.728º*

Figure 6.22: Skin Friction distribution over airfoil with cavity located at 0.50c, during up and down-stroke motion

6.2 CIRCULAR PROTRUSION ON DYNAMIC STALL

Numerical analysis is performed to investigate the effect of circular protrusion on dynamic stall characteristics of NACA 0012 at a Reynolds number of 135000. The protrusion is placed at 0.05c, and 0.10c locations on the suction surface and the height of these protrusions is kept to be 0.005c, 0.01c, or 0.02c. The dynamic stall characteristics are assessed by allowing the airfoil to pitch about the quarter chord with mean AOA at α =10°, with α = -5° and α = 25° being the minimum and the maximum angle during this pitching motion.

6.2.1 EFFECT OF CIRCULAR PROTRUSION AT 0.05C LOCATION

The aerodynamic characteristics of a clean airfoil and airfoil with protrusions located at 0.05c, on the suction surface are illustrated in Fig. 6.23. As can be seen in Fig. 6.23, the addition of protrusion other than the one with h = 0.02c does not affect the lift values much during the upstroke motion. The stalling angle, however, reduces progressively as the height of the protrusion is increased. The airfoil with the smallest protrusion stalls at α = 22.5°, which is very close to the stalling angle of the clean airfoil, i.e. α = 23.5°, while the airfoil with the largest protrusion stalls as early as α = 17°. As far as the drag is concerned, there is a detrimental rise in the drag coefficient for an airfoil with

larger protrusions of height h= 0.01c and 0.02c, compared to the clean configuration. These increments start at very low AOAs during the upstroke motion as can be seen in Fig. 6.23 (b). The larger protrusions on the other hand stabilize the flow by eliminating the formation of roll-up vortices on the suction during the upstroke motion, as can be seen in Fig. 6.24. As can be seen in Fig. 6.24, the flow over the airfoil smallest protrusion and the clean airfoil is highly unsteady as the vortex shedding phenomena continues up to α =14°, due to the laminar nature of the boundary layer on the pressure surface. On the airfoils with a larger protrusion, on the other hand, the shear layer detached from the protrusion reattaches as a turbulent boundary layer, eliminating roll-up vortices from the suction surface. This enhances the lift coefficient as well as the frictional drag of the airfoil at low to moderate AOAs.

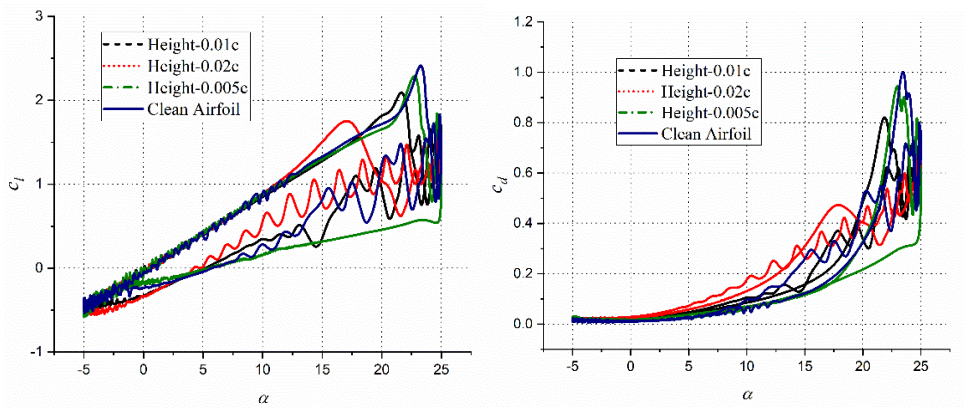

(a) Coefficient of Lift versus α *(b) Coefficient of Drag versus α*

Figure 6.23: Aerodynamic characteristics of the circular protrusion at 0.05c location

The turbulent separation at higher AOAs, for an airfoil with larger protrusions also enhances the pressure drag significantly. A large increase in the lift observed before stalling for an airfoil with the largest protrusion is because of the presence of a dominant clockwise vortex aft of the protrusion. As the AOA is increased beyond stall, vigorous vortex shedding starts alternately from the leading and trailing edge of the airfoil with protrusion as seen in Fig. 6.24. This causes high amplitude oscillations in the lift and drag coefficients, as seen in Fig. 6.23.

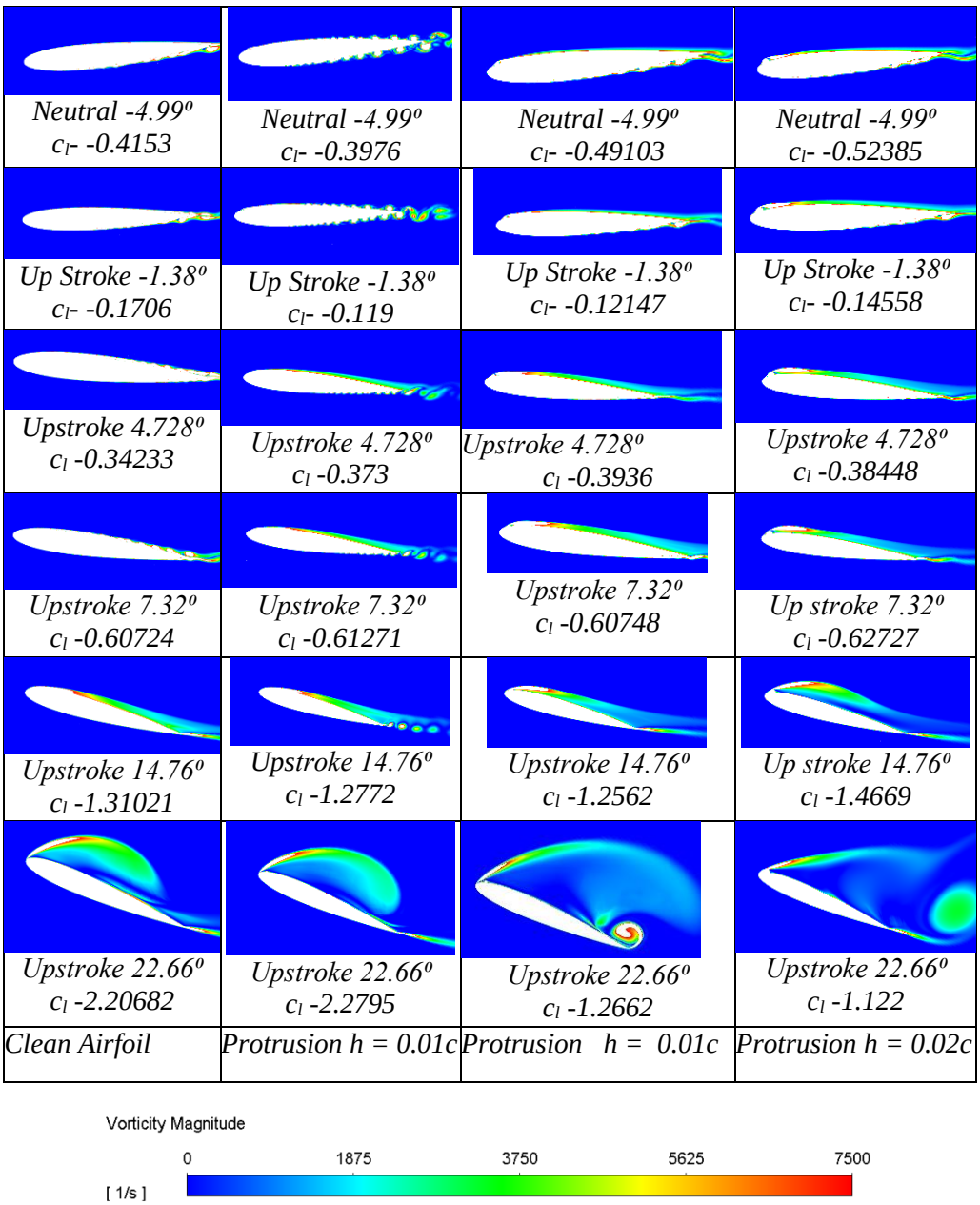

Figure 6.24: Vorticity contours for airfoils with protrusion at 0.05c location, during upstroke motion

Surface pressure distribution for selected AOAs, during the upstroke motion, for various airfoil configurations with a protrusion at 0.05c location is presented in Figs. 6.25 (a) – (f). As can be seen in Figs. 6.25 (a) and (b), at negative AOA, there is larger suction on the pressure surface, but the protrusions create a large local suction on the suction surface. This suction, however, is not sufficient to

create a positive lift and multiple roll-up vortices with sinusoidal pressure variations on both surfaces are observed at these small negative AOAs, during the upstroke motion. As the AOA is increased to positive values, a strong local suction is provided by the protrusions aft of the protrusion, as can be seen in Figs. 6.25 (c) and (d). This enhancement in protrusion aft of the protrusion comes with some local suction destruction on the protrusion itself. The loss in suction at the protrusion is higher for the larger protrusion height whereas the enhancement in the suction aft of the protrusion, due to the formation of separation bubble, is larger in extent for the bigger protrusion. Even the roll-up vortices disappear for larger protrusions at α =7.32° and above. This trend of reduced suction ahead of the protrusion and enhanced suction aft of the protrusion continues for moderate AOAs, as can be seen in Fig. 6.25(e). Both the destruction in suction and the enhancement in suction is increase with the size of the protrusion, making the lift for larger protrusion, higher at these moderate AOAs.

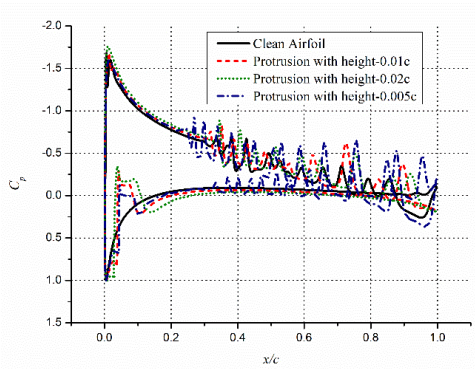

(a) Neutral -4.99º

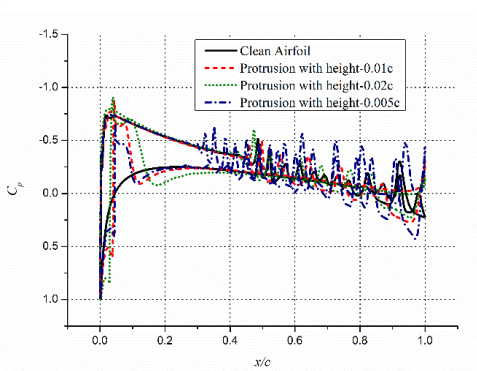

(b)Up Stroke -1.38º

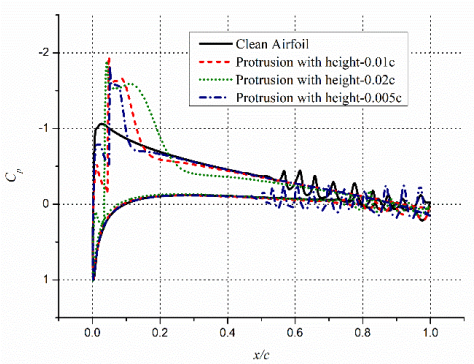

(c) Upstroke 4.728º

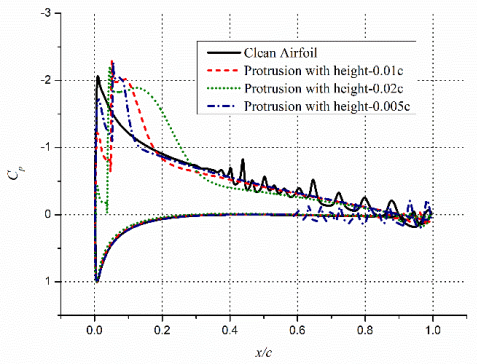

(d) Up stroke 7.32º

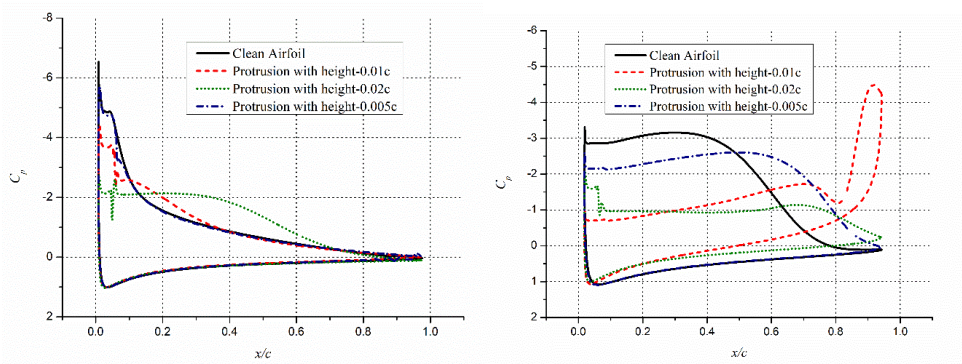

(e) Up stroke 14.76⁰ *(f) Upstroke 22.66⁰*

Figure 6.25: Surface pressure distribution over airfoil with protrusion located at 0.05c, during upstroke motion

However, as the AOA is further increased, the flow separated at the protrusion reattachs near the trailing edge, for larger protrusion, giving a large vortical lift before the stall. As the vortex leaves the surface, the airfoil stall, with the most lift coming from the suction produces by a vortex at the trailing edge as can be seen in Fig. 6.25 (f). Figure 6.25 (f) shows the instantaneous pressure distribution where the airfoils with larger protrusions are in stalled condition whereas the clean airfoil and the airfoil with the smallest protrusion at AOA before the respective stall.

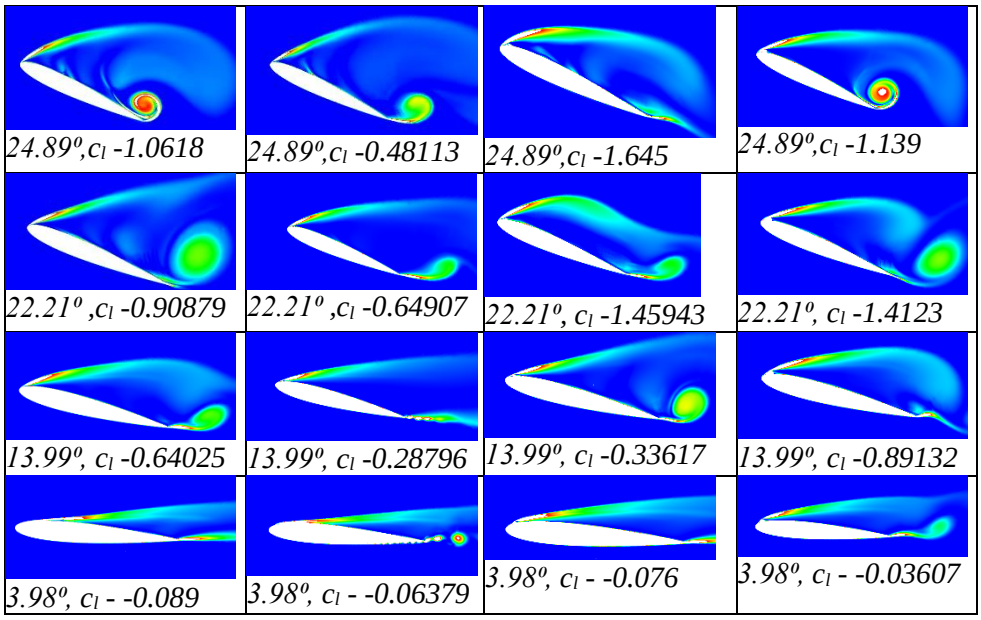

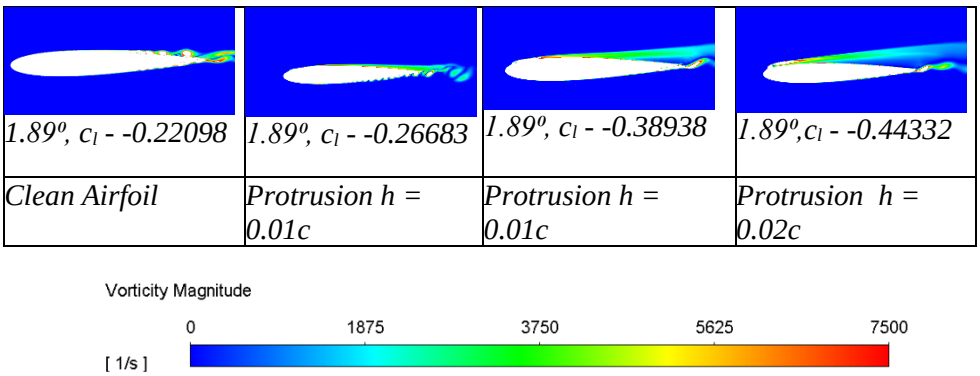

Figure 6.26: Vorticity contours for airfoils with protrusion at 0.05c location, during down-stroke motion

During the down-stroke motion, the lift produced is of vortical source for all configurations as can be seen in Fig. 6.26. The shedding of these vortices alternately from the leading and trailing edges make the lift and drag oscillation in nature as was seen in Fig. 6.23. At the start of down-stroke motion, i.e. α = 24.89°, all the configurations are in a stalled condition, but they are at different phases of their respective vortex shedding cycles. The clean airfoil has a strong anticlockwise vortex at the trailing edge while the airfoil with the smallest protrusion has its anticlockwise vortex just shed and downstream of the trailing edge. For protrusions with h= 0.01c, the shed vortex is at a relatively larger distance downstream and the clockwise vortex build-up is seen while the airfoil with the largest protrusion is in its next cycle with an anticlockwise vortex at the trailing edge. The result is strong at the trailing edge for the clean airfoil with destroyed leading suction, while smaller trailing edge suction and larger leading suction for airfoils with protrusion as can be seen in the surface pressure distribution diagrams of Fig. 6. 27.

As the AOA reduces during the down-stroke motion, the cyclic phenomena of vortex shedding continue. The strength of the vortices shed and the frequency at which they are shed change with protrusion height and AOA. The clean airfoil and the airfoil with protrusion of height 0.01c, show vortex shedding of similar strength and frequency at moderate AOAs, the phase of the cycles are different. At α =22.21°, the clean airfoil has a small vortex build-up at the

trailing edge while the airfoil with the largest protrusion has the strongest vortex build-up. As can be seen in Fig. 6.27 (b), the anticlockwise vortex is centered between the protrusion and the trailing edge providing strong and uniform suction with enhanced lift. Even though the suction before the protrusion is detrimentally reduced, the suction aft of the protrusion makes the lift significantly. However, this enhancement in lift comes with increased pressure drag.

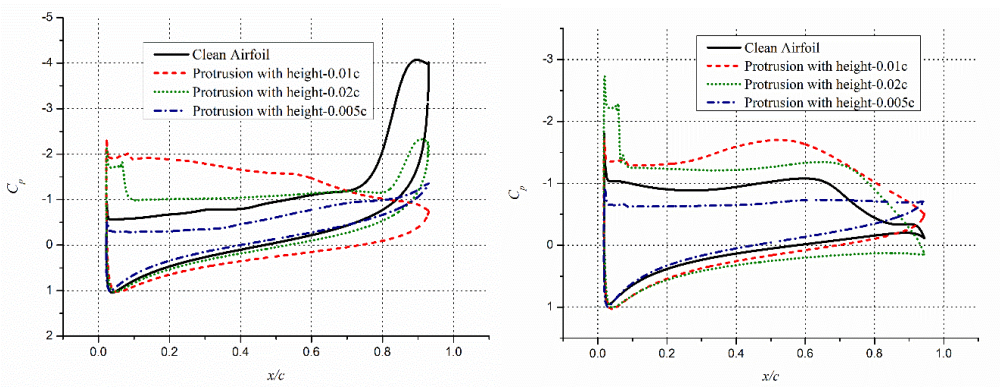

(a) Down-Stroke 24.89º *(b) Down-stroke 22.21º*

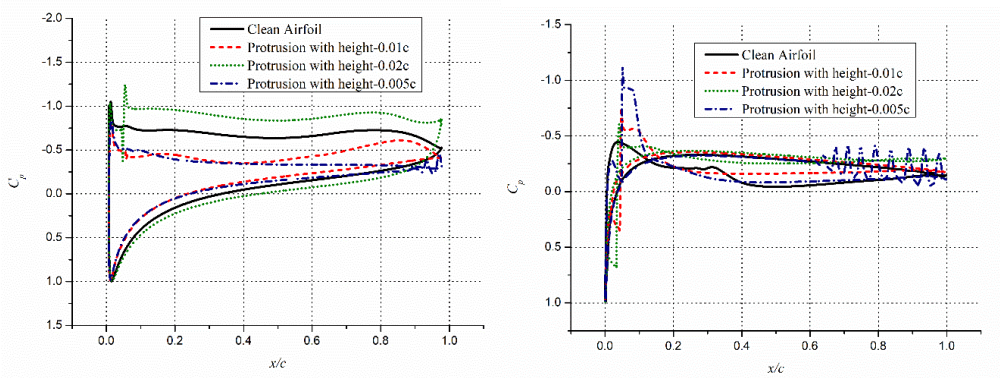

(c) Down-stroke 13.99º *(d) Down-stroke 3.98º*

Figure 6.27: Surface pressure distribution over airfoil with protrusion located at 0.05c, during down-stroke motion

As the AOA reduces below α =15°, the amplitude of oscillations in lift and drag reduces for the clean airfoil and the airfoil with larger protrusions. For the airfoil with the smallest protrusion of h = 0.05c, the large-scale oscillations are not observed either during the upstroke or the downstroke motion, other than near

the stall. This is because of the transition of the boundary layer into turbulent because of the protrusion without forming a separation bubble aft of the protrusion. Therefore, the oscillations in lift and drag observed for the clean airfoil due to laminar roll-up vortices and for the airfoil with a protrusion, due to formation separation bubble aft of protrusion, is not observed for an airfoil with the smallest protrusion.

At AOAs below α =10°, the vortex shedding and oscillations die out even for an airfoil with protrusion of height 0.01c. The oscillations for the airfoil with the largest protrusion, however, continue until very low AOAs during the downstroke. The time-averaged value of lift coefficient for the airfoil with the largest protrusion at 0.05c however, is significantly higher than all other configurations at AOA above α = 5°. On further reduction of the AOA below α = 5°, the lift coefficient turns negative as the suction on the pressure surface exceeds the suction on the suction surface. As can be observed in Fig. 6.27 (d), even at such a small AOA of α =3.98°, the local suction produced by a protrusion of height h = 0.005c is significantly high, but fails to provide overall positive lift like other configurations.

6.2.2 EFFECT OF CIRCULAR PROTRUSION AT 0.10C LOCATION

The aerodynamic characteristics of an airfoil with circular protrusions of various heights, located at 0.1c on the suctions surface, are illustrated in Fig. 6.28. The lift and the drag variation are for an airfoil in harmonic pitch motion about quarter-chord with α = 10° as the mean AOA. As with the airfoils with a protrusion at 0.05c, the airfoils with a protrusion at 0.1c also exhibit time-averaged lift coefficient values similar to those for a clean airfoil, during upstroke motion as can be seen in Fig. 6.28 (a). The stalling angle, however, is reduced progressively as the height of the protrusion is increased. For the largest protrusion of height of h= 0.02c, the airfoil stalls at AOA as low as α = 17° while the airfoil with the smallest protrusion of height 0.005c stalls at α = 23°, very close to the stalling angle of the clean airfoil.

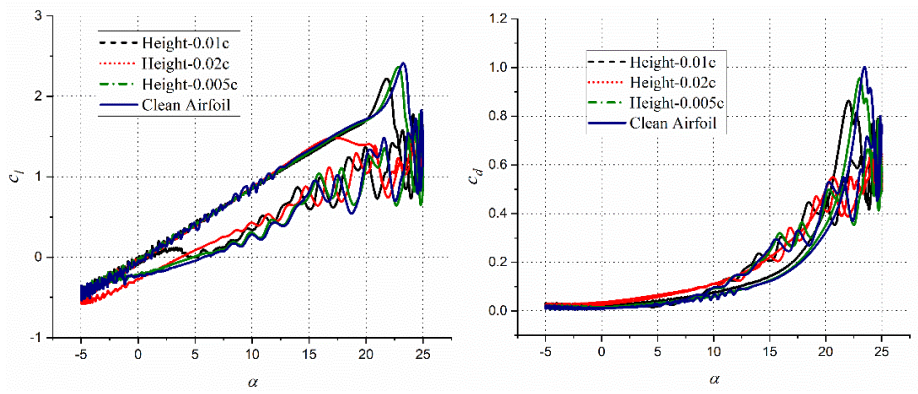

(a) Coefficient of Lift versus α *(b) Coefficient of Drag versus α*

Figure 6.28: Aerodynamic characteristics of the circular protrusion at 0.10c Location

The larger protrusions besides making the airfoil stall early eliminate high-frequency low amplitude oscillations in lift values due to the elimination of roll-up vortices as can be seen in Fig. 6.29. At small negative AOAs, during the upstroke, numerous roll-up vortices are seen on the pressure surface for all configurations as can be seen in the first two rows of Fig. 6.29. Despite strong local suction aft of the protrusion, as can be seen in Figs. 6.230 (a) and (b), the overall lift is negative for all configurations. As the AOA increases to positive values, the suction on the suction surface exceeds the suction on the pressure side for all configurations and a positive lift is realized. For the clean airfoil oscillations in the lift is observed due to small vortices on the suction surface while the airfoil with protrusions of height h = 0.01c, numerous small vortices are seen on the pressure surface as can also be observed in the third and fourth rows of Fig. 6.29.

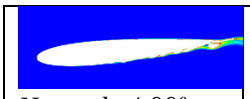 *Neutral -4.99⁰* c_l- *-0.41538*	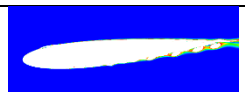 *Neutral -4.99⁰* c_l- *-0.47066*	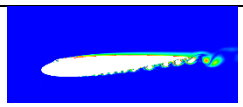 *Neutral -4.99⁰* c_l- *-0.45038*	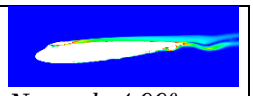 *Neutral -4.99⁰* c_l- *-0.54633*
Up Stroke -1.38⁰- c_l- *-0.1706*	*Up Stroke -1.38⁰* c_l- *-0.17245*	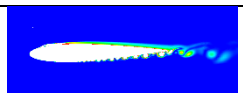 *Up Stroke -1.38⁰* c_l- *-0.15286*	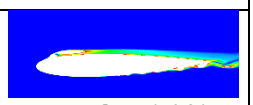 *Up Stroke -1.38⁰* c_l- *-0.1924*

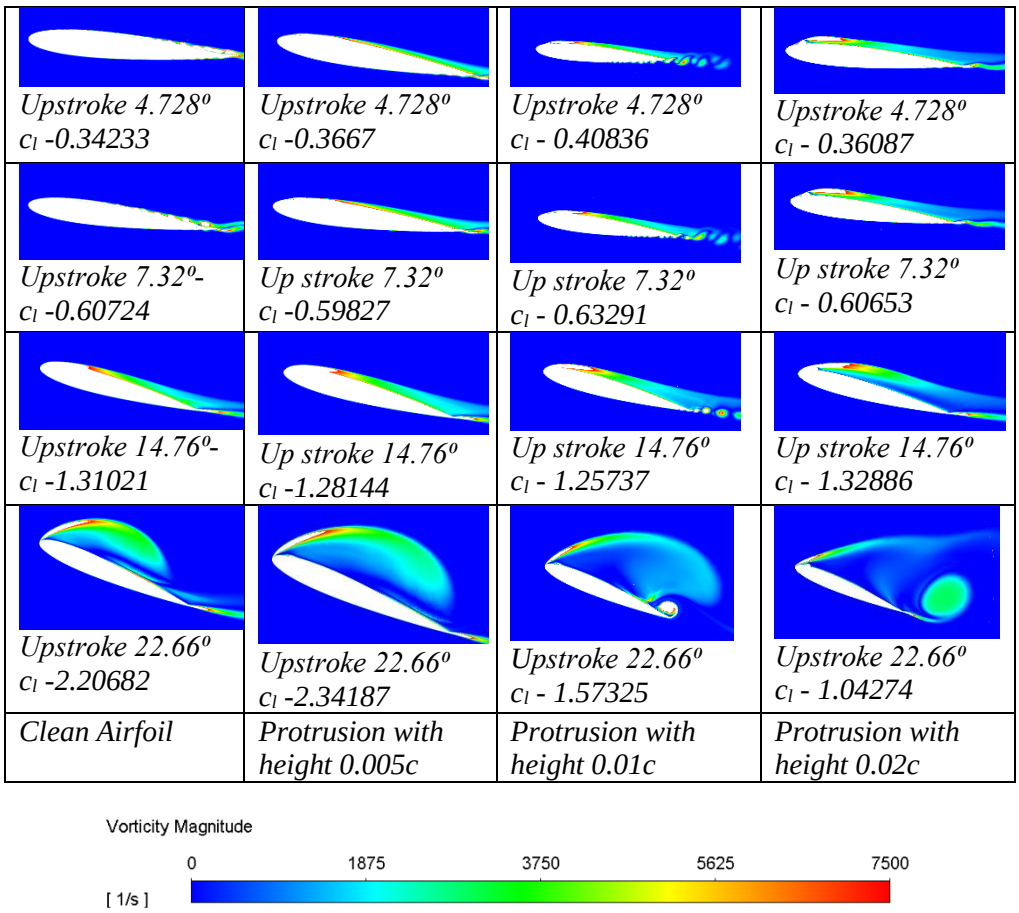

Figure 6.29: Vorticity contours for airfoils with protrusion at 0.1c location, during upstroke motion

All protrusions, at these small positive AOAs, create a strong suction aft of the protrusion while destroying the suction ahead of it as can be seen in Figs. 6.30 (c) and (d). The destruction in the suctions ahead of the protrusion is larger for the larger protrusion and so is the suction aft of the protrusion.

So the lift coefficient increases for all airfoils protrusion at α = 4.73°, while the lift is reduced for the largest protrusion at 0.1c.location at α =7.32°, due to a large reduction in suction before protrusion. At AOA of α =7.32° and above, the boundary layer aft of the protrusion is turbulent in all cases and the roll-up vortices are not observed for airfoils with protrusions at 0.1c location.

At α = 14.76°, during the upstroke motion, the roll-up vortices on the suction surface disappear even for the clean configuration. The turbulent separation

point aft of the protrusion, however, moves upstream as the height of the protrusion is increased, as can be seen in the fourth row of Fig. 6.29. This makes the wake wider with an increase in pressure drag with increasing protrusion height. The protrusions also destroy the suction ahead of it and this destruction is highest for the largest protrusion, as can be seen in Fig. 6.30 (e). The vortex centered aft of the protrusion keeps the suction and the lift value close to those for the clean configuration and higher than airfoils with smaller protrusions. As the AOA is increased during the upstroke motion, the airfoil with the largest protrusion stalls, the stall, however, is a light stall with a smaller negative gradient in lift curve.

This is because of the build-up of a clockwise vortex aft of the protrusion, which provides significant lift. As this vortex leaves the surface after attaining full strength, the lift of the airfoil with the largest protrusion falls significantly at around α =20°. As can be seen in Fig. 6.30 (f), at α =22.66°, the airfoil with the largest protrusion is in a deep stall with almost constant pressure on the suction surface. On the other hand, the airfoil with the smallest protrusion and clean airfoil show strong suction near the leading edge showing the presence of a dominant clockwise vortex centered well ahead of the mid-chord location. The airfoil with protrusion of height h = 0.01c however, is also in a stalled condition, but the suction from the anticlockwise vortex at the trailing edge keeps the lift higher than the airfoil with the largest protrusion.

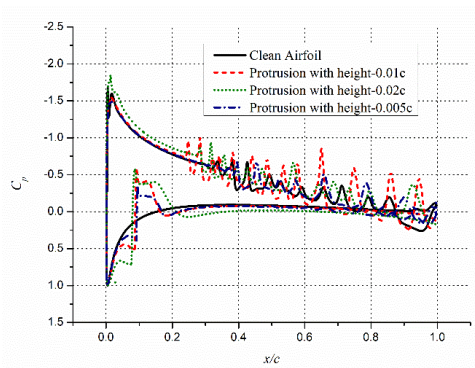

(a) Neutral -4.99⁰

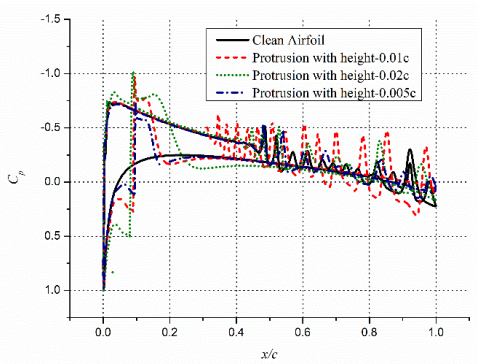

(b)Up Stroke -1.38⁰

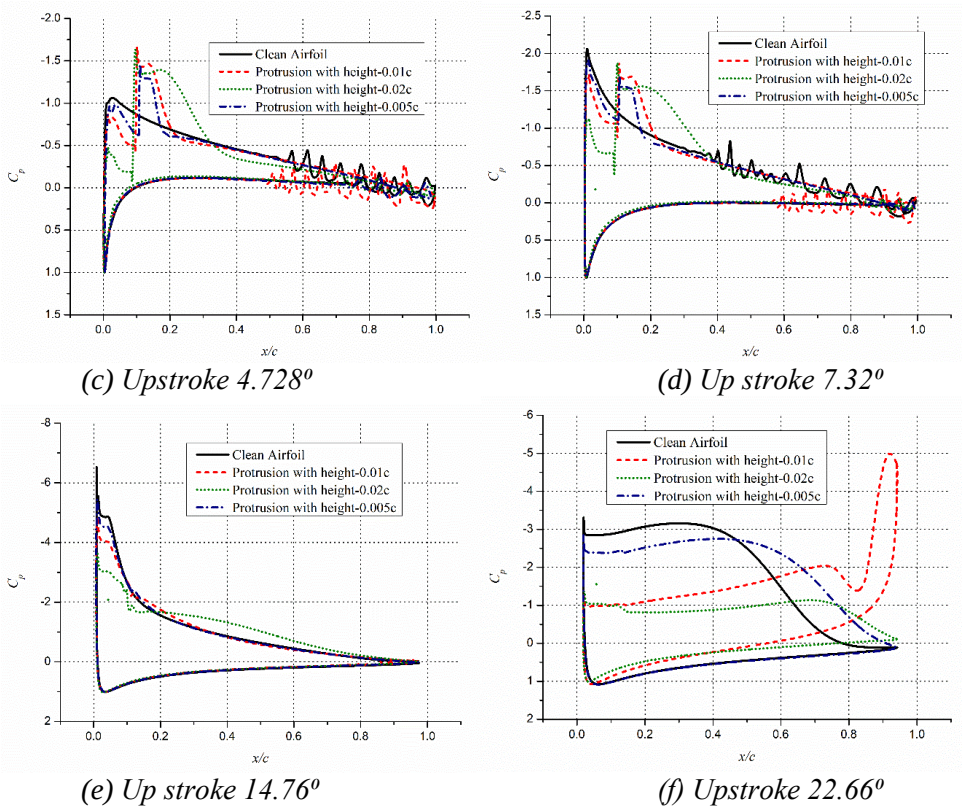

(c) Upstroke 4.728º *(d) Up stroke 7.32º*

(e) Up stroke 14.76º *(f) Upstroke 22.66º*

Figure 6.30: Surface pressure distribution over airfoil with protrusion located at 0.1c, during upstroke motion

After the stall, a vigorous vortex shedding cycle starts for all configurations causing oscillations in lift and drag. These oscillations are, however, not in phase with one another as can be seen in Fig. 6.28. As the maximum AOA is achieved and airfoil pitches downwards during the down-stroke motion, this vortex shedding phenomena continues as can be seen in Fig. 6.31. Therefore, during the down-stroke motion both the lift and drag oscillate, in different phases, however. These oscillations continue until very small AOAs when the shear layer separated on the protrusion reattaches on the suction surface. This happens at AOA below α =8°, for the clean airfoil as well as the airfoils with a protrusion, other than the protrusion of height h = 0.01c, as can be seen in Fig 6.31, for α = 3.98°. For these particular configurations, the formation of vortices on the pressure surface and their drifting downstream cause the oscillations in lift and drag, the scale of oscillation is, however, small. These low amplitude

oscillations, keep the time-averaged lift coefficient positive for this configuration, as the lift for other configurations plunges to negative values.

During the downstroke motion, different configurations with a protrusion at 0.1c location are at different phases of their vortex shedding cycles. This fact can be illustrated through the surface pressure distribution graphs for AOAs during the downstroke as shown in Figs. 6.31 (a)-(d). As can be seen in Fig. 6.31 (a), at α = 24.89°, strong suction at the trailing can be observed for the clean configuration, which suggests a strong anticlockwise vortex on the suction surface near the trailing edge. A similar anticlockwise vortex can also be seen, in Fig. 6.27 at α = 24.89°, for the airfoil with the smallest protrusion of h =0.005c. The suction from this vortex is, however, less due to the difference in phase as shown in Fig. 6.31 (a). For airfoils with larger protrusions, the shed anticlockwise vortex is at a distance from the trailing edge, and suction has seen in Fig. 6.231 (a), is from the clockwise vortex starting near the leading edge. At α = 22.21°, during the downstroke, the anticlockwise vortex at the trailing edge, after gaining maximum strength, has just left the surface, for the clean and the airfoil with the smallest protrusion as can be seen in the second row of Fig. 6.31.

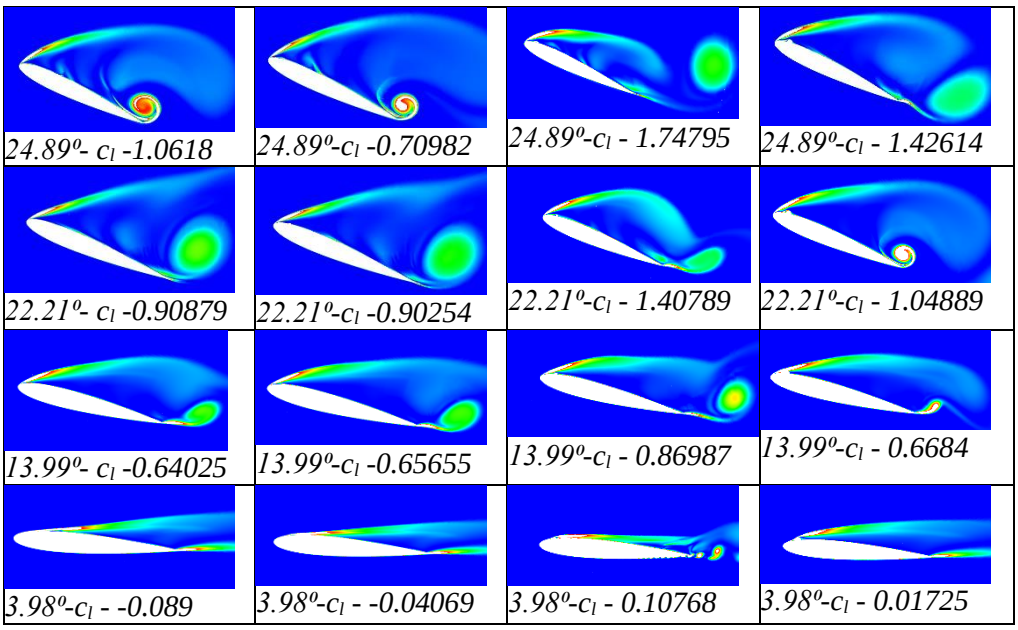

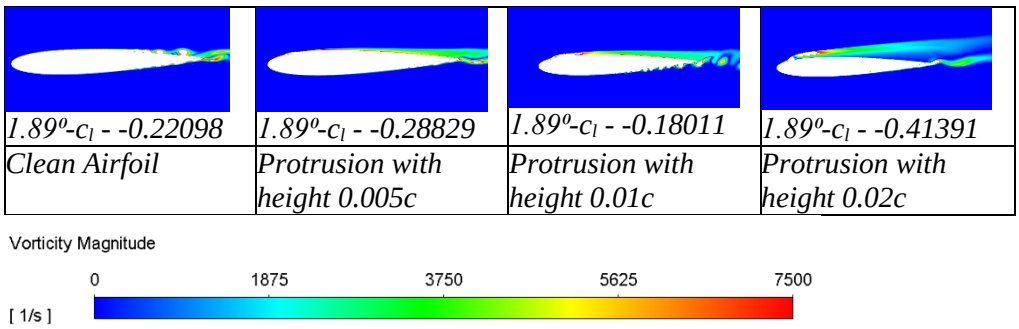

Figure 6.31: Vorticity contours for airfoils with protrusion at 0.1c location, during down-stroke motion

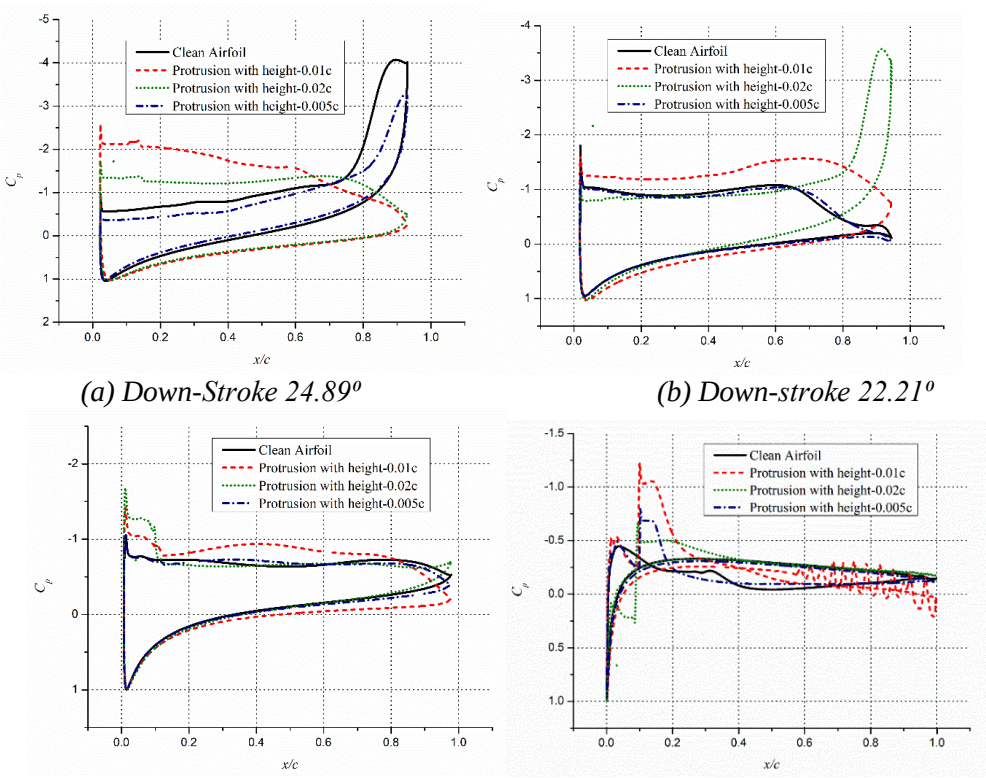

(a) Down-Stroke 24.89⁰

(b) Down-stroke 22.21⁰

(c) Down-stroke 13.99⁰

(d) Down-stroke 3.98⁰

Figure 6.32: Surface pressure distribution over airfoil with protrusion located at 0.1c, during down-stroke motion

The pressure distribution graph in Fig. 6.32 (b), thus shows a diminished suction near the trailing edge, for these two configurations. The airfoils with protrusion of heights h =0.01c and 0.02c are at different phases with a small vortex at the trailing edge, progressively stronger, is observed for these airfoils. As the AOA further diminishes during the down-stroke, the vortex shedding phenomena continues, the strengths of vortices shed, however, diminished with AOA, as

can be seen in the third row of Fig. 6.31. Because of differences in the time period, at α =13.99°, all configurations are in similar phases and have similar pressure distribution aft of the protrusion, as can be seen in Fig. 6.32 (c).

On further reduction of AOA, during the down-stroke, the shear layer, separated on the protrusion, attaches onto the suction surface, eliminating large-scale vortex shedding phenomena from the airfoils. There is a turbulent separation aft of the protrusion, causing increased wake size as can be seen in the fourth row of Fig. 6.31. The turbulent separation point moves upstream with decreasing AOA, causing a severe reduction in suction from the upper surface. As can be seen in Fig. 6.32 (d), at α =3.98°, during the downstroke, the windward surface provides more suction than the leeward surface resulting in a negative lift at this positive AOA. A strong suction aft of the protrusion, especially for larger heights, keeps the reduction in the lift to small values, though.

6.3 SUMMARY

Numerical simulations are done for airfoils with triangular cavities and circular protrusion, to assess the dynamic stall characteristics of NACA 0012 airfoil. A shallower cavity of depth 0.025c and a deeper cavity of depth 0.05c is placed at one of the three locations viz. 0.10c, 0.25c and 0.50c on the suction surface. Three protrusions, of heights 0.005c, 0.01c and 0.02c are placed at, either 0.05c or 0.10c on the suction surface. The dynamic stall characteristics of all these configurations are assessed by allowing the airfoil to pitch about the quarter chord with mean AOA at α =10°, and amplitude of 15°.

For a cavity at 0.1c, the stalling angle and the maximum Cl are both reduced for the airfoil. The stalling angle for the clean airfoil is 23.5° while with a cavity of depth 0.05c, the stalling angle falls to α = 22°. The losses in the maximum lift and the stalling are bigger for the deeper cavity. At low and moderate AOAs however, the cavities eliminate the small-scale oscillations observed for clean

airfoil during the upstroke. During the downstroke, the lift curve is highly oscillatory for the shallower cavity. The cavities at 0.1c also add to the drag during both upstroke motion and downstroke motion. The increments in drag are higher for the deeper cavity. During the downstroke, at AOAs below α = 19°, the mean lift and drag values for airfoils with the cavity are higher due to suction induced by the trapped vortex inside the cavity.

As the cavity locations shifts downstream to quarter-chord, the shallower and deeper cavities reduce the stalling angle of the airfoil to α = 22.5° and α = 20°, respectively. The cavities at 0.25c diminish the oscillations in lift and drag are significant, with no degradation in Cl during the upstroke, severe increase in drag though above α = 15°. Also unlike the airfoil with a cavity at 0.1c location, the lift produced by the airfoil with the shallower cavity is oscillatory up to moderate AOAs. For the airfoils with a deeper cavity though, the transition of boundary to turbulent takes place at the cavity, at smaller AOAs, making the flow attached and stable. The attached turbulent flow produces significant suction on the upper surface resulting in enhanced lift up to moderate AOAs with a significant reduction in drag as well. During the downstroke, the vortex shedding and the oscillations in lift finally die out at AOAs below α = 8° for both clean airfoil and the airfoil with a shallower cavity as the shear layer attaches on the leeward surface. The airfoil with a deeper cavity, however, shows significant improvement in a lift at low AOAs during the downstroke motion, with positive Cl values, while all other configurations yield negative lift below α =5°. This lift is caused by the improved suction ahead of the cavity and a turbulent boundary layer aft of the cavity that keeps flow oscillations at bay. A significant improvement in the dynamic stall characteristics is thus, obtained for a deeper cavity at quarter-chord.

A cavity at 0.5c alters improves the aerodynamic characteristics of an airfoil, more than the cavity at other locations investigated. The airfoil with a deeper cavity shows no stall during the upstroke motion i.e. up to α = 25°, with favorable reductions in the drag as well. Beyond α =16°, during the upstroke,

the drag coefficient for an airfoil with a shallower cavity is increased, whereas, for an airfoil with the deeper cavity, it decreases as compared to the clean airfoil. This decrement in the drag is the smaller size of the clockwise vortex, ahead of the cavity, that remains attached to the surface for a longer period. The smaller size of the vortex is due to the splitting of the large vortex at the cavity. The airfoil with a cavity at 0.5c however, shows severe oscillations during the downstroke, even for small AOAs. The lift values also go to high negative values at these small AOAs.

The addition of protrusion other than the one with h = 0.02c, at 0.05c location, does not affect the lift values much during the upstroke motion. The stalling angle, however, reduces progressively as the height of the protrusion is increased. The smallest protrusion stalls the airfoil at $\alpha = 22.5°$, while the largest protrusion stalls the airfoil as early as $\alpha = 17°$, with an increased vortical lift before the stall. There is also a detrimental rise in the Cd, for an airfoil with larger protrusions at 0.05c. The larger protrusions on the other hand stabilize the flow by eliminating the formation of roll-up vortices on the suction during the upstroke motion. A noticeable difference is observed for the airfoil with the smallest protrusion, wherein no large-scale oscillations are observed during either the upstroke or the downstroke motion, except at stall. So the airfoil with protrusion of h = 0.005c has the largest hysteresis.

CHAPTER 7. CONCLUSION AND FUTURE WORK

Numerical simulations, augmented by experimental validations, are conducted to assess the effect of spanwise protrusions and cavities on the aerodynamic characteristics of an airfoil, viz. NACA 0012, at moderately low Reynolds numbers. The research presents the effect of these surface protrusions at both static and dynamic conditions with airfoil pitching about its quarter chord. The Reynolds numbers chosen for the analysis are 50000 and 100000 for the static airfoil case, while a Reynolds number of 135000 was selected for the dynamic airfoil case. As the flows at low Re are susceptible to laminar separation and a turbulent reattachment, wherein the conventional turbulence models fail to capture the transition and give erroneous results, the 4-equation transition SST model viz. the γ-Re_θtransition turbulence model is selected. The transient conservation equations are solved using a pressure-based solver with second-order accuracy in both time and space. All the geometric and the multi-block structured grid of C-topology around it was generated using ANSYS ICEMCFD® software. The meshes generated were further adapted dynamically during simulation, in the finite volume solver FLUENT®. Along with the grid independence study, solver validation studies were conducted against the experimental observations by Ohtake et al., Rinoie, and Takemura and at the in-house experimental facility for the static case. For the dynamic airfoil case, the experimental validation was done against the findings of Lee et al.

On Static Aerodynamic Characteristics of an Airfoil

To examine the effect of protrusion on the aerodynamics of a static airfoil, circular and triangular protrusions are placed at the leading edge, 0.05c, 0.25c, and 0.5c locations on the suction surface and 0.05c location on the pressure surface. The angles of attack (AOA) are varied between $\alpha = 0^o$ and $\alpha = 20^o$ with a 2° interval and the protrusions have heights of 0.005c, 0.01c, and 0.02c. For Re = 105, the airfoils with circular protrusions of smaller heights at the leading edge show marginal improvements in the Cl, along with significant

improvements in L/D values. The improvement of up to 8% in L/D values in the pre-stall regime is due to a reduction in pressure drag because of the transition of boundary layer into turbulent one by the presence of protrusion. However, for larger protrusions at the leading edge, small reductions in the lift are observed with a significant reduction of 13% to 34% in the L/D values, in the pre-stall regime, due to turbulent separation aft of the protrusion. In the post-stall regime, circular protrusions at the leading edge add to the flow unsteadiness as the airfoil undergoes high-frequency vortex shedding, with the enhanced time-averaged lift and frequencies of vortex shedding. Although the time-averaged, Cl is increased by up to 60%, 48.8%, and 48% for the protrusions of heights 0.005c, 0.01c, and 0.02c, no significant improvement in the L/D ratio is observed at high AOAs.

A circular protrusion at 5% chord location on suction surface significantly destroys the lift produced in the pre-stall regime, for a Reynolds number of 105. Even the smallest protrusion of height 0.005c reduces the lift and L/D values by up to 5% and 29% respectively, at $\alpha = 6°$. The larger protrusions, on the other hand, diminishes the Cl values by up to 39% and the L/D values by up to 87%

at $\alpha = 8°$, due to the inability of the shear layer separated at the protrusion to reattach onto the suction surface. Despite the deterioration of aerodynamic performance in the pre-stall regime, the time-averaged lift curves for larger protrusions at 0.05c location increases monotonically with the AOA, showing no sign of stall. Even the airfoil with the smallest protrusion at 0.05c locations recovers immediately from the stall and displays very high values of time-averaged lift values in the post-stall regime. These increments are, however, associated with vigorous vortex shedding, alternately from the leading and trailing edge, which also increases the drag of the airfoil. Thus, despite increments of up to 63% in the vortical lift, only marginal increments in L/D values are observed in the post-stall regime.

Similar to the protrusion at location 0.05c, the larger protrusions degrades the lift and L/D ratio by up to 37% and 85%, respectively, in the pre-stall regime. The smallest protrusion at 0.1c on the other hand significantly improves the aerodynamic performance of the airfoil. With marginal increments in a lift in the pre-stall regime, the aerodynamic efficiency is improved by up to 94% in the pre-stall regime. This increment is realized because of the turbulent reattachment of the shear layer on the suction surface, which reduces the drag by reducing the wake width. In the post-stall regime, as the vortex shedding phenomena takes over the time-averaged Cl values are increased by 9% to 63% for various AOAs between $\alpha = 12°$ to $\alpha = 20°$. Other than the smallest protrusion of h = 0.005c, the larger protrusions at 0.25c location on the suction surface significantly deteriorate the performance of the airfoil in the pre-stall regime. The smallest protrusion enhances the aerodynamic efficiency 16% at $\alpha = 6°$, due to the turbulent reattachment of the boundary layer aft of the protrusion. As the height of the protrusion at 0.25c is increased, the pre-stall L/D ratio values diminish, by up to 64% for the largest protrusion. In the post-stall regime, the time-averaged lift increases at AOA beyond $\alpha = 14°$, for all protrusion height, without a significant increase in the aerodynamic efficiency. These increments come with an increased frequency of vortex shedding, as compared to the clean configurations. The amplitude of oscillation in the lift, however, the largest for the airfoil with the smallest protrusion at these large AOAs. The effect of circular protrusion at the mid-chord location is also similar with the smallest protrusion providing some improvements in L/D values at small AOAs, while the significant deterioration in the aerodynamic performance is observed for larger protrusions in the pre-stall regime. The reduction in lift and aerodynamic efficiency, however, is reduced as compared to protrusion at 0.25c.

A circular protrusion at 0.05c on the pressure, however, does not affect the lift values in the pre-stall regime at Re = 105, with the largest reduction of 7% in Cl values for the largest protrusion. As with protrusions at other locations, the time-averaged lift values are improved in the post-stall regime due to vigorous

vortex shedding, without significant improvement in aerodynamic efficiencies though. Protrusions at all locations thus, enhance the flow unsteadiness by increasing the vortex shedding frequency or the Strouhal number. As with the clean airfoil, these Strouhal numbers decrease with increasing AOA, the values of Strouhal number for airfoils with circular protrusions are, however, 4 to 5 times higher than the Strouhal numbers for the clean airfoil, in the post-stall regime.

At a Reynolds number of 50000, the effect of a circular protrusion at the leading edge is significantly different from those at a Re = 105. The smallest protrusion at the leading edge enhances the lift values marginally while providing significant improvements in the aerodynamic efficiency, in the pre-stall regime at Re = 50000. The time-averaged lift curve for even larger protrusions overlaps the lift curve for the clean airfoil with no major loss of lift in the pre-stall regime. All protrusions at the leading edge, however, show significant improvement in the aerodynamic efficiency, with a 20% increment in L/D ratio for the smallest protrusion and up to 24% increase for larger protrusions. As with the case of Re = 105, the aerodynamic performance of the airfoil is significantly degraded with a circular protrusion at 0.05c location in the suction surface. Although there is no significant degradation in aerodynamic performance for the smallest protrusion, a reduction of up to 36% and 78% in Cl and L/D values is observed for the largest protrusion, in the pre-stall regime. These degradations for larger protrusions are due to the inability of the shear layer detached from the protrusion to reattach onto the suction surface. The protrusion at 0.05c on the suction surface on the other hand makes the flow highly unsteady with degradation in aerodynamic performance similar to those shown by protrusions at 0.05c on the suction surface. The contrast between the protrusions at these two locations being the time-averaged lift at $\alpha = 0°$, wherein a positive lift is observed for a protrusion on the suction surface while a negative lift is observed for a protrusion on the pressure surface.

As with the case of Re = 105, the protrusion enhances the frequency of vortex shedding in the post-stall regime. The Strouhal number for airfoils with protrusions have similar values in the post-stall regime irrespective of the size and location of the circular protrusion. The protrusion, however, eliminates the vortex shedding at α =14° seen for the clean airfoil at Re = 50000. At α = 0°, the vortex shedding seen for clean airfoil is eliminated by protrusions at the leading edge. The protrusions, however, enhances the vortex shedding frequency at α =2° and 4°. Even the protrusions at 0.05c on the pressure surface enhance the vortex shedding frequency at α =2° while subsiding it at α =4°. The circular protrusion at 0.05c on the suction surface, on the other hand, eliminates the vortex shedding phenomena in the pre-stall regime with some exceptions at α = 0°.

Triangular protrusions offer better aerodynamic performance to an airfoil at a Reynolds number of 105, as compared to the circular protrusions. A small triangular protrusion of height h = 0.005c and 0.01c at the leading edge does not alter the pre-stall aerodynamic characteristics of the airfoil, in fact, up to α = 14°. The aerodynamic efficiency, however, diminishes for the larger protrusions, by up to 42% with h = 0.02c, at α = 10°. A small triangular protrusion located at 0.05c on the suction surface, on the other hand, alters the aerodynamic characteristics of the airfoil significantly. The smallest protrusion of height 0.005c, at this location, improves the post-stall Cl of the airfoil without altering the pre-stall characteristics. Although the lift in the post-stall regime is highly unsteady, the time-averaged Cl values are enhanced by up to 54% for the smallest of protrusion at 0.05c. As the height of the protrusion at this location is increased, the pre-stall aerodynamic characteristics deteriorate, with only marginal improvements in the post-stall Cl values. The aerodynamic efficiency diminishes to values between 65% and 88% for the larger protrusion at 0.5c on the suction surface. The protrusion on the pressure surface does not affect the lift and drag coefficients in the pre-stall regime, but affects the stability of the flow, making the flow inherently unsteady at AOAs of α = 12° or more. The

time-averaged Cl values for these unsteady configurations are up to 43% higher than the clean configuration for larger heights of the protrusion. Even the time-averaged L/D do not deteriorate for protrusion of height 0.05c on the pressure surface. For larger protrusions, however, falls of up to 59% in the aerodynamic efficiency are observed, in the pre-stall regime.

Similar to the circular protrusions, the triangular protrusions enhance the flow unsteadiness and vortex shedding that result in the oscillation of Cl values. The triangular protrusion at the LE does not reduce the AOA at which the vortex shedding starts but increases the frequency of vortex shedding and lift oscillation with Strouhal number in between 0.48 and 0.68. For protrusion on the suction surface, the Cl values oscillate between a Strouhal number between 0.5 and 1.0 wherein larger protrusion reduces the Strouhal number for a given AOA in the pre-stall regime. For a protrusion at 0.05c on the pressure surface, the vortex shedding and hence the oscillation in Cl values occur at lower frequencies with a Strouhal number between 0.4 and 0.6. For all triangular protrusions, the Strouhal number reduces as the angle of attack is increased. The triangular protrusions, thus, reduce the AOA at which the vortex shedding starts and increases the vortex shedding frequency as compared to clean NACA 0012.

The enhancements in the time-averaged Cl values, in the post-stall regime, observed for configurations with protrusions are primarily due to the dominance of the vortex lift in this separated regime. As the anticlockwise vortex builds up at the trailing edge, the Cl values are less, and once the counter-clockwise vortex is shed away, a clockwise circulation is imparted to the airfoil, enhancing the instantaneous Cl. This improvement in time-averaged Cl with a triangular protrusion, thus, comes with enhanced flow unsteadiness due to vigorous vortex shedding. For any protrusion height, the vortex shedding frequency and hence the frequency of oscillation in Cl values decreases as the AOA is increased. The amplitude of fluctuations in Cl, on the other hand, is higher for larger protrusion and higher angles of attack.

Unlike protrusions, A circular cavity of depth 0.025c, located at 0.1c on the suction surface does not affect the aerodynamic lift of a NACA 0012 airfoil, in the pre-stall regime, for a Reynolds number of 105. This is because the flow separated at the start of the cavity reattaches as a turbulent flow for all AOAs below α = 10°, and both cavity depths. Because of the transition to turbulence, the flow on the suction surface remains attached in the pre-stall regime and the airfoil behaves similarly to the clean configuration. The aerodynamic efficiency is, however, reduced by up to 20% due to an increase in profile drag of the airfoil. At AOAs higher than α = 10° however, the time-averaged C-l values increase monotonically but the L/D ratios remain close to the ones for clean configuration. An increment of 17% in L/D value is observed at α =8° for the shallower cavity. The aerodynamic characteristics, however, deteriorate for a cavity depth of 0.05c, as the drag coefficient rises without any significant increase in Cls, resulting in degradation of aerodynamic efficiency by 7 % to 35%. For a circular cavity at 0.1c location, the maxima in L/D shifts towards higher AOAs, for smaller depths due to the transition of flow into turbulent, making the flow attached as reducing the wake width. For a deeper cavity, however, the turbulent separation occurs immediately after the cavity increasing the profile drag and hence reducing the aerodynamic efficiency in the pre-stall regime as well.

A shallow circular cavity at 0.25c location on the suctions surface degrades the performance of the airfoil due to the formation of tiny roll-up vortices formation on the surface with reductions of 15% and 56% in the lift and L/D values respectively at α =2°. At other AOAs in the pre-stall regime, the transition of boundary layer into turbulent reduced the pressure drag significantly, improving the aerodynamic efficiency significantly by up to 10%, without any increase in lift. The deeper cavity does not affect the lift much in the pre-stall regime due to transition to turbulence, but the drag rises significantly because of turbulent separation aft of cavity, which leads to a reduction in L/D values. In the post-stall regime, the flow is chaotic for the deeper cavities resulting in bluff body

vortex shedding from the airfoil. The time-averaged lift values are increased by up to 39%, and the L/D values are increased by up to 23%.

The effect of a circular cavity located at 0.5c, on the aerodynamic efficiency is similar to those at 0.25c for a Reynolds number of 105. The shedding of the laminar roll-up vortices at α = 2° causes a reduction of 8% in Cl and 22% in L/D values. The reductions in Cl, at α = 2°, are not observed for a cavity depth of 0.05c, as the laminar flow upstream of the cavity transitions to turbulent inside the cavity and continues as turbulent flow aft of the cavity. In the post-stall regime, the vortex shedding and the oscillations in Cl start as early as α = 14°.

For deeper cavity at 0.5c however, the vortex shedding is less severe due to the transition of a shear layer to turbulence. The oscillation in the lift at α = 14° causes an increase of 26% in the time-averaged Cl, with higher increments for higher AOAs, for both cavity depths.

For a Reynolds number of 105, a circular cavity placed at 0.10c on the suction surface stabilizes the flow in the pre-stall regime, eliminating oscillations in the lift at α = 2° and 4°. In the post-stall regime, however, this cavity adds to the flow unsteadiness, enunciating the vortex shedding at α = 14°, for both cavity depths. In the pre-stall regime, the Strouhal number (St) decreases with the increase in AOA, similar to clean configuration, but the St for airfoils with cavity remains higher than the clean configuration at same AOAs. A cavity located at 0.25c on the suction surface has a similar effect on the vortex shedding frequency, in the post-stall regime, however, it fails to enunciate a vortex shedding at α =14°. In the pre-stall regime, the cavity at 0.25c location significantly reduces the vortex shedding frequency by assisting flow transition to turbulence. The deeper cavity at 0.25c eliminates the vortex shedding at α =2° and 4° while reducing the Strouhal to 3.65 at α =0°. The effect of the circular cavity at 0.5c is slightly different from those at other locations as it fails to contain vortex shedding at small AOAs. In the post-stall regime, the cavity at

0.5c location imparts a larger flow unsteadiness as compared to other cavity locations, with very high Strouhal numbers of 0.84 and 0.6 for depths of 0.025 and 0.05 respectively at α =14°.

For a lower Reynolds number of 50000, a circular cavity placed at 0.1c significantly improves the aerodynamic characteristics of NACA 0012. The shallower cavity depth cavity at 0.1c improves the aerodynamic efficiency significantly in the pre-stall regime, other than α = 2°, with 54% enhancement in L/D ratio at α =10°. These improvements come from the reductions in drag due to the transition of the boundary layer at the cavity. For the deeper circular cavity at 0.1c, a vortex is trapped inside the cavity, with the flow transitioning to turbulent at the cavity, resulting in an attached flow aft of the cavity on the suction surface. This enhances the Cl values for a deeper cavity, in the pre-stall regime, with a 7.5% increment at α = 10°. The corresponding enhancement in the aerodynamic efficiency is 110%, due to further reduction in drag. The time-averaged aerodynamic characteristics of the airfoil with a cavity at 0.1c is similar to those for a clean airfoil at AOAs between α = 12° and α =16°. In the post-stall regime, the time-averaged Cl and L/D values improve by up to 48% and 22% respectively due to vortex-dominated flow.

The aerodynamics characteristics of an airfoil with a circular cavity at 0.25c is very similar to that of an airfoil with a circular cavity at 0.01c, for a Reynolds number of 50000, especially at low AOAs. The airfoil with a cavity at 0.25c shows a positive time-averaged C-l at α = 0º with increment in L/D value as well. For the deeper cavity, however, there is no unsteadiness in the flow as the roll-up vortices are absent on the suction surface due to the transition of a shear layer into turbulent. This increase in lift comes with no drag penalty and the L/D ratio of 3.0 and 6.0 is observed of an airfoil with cavity depths 0.025c and 0.05c respectively, at an AOA of α = 0°. The lift curve for an airfoil with a cavity at 0.25c is similar to that for the clean configuration in the pre-stall regime, except for α = 8 °, for the deeper cavity. At α = 6°, the aerodynamic efficiency of the airfoil with a cavity at 0.25c is remarkably improved by 12%

and 24% for depths of 0.025c and 0.05c respectively, due to a reduction in drag. In the post-stall regime, no major unsteadiness in flow is observed for AOAs up to α = 16° and the time-averaged Cl values and L/D values for configuration with the cavity of either depth, are similar to those of the clean airfoil. At high AOAs, improvements of up to 45.4% in Cl values are observed due to vortex-dominated lift.

As the location of the circular cavity is changed to a 0.50c location, no significant change in the aerodynamic characteristics is observed. Similar to the cavity at upstream locations, the airfoil with the cavity at 0.5c shows a high degree of unsteadiness at low AOAs small AOAs, especially for smaller depth. For a cavity depth of 0.025c, the time-averaged lift curve overlaps the time-averaged curve for the clean airfoil up to an AOA of α =14°. For the deeper cavity, however, a severe degradation in the lift and aerodynamic efficiency of about 15% and 59% respectively, at α = 2º, is observed. In the post-stall regime, the time-averaged Cl values are improved by up to 40.3%, without any improvement in the aerodynamic efficiency.

The flow around NACA 0012 at a low Reynolds number of 50000 is inherently unsteady at low AOAs and a cavity of depth 0.025c, located at 0.1c location, enhances the vortex shedding frequencies at α = 0° and 2°, but diminishes the Strouhal number slightly at α = 4°while inducing vortex shedding at α = 6°. The deeper cavity located at 0.1c on the suction surface eliminates the vortex shedding and fluctuations in lift values at all small AOAs other than zero incidences. The deeper cavity eliminates the vortex shedding even when placed at a 0.25c location on the suction surface. The reduction in vortex shedding frequencies is because of the transition of the shear layer aft of the cavity. The cavity with a depth of 0.025c diminishes the vortex shedding frequencies at AOAs of α= 0°, 2°, and 4°, whereas the deeper cavity enhances the vortex shedding frequencies at these AOAs. At α = 4°, the shallower cavity reduces the Strouhal number by 29% while the deeper cavity increases the Strouhal number by 100% when placed at mid-chord location on the suction surface. In

the post-stall regime, the cavities affect similar to the protrusions and cavities at 105 Reynolds number. The cavities enhance the vortex shedding frequencies by a similar amount for all depths and locations except for a deeper cavity at 0.25c location which eliminates the vortex shedding at α = 16°.

Unlike a circular cavity at 0.1c location, a shallower triangular cavity of depth 0.025c deteriorates the performance of the airfoil at α = 2° and 4° with reductions of up to 12% and 34% in Cl values and L/D values respectively. The Cl and L/D values for an airfoil with a cavity at 0.1c location, are similar to those for clean configuration between α = 6° and 10°, with loss in the lift for deeper cavities. For the deeper cavity, however, significant reductions in L/D ratio are observed for all AOA below α = 12°, despite only marginal reductions in the Cl, suggesting a drastic rise in drag coefficients. As the AOA is increased to α =12°, severe vortex shedding is enunciated causing fluctuations in lift coefficient values with the enhanced time-averaged Cl values irrespective of the cavity depth. Interestingly, the conventional stall is not seen for an airfoil with a triangular cavity at 0.1c, due to enhancement of lift at α = 12°. At AOAs between α = 12° and 20°, enhancements in the time-averaged Cl values of 16% - 75.5%, are observed with increments of 8.5% to 31% in the L/D ratios.

In the pre-stall regime, the effect of a triangular cavity located at 0.25c is similar to those of a circular cavity at the same location and Reynolds number and similar to the triangular cavity at 0.1c location. The loss in lift seen at α =2°, for circular cavity at 0.25c location and triangular cavity at 0.1c, is not observed for the airfoil with a triangular cavity at 0.25c. Another contrasting difference in the lift curve of an airfoil with a circular cavity at 0.25c and one with a triangular cavity at 0.25 can be observed between α=10° and α =14°. While the lift curve of an airfoil with circular at 0.25c location follows the trend of clean airfoil up to α = 14°, with significant loss of lift at both α=12° and 14°, the lift curve of an airfoil with a triangular cavity at 0.25c shows no stall. Nevertheless, the lift coefficients are enhanced by 28% to 64% with a corresponding increase in the L/D values by 5.2 % to 27%, in the AOA between α=12° and 20°. Even for the

deeper cavity absence of stall is observed with an increment of 37.5% at α =12°. There is also no reduction in the Cl values in the pre-stall regime but decrements in the L/D values between 2% to 36%, are observed.

The effects of the triangular cavity at 0.5c, are significantly different from those for cavities at different locations at a Reynolds number of 105, in the post-stall regime. The typical stall seen for the clean airfoil is absent but the Cl values at α = 12° and 14° are smaller than for airfoil with a triangular cavity at 0.25c. Nevertheless, the lift coefficient values increase monotonically from α = 12° to α =20°. Another contrasting result as compared to an airfoil with a triangular cavity at 0.25c, is the absence of severe flow unsteadiness, at α = 12° and α = 14°. At AOAs between α = 12º to α = 20º, improvements in the time-averaged Cl values of 15% to 75.5% are observed. In the pre-stall regime, for both cavity depths, at α=6°, the shear layer turns turbulent well ahead of the cavity. The turbulent separation for the deeper cavity, however, occurs at an upstream point as compared to the shallower cavity. This makes the pressure drag for the deeper cavity slightly higher with a reduced L/D ratio.

A triangular cavity at 0.1c location reduces the unsteady oscillations in Cl values, but not as effective as a circular cavity at the same location on the airfoil, for Re =105. Triangular cavities at 0.1c location, fail to eliminate the severe flow unsteadiness at α = 0°. The deeper cavity, however, reduces the frequency of oscillations by 16% and can eliminate the vortex shedding at α = 2° and 4°. The shallower cavity at 0.1c on the other hand reduced the frequency of oscillations at α=2° and 4° significantly. In the post-stall regime, the presence of a triangular cavity at 0.1c enunciates a high-frequency vortex shedding at AOA as early as α = 12°, with St = 0.7, for both depths. As the AOA is further increased, St reduces, but remains, significantly higher than clean airfoil. The triangular cavity at 0.25c also has a similar effect on the Strouhal number at low AOAs as for the triangular cavity at 0.1c. For both cavity depths, the Strouhal number at α = 0°, is reduced by 24%. At α = 2° and 4°, the fluctuations are eliminated by the presence of a deeper triangular cavity at 0.25c while the

shallower cavity reduces the Strouhal number by up to 58% at α = 4°. These reductions are, however, very less compared to those by a circular cavity, at the same location on the airfoil. The triangular cavity located at 0.5c on the contrary reduces St only slightly. Even the deeper cavity of 0.05c depth is unable to eliminate the oscillation in a lift at α =4°.

The aerodynamic characteristics of an airfoil are highly improved by the presence of a triangular cavity at 0.1c for a Reynolds number of 50000. The deeper cavity affects a significant improvement in the Cl values with greatly reduced flow unsteadiness. As with the circular cavity at this location, a highly positive lift observed for the deeper triangular cavity is due to the trapping of a vortex inside the cavity. A deeper triangular cavity at 0.1c, making the flow steady by transitioning the flow turbulent, aft of the cavity. The turbulent nature of the boundary layer increases the viscous drag causing a significant reduction L/D ratio at small AOAs. At moderate AOAs, an enhancement of up to 33% in the L/D value is observed due to a reduction in pressure drag. At α = 12° and higher, the vortex shedding sets in, with increments of 13% and 21% in Cl values at α=12° and 14° respectively, but these increments in time-averaged Cl are smaller, as compared to Re = 105 cases. These increments are also in contrast to the circular cavity at 0.1c, wherein no increases in Cl are observed for Re = 50000. At higher AOAs the times averaged Cl values are increased by 57%.

For a Reynolds number of 50000, a triangular cavity located at 0.25c causes high amplitude oscillations in Cl values is observed at α = 0°, 2° or 4°, irrespective of cavity depth. Unlike the circular cavity, this unsteadiness results in a positive Cl at α = 0° for the larger depth. The aerodynamic characteristics of the airfoil with a deeper cavity, however, are severely deteriorated at α = 2° with reductions of 22% and 85%, in Cl and L/D values respectively, due to enhancement in pressure drag. This deterioration of lift was not observed for the deeper circular cavity at Re = 50000. At a Reynolds number of 105 however, a similar deterioration in time-averaged Cl was observed for the shallower

cavity at 0.025c location. The aerodynamic efficiency however improves by 22% at α = 6°, as the cavity turns the flow into turbulent. As with triangular cavity 0.1c, significant improvements of 14%, 23%, and 52% in the time-averaged Cl at α = 12°, 14° and 16° respectively, for a cavity at 0.25c, due to vortex dominated lift enhancement. The corresponding enhancements are L/D values are 7.2%, 16%, and 20% respectively.

In contrast to a circular cavity at 0.05c location, a triangular cavity does not affect the Cl values in the pre-stall regime, for Re = 50000. The deeper cavity, however, reduces the amplitude of oscillations in lift values by inducing transition to turbulence. Despite time-averaged Cl values being similar to those for the clean configuration, the shallower cavity at 0.5c offers marginal reductions in drag at all AOAs in the pre-stall regime, due to reduction in skin friction aft of the cavity resulting in enhancements of up to 29% in L/D values in the pre-stall regime. As the AOA is increased beyond α =10°, significant improvements in the time-averaged Cl values are observed, similar to those observed for a Reynolds number of 105. Improvements of up to 56.3% in the Cl values and up to 24% in L/D values are observed at these high AOAs.

For Re = 50000, a shallower triangular cavity at 0.1c location reduces the frequency of oscillations in lift slightly at α = 0° but enhances St at α = 2°, while eliminating it at α = 4°. The deeper cavity on the other hand inhibits the vortex shedding at α =2° and 4°. In the post-stall regime, the triangular cavity induces vortex shedding at AOA as early as α = 12°, irrespective of its depth. The St, however, fall linearly with AOAs but, remain significantly higher than those for a clean airfoil. As the cavity moves downstream to 0.25c, its effect on St in the pre-stall regime, diminishes, with the cavity affecting the St values at α = 0° only. At α = 0°, the shallower cavity reduces St by 22% while the deeper cavity enhances St by 12%. As the triangular moves further downstream to 0.5c, the shallower cavity reduces the St at low AOAs, with the highest reduction of about 25% at α = 0°. The deeper cavity, however, enhances the St at α = 0° and

2°. In the post-stall regime, the effect of all triangular cavities is similar as they enhance the St values for α = 12° and above.

Circular protrusions at the leading do not destroy the lift much but increases drag irrespective of height. The circular protrusion at all other locations on the suction surface diminishes lift with enhancement in drag. An exception is observed for a smaller protrusion at 10% chord wherein the lift marginally with increased aerodynamic efficiency at moderate AOAs, mitigating the phenomena of the stall. The circular protrusion on the suction surface also does not provide any improvement in the lift. All these protrusions enhance the vortex shedding at higher AOAs with the higher time-averaged lift in the post-stall regime. With the reduction in Reynolds number, the lift further deteriorates, especially at low AOAs. Even triangle-shaped protrusions at the leading edge and 5% chord on the pressure surface offer no improvement in the lift or aerodynamic efficiency. The small triangular protrusion at 5% chord on the suction surface, however, mitigates the stall without degrading aerodynamic efficiency. The larger protrusion of both shapes, however, eliminates vortex shedding and flow unsteadiness at low AOAs.

Even circular cavities on the suction surface, offer no improvement in the lift in the pre-stall regime, with significant reductions in aerodynamic efficiency, other than the shallower cavity at 0.1c location at a Reynolds number of 105. This configuration offers some improvement in aerodynamic efficiency at moderate AOAs, due to reduced drag. The circular cavities at 10% chord and 25% chord however diminish the vortex shedding frequency at low AOAs the deeper cavities eliminates them in most cases. At a Reynolds number of 50000 however, these cavities offer significant improvements in aerodynamic efficiency due to reduction drag primarily, at moderated AOAs, when located at 10% chord. Cavities at other locations offer no improvements in either lift or aerodynamic efficiency, except at a few AOAs. The deeper cavity that offers reductions in drag also eliminates vortex shedding in the pre-stall regime. The circular shallower cavity at all locations, however, enhances the frequency of

vortex shedding. The triangular cavity at a Reynolds number of 105 mitigates the stall with lift increasing monotonically with AOAs, but comes with a penalty of drag rise. The drag rise and reductions in aerodynamic efficiency diminish as the cavity moves downstream. However, the triangular cavity at the downstream location induces vortex shedding at lower AOAs in the post-stall regime. The triangular cavity offers mitigation of stall even for a Reynolds number of 50000, however, with little or no reduction in aerodynamic efficiency at almost all AOA. Significant improvements in L/D values can be observed at some AOAs and all AOAs for the mid-chord location. The triangular cavities, however, fail to eliminate vortex shedding though.

The three major findings on the effect of protrusions and cavity on the static aerodynamic characteristics of NACA 0012 are,

(i) The stall is mitigated for a small triangular protrusion at 5% chord, and all triangular cavities, with improvements in aerodynamic efficiency as well, for Re = 50000,

(ii) Deeper circular cavity at 10%c improves aerodynamic efficiency at Re = 50000 and eliminates vortex shedding

(iii) Deeper circular cavities eliminate vortex shedding at low AOAs while all protrusions and cavities enhance vortex-shedding frequencies in the post-stall regime.

The mitigation of stalls and improvements in aerodynamic efficiency suggested by current findings can prove to be crucial for flights of UAVs and MAVs at low Reynolds numbers. The small triangular protrusion at 5%chord, the deeper circular cavity at 10% chord, and the triangular cavities provide significant improvements and can be considered during the design of Mavs and UAVs meant to fly with fixed wings. The deeper cavities can be used to make the over wings of MAVs and UAVs more steady. The protrusions and cavities that show enhancements in vortex shedding frequencies can be used to extract maximum

energy from VIV-based energy generators, as the power generation is proportional to the frequency of oscillation. Therefore, the current findings may provide valuable inputs into the design of the wings of UAVs, MAVs, and VIV-based wind energy generators.

On Dynamic Aerodynamic Characteristics of an Airfoil

Numerical simulations are done for airfoils with triangular cavities and circular protrusion, to assess the dynamic stall characteristics of NACA 0012 airfoil. A shallower cavity of depth 0.025c and a deeper cavity of depth 0.05c is placed at one of the three locations viz. 0.10c, 0.25c and 0.50c on the suction surface. Three protrusions, of heights 0.005c, 0.01c and 0.02c are placed at, either 0.05c or 0.10c on the suction surface. The dynamic stall characteristics of all these configurations are assessed by allowing the airfoil to pitch about the quarter chord with mean AOA at $\alpha = 10°$, and amplitude of 15°.

For a cavity at 0.1c, the stalling angle and the maximum Cl are both reduced for the airfoil. The stalling angle for the clean airfoil is 23.5° while with a cavity of depth 0.05c, the stalling angle falls to $\alpha = 22°$. The losses in the maximum lift and the stalling are bigger for the deeper cavity. At low and moderate AOAs however, the cavities eliminate the small-scale oscillations observed for clean airfoil during the upstroke. During the downstroke, the lift curve is highly oscillatory for the shallower cavity. The cavities at 0.1c also add to the drag during both upstroke motion and downstroke motion. The increments in drag are higher for the deeper cavity. During the downstroke, at AOAs below $\alpha = 19°$, the mean lift and drag values for airfoils with the cavity are higher due to suction induced by the trapped vortex inside the cavity.

As the cavity locations shifts downstream to quarter-chord, the shallower and deeper cavities reduce the stalling angle of the airfoil to $\alpha = 22.5°$ and $\alpha = 20°$, respectively. The cavities at 0.25c diminish the oscillations in lift and drag are significant, with no degradation in Cl during the upstroke, severe increase in drag though above $\alpha = 15°$. Also unlike the airfoil with a cavity at 0.1c location,

the lift produced by the airfoil with a shallower cavity is oscillatory up to moderate AOAs. For the airfoils with a deeper cavity though, the transition of boundary to turbulent takes place at the cavity, at smaller AOAs, making the flow attached and stable. The attached turbulent flow produces significant suction on the upper surface resulting in enhanced lift up to moderate AOAs with a significant reduction in drag as well. During the downstroke, the vortex shedding and the oscillations in lift finally die out at AOAs below $\alpha = 8°$ for both clean airfoil and the airfoil with a shallower cavity as the shear layer attaches on the leeward surface. The airfoil with a deeper cavity, however, shows significant improvement in a lift at low AOAs during the downstroke motion, with positive Cl values, while all other configurations yield negative lift below $\alpha = 5°$. This lift is caused by the improved suction ahead of the cavity and a turbulent boundary layer aft of the cavity that keeps flow oscillations at bay. A significant improvement in the dynamic stall characteristics is thus, obtained for a deeper cavity at quarter-chord.

A cavity at 0.5c alters improves the aerodynamic characteristics of the airfoil, more than the cavity at other locations investigated. The airfoil with a deeper cavity shows no stall during the upstroke motion i.e. up to $\alpha = 25°$, with favorable reductions in the drag as well. Beyond $\alpha = 16°$, during the upstroke, the drag coefficient for an airfoil with a shallower cavity is increased, whereas, for an airfoil with a deeper cavity, it decreases as compared to the clean airfoil. This decrement in the drag is the smaller size of the clockwise vortex, ahead of the cavity, that remains attached to the surface for a longer period. The smaller size of the vortex is due to the splitting of the large vortex at the cavity. The airfoil with a cavity at 0.5c however, shows severe oscillations during the downstroke, even for small AOAs. The lift values also go to high negative values at these small AOAs.

The addition of protrusion other than the one with h = 0.02c, at 0.05c location, does not affect the lift values much during the upstroke motion. The stalling angle, however, reduces progressively as the height of the protrusion is

increased. The smallest protrusion stalls the airfoil at α = 22.5°, while the largest protrusion stalls the airfoil as early as α = 17°, with an increased vortical lift before the stall. There is also a detrimental rise in the Cd, for an airfoil with larger protrusions at 0.05c. The larger protrusions on the other hand stabilize the flow by eliminating the formation of roll-up vortices on the suction during the upstroke motion. A noticeable difference is observed for the airfoil with the smallest protrusion, wherein no large-scale oscillations are observed during either the upstroke or the downstroke motion, except at stall. So the airfoil with protrusion of h = 0.005c has the largest hysteresis.

As with the airfoil with a protrusion at 0.05c, the airfoils with a protrusion at 0.1c also exhibit Cl values similar to a clean airfoil, during upstroke motion. Besides, the stalling angle reduces progressively with the height of the protrusion. For the largest protrusion, the airfoil stalls at α = 17° while for the smallest protrusion it stalls at α = 23°. The stall for large protrusion is, however, light with a smaller negative gradient in the lift curve. This is because of the build-up of a clockwise vortex aft of the protrusion, which provides significant lift. The larger protrusions besides making the airfoil stall early, eliminate high-frequency low amplitude oscillations in lift values.

All protrusions, at small positive AOAs, create a strong suction aft of the protrusion while destroying the suction ahead of it. The only noticeable favorable finding for the protrusion on an airfoil is the occurrence of positive lift for a protrusion height of 0.01c, at very low AOAs.

The protrusions on the suction surface deteriorate the performance of the airfoil in pitch motion with enhanced drag and reduced dynamic stalling angle. The only favorable finding for the protrusion on an airfoil is the occurrence of positive lift for a protrusion height of 0.01c, at very low AOAs. The cavities on the other hand provide significant improvements in the dynamic aerodynamic characteristics, which can be listed as,

(i) Most cavities eliminate the small-scale oscillations in lift and drag during upstroke motion at low and moderate AOAs.

(ii) For all cavities, the time-averaged lift is increased during downstroke motion, reducing the hysteresis loss. Even a positive lift is obtained for the deeper cavity at quarter-chord, at low AOAs during downstroke motion.

(iii) Lift is increased marginally, with reductions in drag as well, during the upstroke motion for the deeper cavity at the quarter chord.

(iv) The airfoil with a deeper cavity at mid-chord shows no stall during the upstroke motion i.e. up to $\alpha = 25°$, with favorable reductions in the drag as well. The Cl value of 2.5 was observed at this AOA.

Both the cavities at quarter-chord and mid-chord location provide improved aerodynamic efficiency during upstroke motion and an increase in stalling angle for a deeper cavity at the mid-chord location can be used to enhance the performance of flapping-wing MAVs, helicopter rotors, wind turbine blades, as these applications encounter the dynamic stall phenomena frequently. The reduction in hysteresis is also a factor considered during the design of MAVs. Therefore, the current findings are novel and significant with very wide ramifications on the design of MAVs, UAVs, and wind energy harvester. A deeper three-dimensional analysis, however, should be done, through wind tunnel experiments, before these passive devices are implemented.

Future Work

Many novel findings have been observed and reported with supporting discussion, in this doctoral dissertation. The work, however, is mostly numerical in nature and the analysis done is limited to two dimensions only, due to constraints on computing power required. In view of this, the following future

can be carried out take this in a forward direction and a meaningful conclusion, for the societal service.

- A complete 3-dimensional numerical analysis can be done using Large Eddy Simulation to obtain a more accurate observation on the effect of protrusions and cavities on static aerodynamic characteristics of an airfoil.
- In a 3-dimensional experimental setup, the effect of cavities and protrusions on various spanwise locations, the effect of the spanwise width of these protrusions can be studied.
- In a three-dimensional study, the effect of wing sweep, wing taper, and aspect ratio on the effectiveness of these protrusions and cavities can be investigated.
- The research is done at selected Reynolds numbers and should be extended to further smaller Reynolds numbers as the flow at lower Reynold numbers are more susceptive to separation and surface irregularities.
- The dynamic stall analysis for airfoils with a cavity may be extended to lower Reynolds numbers for wider applications.
- The research can be extended to other cambered NACA airfoils and other low Reynolds number airfoils.
- The dynamic stall analysis is done for a single reduced frequency, and thus, the analysis should be done at various reduced frequencies.

The current and upcoming research on the effect of protrusions and cavities at low Reynolds numbers will pave an illustrious path for the scientists and designers of MAVs, UAVs, Rotorcrafts, Wind Energy harvesters, and Wind Turbines.

REFERENCES

[1] Selig, Donovan, and Fraser. *Airfoils at Low Speeds*. 1989.

[2] Lissaman, P. B. S. "Low-Reynolds-Number Airfoils." *Ann. Rev. Fluid Mech.*, Vol. 15, 1983, pp. 223–239.

[3] Nonami, K., Kendoul, F., Suzuki, S., Wang, W., and Nakazawa, D. *Autonomous Flying Robots (Unmanned Aerial Vehicles and Micro Aerial Vehicles*. 2010.

[4] McKinney, W., and DeLaurier, J. D. "The Wingmill: An Oscillating-Wing Windmill." *AIAA 80-0621R*, Vol. 5, No. 2, 1981, pp. 109–115. https://doi.org/10.2514/3.62510.

[5] Davids, S., Platzer, M. F., and Jones, K. D. Oscillating-Wing Power Generator. 1999.

[6] Kinsey, T., and Dumas, G. "Parametric Study of an Oscillating Airfoil in a Power-Extraction Regime." *AIAA Journal*, Vol. 46, No. 6, 2008, pp. 1318–1330. https://doi.org/10.2514/1.26253.

[7] Xiao, Q., and Zhu, Q. "A Review on Flow Energy Harvesters Based on Flapping Foils." *Journal of Fluids and Structures*, Vol. 46, 2014, pp. 174–191. https://doi.org/10.1016/j.jfluidstructs.2014.01.002.

[8] Xiao, Q., Liao, W., Yang, S., and Peng, Y. "How Motion Trajectory Affects Energy Extraction Performance of a Biomimic Energy Generator with an Oscillating Foil?" *Renewable Energy*, Vol. 37, No. 1, 2012, pp. 61–75. https://doi.org/10.1016/j.renene.2011.05.029.

[9] Cherubini, A., Papini, A., Vertechy, R., and Fontana, M. "Airborne Wind Energy Systems: A Review of the Technologies." *Renewable and Sustainable Energy Reviews*, Vol. 51, 2015, pp. 1461–1476. https://doi.org/10.1016/j.rser.2015.07.053.

[10] Perković, L., Silva, P., Ban, M., Kranjčević, N., and Duić, N. "Harvesting High Altitude Wind Energy for Power Production: The Concept Based on Magnus' Effect." *Applied Energy*, Vol. 101, 2013, pp. 151–160. https://doi.org/10.1016/j.apenergy.2012.06.061.

[11] Argatov, I., Rautakorpi, P., and Silvennoinen, R. "Estimation of the Mechanical Energy Output of the Kite Wind Generator." *Renewable Energy*, Vol. 34, No. 6, 2009, pp. 1525–1532. https://doi.org/10.1016/j.renene.2008.11.001.

[12] Wang, D. A., Chiu, C. Y., and Pham, H. T. "Electromagnetic Energy Harvesting from Vibrations Induced by Kármán Vortex Street." *Mechatronics*, Vol. 22, No. 6, 2012, pp. 746–756. https://doi.org/10.1016/j.mechatronics.2012.03.005.

[13] Wang, D. A., and Chang, K. H. "Electromagnetic Energy Harvesting from Flow Induced Vibration." *Microelectronics Journal*, Vol. 41, No. 6, 2010, pp. 356–364. https://doi.org/10.1016/j.mejo.2010.04.005.

[14] Rostami, A. B., and Armandei, M. "Renewable Energy Harvesting by Vortex-Induced Motions: Review and Benchmarking of Technologies." *Renewable and Sustainable Energy Reviews*, Vol. 70, No. September 2016, 2017, pp. 193–214. https://doi.org/10.1016/j.rser.2016.11.202.

[15] He, X. F., and Gao, J. "Wind Energy Harvesting Based on Flow-Induced-Vibration and Impact." *Microelectronic Engineering*, Vol. 111, 2013, pp. 82–86. https://doi.org/10.1016/j.mee.2013.02.009.

[16] Peng, Z., and Zhu, Q. "Energy Harvesting through Flow-Induced Oscillations of a Foil." *Physics of Fluids*, Vol. 21, No. 12, 2009, pp. 1–9. https://doi.org/10.1063/1.3275852.

[17] Kumar, S. K., Bose, C., Ali, S. F., Sarkar, S., and Gupta, S. "Investigations on a Vortex Induced Vibration Based Energy Harvester."

Applied Physics Letters, Vol. 111, No. 24, 2017. https://doi.org/10.1063/1.5001863.

[18] Dunnmon, J. A., Stanton, S. C., Mann, B. P., and Dowell, E. H. "Power Extraction from Aeroelastic Limit Cycle Oscillations." *Journal of Fluids and Structures*, Vol. 27, No. 8, 2011, pp. 1182–1198. https://doi.org/10.1016/j.jfluidstructs.2011.02.003.

[19] Barrero-Gil, A., Pindado, S., and Avila, S. "Extracting Energy from Vortex-Induced Vibrations: A Parametric Study." *Applied Mathematical Modelling*, Vol. 36, No. 7, 2012, pp. 3153–3160. https://doi.org/10.1016/j.apm.2011.09.085.

[20] Bodavula, A., Guven, U., and Yadav, R. "Numerical Analysis of Protrusion Effect over an Airfoil at Reynolds Number -10 5." No. 2, 2019, pp. 2583–2588. https://doi.org/10.35940/ijrte.B2809.078219.

[21] Meara, M. M. O., and Mueller, T. J. "Laminar Separation Bubble Characteristics on an Airfoil at Low Reynolds Numbers." *AIAA Journal*, Vol. 25, No. 8, 1987.

[22] Tani, I. "Low Speed Flows Involving Bubble Separations." *Progress in Aerospace Sciences*, 1954, pp. 70–103. https://doi.org/10.1016/0376-0421(64)90004-1.

[23] Saliveros, E. (1988). *"THE AERODYNAMIC PERFORMANCE OF THE NACA-4415 AEROFOIL SECTION AT LOW REYNOLDS NUMBERS."* University of Glasgow, 1988.

[24] Horton, H. P. *Laminar Separation BUBBLES IN TWO AND THREE Dimensional Incompressible Flow*. 1968.

[25] McCullough, G. B., and Gault, D. E. Examples of Three Representative Types of Airfoil-Section Stall at Low Speed. *National Advisory*

Committee for Aeronautics. September 1951. Volume 2502, 263.

[26] Chappell, P. D. "Flow Separation and Stall Characteristics of Plane, Constant-Section Wings in Subcritical Flow." *The Aeronautical Journal*, Vol. 72, No. 685, 1968, pp. 82–90. https://doi.org/10.1017/s0001924000083585.

[27] Carmichael, B. H. *Low Reynolds Number Airfoil Survey*. 1982.

[28] Gad-el-Hak, M., and Bushnell, D. M. "Separation Control : Review." *Journal of Fluids Engineering*, Vol. 113, No. 5, 1991.

[29] Liebeck, R. H. "Design of Subsonic Airfoils for High Lift." *Journal of Aircraft*, Vol. 15, No. 9, 1978, pp. 547–561. https://doi.org/10.2514/3.58406.

[30] Gudmundsson, S. *The Anatomy of Lift Enhancement*. 2014.

[31] Gerontakos, P., and Lee, T. "Particle Image Velocimetry Investigation of Flow over Unsteady Airfoil with Trailing-Edge Strip." *Experiments in Fluids*, Vol. 44, No. 4, 2008, pp. 539–556. https://doi.org/10.1007/s00348-007-0414-z.

[32] Selig, M., Guglielmo, J. J., Broeren, A. P., and Giguere, P. *Summary of Low-Speed Airfoil Data*. 1995.

[33] Selig, M., A.Lyon, C., Giguere, P., Ninham, C. P., and Guglielmo, J. J. *Summary of Low-Speed Airfoil Data*. 1996.

[34] Mueller, T. J. *Low Reynolds Number Vehicles*. 1985.

[35] Schlichting, H., and Gersten, K. *Boundary-Layer Theory (Ninth Edition)*. 2017.

[36] Ward, J. W. "The Behaviour and Effects of Laminar Separation Bubbles on Aerofoils in Incompressible Flow *." *Journal of the Royal*

Aeronautical Society, Vol. 67, 1963, pp. 783–790.

[37] Hsiao, F., Liu, C., and Tang, Z. "Aerodynamic Performance and Flow Structure Studies of a Low Reynolds Number Airfoil." *AIAA Journal*, Vol. 27, No. 2, 1989.

[38] Lin, J. C. M., and Pauley, L. L. "Low-Reynolds-Number Separation on an Airfoil." *AIAA Journal*, Vol. 34, No. 8, 1996.

[39] Rinoie, K., and Takemura, N. "Oscillating Behaviour of Laminar Separation Bubble Formed on an Aerofoil near Stall." *The Aeronautical Journal*, Vol. 1, 2004, pp. 153–163.

[40] Yarusevych, S., Sullivan, P. E., and Kawall, J. G. "Coherent Structures in an Airfoil Boundary Layer and Wake at Low Reynolds Numbers." *Physics of Fluids*, Vol. 044101, 2006. https://doi.org/10.1063/1.2187069.

[41] Yarusevych, S., Sullivan, P. E., and Kawall, J. G. "Investigation of Airfoil Boundary Layer and Wake Development at Low Reynolds Numbers." *34th AIAA Fluid Dynamics Conference and Exhibit*, No. July, 2004, pp. 1–11.

[42] Yuan, W., Khalid, M., J.Windte, U. Scholz, and Radespiel, R. "Computational and Experimental Investigations of Low-Reynolds-Number Flows Past an Aerofoil." *The Aeronautical Journal*, No. 3109, 2007, pp. 17–29.

[43] Yuan, W., Khalid, M., Windte, J., Scholz, U., and Radespiel, R. An Investigation of Low-Reynolds-Number Flows Past Airfoils. 2005.

[44] Counsil, J. N. N., and Boulama, K. G. "Validating the URANS Shear Stress Transport Re ™ Model for Low-Reynolds-Number External Aerodynamics." *International Journal for Numerical Methods in Fluids*,

2011. https://doi.org/10.1002/fld.

[45] Juanmian, L., Feng, G., and Can, H. “Numerical Study of Separation on the Trailing Edge of a Symmetrical Airfoil at a Low Reynolds Number.” *Chinese Journal of Aeronautics*, Vol. 26, No. 4, 2013, pp. 918–925. https://doi.org/10.1016/j.cja.2013.06.005.

[46] Kojima, R., Nonomura, T., Oyama, A., and Fujii, K. “Large-Eddy Simulation of Low-Reynolds-Number Flow Over Thick and Thin NACA Airfoils.” *Journal of Aircraft*, Vol. 50, No. 1, 2013, pp. 187–196. https://doi.org/10.2514/1.C031849.

[47] Boutilier, M. S. H., and Yarusevych, S. “Separated Shear Layer Transition over an Airfoil at a Low Reynolds Number.” *Physics of Fluids*, Vol. 24, 2014. https://doi.org/10.1063/1.4744989.

[48] Gerakopulos, R., Boutilier, M. S. H., and Yarusevych, S. Aerodynamic Characterization of a NACA 0018 Airfoil at Low Reynolds Numbers. 2010.

[49] Wang, S., Zhou, Y., Alam, M., Yang, H., Wang, S., Zhou, Y., Alam, M., and Yang, H. “Turbulent Intensity and Reynolds Number Effects on an Airfoil at Low Reynolds Numbers.” *Physics of Fluids*, Vol. 26, 2014. https://doi.org/10.1063/1.4901969.

[50] Lee, D., Kawai, S., Nonomura, T., Anyoji, M., Aono, H., Oyama, A., Asai, K., and Fujii, K. “Mechanisms of Surface Pressure Distribution within a Laminar Separation Bubble at Different Reynolds Numbers.” *Physics of Fluids*, Vol. 27, No. 2, 2015. https://doi.org/10.1063/1.4913500.

[51] Choudhry, A., Arjomandi, M., and Kelso, R. “A Study of Long Separation Bubble on Thick Airfoils and Its Consequent Effects.” *International Journal of Heat and Fluid Flow*, Vol. 52, 2015, pp. 84–96.

https://doi.org/10.1016/j.ijheatfluidflow.2014.12.001.

[52] Ducoin, A., Loiseau, J., and Robinet, J. “Numerical Investigation of the Interaction between Laminar to Turbulent Transition and the Wake of an Airfoil.” *European Journal of Mechanics B/Fluids*, Vol. 57, 2016, pp. 231–248. https://doi.org/10.1016/j.euromechflu.2016.01.005.

[53] Almutairi, J., Eljack, E., and Alqadi, I. “Dynamics of Laminar Separation Bubble over NACA-0012 Airfoil near Stall Conditions.” *Aerospace Science and Technology*, Vol. 68, 2017, pp. 193–203. https://doi.org/10.1016/j.ast.2017.05.015.

[54] Winslow, J., Otsuka, H., Govindarajan, B., and Chopra, I. “Basic Understanding of Airfoil Characteristics at Low Reynolds Numbers.” *Journal of Aircraft*, 2017, pp. 1–12. https://doi.org/10.2514/6.2018-2061.

[55] Koca, K., Genç, M. S., Açıkel, H. H., Çağdaş, M., and Bodur, T. M. “Identification of Flow Phenomena over NACA 4412 Wind Turbine Airfoil at Low Reynolds Numbers and Role of Laminar Separation Bubble on Flow Evolution.” *Energy*, Vol. 144, 2018, pp. 750–764. https://doi.org/10.1016/j.energy.2017.12.045.

[56] Rojratsirikul, P., Genc, M. S., Wang, Z., and Gursul, I. “Flow-Induced Vibrations of Low Aspect Ratio Rectangular Membrane Wings.” *Journal of Fluids and Structures*, Vol. 27, No. 8, 2011, pp. 1296–1309. https://doi.org/10.1016/j.jfluidstructs.2011.06.007.

[57] ARUNVINTHAN, S., and NADARAJA PILLAI, S. “Aerodynamic Characteristics of Unsymmetrical Aerofoil at Various Turbulence Intensities.” *Chinese Journal of Aeronautics*, Vol. 32, No. 11, 2019, pp. 2395–2407. https://doi.org/10.1016/j.cja.2019.05.014.

[58] Bartl, J., Sagmo, K. F., Bracchi, T., and Sætran, L. “Performance of the

NREL S826 Airfoil at Low to Moderate Reynolds Numbers—A Reference Experiment for CFD Models." *European Journal of Mechanics, B/Fluids*, Vol. 75, 2019, pp. 180–192. https://doi.org/10.1016/j.euromechflu.2018.10.002.

[59] Marchman, J. F., and Werme, T. D. Clark-Y Airfoil Performance at Low Reynolds Numbers. 1984.

[60] Kim, Dong-ha, Jo-Won Chang, J. C. "Low-Reynolds-Number Effect on Aerodynamic Characteristics of a NACA 0012 Airfoil." *Journal of Aircraft*, Vol. 48, No. 4, 2011, pp. 1212–1215. https://doi.org/10.2514/1.C031223.

[61] Zhang, S., Li, H., and Abbasi, A. A. "Design Methodology Using Characteristic Parameters Control for Low Reynolds Number Airfoils." *Aerospace Science and Technology*, Vol. 86, 2019, pp. 143–152. https://doi.org/10.1016/j.ast.2019.01.003.

[62] Lienhard, J. H. Synopsis of Lift, Drag, and Vortex Frequency Data for Rigid Circular Cylinders. *Bull. 300*. 1--32, Washington State University. www.uh.edu.

[63] Roshko, A. "Experiments on the Flow Past a Circular Cylinder at Very High Reynolds Number." *Journal of Fluid Mechanics*, Vol. 10, No. 03, 1961, p. 345. https://doi.org/10.1017/S0022112061000950.

[64] Zaman, K. B. M. Q., Mckinzie, D. J., and Rumsey, C. L. *A Natural Low-Frequency Oscillation of the Flow over an Airfoil near Stalling Conditions*. 1989.

[65] Pauley, L. L., Moin, P., and Reynolds, W. C. "The Structure of Two-Dimensional Separation." *J . Fluid Mech*, Vol. 220, 1990, pp. 397--411. https://doi.org/10.1017/S0022112090003317.

[66] Ripley, M. D., and Pauley, L. L. “The Unsteady Structure of Two-dimensional Steady Laminar Separation.” *Physics of Fluids A: Fluid Dynamics*, Vol. 5, No. 12, 1993, pp. 3099–3106. https://doi.org/10.1063/1.858719.

[67] Huang, R. F., and Lee, H. W. “Turbulence Effect on Frequency Characteristics of Unsteady Motions in Wake of Wing.” *AIAA Journal*, Vol. 38, No. 1, 2000.

[68] Huang, R. F., and Lin, C. L. “Vortex Shedding and Shear-Layer Instability of Wing at Low Reynolds Number.” *AIAA Journal*, Vol. 33, No. 8, 1995, pp. 1398–1403.

[69] Yarusevych, S., Sullivan, P. E., and Kawall, J. G. “On Vortex Shedding from an Airfoil in Low-Reynolds-Number Flows.” *J. Fluid Mech.*, Vol. 632, 2009, pp. 245–271. https://doi.org/10.1017/S0022112009007058.

[70] Yarusevych, S., and H. Boutilier, M. S. “Vortex Shedding of an Airfoil at Low Reynolds Numbers.” *AIAA Journal*, Vol. 49, No. 10, 2011, pp. 2221–2227. https://doi.org/10.2514/1.J051028.

[71] Rostami, A. B., Mobasheramini, M., and Fernandes, A. C. “Strouhal Number of Flat and Flapped Plates at Moderate Reynolds Number and Different Angles of Attack: Experimental Data.” *Acta Mechanica*, 2018. https://doi.org/10.1007/s00707-018-2292-2.

[72] Pellegrino, A., and Meskell, C. “Vortex Shedding from a Wind Turbine Blade Section at High Angles of Attack.” *Journal of Wind Engineering and Industrial Aerodynamics*, Vol. 121, 2013, pp. 131–137. https://doi.org/10.1016/j.jweia.2013.08.002.

[73] Mueller, T. J., and Batill, S. M. Experimental Studies of the Laminar Separation Bubble on a Two-Dimensional Airfoil at Low Reynolds Numbers. 1980.

[74] Arena, A. V., and Mueller, T. J. "Laminar Separation, Transition, and Turbulent Reattachment near the Leading Edge of Airfoils." *AIAA Journal*, Vol. 18, No. 7, 1980, pp. 747–753. https://doi.org/10.2514/3.50815.

[75] Korkan, K. D., Jr, E. J. C., and Cornellj, C. C. "Experimental Aerodynamic Characteristics of an NACA 0012 Airfoil with Simulated Ice." *J. Aircraft*, Vol. 22, No. 2, 1984, pp. 130–134.

[76] Bragg, M. B. "Effect of Geometry on Airfoil Icing Characteristics." *Journal of Aircraft*, Vol. 21, No. 7, 1984.

[77] Bragg, M. B. "Predicting Rime Ice Accretion on Airfoils." *AIAA Journal*, Vol. 23, No. 3, 1985, pp. 381–387. https://doi.org/10.2514/3.8924.

[78] Bragg, M. B., Gregorek, G. M., and Lee, J. D. "Airfoil Aerodynamics in Icing Conditions." *Journal of Aircraft*, Vol. 23, No. 1, 1985, pp. 76–81.

[79] Potapczuk, M. G. "Numerical Analysis of an NACA 0012 Airfoil with Leading-Edge Ice Accretions." *Journal of Aircraft*, Vol. 25, No. 3, 1988.

[80] Lee, S., and Bragg, M. B. "Investigation of Factors Affecting Iced-Airfoil Aerodynamics." *Journal of Aircraft*, Vol. 40, No. 3, 2003.

[81] Mirzaei, M., Ardekani, M. A., and Doosttalab, M. "Numerical and Experimental Study of Flow Field Characteristics of an Iced Airfoil." *Aerospace Science and Technology*, Vol. 13, No. 6, 2009, pp. 267–276. https://doi.org/10.1016/j.ast.2009.05.002.

[82] Zhang, Y., Igarashi, T., and Hu, H. Experimental Investigations on the Performance Degradation of a Low-Reynolds-Number Airfoil with Distributed Leading Edge Roughness. 2011.

[83] Dropkin, A., Custodio, D., Henoch, C. W., and Johari, H. "Computation of Flowfield around an Airfoil with Leading-Edge Protuberances."

Journal of Aircraft, Vol. 49, No. 5, 2012, pp. 1345–1355. https://doi.org/10.2514/1.C031675.

[84] Hansen, K. L., Kelso, R. M., and Dally, B. B. "Performance Variations of Leading-Edge Tubercles for Distinct Airfoil Profiles." *AIAA Journal*, Vol. 49, No. 1, 2011, pp. 185–194. https://doi.org/10.2514/1.J050631.

[85] Serson, D., and Meneghini, J. R. "Numerical Study of Wings with Wavy Leading and Trailing Edges." *Procedia IUTAM*, Vol. 14, No. 11, 2015, pp. 563–569. https://doi.org/10.1016/j.piutam.2015.03.069.

[86] Peristy, L. H., Perez, R. E., Asghar, A., and Allan, W. D. E. "Reynolds Number Effect of Leading Edge Tubercles on Airfoil Aerodynamics." *AIAA Aviation*, No. June, 2016. https://doi.org/10.2514/6.2016-3260.

[87] Paula, A. A. De, Padilha, B. R. M., Meneghini, J. R., and Paulo, S. The Airfoil Thickness Effect on Wavy Leading Edge. 2016.

[88] Gross, A., and Fasel, H. F. "Numerical Investigation of Passive Separation Control for an Airfoil at Low-Reynolds-Number Conditions." *AIAA Journal*, Vol. 51, No. 7, 2013. https://doi.org/10.2514/1.J051553.

[89] Zhou, Y., and Wang, Z. J. Effects of Surface Roughness on Laminar Separation Bubble over a Wing at a Low-Reynolds Number. 2011.

[90] Corten, G. P., and Veldkamp, H. F. "Aerodynamics: Insects Can Halve Wind-Turbine Power." *Nature*, Vol. 412, No. 6842, 2001, pp. 41–42. https://doi.org/10.1038/35083698.

[91] Huang, G.-Y., Shiah, Y. C., Bai, C.-J., and Chong, W. T. "Experimental Study of the Protuberance Effect on the Blade Performance of a Small Horizontal Axis Wind Turbine." *Journal of Wind Engineering and Industrial Aerodynamics*, Vol. 147, 2015, pp. 202–211. https://doi.org/https://doi.org/10.1016/j.jweia.2015.10.005.

[92] Sudhakar, S., Karthikeyan, N., and Venkatakrishnan, L. “Influence of Leading Edge Tubercles on Aerodynamic Characteristics of a High Aspect-Ratio UAV.” *Aerospace Science and Technology*, Vol. 69, 2017, pp. 281–289. https://doi.org/https://doi.org/10.1016/j.ast.2017.06.031.

[93] Bolzon, M. D., Kelso, R. M., and Arjomandi, M. “Performance Effects of a Single Tubercle Terminating at a Swept Wing’s Tip.” *Experimental Thermal and Fluid Science*, Vol. 85, 2017, pp. 52–68. https://doi.org/https://doi.org/10.1016/j.expthermflusci.2017.02.016.

[94] Wang, H., Zhang, B., Qiu, Q., and Xu, X. “Flow Control on the NREL S809 Wind Turbine Airfoil Using Vortex Generators.” *Energy*, Vol. 118, 2017, pp. 1210–1221. https://doi.org/https://doi.org/10.1016/j.energy.2016.11.003.

[95] Luo, D., Huang, D., and Sun, X. “Passive Flow Control of a Stalled Airfoil Using a Microcylinder.” *Journal of Wind Engineering and Industrial Aerodynamics*, Vol. 170, 2017, pp. 256–273. https://doi.org/https://doi.org/10.1016/j.jweia.2017.08.020.

[96] Sreejith, B. K., and Sathyabhama, A. “Numerical Study on Effect of Boundary Layer Trips on Aerodynamic Performance of E216 Airfoil.” *Engineering Science and Technology, an International Journal*, Vol. 21, No. 1, 2018, pp. 77–88. https://doi.org/10.1016/j.jestch.2018.02.005.

[97] Wei, Z., New, T. H., Lian, L., and Zhang, Y. “Leading-Edge Tubercles Delay Flow Separation for a Tapered Swept-Back Wing at Very Low Reynolds Number.” *Ocean Engineering*, Vol. 181, 2019, pp. 173–184. https://doi.org/https://doi.org/10.1016/j.oceaneng.2019.04.018.

[98] Wei, Z., Toh, J. W. A., Ibrahim, I. H., and Zhang, Y. “Aerodynamic Characteristics and Surface Flow Structures of Moderate Aspect-Ratio Leading-Edge Tubercled Wings.” *European Journal of Mechanics -*

B/Fluids, Vol. 75, 2019, pp. 143–152. https://doi.org/https://doi.org/10.1016/j.euromechflu.2019.01.001.

[99] Chen, W., Qiao, W., and Wei, Z. "Aerodynamic Performance and Wake Development of Airfoils with Wavy Leading Edges." *Aerospace Science and Technology*, Vol. 106, 2020, p. 106216. https://doi.org/https://doi.org/10.1016/j.ast.2020.106216.

[100] W.A, K. Aircraft Wing with Vortex Generation, , 1974.

[101] Wang, Z., Yeo, K. S., and Khoo, B. C. Numerical Simulation of Laminar Channel Flow over Dimpled Surface. 2003.

[102] Faure, T. M., Adrianos, P., Lusseyran, F., and Pastur, L. "Visualizations of the Flow inside an Open Cavity at Medium Range Reynolds Numbers." *Experiments in Fluids*, Vol. 42, 2007, pp. 169–184. https://doi.org/10.1007/s00348-006-0188-8.

[103] Chernyshenko, S., and Quinn, S. *VortexCell2050*. 2009.

[104] Donelli, R. S., Iannelli, P., Iuliano, E., and Rosa, D. De. "Suction Optimization on Thick Airfoil to Trap Vortices." 2010, pp. 1–10.

[105] Donelli, R. S., De Gregorio, F., and Pierluigi, I. "Flow Separation Control by Trapped Vortex." *48th AIAA Aerospace Sciences Meeting Including the New Horizons Forum and Aerospace Exposition*, No. January, 2010, pp. 1–19.

[106] Gregorio, F. De, and Fraioli, G. "Flow Control on a High Thickness Airfoil by a Trapped Vortex Cavity." *14th Int Symp on Applications of Laser Techniques to Fluid Mechanics*, Vol. 228, No. 4, 2012, pp. 557–566. https://doi.org/10.3813/AAA.918541.

[107] Taherian, G., Nili-Ahmadabadi, M., Karimi, M. H., and Tavakoli, M. R. "Flow Visualization over a Thick Blunt Trailing-Edge Airfoil with Base

Cavity at Low Reynolds Numbers Using PIV Technique." *Journal of Visualization*, No. 2010, 2016. https://doi.org/10.1007/s12650-016-0405-3.

[108] J. Olsman, W. F., and Colonius, T. "Numerical Simulation of Flow over an Airfoil with a Cavity." *AIAA Journal*, Vol. 49, No. 1, 2011, pp. 143–149. https://doi.org/10.2514/1.J050542.

[109] Zope, A., and Janus, J. M. Response Surface Analysis of Trapped-Vortex Augmented Airfoils. 2013.

[110] Gunasekaran, S., and Gerham, T. "Effect of Chordwise Slots on Aerodynamic Efficiency and Wingtip Vortex." *AIAA Journal*, 2018, pp. 1–16. https://doi.org/10.2514/1.J057073.

[111] Sun, Z. C., Mao, Y. F., and Fan, M. H. "Performance Optimization and Investigation of Flow Phenomena on Tidal Turbine Blade Airfoil Considering Cavitation and Roughness." *Applied Ocean Research*, Vol. 106, No. December 2020, 2021, p. 102463. https://doi.org/10.1016/j.apor.2020.102463.

[112] Vuddagiri, A., Halder, P., Samad, A., and Chaudhuri, A. "Flow Analysis of Airfoil Having Different Cavities on Its Suction Surface." *Progress in Computational Fluid Dynamics*, Vol. 16, No. 2, 2016, pp. 67–77. https://doi.org/10.1504/PCFD.2016.075151.

[113] Sobhani, E., Ghaffari, M., and Maghrebi, M. J. "Numerical Investigation of Dimple Effects on Darrieus Vertical Axis Wind Turbine." *Energy*, Vol. 133, 2017, pp. 231–241. https://doi.org/https://doi.org/10.1016/j.energy.2017.05.105.

[114] Liu, Y., Li, P., He, W., and Jiang, K. "Numerical Study of the Effect of Surface Grooves on the Aerodynamic Performance of a NACA 4415 Airfoil for Small Wind Turbines." *Journal of Wind Engineering and*

Industrial Aerodynamics, Vol. 206, 2020, p. 104263. https://doi.org/https://doi.org/10.1016/j.jweia.2020.104263.

[115] Ge, M., Zhang, H., Wu, Y., and Li, Y. "Effects of Leading Edge Defects on Aerodynamic Performance of the S809 Airfoil." *Energy Conversion and Management*, Vol. 195, 2019, pp. 466–479. https://doi.org/https://doi.org/10.1016/j.enconman.2019.05.026.

[116] Mohamed, O. S., Ibrahim, A. A., Etman, A. K., Abdelfatah, A. A., and Elbaz, A. M. R. "Numerical Investigation of Darrieus Wind Turbine with Slotted Airfoil Blades." *Energy Conversion and Management: X*, Vol. 5, 2020, p. 100026. https://doi.org/https://doi.org/10.1016/j.ecmx.2019.100026.

[117] Sooraj, P., Sharma, A., and Agrawal, A. "Dynamics of Co-Rotating Vortices in a Flow around a Bio-Inspired Corrugated Airfoil." *International Journal of Heat and Fluid Flow*, Vol. 84, 2020, p. 108603. https://doi.org/https://doi.org/10.1016/j.ijheatfluidflow.2020.108603.

[118] Max Kramer. *Increase in the Maximum Lift of an Airplane Wing Due to a Sudden in Its Effective Angle of Attack Resulting from a Gust*. 1932.

[119] Crimi, P., and Reeves, B. L. *A Method for Analyzing Dynamic Stall of Helicopter Rotor Blades*. 1972.

[120] McCroskey, W. J., Carr, L. W., and McAlister, K. W. "Dynamic Stall Experiments on Oscillating Airfoils." *AIAA Journal*, Vol. 14, No. 1, 1976, pp. 57–63. https://doi.org/10.2514/3.61332.

[121] McCroskey, W., Mcalister, K. W., Cara, L. W., Pucci, S. ., Lambert, O., and Indergand, L. R. F. Dynamic Stall on Advanced Airfoil Sections. 1980.

[122] McAlister, K. W., and Carr, L. W. "Water Tunnel Visualizations of

Dynamic Stall." *ASME, Fluid Engineering*, Vol. 101, 1978, pp. 376–380.

[123] Lee, T., and Gerontakos, P. "Investigation of Flow over an Oscillating Airfoil." *Journal of Fluid Mechanics*, Vol. 512, 2004, pp. 313–341. https://doi.org/10.1017/S0022112004009851.

[124] Wernert, P., Geissler, W., Raffel, M., and Kompenhans, J. "Experimental and Numerical Investigations of Dynamic Stall on a Pitching Airfoil." *AIAA Journal*, Vol. 34, No. 5, 1996, pp. 982–989. https://doi.org/10.2514/3.13177.

[125] Wang, S., Ingham, D. B., Ma, L., Pourkashanian, M., and Tao, Z. "Numerical Investigations on Dynamic Stall of Low Reynolds Number Flow around Oscillating Airfoils." *Computers and Fluids*, Vol. 39, No. 9, 2010, pp. 1529–1541. https://doi.org/10.1016/j.compfluid.2010.05.004.

[126] Gharali, K., and Johnson, D. A. "Dynamic Stall Simulation of a Pitching Airfoil under Unsteady Freestream Velocity." *Journal of Fluids and Structures*, 2013, pp. 1–17. https://doi.org/10.1016/j.jfluidstructs.2013.05.005.

[127] Jung, Y. W., and Park, S. O. "Vortex-Shedding Characteristics in the Wake of an Oscillating Airfoil at Low Reynolds Number." *Journal of Fluids and Structures*, Vol. 20, No. 3, 2005, pp. 451–464. https://doi.org/10.1016/j.jfluidstructs.2004.11.002.

[128] Choudhry, A., Arjomandi, M., and Kelso, R. "Methods to Control Dynamic Stall for Wind Turbine Applications." *Renewable Energy*, Vol. 86, 2016, pp. 26–37. https://doi.org/10.1016/j.renene.2015.07.097.

[129] Xu, H.-Y., Qiao, C.-L., and Ye, Z.-Y. "Dynamic Stall Control on the Wind Turbine Airfoil via a Co-Flow Jet." *Energies*, Vol. 9, No. 6, 2016, p. 429. https://doi.org/10.3390/en9060429.

[130] Niu, J., Lei, J., and Lu, T. “Numerical Research on the Effect of Variable Droop Leading-Edge on Oscillating NACA 0012 Airfoil Dynamic Stall.” *Aerospace Science and Technology*, Vol. 72, 2018, pp. 476–485. https://doi.org/10.1016/j.ast.2017.11.030.

[131] Hand, B., Kelly, G., and Cashman, A. “Numerical Simulation of a Vertical Axis Wind Turbine Airfoil Experiencing Dynamic Stall at High Reynolds Numbers.” *Computers & Fluids*, Vol. 149, 2017, pp. 12–30. https://doi.org/https://doi.org/10.1016/j.compfluid.2017.02.021.

[132] Guoqiang, L., Weiguo, Z., Yubiao, J., and Pengyu, Y. “Experimental Investigation of Dynamic Stall Flow Control for Wind Turbine Airfoils Using a Plasma Actuator.” *Energy*, Vol. 185, 2019, pp. 90–101. https://doi.org/https://doi.org/10.1016/j.energy.2019.07.017.

[133] Rezaeiha, A., Montazeri, H., and Blocken, B. “CFD Analysis of Dynamic Stall on Vertical Axis Wind Turbines Using Scale-Adaptive Simulation (SAS): Comparison against URANS and Hybrid RANS/LES.” *Energy Conversion and Management*, Vol. 196, 2019, pp. 1282–1298. https://doi.org/https://doi.org/10.1016/j.enconman.2019.06.081.

[134] Wang, L., Wang, C., and Sun, L. “Study on Influence of Environmental Parameters on Dynamic Stall Characteristics of Wind Turbine Blades.” *Journal of The Institution of Engineers (India): Series C*, 2020. https://doi.org/10.1007/s40032-020-00565-8.

[135] Huang, X., Albers, M., Meysonnat, P. S., Meinke, M., and Schröder, W. “Analysis of the Effect of Freestream Turbulence on Dynamic Stall of Wind Turbine Blades.” *International Journal of Heat and Fluid Flow*, Vol. 85, 2020, p. 108668. https://doi.org/https://doi.org/10.1016/j.ijheatfluidflow.2020.108668.

[136] Anderson, J. D. *Computational Fluid Dynamics, Second Edition*. 2010.

[137] Anderson, J. D. *Fundamental of Aerodynamics*. 2011.

[138] Menter, F. R., Langtry, R. B., Likki, S. R., Suzen, Y. B., Huang, P. G., and Völker, S. "A Correlation-Based Transition Model Using Local Variables: Part I — Model Formulation." *Volume 4: Turbo Expo 2004*, 2004, pp. 57–67. https://doi.org/10.1115/GT2004-53452.

[139] Menter, F. R. "Two-Equation Eddy-Viscosity Turbulence Models for Engineering Applications." *AIAA Journal*, Vol. 32, No. 8, 1994, pp. 1598–1605. https://doi.org/10.2514/3.12149.

[140] Suzen, Y. B., Huang, P. G., Hultgren, L. S., and Ashpis, D. E. "Predictions of Separated and Under Low-Pressure Turbine Airfoil Conditions Using An." *Journal of Turbomachinery*, Vol. 125, 2003, pp. 455–464. https://doi.org/10.1115/1.1580159.

[141] Menter, F. R., Langtry, R., and Völker, S. "Transition Modelling for General Purpose CFD Codes." *Flow, Turbulence and Combustion*, Vol. 77, Nos. 1–4, 2006, pp. 277–303. https://doi.org/10.1007/s10494-006-9047-1.

[142] Langtry, R. B., and Menter, F. R. "Correlation-Based Transition Modeling for Unstructured Parallelized Computational Fluid Dynamics Codes." *AIAA Journal*, Vol. 47, No. 12, 2009, pp. 2894–2906. https://doi.org/10.2514/1.42362.

[143] Chorin, A. J. "Numerical_solution_of_the_Navier-Stokes.Pdf." *Mathematics of Computation*, Vol. 22, No. 104, 1968, pp. 745–762.

[144] ANSYS Inc. *ANSYS Fluent Theory Guide*. 2013.

[145] Ohtake, T., Nakae, Y., and Motohashi, T. "Nonlinearity of the Aerodynamic Characteristics of NACA0012 Aerofoil at Low Reynolds

Numbers." *JOURNAL OF THE JAPAN SOCIETY FOR AERONAUTICAL AND SPACE SCIENCES*, Vol. 55, No. 644, 2007, pp. 439–445.

[146] Joshua N. N. Counsil and Kiari Goni Boulama. "Low-Reynolds-Number Aerodynamic Performances of the NACA0012 and Selig-Donovan 7003 Airfoils." *Journal of Aircraft*, Vol. 50, No. 1, 2013. https://doi.org/10.2514/1.C031856.

[147] Barlow, J. B., H. Rae, W., and Pope, A. *Low-Speed Wind Tunnel Testing, 3rd Edition*. 1999.

[148] Measurements, S. *Six Component Balance System For Wind Tunnel*. 2019.

[149] Measurements, S. *Hot-Wire Anemometer and Its Related Instruments Instruction Manual*. 2019.

[150] Hunt, J. C. R., Wray, A. A., and Moin, P. Eddies, Streams, and Convergence Zones in Turbulent Flows. 1988.

APPENDICES

APPENDIX A

Table A.1: Locations of Pressure Tapings on Wind Tunnel Model

S. No	**Location (in terms of Chord)**
1	Leading Edge
2	Suction Surface – 0.05c
3	Suction Surface – 0.10c
4	Suction Surface – 0.15c
5	Suction Surface – 0.20c
6	Suction Surface – 0.35c
7	Suction Surface – 0.50c
8	Suction Surface – 0.70c
9	Suction Surface – 0.80c
10	Pressure Surface – 0.05c
11	Pressure Surface – 0.10c
12	Pressure Surface – 0.20c
13	Pressure Surface – 0.35c
14	Pressure Surface – 0.50c
15	Pressure Surface – 0.70c
16	Pressure Surface – 0.80c

APPENDIX B

CIRCULAR PROTRUSION

Circular Protrusion at 0.75c on Suction Surface

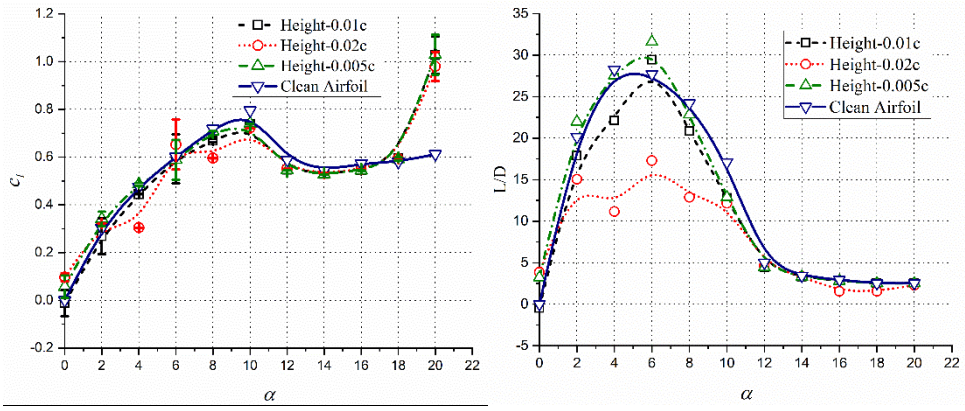

(a) *Lift Coefficient versus α* (b) *Time-averaged L/D versus α*

Figure B.1: Aerodynamics characteristic of an airfoil with protrusion located at 0.75c on the suction surface

Circular Protrusion at 0.10c on Pressure Surface

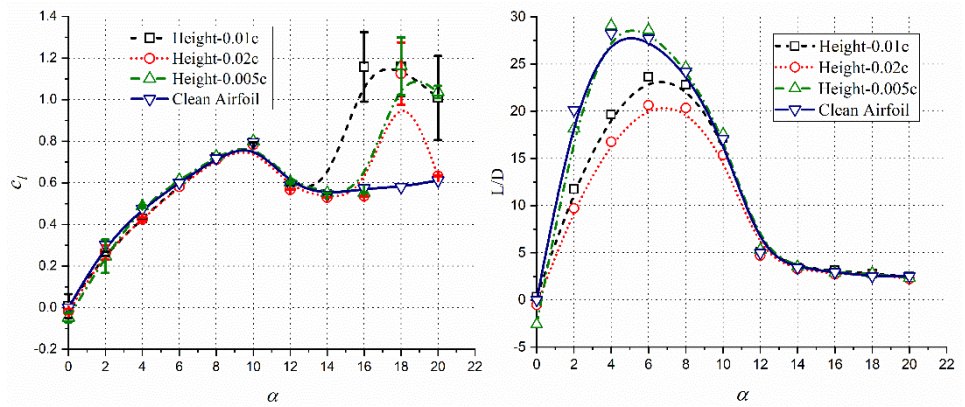

(a) Lift Coefficient versus α *(b) Time-averaged L/D versus α*

Figure B.2: Aerodynamics characteristic of an airfoil with protrusion located at 0.10c on the Pressure surface

Circular Protrusion at 0.25c on Pressure Surface

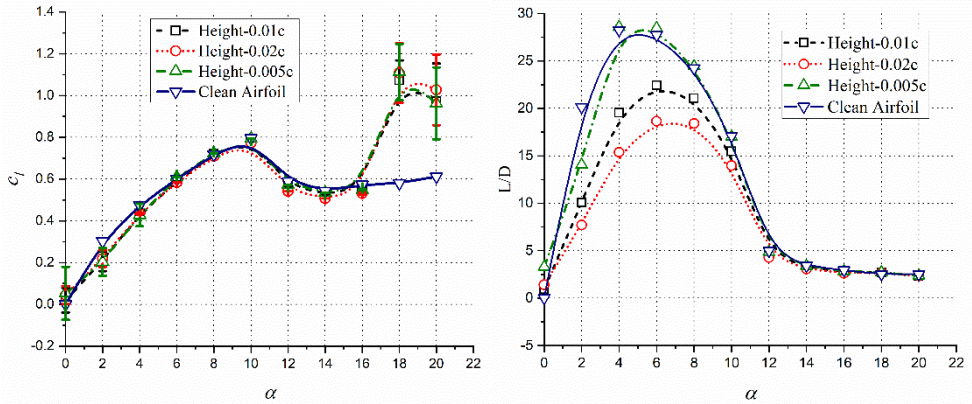

(a) Lift Coefficient versus α *(b) Time-averaged L/D versus α*

Figure B.3: Aerodynamic coefficients of an airfoil with a circular protrusion at 0.25c on the lower surface

Circular Protrusion at 0.50c on Pressure Surface

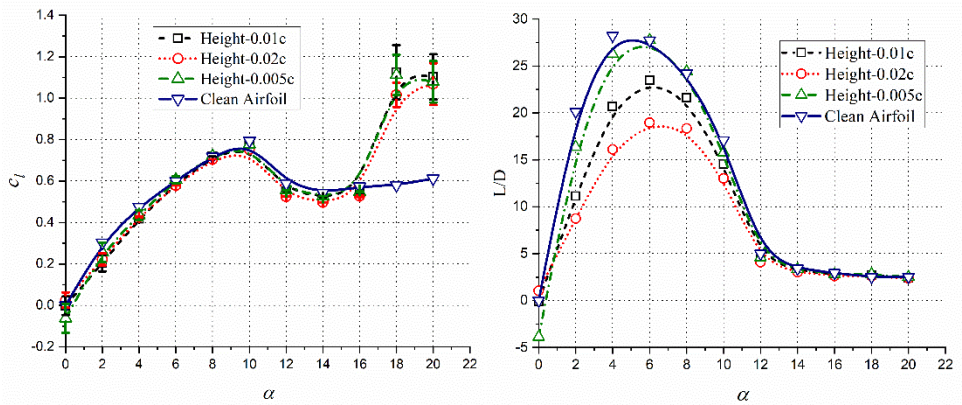

(a) Lift Coefficient versus α *(b) Time-averaged L/D versus α*

Figure B.4: Aerodynamic coefficients of an airfoil with a circular protrusion at 0.50c on the lower surface

Circular Protrusion at 0.75c on Pressure Surface

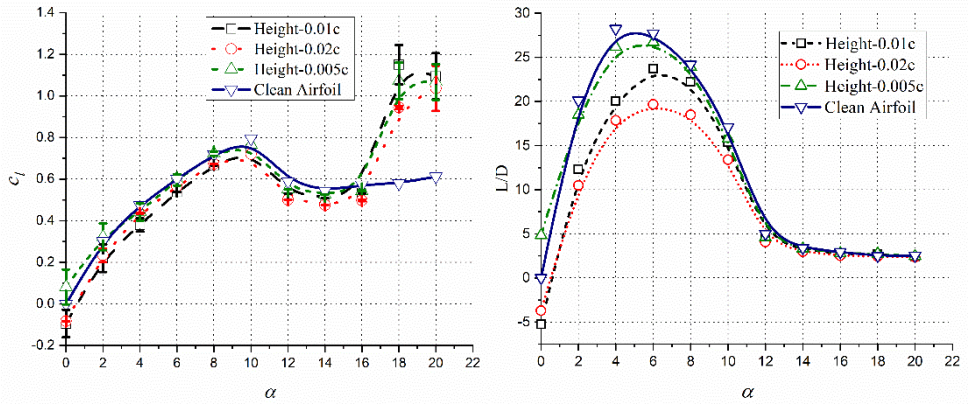

(a) Lift Coefficient versus α *(b) Time-averaged L/D versus α*

Figure B.5: Aerodynamic coefficients of an airfoil with a circular protrusion at 0.75c on the lower surface

TRIANGULAR PROTRUSION

Triangular Protrusion at 0.10c on Suction Surface

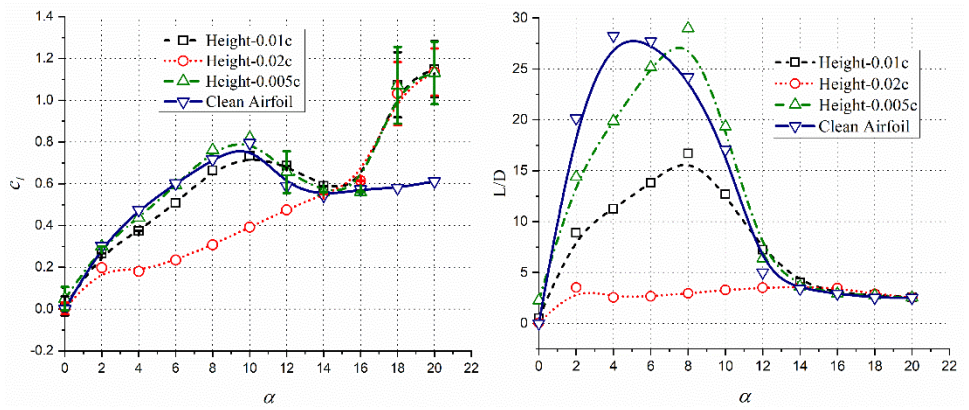

(a) Lift Coefficient versus α *(b) Time-averaged L/D versus α*

Figure B.6: Aerodynamic characteristics of Triangular Protrusion on Suction surface at 0.10c

Triangular Protrusion at 0.25c on Suction Surface

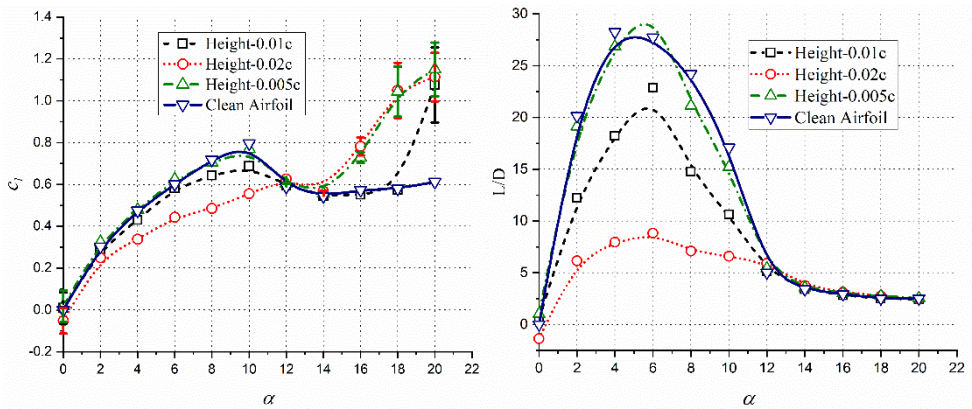

(a) Lift Coefficient versus α *(b) Time-averaged L/D versus α*

Figure B.7: Aerodynamic characteristics of Triangular Protrusion on Suction surface at 0.25c

Triangular Protrusion at 0.50c on Suction Surface

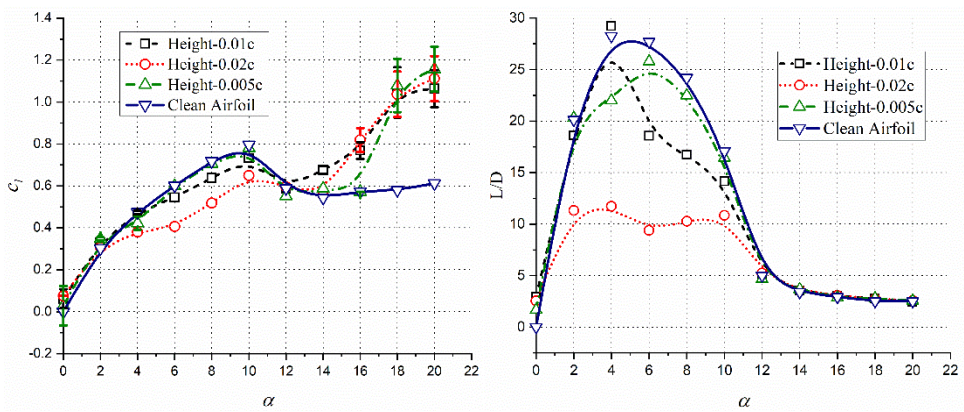

(a) Lift Coefficient versus α *(b) Time-averaged L/D versus α*

Figure B.8: Aerodynamic characteristics of Triangular Protrusion on Suction surface at 0.5c

Triangular Protrusion at 0.75c on Suction Surface

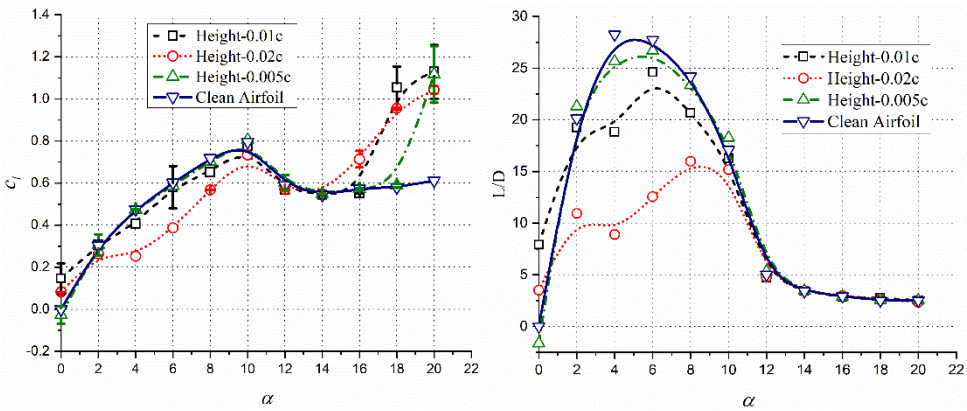

(a) Lift Coefficient versus α *(b) Time-averaged L/D versus α*

Figure B.9: Aerodynamic characteristics of Triangular Protrusion on Suction surface at 0.75c

Triangular Protrusion at 0.10c on Pressure Surface

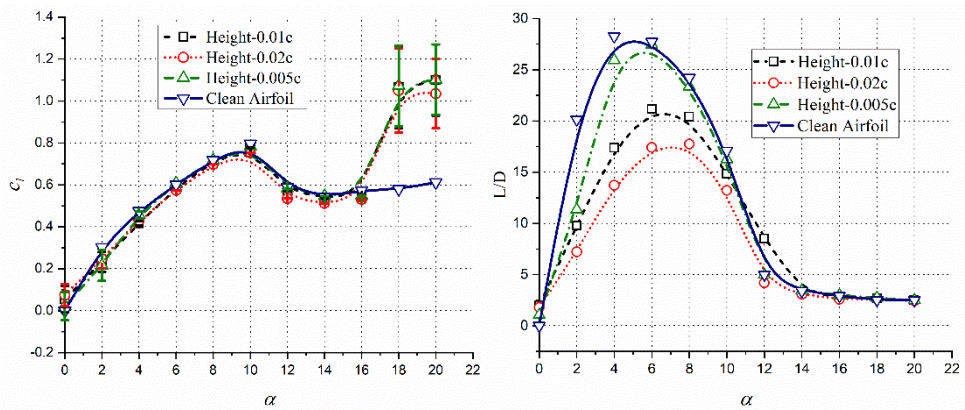

(a)Lift Coefficient versus α *(b) Time-averaged L/D versus α*

Figure B.10: Lift and drag variations of NACA0012 with a protrusion at 10%c on the pressure surface

Triangular Protrusion at 0.25c on Pressure Surface

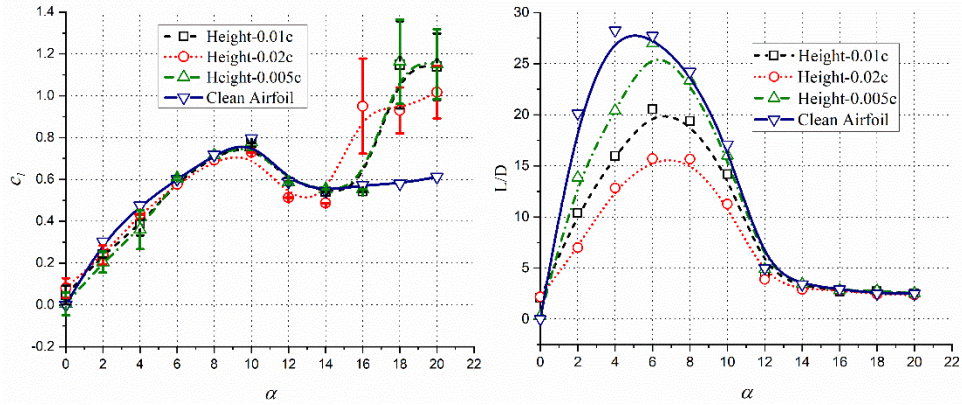

(a)Lift Coefficient versus α *(b) Time-averaged L/D versus α*

Figure B.11: Lift and drag variations of NACA0012 with a protrusion at 25%c on the pressure surface

Triangular Protrusion at 0.10c on Pressure Surface

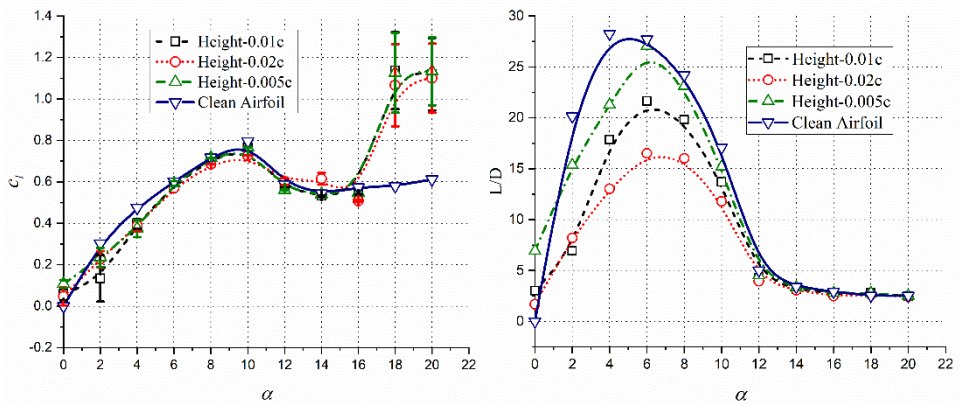

(a)Lift Coefficient versus α *(b) Time-averaged L/D versus α*

Figure B.12: Lift and drag variations of NACA0012 with a protrusion at 50%c on the pressure surface

Triangular Protrusion at 0.10c on Pressure Surface

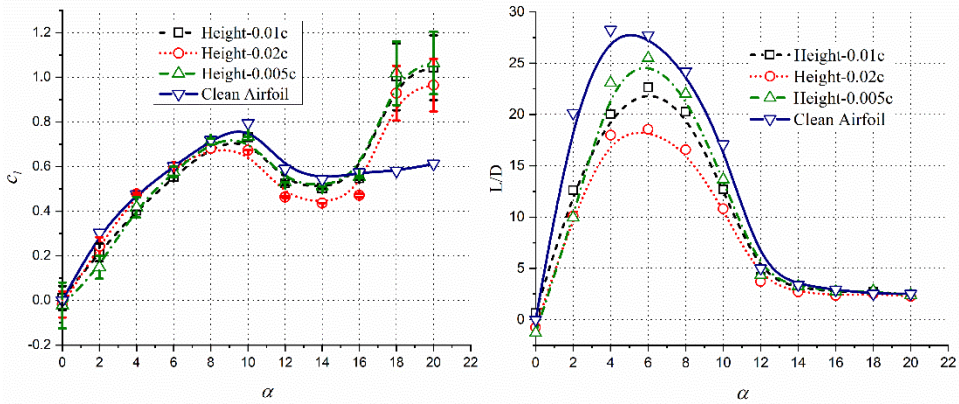

(a)Lift Coefficient versus α *(b) Time-averaged L/D versus α*

Figure B.13: Lift and drag variations of NACA0012 with a protrusion at 75%c on the pressure

APPENDIX C

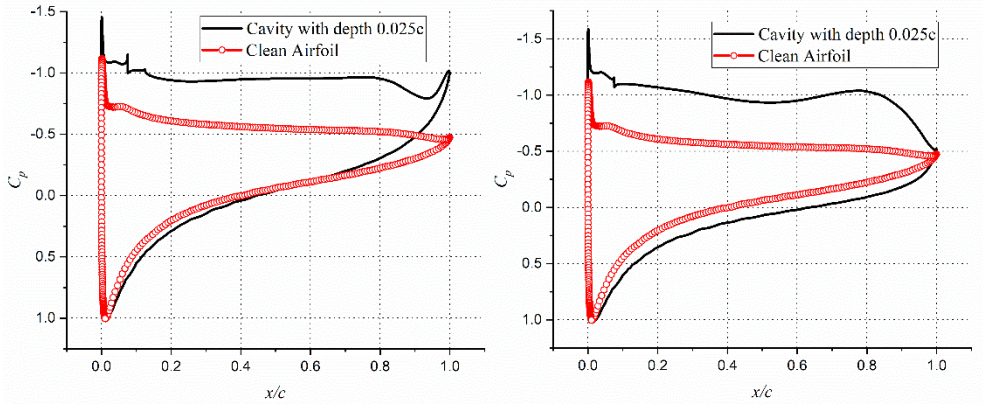

(a) Lower Lift coefficient *(b) Higher Lift coefficient*

Figure C.1: Pressure distribution over an NACA 0012 airfoil with cavity at 0.10c location at 16º

Figure C.2: Small Bubbles on the Surface of the airfoil with cavity depth 0.025c at 0.10c location, 2º

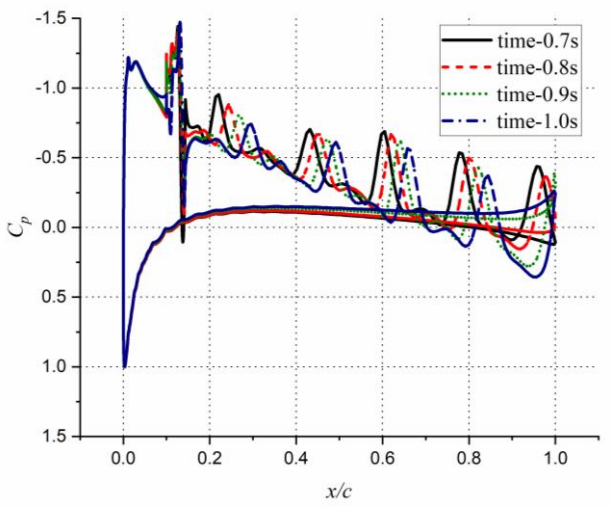

Figure C.3: Pressure distribution of cavity with depth 0.025c at 0.10c location, at 4º

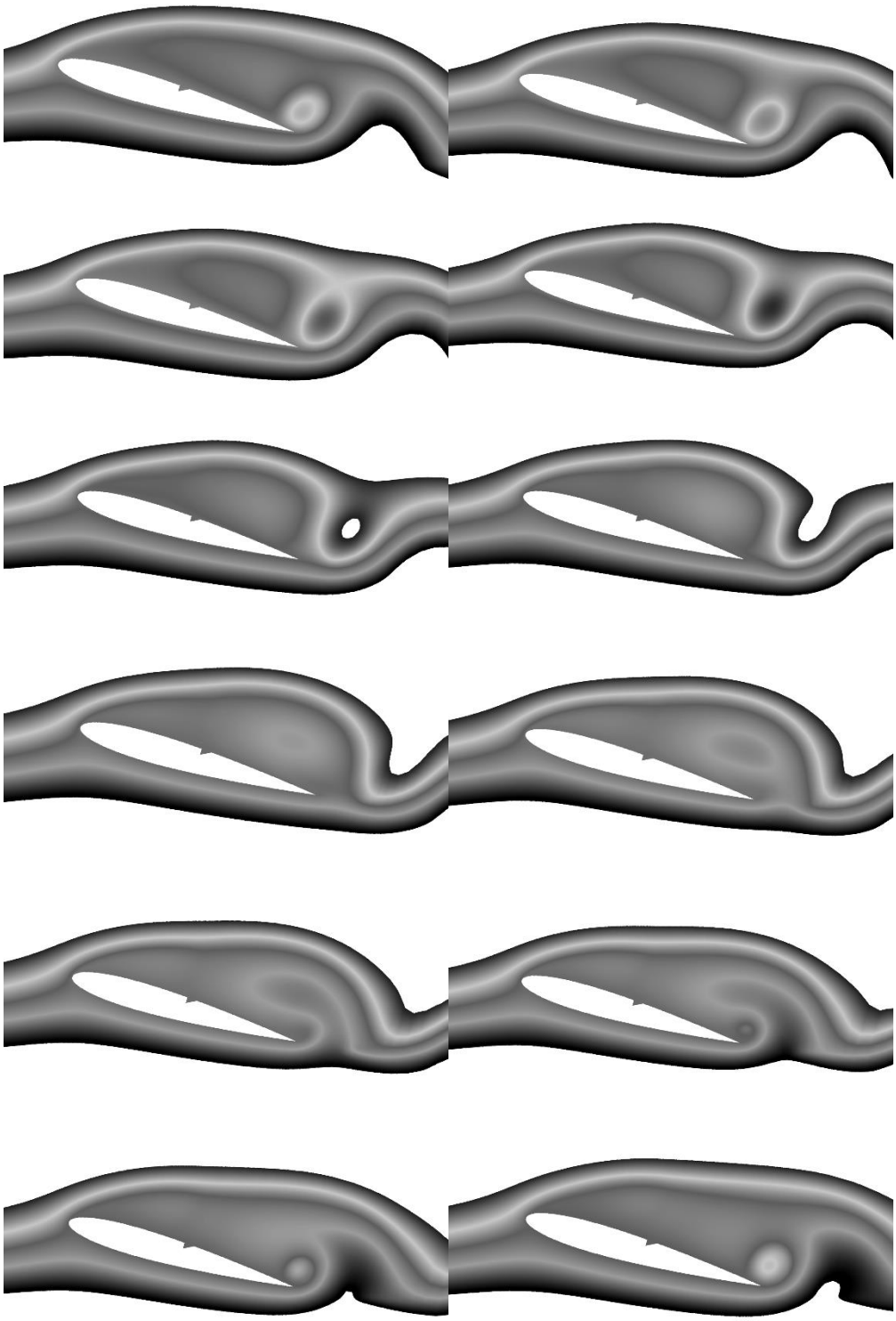

Figure C.4: Instantaneous vortices with cavity depth 0.025c at 0.50c location at 16º

APPENDIX D

Circular Protrusion at 0.05c Location

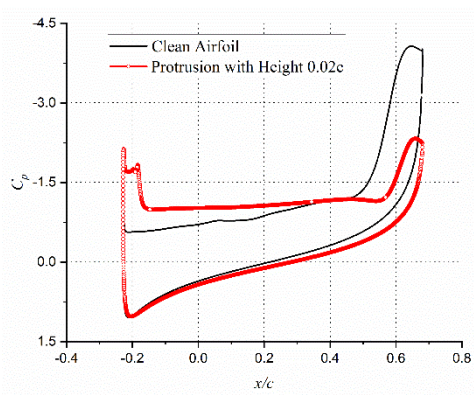

(a) Down-stroke – 24.89º

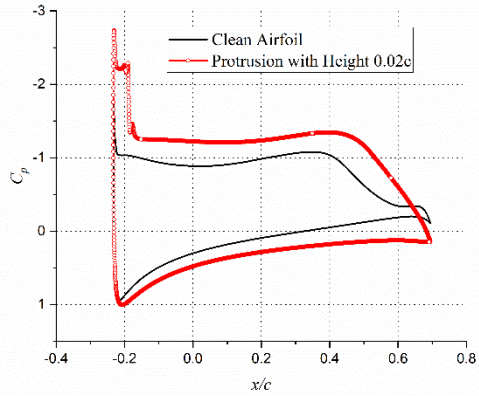

(b) Down-Stroke – 22.21º

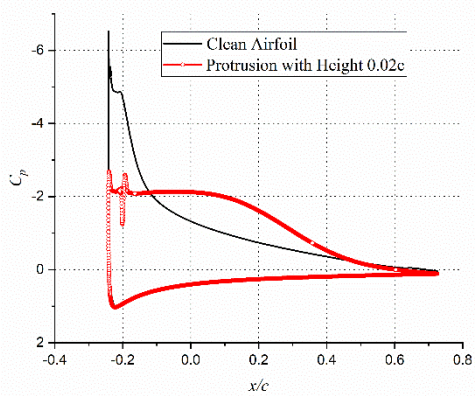

(c) Up-stroke – 14.76º

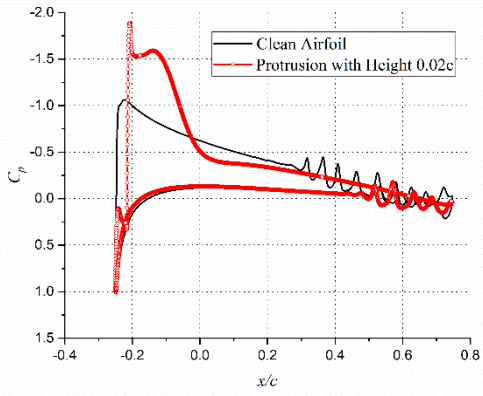

(d) Up-Stroke – 4.728º

Figure D.1: Pressure Distribution over airfoil with protrusion located at 0.05c

Circular Protrusion at 0.25c Location

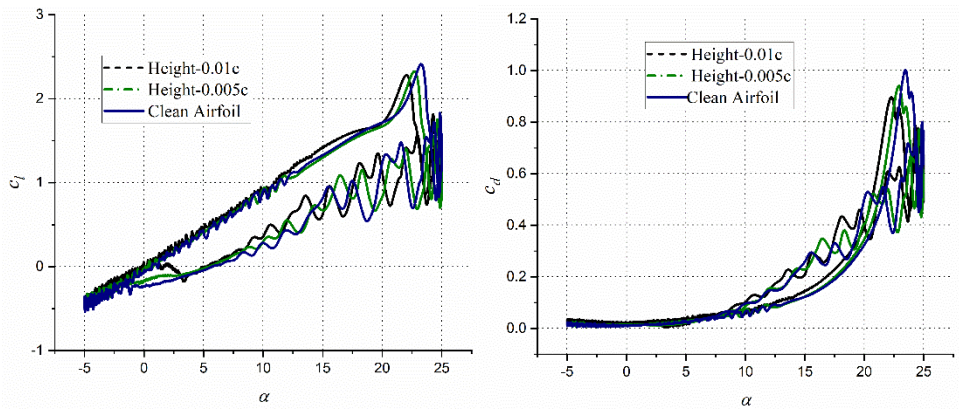

(a) Coefficient of Lift versus α *(b) Coefficient of Drag versus α*

Figure D.2: Aerodynamic characteristics of the circular protrusion at 0.25c Location

Bodavula Aslesha

EDUCATION

2013-2015	M.Tech in Computational Fluid Dynamics (CFD), University of Petroleum & Energy Studies (UPES), Dehradun
2009-2013	B.Tech in Aeronautical Engineering, Jyothishamthi College of Engineering and Technology affiliated to JNTU-Hyderabad, Shamirpet, Andhra Pradesh

JOURNAL PUBLICATIONS

- A Bodavula, R Yadav, U Guven, "Numerical Investigation of the Unsteady Aerodynamics of NACA0012 with Suction Surface Protrusion", Aircraft Engineering and Aerospace Technology, Vol. (92), Issue-2, pp. 186-200
- A Bodavula, R Yadav, U Guven., "Stall Mitigation and Lift Enhancement of NACA 0012 with Triangle Shaped Surface Protrusion at a Reynolds Number of 10^5", SAE International Journal of Aerospace, Vol. (12), Issue(2),2019
- A Bodavula, U Guven, R Yadav., "Numerical Analysis of Protrusion effect over an Airfoil at Re-10^5" International Journal of Recent Technology and Engineering, Vol. (8), Issue-2, 2019.
- A Bodavula , R Yadav "Effect of Suction Surface Cavity on the Dynamic Stall Characteristics of an Airfoil" Under review in Part G: Journal of Aerospace Engineering **(Sci-E).**
- A Bodavula , R Yadav "Effect of Triangular Cavity on the Unsteady Aerodynamics of an Airfoil" under review in Part G: Journal of Aerospace Engineering **(Sci-E).**

- A Bodavula**,** R Yadav“Aerodynamic Efficiency Enhancement of an Airfoil at Low Reynolds Number with a Transverse Semi-circular Groove” under review in European Journal of Mechanics / B Fluids **(Sci-E)**

CONFERENCE

“The study of the effect of the cavity on the flow over NACA 0012 and Selig 7003 aerofoil at Low Reynolds number using Vortex Shading Method” AIAA SciTech Forum, Orlando, January 2020.

urkund

Document Information

Analyzed document	Final_Thesis_Done.docx (D80591077)
Submitted	10/3/2020 2:01:00 PM
Submitted by	Rajesh
Submitter email	rajeshyadav@ddn.upes.ac.in
Similarity	1%
Analysis address	rajeshyadav.upes@analysis.urkund.com

Sources included in the report

SA	**MSc_Thesis_Dedeic.pdf** Document MSc_Thesis_Dedeic.pdf (D11831179)	3
SA	**Thesis 20.1.19.pdf** Document Thesis 20.1.19.pdf (D47135787)	3
W	URL: https://www.researchgate.net/publication/277833455_Transitional_separation_bubbles ... Fetched: 11/1/2019 10:53:46 AM	5
W	URL: https://faculty.eng.ufl.edu/aprg/wp-content/uploads/sites/130/2019/01/AIAA_ASM2012 ... Fetched: 11/16/2019 12:24:10 AM	2
W	URL: https://www.researchgate.net/publication/23617561_Experimental_studies_of_separati ... Fetched: 12/14/2019 9:41:51 AM	5
W	URL: https://www.researchgate.net/publication/335664557_Low-Frequency_Oscillation_over_ ... Fetched: 1/23/2020 11:48:45 AM	1
W	URL: https://www.researchgate.net/publication/269193369_Effects_of_Reynolds_Number_and_ ... Fetched: 12/22/2019 11:25:54 AM	1
J	**International Journal of Rotating Machinery** URL: 90c2bf4e-c65a-42c7-baaf-18f0807e2e59 Fetched: 3/23/2019 8:07:42 AM	3
SA	**14788141.pdf** Document 14788141.pdf (D57657086)	2
SA	**fym final.docx** Document fym final.docx (D73796516)	1
SA	**11210332005-1.docx** Document 11210332005-1.docx (D43263186)	1